



**HAL**  
open science

# Étude d'un écoulement en circulation naturelle d'hélium diphasique en régime transitoire

Hernan Furci

► **To cite this version:**

Hernan Furci. Étude d'un écoulement en circulation naturelle d'hélium diphasique en régime transitoire. Fluid mechanics [physics.class-ph]. Université Paris Saclay (COMUE), 2015. English. NNT : 2015SACLS243 . tel-01350866

**HAL Id: tel-01350866**

**<https://theses.hal.science/tel-01350866>**

Submitted on 2 Aug 2016

**HAL** is a multi-disciplinary open access archive for the deposit and dissemination of scientific research documents, whether they are published or not. The documents may come from teaching and research institutions in France or abroad, or from public or private research centers.

L'archive ouverte pluridisciplinaire **HAL**, est destinée au dépôt et à la diffusion de documents scientifiques de niveau recherche, publiés ou non, émanant des établissements d'enseignement et de recherche français ou étrangers, des laboratoires publics ou privés.

NNT : 2015SACL243

THESE DE DOCTORAT  
DE L'UNIVERSITE PARIS-SACLAY,  
préparée à l'Université de Paris Sud

ÉCOLE DOCTORALE N°576

Particules hadrons énergie et noyau : instrumentation, image, cosmos et simulation

Spécialité de doctorat : Physique d'accélérateurs

Par

**M. Hernán Furci**

Etude d'un écoulement en circulation naturelle  
d'hélium diphasique en régime transitoire

**Thèse présentée et soutenue à Gif-sur-Yvette, le 13 Novembre 2015 :**

**Composition du Jury :**

M. J. Bonjour, Professeur, INSA de Lyon, Présidente du Jury et Rapporteur  
M. M. Breschi, Professeur, Università di Bologna, Rapporteur  
M. J. Amrit, Docteur, Maître de Conférences, Université Paris-Sud, Examineur  
M. L. Bottura, Docteur, CERN, Examineur  
M. J.-L. Duchâteau, Docteur, Conseiller Scientifique, CEA de Cadarache, Examineur  
M. R. van Weelderen, Docteur, CERN, Examineur  
M. B. Baudouy, Docteur HDR, CEA de Saclay, Directeur de thèse  
Mme. C. Meuris, Docteur, Invitée





**Titre :** Etude d'un écoulement en circulation naturelle d'hélium diphasique en régime transitoire

**Mots clés :** hélium, circulation naturelle, échange thermique, transitoire, cryogénie

**Résumé :** Les boucles de circulation naturelle d'hélium diphasiques sont utilisées comme systèmes de refroidissement d'aimants supraconducteurs de grande envergure, vus leurs avantages inhérents de sûreté et d'entretien. Des exemples sont le détecteur CMS au CERN (déjà en opération) ou les aimants du spectromètre R3B-GLAD au GSI (en installation). Une des préoccupations majeures lors du refroidissement par ébullition est la crise d'ébullition : la dégradation soudaine du transfert de chaleur pariétal au-delà d'une certaine valeur de flux de chaleur, dénommée critique. L'augmentation de température de paroi qui en résulte peut entraîner la perte de l'état supraconducteur de l'aimant.

Les boucles de circulation naturelle à l'hélium ont déjà été étudiées expérimentalement et numériquement en régime permanent, spécialement en régimes pré-critiques (ébullition nucléée). Les travaux sur les transferts de masse et de chaleur en hélium en ébullition en régime transitoire présents dans la littérature ciblent principalement des systèmes de petites dimensions, des canaux très étroits ou trop courts, ou l'ébullition en bain. Bien que des comportements qualitativement similaires sont attendus, l'extrapolation de ces résultats à une boucle de circulation naturelle n'est pas évident, si possible. C'est pourquoi une étude particulière du comportement thermohydraulique transitoire de boucles d'hélium en circulation naturelle, lors d'une augmentation soudaine de la charge thermique, est nécessaire.

Une partie de cette étude consiste en des expériences sur une boucle d'hélium diphasique en circulation naturelle de 2 m de haut, à 4,2 K. Deux sections chauffées verticales de diamètre différent (10 et 6 mm) et d'environ 1 m de longueur ont été testées. Les transitoires sont induits par une marche soudaine de puissance. Deux types de condition initiale ont été considérés : statique (sans puissance initiale), et en équilibre dynamique (puissance initiale non-nulle). L'évolution de la température de paroi le long de la section, le débit massique et la perte de charge a été mesurée.

Parmi d'autres phénomènes, un fort intérêt a été porté au début de la crise d'ébullition. Les valeurs limites de flux de chaleur final auxquelles la crise arrive ont été déterminées. D'un côté, on a observé que la crise peut avoir lieu de façon temporaire ou permanente à une puissance appréciablement plus faible qu'en régime permanent. De l'autre côté, l'augmentation de la circulation initiale, à travers le flux de chaleur initial, peut inhiber partiellement ou totalement cette crise d'ébullition prématurée. On a déterminé que cette dégradation du transfert de chaleur est le résultat de deux phénomènes en compétition, véritablement inhérents à la circulation naturelle : une étape initiale d'accumulation uniforme de vapeur, avec inversion ou diminution de la vitesse d'entrée, et l'établissement ultérieur de la circulation, avec le transit d'un front froid depuis l'entrée. Une analyse semi-empirique nous a permis de déterminer un critère, basé sur l'évolution dynamique du profil spatial du titre massique, pour prédire le déclenchement de la crise. Néanmoins, il est nécessaire de connaître à priori l'évolution du débit massique pour pouvoir appliquer ce critère.

La dernière partie de ce travail est dédiée à la production et validation de modèles et outils de calcul pour la simulation du comportement thermohydraulique d'un tel système. Deux options de modélisation sont présentées. L'une est une simplification des équations du modèle homogène 1D des écoulements diphasiques (mise en place en COMSOL) ; l'autre reprend le modèle homogène tel quel (programmé en C). Les simulations d'évolution du débit massique sont en assez bon accord avec les mesures, à l'exception d'un léger déphasage temporel. Ceci pourrait être dû à la combinaison d'un retard de l'instrumentation pour la mesure du débit et de l'inexactitude des hypothèses de base du modèle homogène lors de transitoires très violents.

**Title :** Study of two-phase boiling helium natural circulation loops in transient regime

**Keywords :** helium, natural circulation, heat transfer, transient, cryogenics

**Abstract :** Boiling helium natural circulation loops are used as the cooling system of large superconducting magnets because of their inherent safety and maintenance advantages. Examples are the cooling systems of the CMS detector solenoid magnet at CERN (already in operation) or the R3B-GLAD spectrometer magnet at GSI (in installation phase). A major concern in boiling cooling systems is that of boiling crisis: a sudden deterioration of the wall heat transfer takes place when the surface heat flux exceeds a certain value, called the critical heat flux (CHF). The resulting high temperatures on the wall could ultimately entail the loss of superconducting state of the magnet.

Helium natural circulation loops have already been studied experimentally and numerically in steady state, especially in the pre-critical heat and mass transfer regimes (nucleate boiling). Works on transient boiling heat and mass transfer in helium present in the literature are mostly focused on small systems, very narrow channels, too short pipes or pool boiling. Although it is expected to find qualitative similarities with already observed behavior, the extrapolation to a natural circulation loop is not easy, if even possible. Hence the need for a particular study on the transient thermohydraulic behavior of helium natural circulation loops, after sudden increases in the heat load of the circuit.

A part of this study consists of experiments conducted in a 2-meter high two-phase helium natural circulation loop at 4.2 K temperature. Two vertical heated sections with different diameters (10 and 6 mm) and around 1 m length were tested. Heat load transients were driven by a step-pulsed heat load. Transients with two types of initial conditions have been studied: static loop (no initial power applied) and in-dynamic-equilibrium loop (non-zero initial power applied). The evolutions of wall temperature along the heated section, total mass flow rate and pressure drop were measured.

Among other phenomena, the nature of the onset of boiling crisis has received a special attention. The values of final heat flux limits for its occurrence have been determined. On the one hand, we observed that boiling crisis can take place in temporary or stable fashion at power significantly lower than in steady state. On the other hand, the increase of initial circulation, by raising initial heat flux, can inhibit partially or completely this power-premature boiling crisis. We could determine that this heat transfer deterioration is the result of two competing phenomena, veritably inherent to the natural circulation feature of the system: an initial stage of uniform vapor accumulation with inlet back-flow or velocity reduction, and the ulterior onset of circulation with the transit of a cold front from the entrance. A semi-empirical analysis of data allowed determining a criterion, based on the dynamic evolution of the quality profile in the section, to predict the incipience of boiling crisis. It became evident that it is necessary to know how the mass flow rate of the system is going to evolve, in order to apply the mentioned criterion.

Hence, the other part of this work is aimed to the production and validation of models and calculation tools in order to simulate the thermohydraulic behavior of a two-phase helium natural circulation loop. Two modeling options are proposed. One of them consists of a simplification of the 1D two-phase homogeneous model equations (implemented in COMSOL) and the other of their full version (coded in C language). The simulated mass flow rate represents reasonably well the measured evolution except for a relatively small time phase-shift. This could be due to a combination of the delay of flow-metering instrumentation with the inaccuracy of the basic homogeneous model assumptions during violent transients.



*A mis padres, Lidia y Franco,  
por haberme enseñado a leer o las fases de la luna  
y, sobre todo, aquello que no se aprende en la escuela.*



# Avant-propos

Cet ouvrage est le fruit de trois ans de travail de recherche. Heureusement, je n'ai pas parcouru ce chemin en solitude. Ces quelques lignes ont le but de remercier les personnes qui m'ont accompagné et qui ont contribué à ce que cette période se déroule de la meilleure façon possible.

Les activités dont ce document est le résultat ont été réalisées au Commissariat à l'Energie Atomique et aux Energies Alternatives (CEA) à Saclay, au sein du Laboratoire de Cryogénie et Station d'Essais (LCSE) du Service d'Accélérateurs, Cryogénie et Magnétisme (SACM) de l'Institut de Recherche sur les Lois Fondamentales de l'Univers (IRFU), dans la Division de Sciences de la Matière (DSM).

Dans ce cadre, je veux commencer par remercier le CEA pour avoir entièrement financé mes travaux. Je tiens aussi à remercier la direction du SACM et du LCSE, Mess. Antoine Daël, Philippe Chesny, Pierre Vedrine, Philippe Bredy, Olivier Napoly, Christophe Mayri et Madame Roser Vallcorba: je les remercie pour l'accueil chaleureux dans leurs équipes et de leur attention pour que toutes les ressources humaines, matérielles et techniques soient disponibles. Merci aussi d'avoir rendu possible financièrement ma participation à des conférences et des workshops internationaux qui m'ont permis de découvrir et m'intégrer à cette communauté de la cryogénie et des aimants supraconducteurs.

Au sein du LCSE, je veux remercier Mess. Michel Sueur et Gilles Authelet d'avoir été très disponibles pour livrer une des ressources fondamentales pour mes travaux, l'hélium, et d'avoir fait tout ce qui était possible même quand je le commandais avec peu d'anticipation.

Je tiens aussi à remercier les personnes qui ont travaillé plus directement avec moi le long de ces trois ans.

En premier lieu, je dois mentionner Mme. Chantal Meuris, qui était initialement la directrice de ce travail. Nos réunions d'avancement et discussions plus informelles ont été très utiles pour orienter et cadrer ma recherche, grâce à son regard très expérimenté depuis un angle beaucoup plus large.

Ensuite, je veux remercier de leur apport Mess. Guillaume Meyer et Vincent Balssa, qui ont travaillé avec moi en tant que stagiaires. Les encadrer a été une expérience enrichissante et j'ai beaucoup apprécié la façon dans laquelle leurs questions ont apporté de l'air frais à mes analyses.

Pour la réalisation des expériences j'ai compté avec l'aide de Mess. Antoine Bonelli et Aurélien Four. Je remercie Antoine pour quelques petits conseils pour souder des tous petits fils et pour avoir préparé un ensemble des capteurs de température dont je me suis servi. Je remercie Aurélien pour m'avoir transmis avec beaucoup de patience et pédagogie une énorme quantité de savoir-faire technique, spécialement au tout début de ce travail, et pour m'avoir offert un support indispensable lors de toutes les campagnes expérimentales.

Si ce travail a été très fructueux, c'est en grande mesure grâce à M. Bertrand Baudouy, mon directeur de thèse. Je le remercie de sa présence constante, de sa générosité, de son humour et de sa sympathie, juste pour mentionner quelques-unes de ses qualités humaines. Je veux lui exprimer ma reconnaissance non seulement pour son professionnalisme et son vaste savoir du domaine, mais aussi pour sa franchise, sa critique, ses paroles d'encouragement et ses conseils (techniques ou pas) le long de ces trois ans. C'est un vrai honneur qu'il m'ait confié la réalisation de ce projet et qu'il ait été le premier lecteur de tous les écrits qui en ont résulté.

Je me sens très honoré d'avoir compté avec la présence de Mess. Jocelyn Bonjour, Marco Breschi, Luca Bottura, Rob van Weelderen, Jay Amrit et Jean-Luc Duchâteau dans mon jury de thèse. Je les remercie de l'intérêt qu'ils ont prêté à mon sujet et d'avoir contribué à la qualité de

ce manuscrit par leurs corrections ou suggestions écrites et par leurs questions très intéressantes lors de la soutenance.

Cette période n'aurait pas été pareille sans les nombreuses personnes que, sans être impliquées dans mon travail, j'ai côtoyées au sein du SACM. J'adresse un merci spécial à tous ceux avec qui j'ai partagé des innombrables déjeuners et pauses café, pour les discussions sur tout et n'importe quoi et les moments de bonne humeur.

En dernier, je veux exprimer ma gratitude à toutes ces personnes qui font partie de ma vie personnelle et qui m'ont soutenu le long de mon doctorat, et même depuis toujours. Pour les petits et grands gestes, pour me corriger le français, pour me faire à manger quand j'avais peu de temps, pour l'encouragement, pour l'écoute, pour les conseils... Mais surtout, pour les rires, pour les moments de joie et de célébration.

Merci !

# Contents

<b>Contents</b>	<b>i</b>
<b>List of Figures</b>	<b>v</b>
<b>List of Tables</b>	<b>ix</b>
<b>Nomenclature</b>	<b>xi</b>
<b>Introduction</b>	<b>1</b>
<b>1 Technological context</b>	<b>5</b>
1.1 Cryogenics . . . . .	5
1.2 Superconductivity . . . . .	5
1.2.1 A brief history . . . . .	5
1.2.2 The transition from normal to superconducting . . . . .	6
1.2.3 Superconducting magnets materials . . . . .	7
1.2.4 Superconducting magnets cables . . . . .	8
1.3 Magnet cooling techniques . . . . .	9
1.4 Superconducting magnets cooled by natural circulation . . . . .	11
1.4.1 The superconducting solenoid for the CMS detector . . . . .	11
1.4.2 The GLAD superconducting spectrometer for R3B . . . . .	13
Final comments . . . . .	16
<b>2 Physical background</b>	<b>17</b>
2.1 Boiling heat transfer . . . . .	17
2.1.1 Pool boiling regimes . . . . .	17
2.1.2 Forced convective boiling regimes . . . . .	20
2.1.3 Boiling crisis prediction in channel flow . . . . .	21
2.1.4 Heat transfer in the nucleate boiling regime . . . . .	24
2.2 Two-phase flow modeling . . . . .	28
2.2.1 Basic definitions and conservation equations . . . . .	29
2.2.2 The homogeneous two-phase flow model . . . . .	31
2.3 The natural circulation principle . . . . .	33
2.3.1 Dynamics of a natural circulation loop . . . . .	33
2.3.2 Two-phase loop equilibrium . . . . .	34
2.4 Helium flows . . . . .	37
2.4.1 Phase diagram . . . . .	37
2.4.2 Physical properties at saturation . . . . .	38
2.4.3 Flow Patterns . . . . .	39
2.4.4 Void fraction . . . . .	40
2.4.5 Review on two-phase friction estimation . . . . .	41
2.5 Review on transient boiling heat transfer in helium . . . . .	43

2.5.1	The findings of pool boiling experiments . . . . .	44
2.5.2	Transient boiling in channels . . . . .	46
2.6	The contribution of this work . . . . .	48
<b>3</b>	<b>The experimental facility</b>	<b>51</b>
3.1	The cryostat . . . . .	51
3.2	The insert . . . . .	53
3.3	The elements of the loop . . . . .	54
3.4	Heating configurations . . . . .	56
3.5	Instrumentation and measurements techniques . . . . .	56
3.5.1	Wall temperature . . . . .	57
3.5.2	Mass flow rate . . . . .	61
3.5.3	Pressure drop . . . . .	62
3.5.4	Power supply and measurement . . . . .	63
3.5.5	Other Instrumentation . . . . .	64
3.6	Signal data acquisition . . . . .	66
3.7	Preparation of the experiment . . . . .	68
3.7.1	Check-up actions . . . . .	68
3.7.2	Start up actions . . . . .	69
	Final comments . . . . .	69
<b>4</b>	<b>Study of the onset and hysteresis of boiling crisis in steady state</b>	<b>71</b>
4.1	Realization of experiments . . . . .	71
4.1.1	Experimental protocol . . . . .	71
4.1.2	Data treatment . . . . .	72
4.1.3	Measured evolution of thermohydraulic variables . . . . .	73
4.2	Determination and characterization of flow boiling regimes . . . . .	73
4.2.1	Experimental observations on boiling crisis onset . . . . .	73
4.2.2	Prediction of the critical heat flux . . . . .	78
4.2.3	Description of post-CHF heat transfer features . . . . .	80
4.2.4	Observations on rewetting during the decreasing power experiment . . . . .	83
4.3	Study of the hydraulic effects of boiling crisis . . . . .	85
4.3.1	Experimental observations on pressure drop and mass flow rate during crisis development . . . . .	86
4.3.2	Evaluation of pressure drop prediction methods during boiling crisis . . . . .	87
4.3.3	Creation of a new film boiling pressure drop prediction model . . . . .	91
	Summary . . . . .	95
<b>5</b>	<b>Study of stepwise heat load induced transients with static initial condition</b>	<b>97</b>
5.1	Realization of experiments . . . . .	97
5.1.1	Experimental protocol . . . . .	98
5.1.2	Measured time evolution overview . . . . .	99
5.2	Characterization of the initiation of the transient . . . . .	99
5.2.1	Study of the effect of heat flux on time evolution . . . . .	99
5.2.2	Characterization of the mass flow rate evolution . . . . .	104
5.2.3	Characterization of heat transfer during the initiation of boiling . . . . .	108
5.3	Characterization of boiling crisis during transients . . . . .	113
5.3.1	Determination of transient critical heat flux . . . . .	114
5.3.2	Identification of interesting time response parameters of transient boiling crisis . . . . .	115
5.3.3	Data treatment for critical transients . . . . .	115
5.3.4	Comparison of transient to quasi-steady temperatures in post-CHF regimes	117

5.3.5	Determination of the dependence of critical time on heat flux . . . . .	120
5.4	Study of transient boiling crisis initiation regimes . . . . .	123
5.4.1	The linear regime . . . . .	124
5.4.2	Comparison of critical time data with models . . . . .	126
5.4.3	Study of incipience of the linear-regime . . . . .	129
5.4.4	The quadratic regime . . . . .	131
5.4.5	The high- $t_c$ regime . . . . .	133
	Summary . . . . .	134
<b>6</b>	<b>Study of the effect of a dynamic equilibrium initial condition on stepwise heat load induced transients</b>	<b>137</b>
6.1	Realization of experiments . . . . .	137
6.1.1	Experimental protocol . . . . .	137
6.1.2	Measured time evolution . . . . .	138
6.1.3	Identification of main effects of initial conditions on transients . . . . .	144
6.2	Experimental determination of behavior boundaries . . . . .	145
6.2.1	Determination of the inhibition heat flux . . . . .	146
6.2.2	Identification of transition between crisis initiation regimes . . . . .	146
6.2.3	Identification of the link between the transition regimes and the inhibition of crisis . . . . .	146
6.2.4	Drawing the experimental behavior maps . . . . .	150
6.3	Theoretical study of the system with arbitrary initial condition . . . . .	151
6.3.1	Simplifying Assumptions . . . . .	151
6.3.2	The equations . . . . .	151
6.3.3	Numerical approach . . . . .	153
6.3.4	Observation of the effect of initial condition on quality evolution . . . . .	153
6.4	Determination of a criterion for boiling crisis initiation . . . . .	155
	Summary . . . . .	158
<b>7</b>	<b>Modeling of the boiling helium loop in transient regime</b>	<b>161</b>
7.1	Representation of the loop in 1D . . . . .	161
7.2	Development of a simplified model . . . . .	162
7.2.1	Simplification of the equations . . . . .	162
7.2.2	The resulting simplified model . . . . .	168
7.3	Implementation of the simplified model in COMSOL . . . . .	171
7.3.1	Description of the environment . . . . .	172
7.3.2	Solving strategy . . . . .	172
7.3.3	Comparison of the simplified model simulations to the experimental data . . . . .	174
7.4	Solution of the non-simplified model . . . . .	175
7.4.1	Structure of the program . . . . .	175
7.4.2	Input parameters . . . . .	178
7.4.3	Numerical method . . . . .	179
7.4.4	Fluid properties . . . . .	181
7.4.5	Initial conditions . . . . .	181
7.4.6	Boundary conditions . . . . .	182
7.4.7	Comparison of simulated and measured evolutions . . . . .	185
7.5	Evaluation of the transition to boiling crisis criteria with the simulators . . . . .	186
	Summary . . . . .	186
	<b>Synthesis and comments</b>	<b>189</b>
	<b>Conclusions and perspectives</b>	<b>193</b>

<b>Appendix A</b>	<b>Résumé substantiel en français</b>	<b>195</b>
A.1	Introduction . . . . .	195
A.2	Montage expérimental . . . . .	196
A.3	Démarche expérimentale . . . . .	198
A.4	Comportement de la crise d'ébullition en régime permanent . . . . .	198
A.4.1	Le début et développement de la crise d'ébullition . . . . .	198
A.4.2	Les effets hydrauliques de la crise d'ébullition . . . . .	199
A.5	Transitoires avec condition initiale statique . . . . .	200
A.5.1	La réponse hydraulique . . . . .	200
A.5.2	Les régimes de transfert de chaleur . . . . .	201
A.6	Transitoires avec condition initiale dynamique . . . . .	203
A.6.1	Résumé des principaux effets observés . . . . .	203
A.6.2	Carte de comportements . . . . .	204
A.6.3	Un critère empirique pour l'arrivée de la crise . . . . .	204
A.7	Modélisation de l'écoulement diphasique . . . . .	205
A.7.1	Un modèle simplifié . . . . .	205
A.7.2	Le modèle non-simplifié . . . . .	205
A.7.3	Validation et limitations des simulations numériques . . . . .	205
A.8	Conclusions . . . . .	206
<b>Appendix B</b>	<b>The film boiling friction model equations</b>	<b>209</b>
<b>Appendix C</b>	<b>Demonstrations concerning loop dynamics modeling</b>	<b>211</b>
C.1	Simplified velocity profile . . . . .	211
C.2	Alternative approach for the integral momentum equation . . . . .	212
C.3	Cross section changes . . . . .	213
<b>List of publications</b>		<b>I</b>
<b>References</b>		<b>III</b>
<b>Article on horizontally heated boiling helium natural circulation loops</b>		<b>IX</b>

# List of Figures

1.1	Critical surface of a superconductor. . . . .	7
1.2	Critical characteristics of some superconductors. . . . .	8
1.3	Cross section of a Rutherford cable. . . . .	9
1.4	Cross-sectional view of ITER conductors . . . . .	10
1.5	The CMS magnet. . . . .	12
1.6	CMS cooling system. . . . .	14
1.7	Illustration of the R3B-GLAD systems. . . . .	15
2.1	Pool boiling curve. . . . .	18
2.2	Pool boiling regimes . . . . .	19
2.3	Forced convective boiling regimes. . . . .	22
2.4	Bubble nucleation in a cavity . . . . .	25
2.5	Nucleate boiling cycle. . . . .	27
2.6	Nucleate boiling heat transfer mechanisms. . . . .	29
2.7	One-dimensional two-phase natural circulation loop . . . . .	33
2.8	Response of the equilibrium point to the overall friction coefficient change in a natural circulation loop. . . . .	36
2.9	Helium phase diagram . . . . .	37
2.10	Two-phase flow pattern chart for helium in vertical channels . . . . .	40
2.11	Void fraction in helium flow . . . . .	41
2.12	Two-phase friction factor in helium for vertical tubes . . . . .	42
2.13	Typical temperature evolutions during transients in pool boiling in a helium bath . . . . .	44
2.14	Temperature evolutions showing the homogeneous nucleation limit . . . . .	45
2.15	Results on nature and duration of quasi-steady nucleate boiling . . . . .	46
3.1	The experimental facility: (left) the insert and (right) the cryostat. . . . .	52
3.2	The loop elements and its instrumentation. . . . .	55
3.3	Diagram of a thermoresistor transducer . . . . .	57
3.4	Cernox sensors used for wall temperature measurements . . . . .	59
3.5	Dimensions of Cernox temperature transducers . . . . .	59
3.6	The support for AA sensors. . . . .	60
3.7	Working principle of a DP10 transducer. . . . .	63
3.8	The heating power controle and measurement technique. . . . .	64
3.9	Liquid level monitors. . . . .	65
3.10	Typical Labview Screen. . . . .	67
3.11	Start up of an experiment . . . . .	68
4.1	Power evolution during a steady state experiment. . . . .	72
4.2	Thermal behavior of the heated sections for steady power . . . . .	74
4.3	Total mass flow rate evolution for steady power . . . . .	75
4.4	Pressure drop evolution for steady power . . . . .	76

4.5	Katto's criteria for the CHF transition type . . . . .	79
4.6	Heat transfer coefficient evolution for steady power. . . . .	81
4.7	Temperature evolutions in transition from post-CHF to NB regime. . . . .	84
4.8	Schematic observed crisis evolution during rewetting experiments . . . . .	85
4.9	Pressure drop prediction . . . . .	88
4.10	Friction pressure drop prediction . . . . .	89
4.11	Schematic velocity profile assumed for the FB model study. . . . .	91
5.1	Schematic heat flux evolution in static initial condition experiments. . . . .	98
5.2	Time evolution in static initial condition transients at different values of $q_f$ (part 1). . . . .	100
5.3	Time evolution in static initial condition transients at different values of $q_f$ (part 2). . . . .	101
5.4	Time evolution in static initial condition transients at different values of $q_f$ (part 3). . . . .	102
5.5	Time evolution in static initial condition transients at different values of $q_f$ (part 4). . . . .	103
5.6	Transient maximum and final mass flow rate values as a function of $q$ . . . . .	105
5.7	Quantitative analysis of the instantaneous hydraulic response. . . . .	105
5.8	Determination of the end of the pure conduction phase. . . . .	111
5.9	Global temperature values during stepwise power transients. . . . .	112
5.10	Parameters characterizing transient boiling crisis . . . . .	116
5.11	Temperature maximum and final values compared to quasi-steady state, V10. . . . .	118
5.12	Temperature maximum and final values compared to quasi-steady state, V06. . . . .	119
5.13	Simultaneous temperature evolutions for V06. . . . .	121
5.14	Critical time vs. final wall heat flux. . . . .	122
5.15	Critical time as a function of volume-averaged power. . . . .	125
5.16	Spatial dependence of $t_c \times q_v$ . . . . .	126
5.17	Critical product $t_c \times q_v$ vs. final volume specific power. . . . .	128
5.18	Evaluation of the transient boiling crisis incipience criterion in the linear regime by the 'uniform expansion-transit time' model . . . . .	132
6.1	Schematic heat flux evolution in non-static initial condition experiments. . . . .	138
6.2	The effect of initial heat flux on time evolution (Part 1) . . . . .	139
6.3	The effect of initial heat flux on time evolution (Part 2) . . . . .	140
6.4	The effect of initial heat flux on time evolution (Part 3) . . . . .	141
6.5	The effect of initial heat flux on time evolution (Part 4) . . . . .	142
6.6	The effect of initial heat flux on time evolution (Part 5) . . . . .	143
6.7	The effect of initial heat flux on time evolution (Part 6) . . . . .	143
6.8	Criterion for finding the crisis inhibition heat flux . . . . .	147
6.9	Effect of $q_f$ on $q_{inh}$ . . . . .	147
6.10	The effect of initial heat flux on critical time in V10 . . . . .	148
6.11	The effect of initial heat flux on critical time in V10 — linear regime life at a given position as a function of $q_i$ and $q_f$ . . . . .	148
6.12	The effect of initial heat flux on critical time in V06 . . . . .	149
6.13	The effect of initial heat flux on critical time in V06 — linear regime life at a given position as a function of $q_i$ and $q_f$ . . . . .	149
6.14	Experimental boiling crisis transient behavior maps . . . . .	152
6.15	Alternative types of behavior maps . . . . .	153
6.16	Simulation of thermodynamic quality for non-static initial condition . . . . .	154
6.17	Simulated transient quality key values for incipient cases, vs. $q_i$ . . . . .	158

---

7.1	Transformation of the loop into a 1D domain. . . . .	163
7.2	Comparison of simplified model simulations to experiments. . . . .	176
7.3	Simulated time evolution of property profiles with the simplified model. . . . .	177
7.4	Comparison of simulations with the two models to experiments. . . . .	184
7.5	Quality-based incipient cases analysis using the developed models. . . . .	186
7.6	Quality-based incipient cases analysis: comparison with experiments. . . . .	187
B.1	FB model chart: $\tilde{V}_f$ vs. $\tilde{B}$ . . . . .	210



# List of Tables

2.1	Saturation properties of water, nitrogen and helium. . . . .	38
3.1	Heating section parameters . . . . .	56
4.1	CHF and RHF values found experimentally . . . . .	77
4.2	Values of CHF predicted by Katto's correlation . . . . .	79
5.1	Transient critical heat flux, $q_{c,t}$ and $q_{c,p}$ . . . . .	115
5.2	Values of the product $t_c \times q_v$ . . . . .	124
5.3	Transit time and quality analysis applied to incipient linear regime boiling crisis cases . . . . .	131
6.1	Quality analysis of linear boundary cases for transients with $q_i \neq 0$ , section V06.	156
6.2	Quality analysis of linear boundary cases for transients with $q_i \neq 0$ , section V06.	157



# Nomenclature

## Roman letters

$A$	cross section area	$\text{m}^2$
$B_c$	superconductor critical magnetic field	T
$B$	FB model parameter	$\text{m}^{3/7} \text{s}^{-3/7}$
$\tilde{B}$	non-dimensional FB model parameter	$= \frac{B}{V_h^{3/7}}$
$C$	specific heat	$\text{J kg}^{-1} \text{K}^{-1}$
$D$	diameter	m
$e$	specific internal energy	$\text{J kg}^{-1}$
$f$	friction factor	
$G$	mass flux	$\text{kg m}^{-2} \text{s}^{-1}$
$H$	Momentum integral: $\int \rho u \, ds$	$\text{kg m}^{-1} \text{s}^{-1}$
$h$	specific enthalpy	$\text{J kg}^{-1}$
$h_{lg}$	vaporization latent heat	$\text{J kg}^{-1}$
$I$	electric current	A
$J_c$	superconductor critical current density	$\text{A m}^{-2}$
$k$	thermal conductivity	$\text{W m}^{-1} \text{K}^{-1}$
$L$	tube length	m
$\dot{m}$	mass flow rate	$\text{kg s}^{-1}$
$P$	pressure	Pa
$p$	pressure	Pa
$q$	heat flux	$\text{W/m}^2$
$q_v$	$= \frac{4q}{D}$ , heat generation rate per unit volume	$\text{W m}^{-3}$
$R$	electric resistance	$\Omega$
$R$	radius	m
$r$	radial position variable	m
$s$	loop curvilinear coordinate	m
$\Delta T$	wall superheat: $T_w - T_l$	K
$t$	time	s
$T_c$	superconductor critical temperature	K
$U$	electric tension	V
$u$	velocity	$\text{m s}^{-1}$
$V$	velocity	$\text{m s}^{-1}$
$v$	specific volume	$\text{m}^3 \text{kg}^{-1}$
$x$	quality	
$z$	position along the heated section from the inlet	m

## Greek letters

$\alpha$	thermal diffusivity	$\text{m}^2 \text{s}^{-1}$
$\alpha$	void fraction	
$\delta$	film thickness	$\text{m}$
$\gamma$	diffusion coefficient	$\text{m}^2 \text{s}^{-1}$
$\kappa$	Von Kármán constant	$= 0.41$
$\mu$	viscosity	$\text{kg m}^{-1} \text{s}^{-1}$
$\Omega$	two-phase expansion rate: $\frac{v_{lg}q_v}{h_{lg}}$	$\text{s}^{-1}$
$\rho$	density	$\text{kg m}^{-3}$
$\sigma$	surface tension	$\text{N m}^{-1}$
$\tau$	shear stress	$\text{N m}^{-2}$
$\tau$	transit time	$\text{s}$

## Indexes and accents

0	at the inlet
1 $\phi$	one-phase
2 $\phi$	two-phase
<i>acc</i>	fluid acceleration contribution
<i>c</i>	critical
<i>d</i>	at bubble departure
<i>d</i>	down-comer
<i>d</i>	duration
<i>e</i>	adiabatic entrance of the ascending branch
<i>eff</i>	effective
<i>f</i>	at the film-liquid interface
<i>f</i>	final
<i>fr</i>	friction contribution
<i>g</i>	saturated vapor
<i>g</i>	when index of $\Delta p$ only, gravitational contribution
<i>h</i>	heated section
<i>h</i>	homogeneous bulk
<i>i</i>	initial
<i>cs</i>	current sharing
<i>l</i>	saturated liquid
<i>lg</i>	difference between liquid and vapor
<i>n</i>	iteration step
<i>p</i>	permanent crisis
<i>r</i>	adiabatic riser
<i>s</i>	quasi-steady state
<i>sat</i>	saturation
<i>sing</i>	concentrated head loss singularity
<i>sub</i>	related to subcooling

$t$	temporary crisis
$u$	horizontal section of the U-shaped loop
$w$	at the wall

### Physical constants

$g$	acceleration of gravity	$\approx 9.81 \text{ m s}^{-2}$
$\bar{g}$	gravity vector	$\text{m s}^{-2}$

### Acronyms

CHF	critical heat flux
DFFB	dispersed flow film boiling
DNB	departure from nucleate boiling
FB	film boiling
HEM	homogeneous equilibrium model
IAFB	inverted annular film boiling
i.d.	inner diameter
LHS	left hand side
ODE	ordinary differential equation
PDE	partial differential equation
RHF	rewetting heat flux
RHS	right hand side
SBC	stable boiling crisis
SNB	stable nucleate boiling
TBC	temporary boiling crisis



# Introduction

Cryogenics is today indispensable for the realization and operation of superconducting magnets, given that low temperature is required for the materials to reach the superconducting state. One option for the cooling system of superconducting magnets is that of a boiling helium natural circulation loop. In most of the cases, these systems are operated in steady state, i.e. with a time-independent heat load. Nevertheless, in some cases, a time-dependent heat load may be exerted on the system, either for operational reasons or in the case of undesired incidents. The system produces a transient response to such solicitations, a response which is not always well known. This arises the question of whether the cooling system is capable of keeping the superconductor within the temperature requirement when reacting to these external excitations. The passage of the material to the resistive state is highly undesired during the operation of a magnet, given that this could conduct to brutal energy deposition on the assembly and brutal mechanical solicitation.

Boiling helium two-phase natural circulation loops have been studied by Baudouy and Benkheira at CEA Saclay [5, 6, 8, 9]. These authors have conducted experiments in which they control the power applied on the heated section of such a system in steady state. They have tested different types of tubes as heated section, with different diameters and orientations. Their observations have allowed a very complete characterization of heat and mass transfer in the nucleate boiling regime. They have also shown that it is possible to reach boiling crisis on the heated section wall using their apparatus. Nonetheless, they have not conducted experiments with time-varying heat loads.

There are a few works on transient boiling heat transfer in helium or other cryogenics in response to time-varying heat load in the literature [43, 63, 67, 71]. Most of these works are focused on the problem of a filament or flat surface immersed in a liquid helium pool, on which power is applied electrically. These experiments have provided very valuable results, especially for the characterization of the different heat transfer regimes that follow a sudden power injection on the heater. In particular, the work by Sinha [68] has proved that, in the case of nitrogen pool boiling around a filament, there can be a significant difference of the boiling crisis power limits in steady state or transient regime, being lower for the latter. However, not all the findings of pool boiling experiments can be extrapolated to internal flow, and in all cases, these works are focused on extremely small systems (never exceeding a few cm of length).

The problem of transient heat transfer in helium channel flow has been tackled by a few authors. Yarmak studied the case of forced flow in very narrow channels [77] and Schmidt [64], and Babitch and Pavlov [4] inside a tube immersed in a pool (flow taking place by natural circulation). These experiments were conducted in tubes shorter than 25 cm and with an internal diameter smaller than 3 mm. These studies highlight a number of phenomena that can take place during transient boiling in channels, with a particular focus on the transition to boiling crisis in unsteady conditions. They point out that transient boiling crisis can happen temporarily at lower heat flux than in steady state. They also point out the existence of a meta-stable nucleate boiling phase before the arrival of boiling crisis and they show that its duration is a function of

the power applied, different from that in pool boiling. Pavlov and Babitch, in particular, attribute this different behavior to the confinement in the channel and propose a model to predict the critical time [61]. Nevertheless, not only these systems are too small compared to the dimensions typical of magnet cooling systems, but also these experiments are not veritably conducted in a circulation loop, the mass flow rate evolution in the heated section is unknown and unstudied and, yet, the boiling crisis incipience heat flux during transients (possibly lower than that in steady state) is not thoroughly discussed and remains unpredictable.

To summarize, large helium natural circulation loops have been studied thoroughly only in steady state and mostly in pre-critical boiling regimes. The literature reveals that in wall boiling cooled systems the critical heat flux limit can be appreciably reduced in the case of violent power injections. However, the studies are restricted to systems in pool boiling or flow in very small channels, with no information on mass flow rate evolution.

For these reasons we saw the need of characterizing the dynamic behavior of a relatively large boiling helium natural circulation loop in transient regime induced by stepwise increase of wall heat flux, which is the objective of the present work.

In chapter 1 we present in more detail the role of cryogenics in the superconducting magnets field and present applications of helium natural circulation loops. In chapter 2 the physical background of phenomena associated to natural circulation loops and boiling is presented. These two chapters will provide the motivation and context for the research presented in this document.

As we will see in the following paragraphs, this work is composed of two parts. The first one consist of an experimental study on a cryogenic loop, and the second one of the modeling and simulation this type of system. The elements of the experimental facility, as well as the instrumentation and the operational procedure are exposed in detail in chapter 3.

Our study starts with the experimental characterization of boiling crisis onset in a helium natural circulation loop with a heated section of more than 5 mm of inner diameter. This was done to know to what extent a link exists between steady state and transient boiling crisis and because available tools for the prediction of boiling crisis are poorly based on helium data, not to mention the anomalies that can take place concerning critical heat flux (CHF) in vertical channels. To do this, we conducted experiments on such a loop with vertical heated sections of 6 and 10 mm i.d. and around 1 m long, dimensions that are representative of the tubes used in magnet cooling. In order to observe the dependence of the most significant thermohydraulic variables on heat flux and to identify the transition to boiling crisis and back to nucleate boiling, increasing and decreasing power progressions were applied on the loop. Heat flux was varied sufficiently slowly, so as to avoid the excitation of transient modes. Simultaneously, wall temperature, mass flow rate and test section pressure drop were measured. On the other hand, we calculated the critical heat flux and pressure drop predicted by the literature in our experimental conditions. We compared our experimental values to these predictions, and we have detected anomalies that can take place in these systems during and after the onset of boiling crisis. A model was conceived and evaluated to improve the prediction of pressure drop in the film boiling regime. All these actions constitute chapter 4.

Our next step was the characterization of transients induced by a stepwise power increase from a static initial condition. This would give us the limit case of the most violent possible solicitation that can be exerted on the system. For this study, we conducted experiments on the same loop, in which power is suddenly increased from zero to a final constant value. The aim was to identify the influence of this parameter on the evolution of mass flow rate and wall temperature, with a particular focus on the boiling crisis transition. Given the great amount of data, automatic data treatment tools were developed. These tools had to be capable of determining the occurrence of crisis and of calculating the characteristic time parameters of both mass flow rate and temperature evolutions. This tool was applied to the data in order to characterize the

influence of heat flux on these parameters, in particular on critical time, i.e. the duration of the meta-stable nucleate boiling stage before boiling crisis. The critical time that can be predicted from previous work in the literature was evaluated and compared to the experimental data. Different mechanisms for the initiation of boiling crisis were identified and described. In order to give an answer to the question of transient boiling crisis incipience heat flux and suspecting that this could be strongly linked to the evolution of natural circulation, the evolution of thermohydraulics in the heated section was modeled and simulated (using as input experimental inlet velocity data) for the incipient cases. These actions are presented in chapter 5.

In order to tackle the more realistic, intermediate situation in which a stepwise heat load increase comes up during the normal operation of the loop at non-nul power, another set of experiments was conducted. In these experiments the system is initially in dynamic equilibrium at a given initial heat flux and power is increased to a final value. In order to identify the influence of the initial condition on the transient, series of experiments are defined by a fixed value of final heat flux, and the initial heat flux is a varying parameter. In general, the final heat flux is chosen so as to have boiling crisis when the initial condition is static; this, with the aim of observing the effect of initial conditions on transient boiling crisis. The critical time of every single case was determined whenever crisis was observed. Its dependence on initial heat flux was systematically studied. By observing the evolution of critical time with initial and final heat flux, we determined quantitative and qualitative effects of the initial condition on the mechanism for transient boiling crisis onset. This allowed defining transient behavior charts on the initial-final heat flux plane. Still with the same hypothesis, that boiling crisis initiation in some of the regimes is governed by the thermohydraulic evolution on the heated section, the model developed before was extended to the case with a dynamic initial condition and applied to the experimental cases near the incipience boundary. The study of time evolution of local vapor fraction was used to define a criterion for boiling crisis incipience during transients. Chapter 6 presents this part of the study.

Having appreciated the importance of the evolution of the thermohydraulic variables on the onset of boiling crisis, it is desirable for future analysis to have validated models and numerical tools for their prediction, without the need of performing new experiments. With this aim, modeling options for boiling helium natural circulation loops were studied. Given the values of helium properties and previous experimental knowledge of helium flows, we found appropriate to take as a departure point the time-dependent homogeneous equilibrium model (HEM). The first approach was the analytical study of the equations with the objective of simplifying them, in order to represent the first order phenomena. Pressure effects were expected to be negligible in systems of our dimensions; neglecting them allowed us to pass from a system with three partial differential equations (PDE), to one with only one PDE and one ordinary differential equation (ODE). The obtained system was implemented in a commercial multi-physics simulation software and the simulated evolution of hydraulic behavior was compared to that measured. In order to verify certain time response discrepancies between model and experiment were due to the pressure effects simplification hypothesis, we decided to solve the full version of the equations of the HEM. To do this, we fully developed a numerical method based on finite differences and a C language code. The differences in behavior due to pressure effects were studied in order to decide if they originate the aforementioned discrepancies. The ability of this type of models to represent boiling helium natural circulation loops and predict boiling crisis was analyzed. All the work related to modeling constitutes chapter 7.

Finally, the last part of this document recapitulates the findings of this work and points out new problems to be addressed.



# Chapter 1

## Technological context

### 1.1 Cryogenics

The word *cryogenics* generally refers to the science and technology of producing a low temperature environment for applications as well as the study of materials, fluids, heat transfer and all other physical phenomena taking place at low-temperature environments. Cryogenics temperature range of interest is generally accepted to be below 120 K approximately, being this the temperature at which the called *permanent gases* (O<sub>2</sub>, N<sub>2</sub>, Ar and methane) are cold enough to be liquified.

Applications of cryogenics are present in a wide variety of technical fields including advanced energy production and storage technologies, transportation and space programs, and a wide variety of physics and engineering research efforts. The field is very interdisciplinary consisting of essentially all the scientific community focused on low temperature technology.

One of these fields where cryogenics plays a key role is superconductivity and superconducting magnets, which constitutes the motivation of this work. In the next section we expose the implications of our research in this field.

### 1.2 Superconductivity

*Superconductivity* is the property of a material by which it is capable of conducting an electrical current without dissipating heat by Joules effect; i.e. we say a material is superconductor when at a given condition *its electrical resistance vanishes*. A material with this property is called *superconductor*.

Immediately, we can see the advantage of superconductors compared to normal conductors, such as copper or aluminum. In applications where huge amounts of electric current (or current density) may be required, the use of superconducting cables may reduce dramatically the cost of operation of the technological device, as less electric power will be required. On the other hand, efforts will be necessary to cool the superconductors, since superconductivity is achieved *only below* a certain temperature.

#### 1.2.1 A brief history

The discovery of superconductivity has been attributed to Heike Kammerlingh-Onnes. In 1911, one of his students, who was measuring the resistivity of a rod of mercury at low temperature, found that below a certain temperature the material completely lost its resistivity. This

experiment could be repeated and the results confirmed, which led to the conclusion that below this *critical temperature*, the material transitioned to a new state named *superconducting* with enhanced electrical current transport properties. In 1913, the Nobel prize was awarded to Heike Kammerlingh-Onnes “for his investigations on the properties of matter at low temperatures which led, inter alia, to the production of liquid helium”.

It is in the 1950’s that superconductivity found its application in the production of very intense magnetic fields thanks to the utilization of superconducting metallic alloys [75]. The two most important examples of these materials are Nb<sub>3</sub>Sn (intermetallic compound of the Niobium-Tin system – critical temperature 18 K at 0 Tesla) and NbTi (an alloy – critical temperature 9 K at 0 T).

More recently, in 1986 and 1987, ceramic materials containing copper, like BaLaCuO[15] and YBaCuO[76] have been found to have a superconducting state; the astonishing aspect about these materials is that their critical temperatures are quite high in comparison with metallic alloys. The ceramics are, thus called *high temperature superconductors* (HTS) as their critical temperatures are in the range of 90-120 K. The impact of these materials is striking since the cooling requirements are significantly lower, simply reachable with liquid nitrogen.

A good compilation of history of superconductivity by applications can be found in the text “100 Years of Superconductivity” [62].

### 1.2.2 The transition from normal to superconducting

Superconducting materials are not in the superconducting state at any condition. We talk about a duality between a *superconducting state* and a *normal state* (with non-zero resistivity). In the absence of magnetic field and with no electrical current going through the material, it is necessary that the temperature be lower than a value called *critical temperature*  $T_c$  to have the superconducting state.  $T_c$  is an intrinsic property of the material.

In the presence of magnetic field  $B$  and/or electrical current density  $J$  in the bulk of the material, the temperature requirement for the existence of superconducting state is more severe. The temperature needs to be even lower than  $T_c$ . In general, the requirement is

$$T < T_{cs}(B, J), \tag{1.1}$$

where  $T_{cs}$  is known as *current sharing temperature*. For all  $B$  and  $J$ ,  $T_{cs}(B, J) \leq T_c$ , the equality being for the case where  $B$  and  $J$  equal 0, i.e.  $T_{cs}(B = 0, J = 0) = T_c$ .

The result of these limitations is that the existence of the superconducting state is limited to a reduced region in the space *current – magnetic field – temperature*. This region is delimited by what we call the *current sharing surface*, which is schematically represented in Fig. 1.1. The surface can be represented by an equation of the form

$$T = T_{cs}(B, J). \tag{1.2}$$

Alternatively, we could have used expressions of the form  $B = B_{cs}(T, J)$  or  $J = J_{cs}(B, T)$  to describe the surface.

The material is for sure in the normal region when any of the three critical values for temperature, magnetic field and current density ( $T_c$ ,  $B_c$  or  $J_c$ , respectively) is surpassed. As can be appreciated in Fig. 1.1, the increase of one of the three parameters reduces the extent of the superconducting region on the plane defined by the other two parameters.

The aim of a superconducting magnet is producing an intense magnetic field, for which a significant current density in the superconducting material is required. As a result, inevitably,

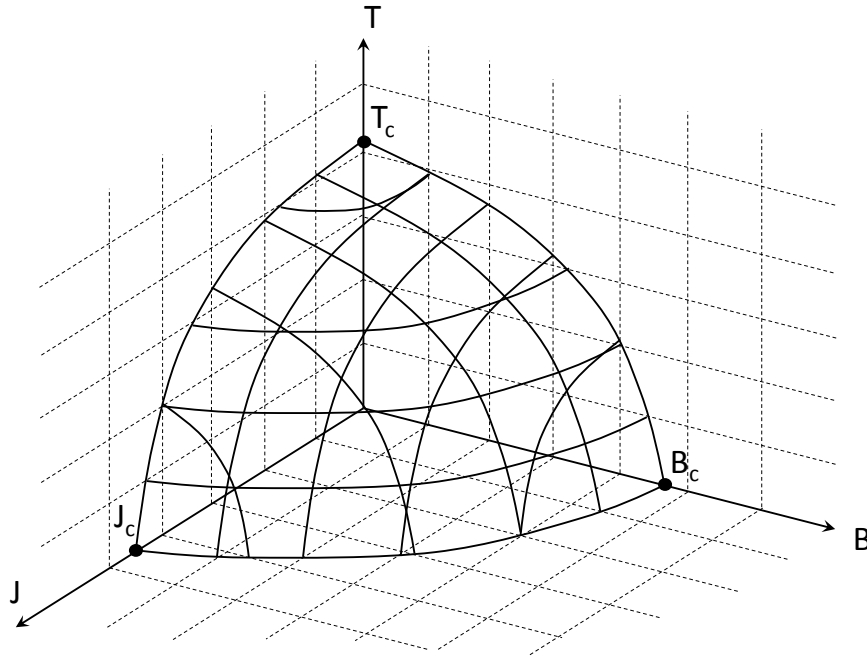


**Figure 1.1.** *Critical surface of a superconductor.*

$T_{cs}$  is significantly lower than  $T_c$  in this case. On the other hand, the lower the temperature, the greater the superconducting operational region in terms of  $J$  and  $B$ .

This is where cryogenics plays a key role in superconducting magnets design and operation: *a cooling systems is necessary that can assure that the superconductor does not surpass its current sharing temperature during operation.* When we look at the typical values of  $T_c$  for the metallic Nb alloys or compounds, we realize that these values are quite low. Moreover, the presence of field and current in the magnet increases further the requirement on the temperature to be achieved. We will formalize this notion by defining the *temperature margin*, i.e. the difference between  $T_{cs}$  at a given condition ( $B, J$ ) at a point in the material and the actual temperature of the superconductor  $T$  at the same point. A design requirement is imposed as a minimum temperature margin, for safety reasons. Cooling techniques with helium (boiling at 4.2 K at atmospheric pressure) are widely present in magnet cooling because they represent in some cases the only way of achieving these requirements.

Before ending this section, we need to mention that there are other factors that can limit (or enhance) the superconducting state. For example, we can mention static elastic strain, which in large amounts can reduce appreciably the extent of the superconducting region in Fig. 1.1, or microstructure, which can play a role in magnetic vortex dynamics.

### 1.2.3 Superconducting magnets materials

The choice of the superconductor to construct a superconducting magnet is a compromise between many factors, such as maximum magnetic field to achieve, cooling possibilities, nature of the operation (pulsed, steady), costs, geometry, manufacturing, etc.. The two most popular materials used are NbTi and Nb<sub>3</sub>Sn.

NbTi is the default material for applications where the fields are below 12 T, given its lower costs and easier technological application. The most used NbTi alloy has a critical temperature of 9 K and a critical field of 14.5 T. The critical current density however depends mostly of the micro-structure. Small-grained micro-structure and the presence of  $\alpha$ -phase precipitates impede

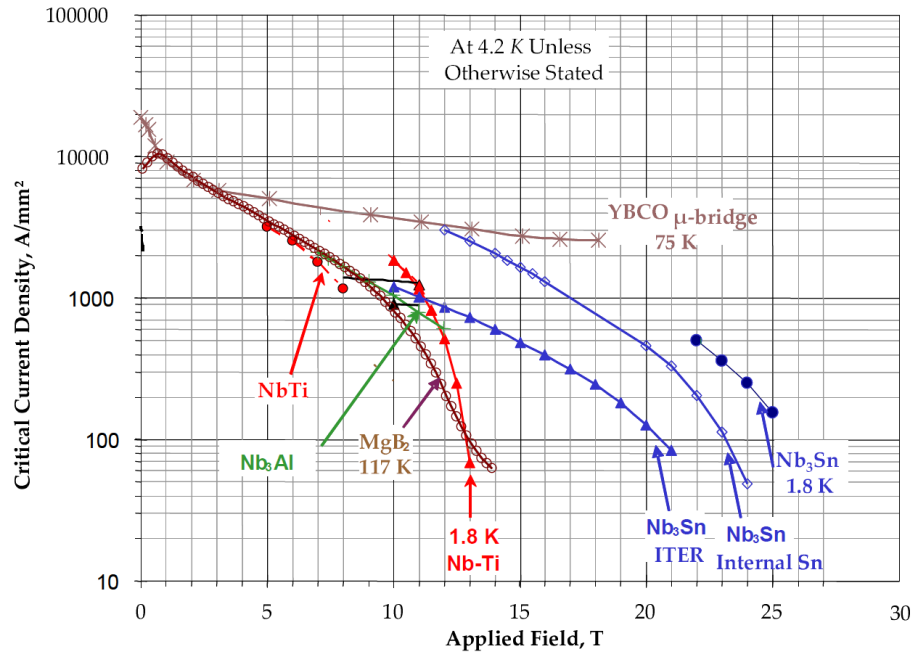


**Figure 1.2.** Critical characteristics of some superconductors.

the displacement of vortices in the mixed state, which allows the material to carry a greater current density. Thus, thermal treatments are done on the material to assure an optimal repartition of precipitates.

Nb<sub>3</sub>Sn is produced from bronze and niobium, by means of a thermal treatment at about 700°C during 250 hours which allows the chemical reaction to take place. The critical parameters depend on the content of Sn and mechanical strain. In general Nb<sub>3</sub>Sn is thermally treated to get a very fine grain, which enhances critical current density in the mixed state. With no mechanical strain, the critical temperature is 18 K and the critical field is 28 T. That is why Nb<sub>3</sub>Sn is the mandatory choice for high field applications, above 12 T. However, its manipulation can be quite difficult since Nb<sub>3</sub>Sn is fragile, it breaks easily, which limits manufacturing possibilities and applications.

The measured current sharing curves at fixed temperature of these two materials and others are presented in Fig. 1.2.

#### 1.2.4 Superconducting magnets cables

The design of superconducting cables is ruled by the fact that superconductors have quite low values of thermal and electric conductivity in the normal state. If any perturbation during operation made the superconductor transit to the normal state large amounts of energy would be deposited by Joules effect and heat would be badly conducted, which in a last instance would produce a hot spot. In order to avoid such a situation a general trend in cable design consists of inserting the superconductor filaments into a matrix of some other *stabilizing* material. The latter is generally a high conductivity metal such as copper or aluminum. If the superconductor transits to normal state, the current is bypassed to the stabilizing material, the Joules dissipation can be moderate and eventually heat can be conducted from the hot point to the cooling system with a good time constant. This is the principle applied in *Rutherford* cables and *over-stabilized* cables. Rutherford cables typically consist of 10 or 20 strands which in turn are composed of

- superconducting filaments of tens of microns diameter,

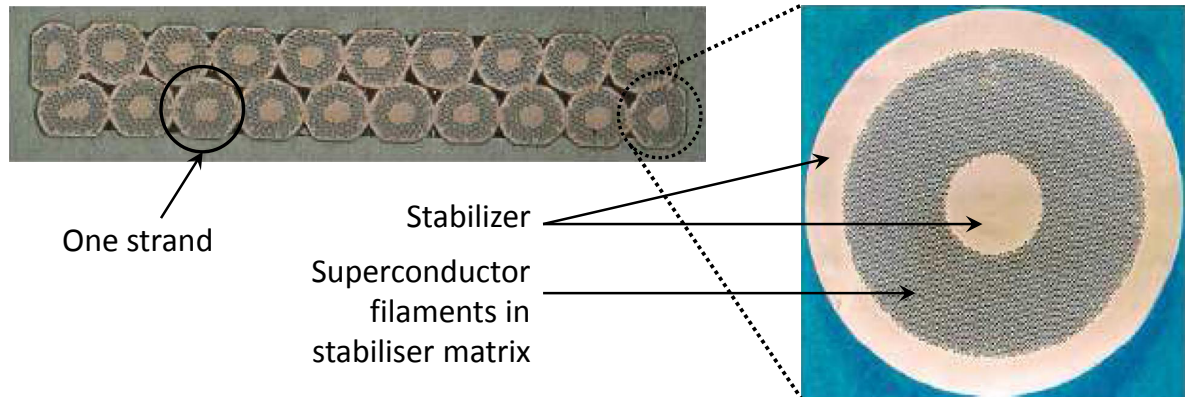


**Figure 1.3.** *Cross section of a Rutherford cable.*

- the stabilizing material matrix.

A typical Rutherford cable is shown in Fig. 1.3. Over-stabilized cables are like the Rutherford type, but in addition to the stabilizing matrix in the strand, a great volume of stabilizing material is placed around the strands.

Another type of cables that deserves mention are the Cable-in-Conduit Conductors (CICC). These are well suited for superconducting systems with high requirements in terms of power to evacuate. That is why they are found especially in fusion related machines like W7X (Wendelstein 7-X) or ITER (International Thermonuclear Experimental Reactor)[24]. They consist of one or many bundles of strands placed inside a cooling tube, through which a forced flow of helium (liquid or supercritical) is imposed. Thus, the strands are in direct contact with the coolant which provides a remarkable thermal stability. ITER conductors are shown in Fig. 1.4.

### 1.3 Magnet cooling techniques

The choice of the cooling system for a magnet depend on the conductor type and the operation requirements. The constraint of this choice are geometry, the amount to power to be evacuated (the heat load), the time distribution of the heat load, the temperature required for the superconductor, costs, etc..

In general it is preferable to use fluids that have their boiling point below the temperature required by the superconductor. Given that phase change is not instantaneous but requires latent heat to be deposited, this provides temperature stability without the need of continuous cooling power if two-phase flow is admitted. However, in theory any sufficiently subcooled fluid can be used.

The most generally used coolant for low temperature superconducting magnets is helium. The properties of this element as a coolant are presented in section 2.4. Helium can be used in its normal liquid state (HeI), in its low temperature superfluid liquid state (HeII) or even as a supercritical fluid (high pressure with no phase change). The possible cooling schemes can be varied:

- Pool natural convection
  - Single-phase
  - Two-phase with boiling

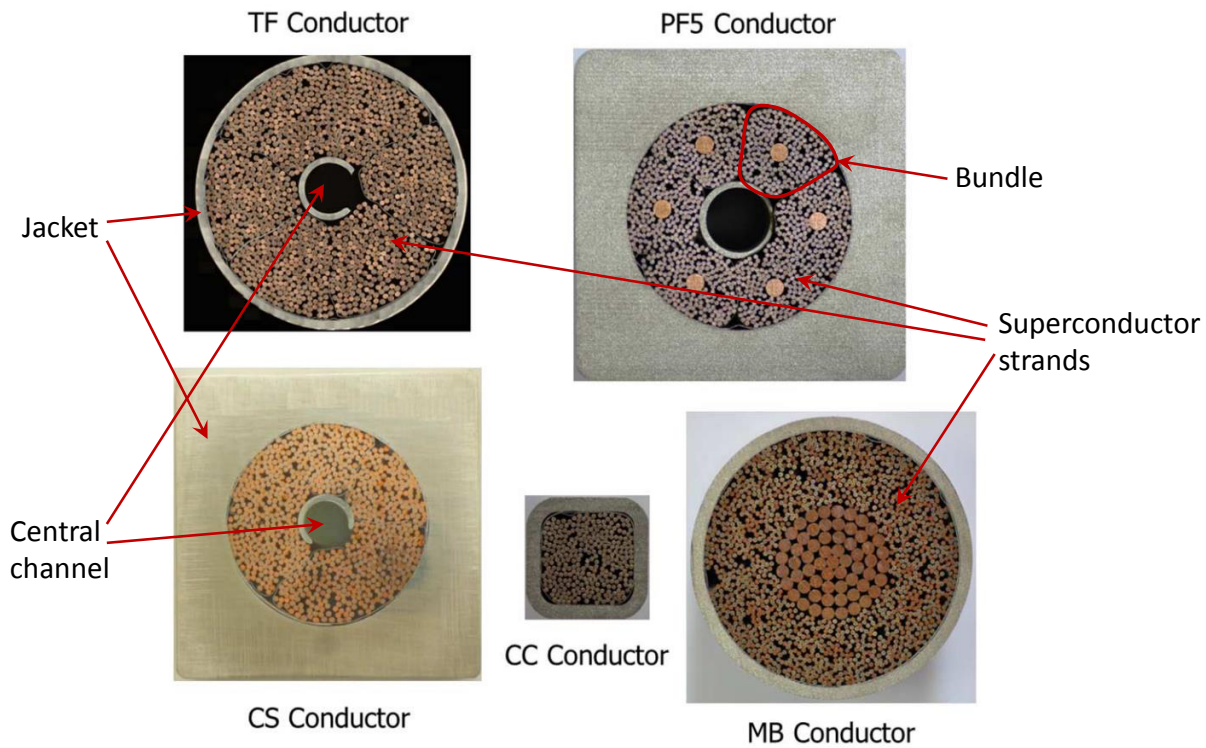


**Figure 1.4.** *Cross-sectional view of ITER conductors [24].*

- Forced convection in tubes
  - Single-phase supercritical helium (CICC)
  - Single-phase subcooled HeII
  - Two-phase with boiling
- Natural circulation (thermosiphon loop)
  - Two-phase with boiling

Pool natural convection consists *grosso modo* of immersing the heated component in a pool filled with the coolant. The fluid is heated in contact with the surface of the component and, either by thermal expansion or by the formation of vapor, a natural convection current appears which transports energy to some other point where a heat exchanger removes it from the pool.

Forced convection in tubes consists of a cooling loop where the momentum of the fluid is produced by an active element, namely a pump. Power is injected in the circuit in order to ensure its circulation. This method is used when the heat load is so high that natural convection would not be able to ensure good temperature margins. The major drawbacks are the presence of mobile elements in the circuit, which get used and need maintenance and the need of electric supply to ensure the cooling. In general these systems need to be redundant in order to provide reliability.

Cooling by natural circulation loop deserves being treated separately in the following section and will be the center of our attention from now on.

## 1.4 Superconducting magnets cooled by natural circulation

The two-phase thermosiphon natural circulation loop is a cooling system well-suited for cases where the heat load is not excessive and where a sufficiently high vertical length can ensure a high gravity driving force. The main advantage of this cooling choice is the absence of pump in the cooling circuit. As the flow is driven by gravity, the presence of the driving force is permanent and automatically regulated by the amount of heat load. Neither maintenance of mobile parts nor electric energy are required for the functioning: it is a passive system with inherent safety features. Additionally, the efficiency of this method relies on the fact that boiling has very big surface heat transfer coefficients.

In the following sections we are going to describe two of the concrete applications of the thermosiphon in superconducting magnets: the CMS detector of the LHC and the GLAD spectrometer for R3B. A mathematical model of a two-phase loop thermosiphon is presented in section 2.3.

### 1.4.1 The superconducting solenoid for the CMS detector

The Compact Muon Solenoid (CMS) is an experimental device incorporated to the Large Hadron Collider of the CERN (European Organization for Nuclear Research)[17]. It is a large general-purpose particle physics detector. The CMS experiment and project was made with the objective of investigating a wide range of physics, including the search for the Higgs boson, extra dimensions, and particles that could make up dark matter. It is a close companion of the ATLAS experiment (also in the LHC). It is located in an underground cavern at Cessy in France, just across the border from Geneva. The astonishing number of 182 scientific institutes and 42 countries form the CMS collaboration are represented by approximately 3,800 people, who built and now operate the detector. The major breakthrough of this project is the recent observation of high energy particle collision events that confirm the existence of the intensely searched *Higgs boson*, the subatomic particle responsible for mass [2, 18, 19].

#### General description of the experiment

CMS is 21.6 metres long, 15 metres in diameter, and weighs about 12,500 tonnes. It is instrumented in order to determine the trajectory, energy and momentum of the particles that are the product of the collision of two opposed proton beams. The main elements involved in detection are:

- the *tracker*: 80 million silicon-made detectors that allow reconstructing the trajectory of a particle.
- the *electromagnetic calorimeter*: a scintillating detector to measure the energies of electrons and photons.
- the *hadronic calorimeter*: made of layers of brass and steel interleaved with plastic scintillators, it measures the energy of hadrons (protons, neutrons, etc.).
- the *magnet*: it produces a 4 T field used to deviate the particles by the Lorentz force in proportion to their mass-charge ratio.
- the *muon detector*: the decay of many new expected particles, e. g. the Higgs boson, produces muons that would testify their existence.

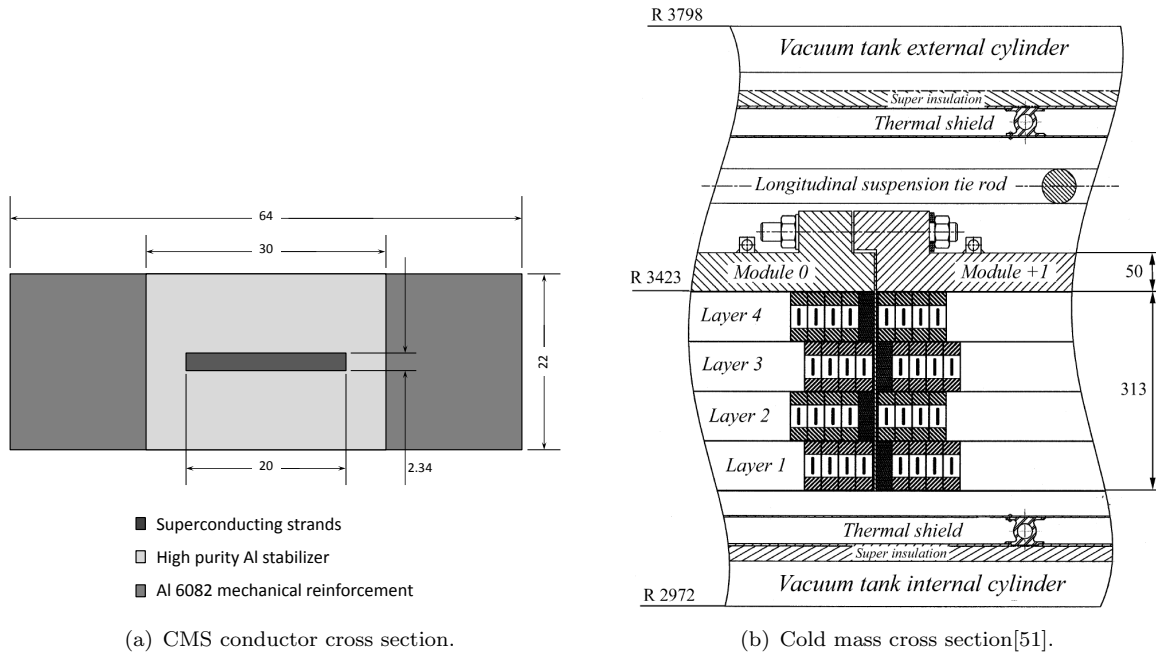


Figure 1.5. The CMS magnet.

### The superconducting solenoid

The CMS experiment is built around the magnet. The magnet is a cylindrical solenoid which provides a 4 T field with a nominal current of 19500 A and a stored electromagnetic energy of 2.66 GJ. The inductance of the solenoid is 14 H, and the circuit total resistance is around 0.1 m $\Omega$ , which gives a time decay constant of current of 39 hours; the discharge of the magnet due to resistance without external action is extremely slow. The amount of power to be injected in the system to keep it in steady state is around 38 kW. A more detailed description of the magnet design can be found in [52].

The superconductor-coolant couple chosen for CMS is NbTi-He, given that the magnetic fields are rather low (<12 T). The operation temperature of the system is 4.5 K. The superconducting cable is an over-stabilized Rutherford conductor, whose geometry is presented in Fig. 1.5. 32 multifilamentary Cu-NbTi strands, with a 1.1 to 1 copper-to-superconductor cross section ratio, are disposed in a two-row layer, immersed inside a high purity Al thermal stabilizer block. The whole is mechanically reinforced by two Al 6082 alloy blocks at each side (see Fig. 1.5(a)).

The magnet is composed of five modules and the winding is done in four layers. The whole magnet (and the cryogenic circuit) is contained inside a *cryostat*, i.e. isolated to minimize the heat transfer from the environment onto the superconductor. The principle of the cryostat is to host the internals under vacuum to minimize heat transfer by conduction and convection and to avoid thermal radiation from reaching them by means of reflecting shields. Everything that is contained inside the cryostat is known as the *cold mass*, whose cross section is shown in Fig. 1.5(b). Reference [51] contains valuable information concerning many aspects of the magnet design.

### The cooling system

CMS modules are cooled indirectly by liquid helium at 4.5 K. The fluid circulates by thermosiphon effect through 14 mm internal diameter aluminum alloy tubes that are welded on the external mandrel of the magnet with a regular spacing of 250 mm. The circuit is redundant for

reliability reasons. Besides these tubes that act as a heat exchanger between the magnet and the coolant, the hydraulic network contains:

- a collector per module;
- ascending return branches that conduct the two-phase fluid through a cryostated chimney to a phase separator on top;
- the phase separator, which acts as a liquid reservoir too;
- a down-comer that transports the liquid to feed the modules from the bottom;
- a feeder per module.

Figure 1.6(b) shows a diagram of the cooling circuit, where all these elements are explicitly identified. In normal operating conditions, the circuit contains a total liquid helium inventory of 600 l, half of it in the separator and the other half in the heat exchanger region.

### 1.4.2 The GLAD superconducting spectrometer for R3B

R3B is an international collaboration for the realization of experiments aiming to study reactions with relativistic radioactive beams. The aim of the R3B is the development and construction of a versatile reaction setup with high efficiency, acceptance, and resolution for kinematically complete measurements.

A central role at the R3B experiment is played by the GSI Large Acceptance Dipole (GLAD), a superconducting spectrometer. The superconducting coils, the cold mass of the magnet, the instrumentation of the device as well as the integration of the dipole magnet inside its cryostat is in charge of CEA Saclay, in collaboration with industrial subcontractors. The magnet will be involved in all the experiments, both for the study of the structure of exotic nuclei and for the study of nuclear reaction mechanisms (spallation reactions in particular).

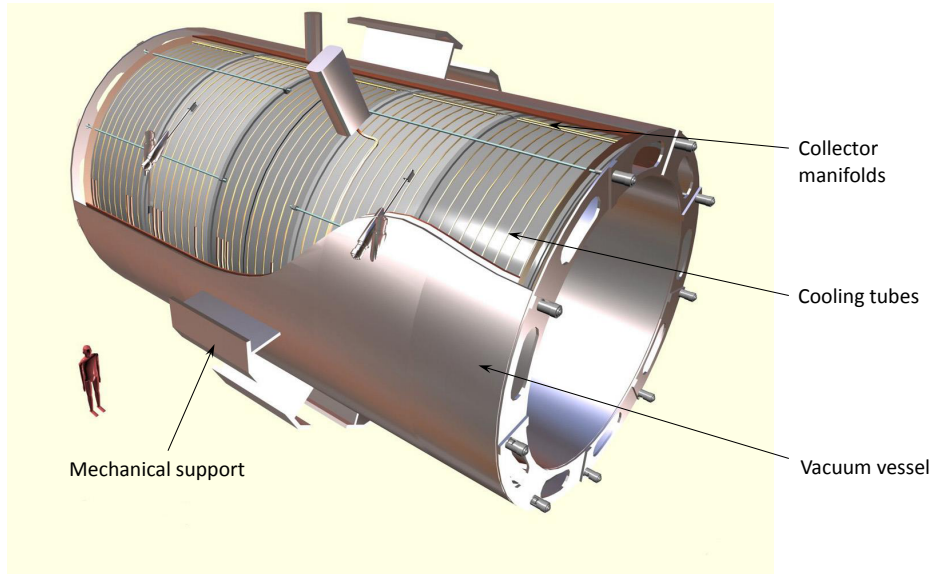
The spectrometer uses a very intense magnetic field to separate efficiently the trajectories of heavy particles from protons. The main objectives of the design are:

- a field integral of 4.8 T.m and 24 MJ stored energy;
- great angular aperture, vertical and horizontal, for light charged particles, charged nuclear fragments and non-deviated neutrons;
- large momentum acceptance to allow for the simultaneous detection of protons and heavy beam residues of the same kinetic energy per nucleon produced at the target point in front of GLAD;
- low fringe field, in order to make possible the use of detectors around the target which are sensitive to the presence of magnetic fields.

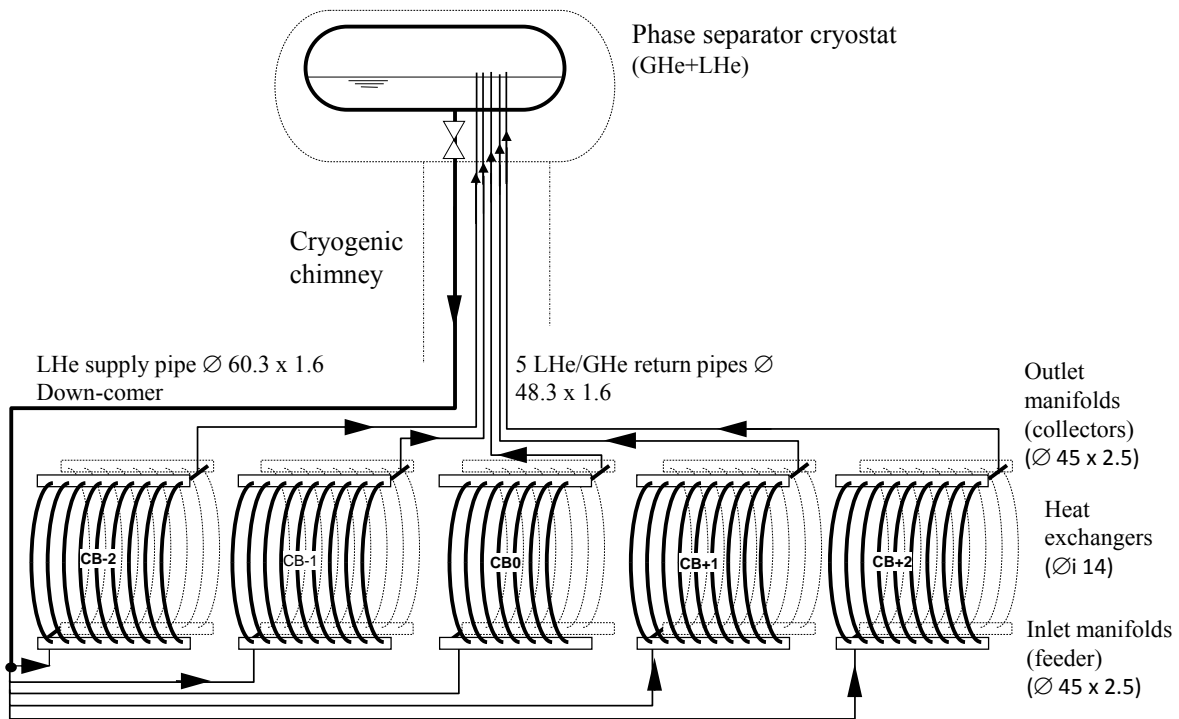
The GLAD magnet will be soon installed at GSI, Darmstadt, Germany.

With a length of 3.5 m, width of 7 m and height of 4 m, the total weight of GLAD is 55 tons, 22 of which are taken by the cold mass. The magnetic field is achieved by 6 magnets (two on the left, two on the right, one on top and one at the bottom), as can be appreciated in Fig. 1.7(a). The magnets contain 16 km of NbTi cables, weighing 4.5 tons. The current density is going to be limited to 80 A/mm<sup>2</sup>, which gives a total current in the coils of 3584 A.

The magnet cooling is provided by conduction of heat through the winding to a two-phase helium flow working in natural circulation configuration [25]. This loop is formed by elements

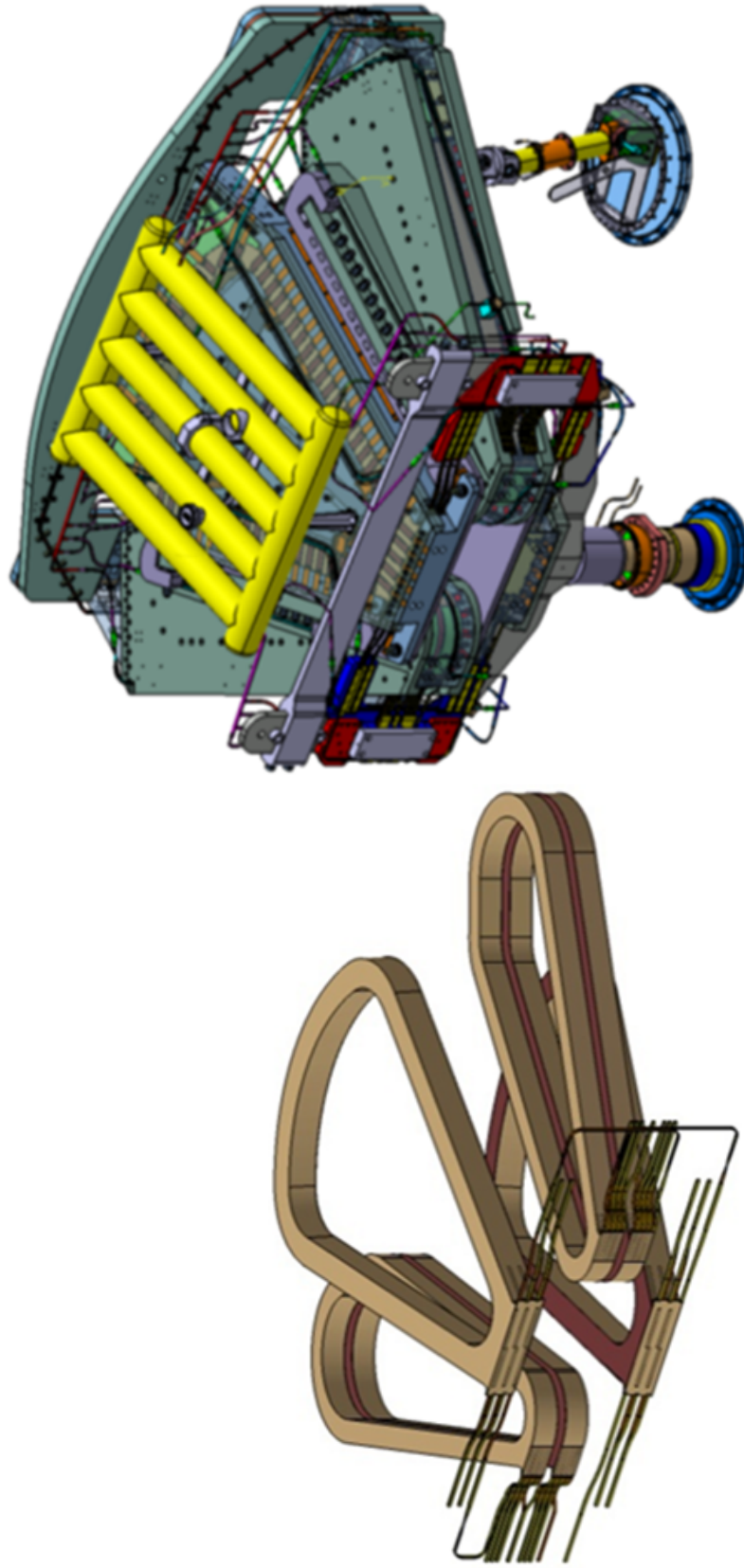


(a) Art work of the cold mass.



(b) Diagram of the circuit.

**Figure 1.6.** CMS cooling system.



(a) The GLAD magnets.

(b) The GLAD cold mass and cooling system.

**Figure 1.7.** *Illustration of the R3B-GLAD systems.*

analog to those in the cooling system of CMS (top phase separator, down-comer, ascending branch in contact with the magnet). A diagram of the cold mass with the cooling loop is presented in Fig. 1.7(b). The main qualitative particularity in the cooling system of R3B-GLAD is that a great part of the heated section of the cooling loop consists of almost horizontal tubes (inclined only  $5^\circ$  with respect to the horizontal). This is a consequence of the fact that the central plane of coils is horizontal. The quasi-absence of gravity force in the heated part of the circuit, where vapor is produced, arose questions about the feasibility and efficiency of this cooling technique. In response to that, experiments were conducted at CEA Saclay [30], that gave positive results.

## Final comments

The contents of this chapter expose the tight link that exists between superconductivity and cryogenics, and how the technical and scientific advancement of the two of them was interwoven. We can appreciate that cryogenics and, in particular, cryogenic natural circulation loops play a major role in the operation of large experimental facilities used in nuclear and particle physics research projects.

Having appreciated the technological implications of this work, in the following chapter we are going to deal with the physical phenomena involved in cooling techniques by boiling helium natural circulation loops.

# Chapter 2

## Physical background

Having appreciated the technological implications, we proceed by presenting previous concepts that will constitute the scientific frame of the work presented in this document. These concepts gravitate around the following fields:

- Two-phase flows;
- Natural circulation loops;
- Helium flows;
- Boiling heat transfer.

Some of the concepts presented in this chapter are quite general but other are quite specific to our work. The exposition of these subjects intends to shed light on the analysis of the results of this research.

### 2.1 Boiling heat transfer

Boiling is the action by which the injection of heat on a liquid, in general through a surface in contact with it, produces the phase transition from the liquid state to the vapor state. If the use of boiling by humans dates back to prehistory, detailed studies of the heat transfer mechanisms involved have not been conducted before the twentieth century. In this section, we will mainly talk about the different heat transfer regimes that can exist in boiling systems in steady state (works on transient boiling will be presented in section 2.5).

#### 2.1.1 Pool boiling regimes

One of the most important problems that led to a first understanding of boiling mechanisms is *pool boiling*: boiling induced by the heat exchange between a body fully immersed in a liquid bulk (the body being hotter than the fluid), and this fluid. Observations about this problem and the existence of different boiling regimes have been first published by Nukiyama [58]. Further research over the years led to a better understanding of the problem.

Let us define two variables that we will use for the description of the phenomena:

- *Heat flux*  $q$ : the heating power per unit surface reaching the fluid from the hot body in contact;

- *Superheat  $\Delta T$* : the temperature difference between the heated surface and the saturation temperature of the fluid.

Experiments have shown that the dependence of  $q$  vs.  $\Delta T$  is not monotonous as would be the case of heat transfer by conduction or natural convection. Figure 2.1 shows the typical shape of this dependence. When the temperature of a the submerged body can be controlled arbitrarily, four regimes can be identified on this curve as  $\Delta T$  is gradually increased:

- *Natural convection in one phase*;
- *Nucleate boiling*;
- *Transition boiling*;
- *Film boiling*.

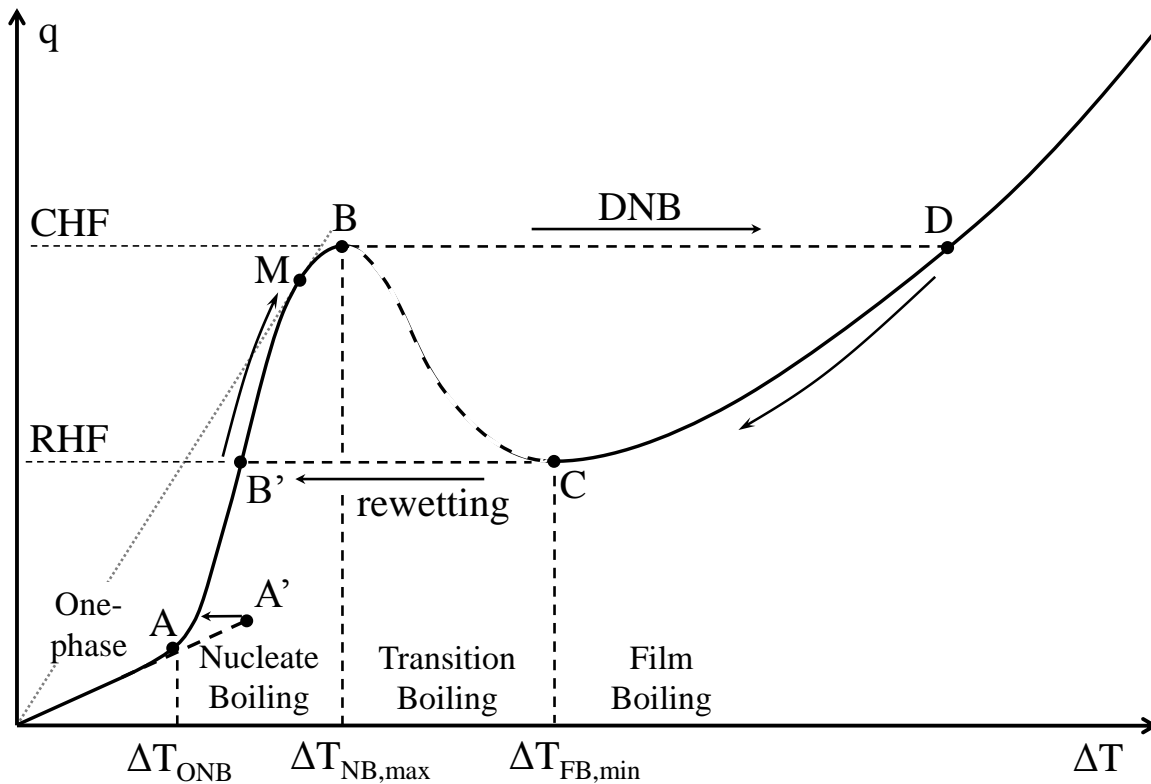


**Figure 2.1.** Pool boiling curve.

Figure 2.2 illustrates the different instances enunciated in this paragraph. At low  $\Delta T$ ,  $q$  shows a linear increase, which indicates that heat transfer is taking place by natural convection in one phase. The wall is not yet hot enough to produce vapor (first frame of Fig. 2.2). At point A the slope of the curve increases due to the onset of *nucleate boiling* (NB): bubbles start forming on the surface at irregularities that act as *nucleation sites* (second frame). This results in an increase of the heat transfer coefficient. The mechanisms responsible for this will be treated in section 2.1.4. As the wall temperature is increased, more and more irregularities can become nucleation sites, and the heat transfer is increasingly enhanced (third frame). At point M the maximum heat transfer coefficient is attained (a straight line from the origin to M would be tangent to the boiling curve at M). Beyond, the production of vapor by nucleation is so intensive on the surface, that bubbles start interacting on the surface before departing, coalescing partially. This

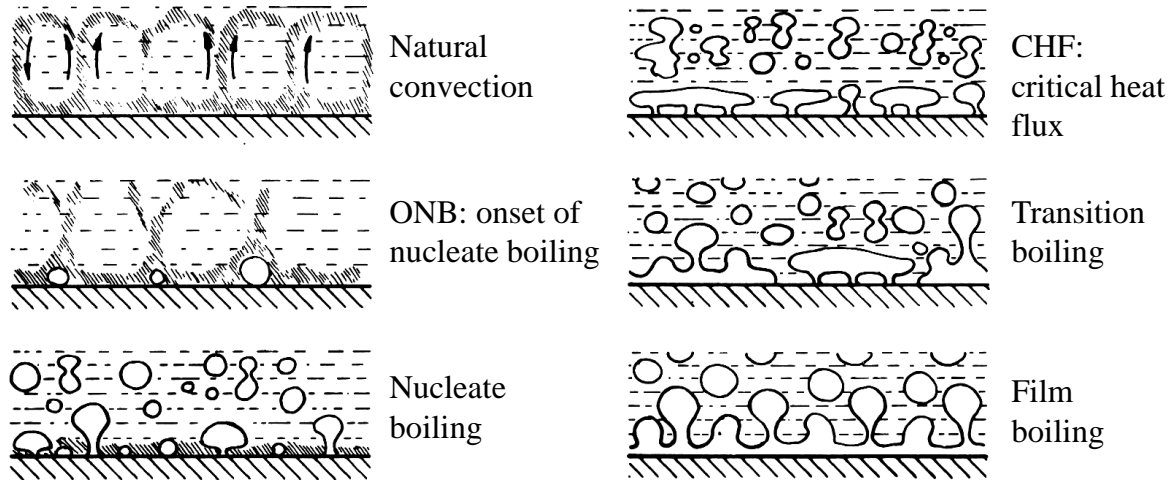


Figure 2.2. Pool boiling regimes as power is increased from 0 to CHF.

deteriorates heat transfer because vapor has a lower thermal conductivity than liquid and stops liquid from touching the surface. At point B (fourth frame) the slope becomes negative, indicating a major deterioration of heat transfer. We enter the *transition boiling* regime: the production of bubbles happens at such a high rate that vapor patches cover in an increasingly stable manner the surface, less and less in contact with liquid (fifth frame). At point C the slope becomes positive indicating that the gradual deterioration of heat transfer is complete. We enter what is called the *film boiling* (FB) regime: A vapor blanket covers entirely the heated surface, acting as a thermal insulator (sixth frame). Waves and turbulence on the liquid vapor interface allow the regular departure of bubbles, thus evacuating heat. The increase of temperature beyond point C will result in an increase of heat flux thanks to conduction/convection mechanisms through the vapor layer and, eventually, to radiation, if the wall absolute temperature is sufficiently high (which happens in the case of regular fluids such as water). However, the heat transfer coefficient in film boiling is orders of magnitude smaller than in nucleate boiling.

The preceding description is valid for a situation where the heated surface temperature can be imposed or controlled externally. This is seldom the case; instead, the imposed parameter is heat flux (or the total power to be evacuated from a system). When controlling heat flux, increasing heat flux gently from 0 we will reach point A. At this point nucleation is activated and further increases of heat flux will take us to point B. In some cases, when increasing heat flux the superheat can evolve along the segment AA', without nucleation, and at some point this metastable state terminates with the activation of nucleate boiling and a sudden drop of the temperature as indicated by the arrow. Once nucleation is active, let us assume that the heat flux value is increased and at point B is surpassed very slightly. We are trying to inject into the fluid more heat that the surface can evacuate at that temperature ( $\Delta T_{NB,max}$ ). A steady state condition is no longer possible at  $\Delta T_{NB,max}$ . The excess of power is accumulated by the surface, whose temperature will rise describing a (fast) transient excursion until point D is reached, where again the equilibrium exists (power injected = power evacuated). The maximum heat flux at which nucleate boiling exists is called *critical heat flux* (CHF) due to the fact that, in a heat flux controlled case, it represents a critical power threshold for the violent transition to film boiling. If power continues to be increased beyond, Nucleate boiling is no longer possible and the rest of the film boiling curve, after D, is found. we call this transition *departure from nucleate boiling* or *DNB*. Once the film boiling condition is reached let us analyze what happens when power is lowered. As long as heat flux is higher than CHF, there is no doubt that the stable regime will be film boiling, when power becomes lower than CHF, we will be able to scan the segment DC.

Point C, also known as the Leidenfrost point, shows the lowest temperature and heat flux at which film boiling can take place. If we lower  $q$  slightly below point C, the surface at  $\Delta T_{FB,min}$  will be evacuating more heat than injected, so there is a sudden temperature decrease down to the point B'. The film has disappeared and the surface is cooled by nucleate boiling. This process is denominated *rewetting* and the heat flux at which it happens is the *rewetting heat flux* (RHF).

When controlling power, a *hysteresis* effect is introduced by the shape of this curve (more than one possible surface temperatures for a given heat flux). Segment B'B can only be found by increasing  $q$  from below B' and segment CD by decreasing  $q$  from above D. The segment BC is not stable when controlling power. These states are only temporarily accessible during the departure from nucleate boiling (DNB) or during the film boiling collapse. The reason is a combination of the facts that:

- a unique value of evacuated  $q$  is possible for each  $\Delta T$  (ignoring the segment AA');
- segment BC has a negative slope;
- at a fixed value of heat flux, any instantaneous state that is above the curve will evolve towards the right (power injected > power evacuated  $\implies$  surface temperature increases), and any state below the curve will evolve towards the left.

It remains to say that the position of the key points of the boiling curve, and the curve itself, are highly dependent on the fluid thermodynamic properties and the geometry (shape, size, orientation) of the immersed body. Furthermore, the curve is obtained for the thermohydraulic steady state, so its validity during transients (like that of cooling of a hot body) is only approximate.

### 2.1.2 Forced convective boiling regimes

Although the description in section 2.1.1 is strictly valid for the pool boiling problem, similar behavior has been observed in other boiling systems, such as internal flow in vertical wall-heated channels. In this section we are going to treat boiling in such a system.

Let us first consider the case of a vertical tube to which a *low* heat flux is applied. The temperature profile as well as the two-phase flow pattern is depicted in Fig. 2.3(a). Let us define the *thermodynamic quality*, in terms of the average enthalpy  $h$  of the flow:

$$x = \frac{h - h_l}{h_{lg}}, \quad (2.1)$$

with  $h_l$  the liquid saturation enthalpy and  $h_{lg}$  the latent heat of the phase change. For constant wall heat flux,  $x$  will increase linearly with position, allowing us to establish an equivalence (implicit in the figure) between  $x$  and position.

The fluid enters the section in a *subcooled condition*, i.e. its local temperature is lower than the local saturation temperature (given by the local pressure). It may happen that subcooling is so high that no boiling can take place on the wall (region A). At a certain point, the local wall temperature may exceed the nucleation temperature (see section 2.1.4) even if the bulk is still subcooled; at that point *subcooled* nucleate boiling takes place (region B).

As we move downstream, we reach a point where the average cross section temperature is that of saturation. That is the point with  $x = 0$ . Note that the liquid core of the section must be slightly below saturation to allow the wall overheating. From this point on, we are in the *saturated boiling* region. When the section has a high enough content of vapor, bubbles start

interacting with each other in the bulk and coalesce into bigger structures that can reach a characteristic size close to the diameter of the section. We call this flow pattern *slug flow* (region D) due to the shape of the bubbles. As slugs get bigger and more frequent due to  $x$  increase, a new flow pattern appears, *annular flow*, where the core of the flow is vapor and the wall is covered by a thin layer of liquid (region E). Instabilities on the liquid-vapor interface allow the detachment of liquid drops that can be entrained by the vapor core (region F).

In annular flow the liquid film is so thin that its effective thermal conductivity does not allow for wall overheating necessary for nucleate boiling. Heat transfer is done by *convection* in the film and *evaporation* (we do not longer talk about *boiling*) in the interface. Finally, at a certain point the film becomes too thin to exist at the given heat flux and it vanishes, leaving the wall in direct contact with the vapor bulk. At this point, known as *dryout*, the heat transfer coefficient drops dramatically because of the low thermal conductivity of vapor and heat transfer happens by convection in the vapor core and evaporation of the liquid mist (dispersed liquid droplets in the vapor bulk). This region (G) is also called *liquid deficient* for obvious reasons and the flow regime is often referred to in the literature as *dispersed flow film boiling* (DFFB). Eventually, the full evaporation of the liquid takes place and we enter the single-phase vapor region (H).

When a *high* value of heat flux is applied, the situation may be completely different even at the same total mass flow rate. In the subcooled and very low-quality saturated regions the behavior will be similar but downstream it may happen, for high enough power values, that the production of vapor is so high that a transition to *film boiling*, very similar in nature to that of pool boiling, takes place in the low quality region, much before the slug or annular regimes could be established. This transition, by analogy with pool boiling, is called *departure from nucleate boiling* (DNB). The flow pattern consists then of a liquid core with some bubbles dispersed and a vapor film on the wall. This flow regime is referred to as *inverted annular film boiling* (IAFB). The extent of the film over the cross section will increase with quality along the tube and eventually a turbulent flow with vapor matrix will take over the whole section.

We want to emphasize the difference between *dryout* and *departure from nucleate boiling* introduced in section 2.1.1. Dryout takes place in the presence of a vapor matrix core with liquid droplets in suspension right after the full evaporation of a liquid film on the wall. The DNB consists of the formation of a vapor wall layer in the presence of a liquid matrix bulk (with eventual presence of bubbles). For this reason, dryout only takes place in the high quality region at low heat fluxes and sufficiently long sections while DNB happens in the low quality region, or even in the subcooled region only if heat flux is high enough. The two cases are depicted in Fig. 2.3(b). The heat flux at which either dryout or DNB happen is called *critical heat flux* (CHF).

### 2.1.3 Boiling crisis prediction in channel flow

*Boiling crisis* is the term used to refer to the sudden significant deterioration of boiling heat transfer that can take place at a dryout or DNB event. The heat transfer in the post-critical (post-CHF) regime can be orders of magnitude poorer than that of nucleate boiling. Thus, boiling crisis represents a limit in practical applications, in order to assure a good cooling of the heated component. The transition to film boiling in water, for example, exhibits so high wall overheating that it can lead the heated component beyond its melting point. This is a major concern in the design of nuclear reactor cores, for example, where the value of power is the controlled variable. In the case of helium, film boiling can lead to temperature rises of several K. Although no melting of the material can be expected from such an event, the resulting temperature excursion can be unacceptable from the superconductor protection point of view: superconducting state could be lost and the magnet could quench.

Most of the efforts in the literature aim to the determination of the CHF and post-CHF heat

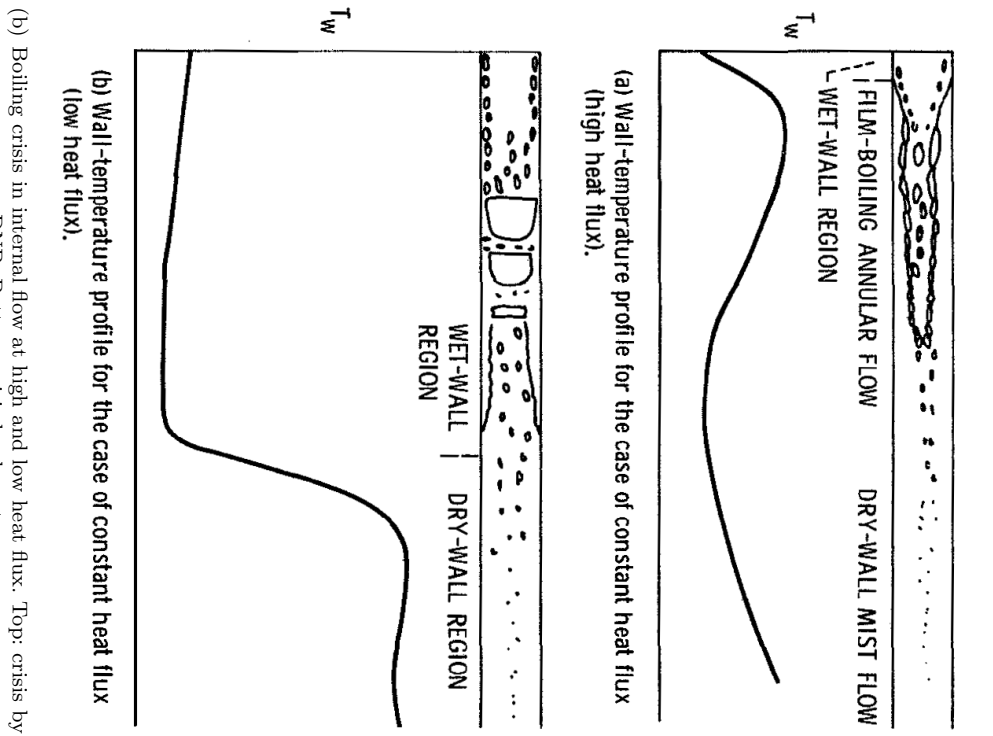
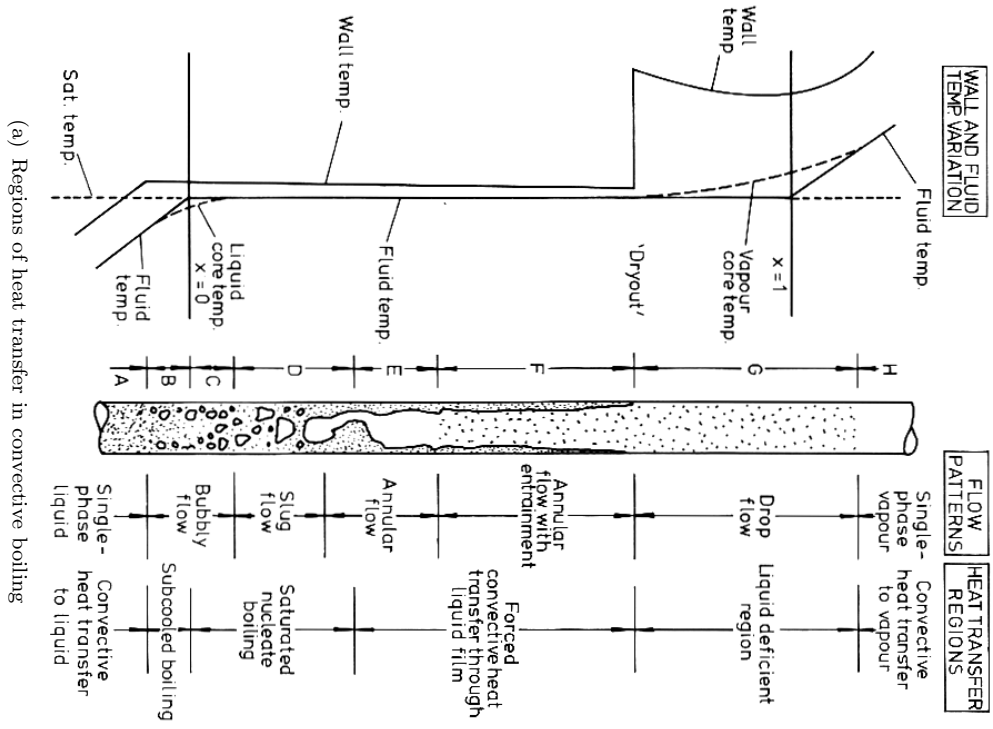


Figure 2.3. Forced convective boiling regimes.

(a) Wall-temperature profile for the case of constant heat flux (high heat flux).  
 (b) Wall-temperature profile for the case of constant heat flux (low heat flux).  
 (c) Boiling crisis in internal flow at high and low heat flux. Top: crisis by DNB; Bottom: crisis by dryout.

transfer coefficients. The correlations and lookup tables for the prediction of CHF are numerous [47, 60, 66] and, in many cases, the results they provide do not coincide with each other. This may be a consequence that the phenomenon is highly sensitive to the geometry, heating configuration and fluid properties, and the number of intervening parameters is considerable. Nevertheless, there are a few correlations that have a great level of acceptance in the field. The most complete and general of these is that one provided by successive works by Katto and collaborators [44–46, 48]. These group of researchers have made a thorough survey of experimental data of boiling crisis in convective boiling in vertical tubes with a very wide variety of fluids, including helium and other cryogenes. They identified the different mechanisms by which boiling crisis can take place and defined a criterion based on non-dimensional analysis to predict the correct mechanism. Then, for each mechanism, they determined formulas for estimating the CHF. This author has considered particularly the case of helium [49] and his correlation fits the experimental data too. However, data for helium included in the correlations is not overabundant and correspond mostly to small diameter tubes (1 or 2 mm of i. d.). Two very valuable results are presented:

- A chart/map that allows identifying the mechanism causing the transition from nucleate boiling to crisis (mainly dryout of annular liquid film or DNB with apparition of film boiling).
- Several equations that allow the calculation of CHF according to the mechanisms of crisis onset.

The transition mechanism map presented by Katto is a set of curves and regions on the plane  $(\frac{\sigma\rho_l}{G^2z}, \frac{z}{D})$  whose positions depend on the density ratio  $\frac{\rho_g}{\rho_l}$ . The symbols  $\sigma$ ,  $G$ ,  $z$  and  $D$  represent surface tension, mass flux, distance from the entrance of the heated section and tube inner diameter, respectively. Equations for the boundaries between the regions in which one of the transition mechanisms prevails are provided in their papers. The transition regimes are the following:

- *L-regime*. Dryout of liquid film in annular flow with direct transition to dispersed flow film boiling (DFFB).
- *N-regime*. DNB to inverted annular film boiling (IAFB).
- *H-regime*. An intermediate regime between L and N that we assimilate to a DNB to IAFB modified by the high void fraction flow pattern.
- *HP-regime*<sup>1</sup>. DNB to inverted annular film boiling (IAFB) at high  $\frac{\rho_g}{\rho_l}$  and high  $z/D$ .

The equations used for the prediction of the CHF,  $q_c$ , in each of the regimes are listed below. We recall that  $h_{lg}$  is the latent heat.

L-regime:

$$\frac{q_c}{Gh_{lg}} = C \left( \frac{\sigma\rho_l}{G^2z} \right)^{0.043} \frac{1}{z/D} \quad (2.2)$$

with

$$C = \begin{cases} 0.25 & \text{if } z/D < 50 \\ 0.25 + 0.09 \frac{z/D-50}{100} & \text{if } 50 < z/D < 150 \\ 0.34 & \text{if } z/D > 150 \end{cases} \quad (2.3)$$

<sup>1</sup>HP stands for *High Pressure*, where the density ratio for classical fluids is high. It consists of an observed property of these systems at high  $z/D$  that in certain conditions present higher CHF than predicted by the N-regime.

N-regime:

$$\frac{q_c}{Gh_{lg}} = 0.098 \left( \frac{\rho_g}{\rho_l} \right)^{0.133} \left( \frac{\sigma \rho_l}{G^2 z} \right)^{0.433} \frac{(z/D)^{0.27}}{1 + 0.0031 z/D}, \quad (2.4)$$

H-regime:

$$\frac{q_c}{Gh_{lg}} = 0.1 \left( \frac{\rho_g}{\rho_l} \right)^{0.133} \left( \frac{\sigma \rho_l}{G^2 z} \right)^{1/3} \frac{1}{1 + 0.0031 z/D}, \quad (2.5)$$

HP-regime:

$$\frac{q_c}{Gh_{lg}} = 0.0384 \left( \frac{\rho_g}{\rho_l} \right)^{0.6} \left( \frac{\sigma \rho_l}{G^2 z} \right)^{0.173} \left( 1 + 0.280 \left( \frac{\sigma \rho_l}{G^2 z} \right)^{0.233} \frac{z}{D} \right)^{-1}. \quad (2.6)$$

### 2.1.4 Heat transfer in the nucleate boiling regime

Nucleate boiling is the most common boiling regime and, given it presents the highest values of heat transfer coefficient of all boiling regimes, it is widely present in engineering applications, reason why it has been thoroughly studied. Nucleate boiling takes place on a surface, particularly inside/on irregularities with cavity shape. These provide a site where the initiation, growth and departure of bubbles is easier, in a thermodynamic way of speaking, than anywhere else. We will refer to these sites as *nucleation sites*. In this section we are going to treat the thermodynamic requirements for the existence of nucleation, the dynamics happening in the near-wall region and the heat transfer characteristics resulting from these phenomena.

#### Activation of nucleation sites

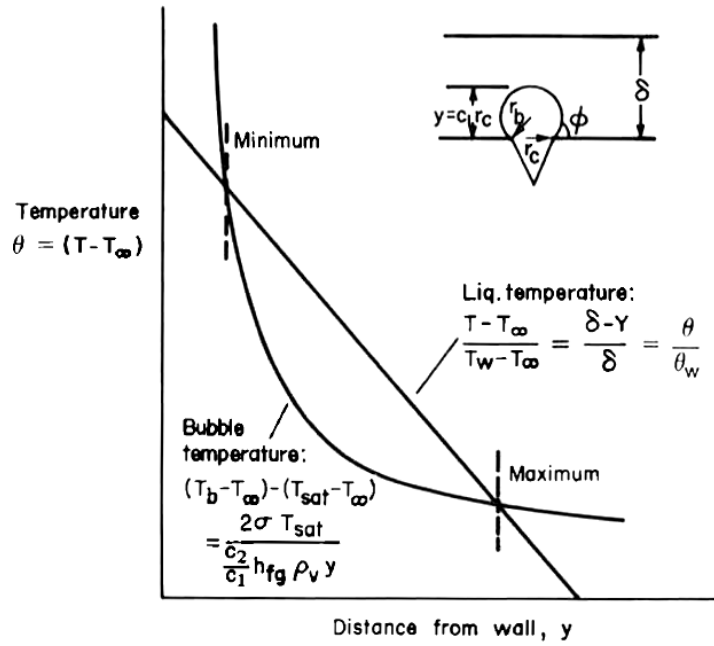
In order for a bubble to form in a liquid bulk, it would be necessary that a great number of molecules with enough energy to be in the vapor state gather at a certain point in order to form a vapor volume. This vapor volume will grow and become a bubble if its growth reduces the total Gibbs free energy. For this to be possible, it is necessary that the gas phase have a lower chemical potential than liquid, which is true at a temperature higher than the saturation point; however, it is not enough. The existence of surface tension between gas and liquid imposes a minimum radius necessary to reach this condition. The higher this required radius, the more improbable that such a vapor cluster can form spontaneously.

In the presence of a wall, theoretical thermodynamic studies show that the free energy difference required for nucleation on a solid phase is lower than in the homogeneous bulk, if the geometry is that of a cavity. That is why, in most boiling problem, we are interested in cavities as nucleation sites, because among all, they are the most probable, activated at lower free energy.

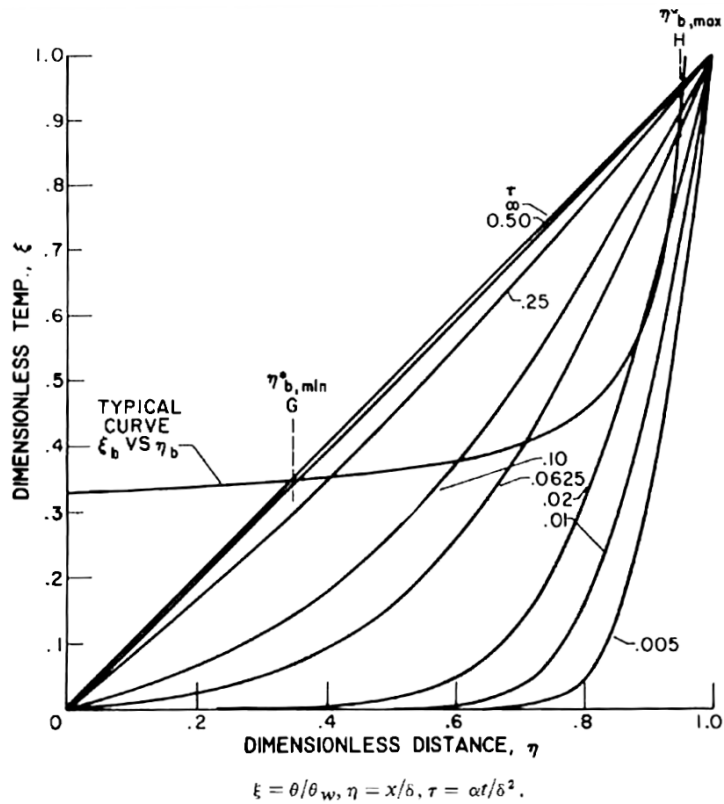
The temperature requirement for the activation of a nucleation site that produces a bubble of radius  $r_b$  is:

$$T_l - T_{sat} \approx \frac{2T_{sat}\sigma}{h_{lg}\rho_g r_b}, \quad (2.7)$$

where  $T_l$  is the temperature of the surrounding liquid. When applying heat flux on wall in contact with a subcooled liquid, we need to considering the near-wall temperature gradient in the liquid. A nucleation site can be activated if the external liquid temperature at the zenith of the bubble is higher than the requirement given by Eq. (2.7). This is represented in Fig. 2.4(a). It is assumed that the minimum radius of the bubble at a nucleation site is directly related to the radius of the cavity by a constant  $C_2$  and that the distance of the zenith of the bubble to the wall is too, by a factor  $C_1$ .  $C_1$  and  $C_2$  depend on the contact angle.



(a) Criterion for site activation in non-uniform temperature field.



(b) Criterion for site activation in transient temperature field.

Figure 2.4. Bubble nucleation in a cavity.

The straight line on the figure represents the temperature profile in the fluid. The curved line shows the required internal bubble temperature as a function of the height of the bubble, the farthest point from the wall (it is not the temperature profile inside the bubble: in all this theory it is assumed that the bubble has an internal homogeneous temperature). When the bubbles are too small or too big the criterion is not met. Only those cavities that produce bubbles of the intermediate height, comprised between the intersection points of the two lines, will be available for nucleation. The minimum wall overheat necessary is such that, for a given boundary layer thickness  $\delta$ , it produces a temperature profile curve tangent to the bubble temperature requirement curve.

This criterion is somehow too restrictive. It could be possible to have bubble growth even if the zenith of the bubble is hotter than the surroundings as long as the overall heat transfer to the bubble is positive. On this fact rely all the more complex criteria for nucleation. Furthermore, more complex phenomena as internal bubble temperature profile or  $T$ -dependent  $\sigma$  with complex bubble shape can be introduced. This is beyond the scope of our aim. Furthermore, it needs to be stated that this model assumes the mechanical equilibrium of the bubble, regarding its contact angle and its size, in order to test the possibility of existence of the bubble. During the growth of the bubble, this model is not applicable; otherwise we would not be able to explain how a size bigger than the required minimum can be obtained in the first place.

A last point that we need to mention is the fact that  $\delta$  is highly dependent on the external flow conditions. It will depend on the orientation of the surface and on the fluid velocity profile (natural convection, forced convection, etc.). It has been proved that under forced convection, as  $\delta$  tends to decrease with the increase of velocity and turbulence, the nucleation can be diminished for a given overheating. This can be still understood under the light of the simple model presented.

### The boiling cycle dynamics

Once the thermodynamic conditions required for activation are fulfilled, a periodic cycle takes place at the nucleation site. This cycle is illustrated in Fig. 2.5. There is a period where the surface is being prepared for the apparition of a bubble, characterized by a wall temperature increase, followed by the bubble formation, which produces a sudden wall temperature decrease.

The following stages are generally accepted:

1. Waiting period
  - (a) transient conduction of heat to liquid
  - (b) activation by fulfillment criteria
2. Growth period
  - (a) Bubble grow rate
  - (b) Evaporation process
  - (c) Agitation or displacement of liquid around a bubble
  - (d) Termination of bubble by departure (or collapse)

The bubbling frequency of a site, given by

$$f = \frac{1}{t_w + t_g}, \quad (2.8)$$

where  $t_w$  and  $t_g$  are the waiting and growth periods durations, for which the sum is the total duration of a cycle.

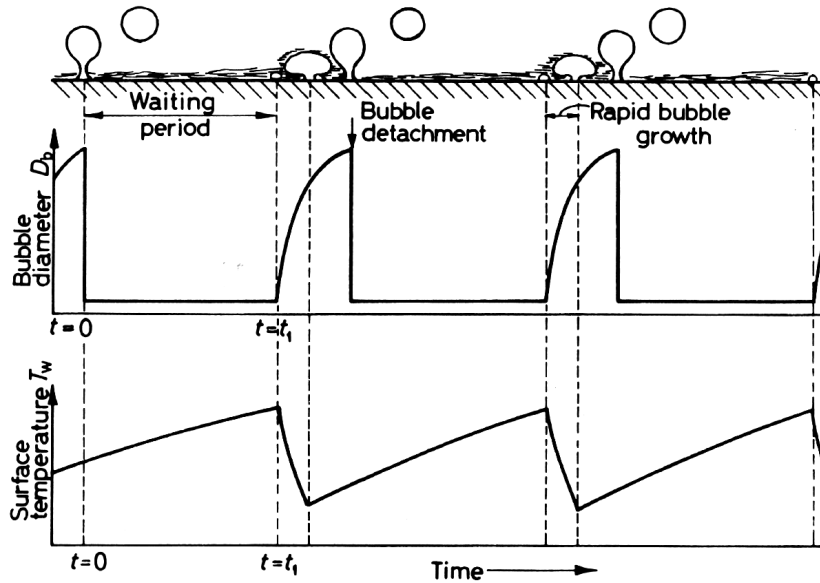


Figure 2.5. Nucleate boiling cycle.

The waiting period is the period over which the temperature profile in the boundary layer is established for allowing a bubble embryo in the cavity to grow into a big bubble. It takes place after a bubble has left the surface and cold fluid has occupied the place it left. Its duration can be estimated from the evolution of the transient temperature profile and the activation criteria. This is depicted in Fig. 2.4(b). We can postulate that the waiting period ends when the transient temperature at the zenith of the bubble embryo ( $y = Cr_c$ ) is higher than  $T_b$ , for a particular cavity size. Thus, by looking at Fig. 2.4(b) there is a minimum waiting period, which corresponds to the transient profile that is tangent to the bubble temperature requirement curve. This minimal waiting period (around  $\tau = 0.2$  for the example in the figure) corresponds to the cavity that has a radius for which the zenith is at the distance given by the point where the curves are tangent. For later times, there is an interval of activated cavity radii, comprised between the two intersection points of successive profiles and the bubble temperature curve. Thus we see how the waiting period depends on cavity radius and there are too small or too big cavities that have infinite waiting periods: those that are not even reached by the steady state  $\tau = \infty$ . This model can be improved by considering the wall heat capacity with power production in the wall but the main ideas have been exposed with this simple example.

Once the site is active again because the thermal boundary layer provides the good conditions, the growing period starts. The bubble will grow to its final size before being removed from the wall or collapsing. The main concern of studying this phase is determining the growth rate of a bubble.

Very simple theories predict a single bubble radius evolution given by

$$R \propto t^{1/2}. \quad (2.9)$$

However, experimental research on bubble growth rate reveals that individual bubble growth rate analysis is futile and a statistical approach is necessary. A law

$$R = \alpha t^n \quad (2.10)$$

with a statistical normal distribution for  $\alpha$  and  $n$  proves to be useful.

In order to determine the growing time, it is necessary to know at what size of bubble, i.e. diameter, the buoyant forces and hydrodynamic drag forces overcome resisting forces, namely,

a cocktail of surface tension and liquid inertia forces. A model that is relatively simple to use is that of Hatton and Hall [39], which states that bubble departure is relatively independent of heat flux, but highly dependent of cavity size and pressure.

Theoretically, we have all the ingredients to calculate the bubble frequency (Eq. (2.8)). In reality, given the difficulties to determine the two times involved, it would be practical to correlate the frequency with only one parameter, such as the departure diameter  $d_d$ . Accepted relations are of type

$$fd_d^n = Ctt. \quad (2.11)$$

Unfortunately, experiments have not been conclusive regarding what the exponent  $n$  should be. This could be due mainly to the fact that this law is highly dependent on what the dominant forces are, which is dependent on cavity diameter.

### Heat transfer mechanisms

Three main mechanisms are accounted for the heat transfer in nucleate boiling:

- *Bubble agitation*: The fluid motion induced by bubble growth modifies the natural one-phase convection of the liquid face, creating a forced convection heat transfer process. Heat is transported as the sensible heat in the superheated fluid being chased away by bubbles.
- *Thermal boundary layer stripping*: When a bubble leaves the site, it drags with itself the superheated layer in the vicinity of the wall, the one formed during the waiting period. Heat is transported in the form of sensible heat of the overheated fluid.
- *Evaporation*: Bubbles are formed by the evaporation of the liquid around the bubbles and in a thin film microlayer between it and the surface. When the bubble departs it transports heat in the form of latent heat.

Figure 2.6 depicts them schematically. The combination of these three mechanisms is responsible for the enhanced heat transfer coefficient of nucleate boiling compared to single-phase convection.

### Bubble coalescence

The reader may find that the nucleation problem is complicated enough, but we have just described rapidly what happens at a sole isolated cavity. When too many sites are active on the surface (i.e. at high overheat or heat flux) there is a great probability that bubbles start interacting with those produced at neighbouring sites. Also, if the cycle duration becomes too short, it could also happen that a bubble interacts with the bubble that has just left the same cavity before the latter had enough time to get far from the site. These two types of interactions can lead to bubble coalescence. The bigger bubble formed has a different dynamic given its greater size, which affects the arrival of fresh liquid to the wall, the turbulence of the liquid phase and finally the heat transfer characteristics of the regime. If coalescence is too high, dry patches that impede wall wetting can happen, deteriorating heat transfer. This is a simplistic explanation of what happens in transition boiling.

## 2.2 Two-phase flow modeling

The field of two-phase flow is quite vaste; in this section we are going to restrict our scope to the mathematical representation of the conservation laws in two-phase liquid-vapor flows. The aim is to expose the equations that will be useful for the description of the dynamics of two-phase helium natural circulation loops.

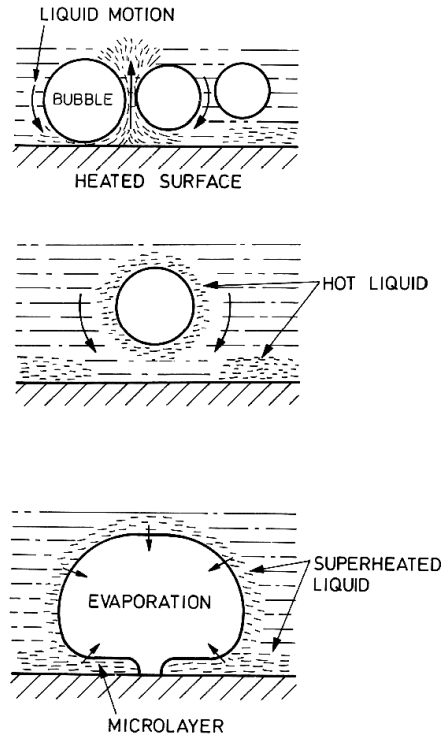


Figure 2.6. Nucleate boiling heat transfer mechanisms.

### 2.2.1 Basic definitions and conservation equations

A phase is characterized by its saturation properties, especially its density  $\rho_k$ . Let us consider the case of a two-phase mixture flowing through a long pipe with cross section  $A$ . Such two-phase flow can be locally (at each point along the pipe) characterized by the following parameters:

- the cross section area occupied by each phase,  $A_k$
- the volumetric fraction of each phase

$$\alpha_k = \frac{A_k}{A}, \quad (2.12)$$

- phase velocity  $u_k$ ,
- phase mass flow rate

$$\dot{m}_k = A\alpha_k\rho_k u_k, \quad (2.13)$$

- total mass flow rate

$$\dot{m} = \sum_k \dot{m}_k \quad (2.14)$$

- phase quality

$$x_k = \frac{\dot{m}_k}{\dot{m}} \quad (2.15)$$

- total mass flux

$$G = \frac{\dot{m}}{A} \quad (2.16)$$

- average density

$$\rho = \sum_k \alpha_k \rho_k \quad (2.17)$$

These parameters need to be interpreted as the time, cross-section average of the value of the physical quantity they represent, as given the presence of turbulence, the ideal steady state does not exist, but a statistically meaningful steady state does.

In the case of liquid vapor flow, the volumetric fraction of vapor  $\alpha_g$  is called *void fraction*  $\alpha$  and the vapor quality  $x_g$  is simply called *quality*  $x$ . These two parameters are defined as  $1 - \alpha$  and  $1 - x$  for the liquid phase. From the definitions above, the relation between  $x$  and  $\alpha$  is

$$\frac{x}{\alpha} = \frac{u_g \rho_g}{G}, \quad \text{or} \quad \frac{1-x}{1-\alpha} = \frac{u_l \rho_l}{G}. \quad (2.18)$$

Thus, the relation between  $x$  and  $\alpha$  depends on the *slip ratio*  $S$ , defined as the ratio between the phases' velocities:

$$S = \frac{u_g}{u_l} = \frac{x}{1-x} \frac{1-\alpha}{\alpha} \frac{\rho_l}{\rho_g}. \quad (2.19)$$

The general conservation equations for a two-phase flow are presented below.

Mass conservation:

$$\frac{\partial}{\partial t} (A \alpha_k \rho_k) + \frac{\partial}{\partial s} (A \alpha_k \rho_k u_k) = \Gamma_k \quad (2.20)$$

$$\sum_{k=l,g} \Gamma_k = 0 \quad (2.21)$$

Momentum conservation:

$$\frac{\partial}{\partial t} (A \alpha_k \rho_k u_k) + \frac{\partial}{\partial s} (A \alpha_k \rho_k u_k^2) = -A \alpha_k \frac{\partial p}{\partial s} - \tau_{kw} P_{kw} + A \alpha_k \rho_k (\mathbf{g} \cdot \mathbf{e}_s) + u_k \Gamma_k + \tau_{kn} P_{kn} \quad (2.22)$$

$$\sum_{k=l,g} (u_k \Gamma_k + \tau_{kn} P_{kn}) = 0 \quad (2.23)$$

Energy conservation:

$$\frac{\partial}{\partial t} \left[ A \alpha_k \rho_k \left( e_k + \frac{u_k^2}{2} \right) \right] + \frac{\partial}{\partial s} \left[ A \alpha_k \rho_k u_k \left( h_k + \frac{u_k^2}{2} \right) \right] \quad (2.24)$$

$$= A \alpha_k \rho_k u_k (\mathbf{g} \cdot \mathbf{e}_s) + q_{wk} P_{wk} + q_{kn} P_{kn} + u_k \tau_{kn} P_{kn} + \Gamma_k \left( h_k + \frac{u_k^2}{2} \right)$$

$$\sum_{k=l,g} \left[ q_{kn} P_{kn} + u_k \tau_{kn} P_{kn} + \Gamma_k \left( h_k + \frac{u_k^2}{2} \right) \right] = 0 \quad (2.25)$$

The new variables that appear in the equations are:

- $s$ , the curvilinear coordinate along the pipe;
- $p$ , the local pressure;
- $e_k$ , the (saturation) internal energy of each phase;
- $h_k$ , the (saturation) enthalpy of each phase;

- $\mathbf{g}$ , the gravity vector;
- $\mathbf{e}_s$ , the unit vector in the direction of  $s$ ;
- $\tau_{kw}$ , the wall shear stress on phase  $k$  (in Pa);
- $q_{wk}$ , the wall heat flux to phase  $k$  (in W/m<sup>2</sup>);
- $P_{wk}$ , the section perimeter on which phase  $k$  is in contact with the wall;
- $\Gamma_k$ , the mass rate of creation of phase  $k$ ;
- $\tau_{kn}$ , the shear stress on the phase interface produced by phase  $n$  on phase  $k$ ;
- $q_{kn}$ , the heat flux through the phase interface from phase  $n$  to phase  $k$ ;
- $P_{kn}$ , the perimeter of the phase interface on the cross section.

Eqs. (2.21), (2.23) and (2.25) are the conservation laws at the phase interface.

The solution of this problem requires additional equations, as there are more unknown variables than equations. Namely, it is necessary to define the phase exchange quantities  $P_{kn}$ ,  $\tau_{kn}$  and  $q_{kn}$  in terms of the average flow properties. For this reason, it is general practice to make further assumptions, about the flow topology (flow pattern, shape of vapor structures, etc.), or the interaction between phases, in order to simplify the set of equations.

### 2.2.2 The homogeneous two-phase flow model

One of the simplest models possible for representing two-phase flow in ducts is the *1D homogeneous equilibrium flow model* (HEM). It results from the following basic assumptions:

- the two phases have the same local velocity;
- the two phases are in thermodynamic equilibrium at the saturation point;
- the two phases form a perfect mixture, i.e. the vapor structures are so small that a sole equivalent continuous phase can be considered.

As a consequence it is possible to derive conservation equations for the equivalent mixture, which naturally divides the number of equations and unknowns by two. This model can be very useful when modeling helium as the hypotheses are accurate given the properties of the fluid (see section 2.4.2).

As a consequence of the hypotheses of the model, we only need to define one fluid velocity

$$u_l = u_g = u, \quad (2.26)$$

and there is a very well determined relation between void fraction and quality:

$$\frac{x}{\alpha} = \frac{\rho_g}{\rho} \quad (2.27)$$

In the most general case, the conservation equations in ducts with variable cross section area  $A$  read:

$$\frac{\partial \rho}{\partial t} + \frac{1}{A} \frac{\partial (\rho u A)}{\partial s} = 0 \quad (2.28a)$$

$$\frac{\partial (\rho u)}{\partial t} + \frac{1}{A} \frac{\partial (\rho u^2 A)}{\partial s} = -\frac{\partial p}{\partial s} - \frac{\partial p_{fr}}{\partial s}(u, \rho) + \rho \mathbf{g} \cdot \mathbf{e}_s \quad (2.28b)$$

$$\frac{\partial \left[ \rho \left( e + \frac{u^2}{2} \right) \right]}{\partial t} + \frac{1}{A} \frac{\partial \left[ \rho u A \left( h + \frac{u^2}{2} \right) \right]}{\partial s} = q_v + \rho \mathbf{g} \cdot \mathbf{u} \quad (2.28c)$$

The conservation equations in a uniform cross section tube are:

$$\frac{\partial \rho}{\partial t} + \frac{\partial (\rho u)}{\partial x} = 0 \quad (2.29a)$$

$$\frac{\partial (\rho u)}{\partial t} + \frac{\partial (\rho u^2)}{\partial x} = -\frac{\partial p}{\partial x} - \frac{\partial p_{fr}}{\partial x} (u, \rho) + \rho \mathbf{g} \cdot \mathbf{e}_x \quad (2.29b)$$

$$\frac{\partial \left[ \rho \left( e + \frac{u^2}{2} \right) \right]}{\partial t} + \frac{\partial \left[ \rho u \left( h + \frac{u^2}{2} \right) \right]}{\partial x} = q + \rho \mathbf{g} \cdot \mathbf{u} \quad (2.29c)$$

The quantity  $q_v$  is the *volume specific power* that results from the wall heat flux  $q$  and is calculated as

$$q_v = \frac{qP}{A} = \frac{4q}{D}. \quad (2.30)$$

As five dependent variables are present in Eq.(2.29) ( $\rho$ ,  $u$ ,  $p$ ,  $h$  and  $e$ ), two more equations are required, which we will refer to as *closure equations*.

$$\rho = f_{\rho}^{h,p} (h, p) \quad (2.31a)$$

$$h = e + \frac{p}{\rho} \quad (2.31b)$$

where  $f_{\rho}^{h,p}$  is a function that gives the density of the homogeneous fluid according to the thermodynamic parameters  $h$  and  $p$ . This implies that the fluid density not only changes with energy changes, but also that it is compressible, i.e. pressure affects density.

In the particular case of the two-phase region on the plane ( $h, p$ ), under the homogeneous model assumptions (S=1),

$$f_{\rho}^{h,p} (h, p) = \left( \frac{h - h_l}{h_{lg} \rho_g} + \frac{h_g - h}{h_{lg} \rho_l} \right)^{-1}, \quad (2.32)$$

where  $\rho_l$ ,  $\rho_g$ ,  $h_l$ ,  $h_g$  and  $h_{lg}$  depend on pressure, as they are saturation line properties.

The 5-equation set is complete and can be solved. The system can be treated as a one phase flow with a varying density, function of pressure and internal energy or enthalpy.

In order for the model to be complete, it is necessary to define the friction term on the RHS of Eqs. (2.28b) or (2.29b) as a function of the system variables. It is generally defined as:

$$\frac{\partial p_{fr}}{\partial z} = f_{2\phi} \frac{G^2 (1 + \rho_l v_{lg} x)}{2D \rho_l}, \quad (2.33)$$

with the two-phase friction factor given by the regular one-phase friction factor correlations. For example, the Blasius law can be used for turbulent flow in smooth pipes:

$$f_{2\phi} = f_{1\phi} (Re_{2\phi}) = 0.316 \left( \frac{GD}{\mu_{2\phi}} \right)^{-1/4}. \quad (2.34)$$

The two-phase viscosity  $\mu_{2\phi}$  [20] is generally given by

$$\frac{1}{\mu_{2\phi}} = \frac{x}{\mu_g} + \frac{1-x}{\mu_l}. \quad (2.35)$$

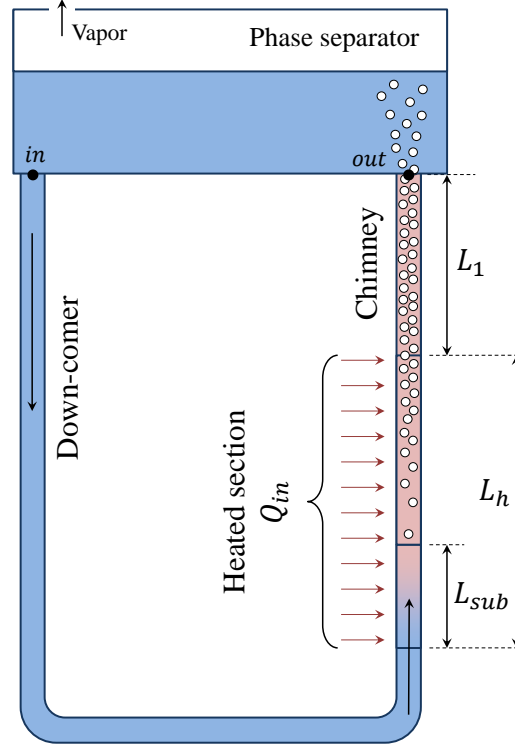


Figure 2.7. Example of a one-dimensional two-phase natural circulation loop.

## 2.3 The natural circulation principle

Natural circulation is a hydrodynamic phenomenon in which continuous fluid motion is produced thanks to the action of gravity and fluid density non-uniformity. In most of the cases, as density of liquids generally decreases with temperature, the density variations in the medium are induced by a temperature gradient and an external heat flux.

### 2.3.1 Dynamics of a natural circulation loop

Along this work, we are going to be interested by the problem of two-phase flow in a natural circulation open loop. The system of study will be formed by a phase separator at the top and a U-shaped circuit below it, as the one illustrated in Fig. 2.7. For practical purposes, given the predominance of length over tube diameter, the circuit can in general be approximated as a 1D internal flow, with variable density.

Let us assume that the loop can be described by the conservation laws for a one dimensional flow in a duct by the homogeneous flow model (Eqs. (2.29)). For simplicity, let us consider a circuit with uniform tube cross section  $A$ . The path integral of the momentum equation (2.29b) between the entrance of the circuit (point *in*) and the exit (point *out*) can be calculated:

$$\underbrace{\int \frac{\partial(\rho u)}{\partial t} ds}_{dH/dt} + \underbrace{\int \frac{\partial(\rho u^2)}{\partial s} ds}_{\Delta p_{acc}} = - \underbrace{\int \frac{\partial p}{\partial s} ds}_{\Delta p} - \underbrace{\int \frac{\partial p_{fr}}{\partial s}(u, \rho) ds}_{\Delta p_{fr}} + \underbrace{\int \rho \bar{g} \cdot \hat{e}_s ds}_{\Delta p_g} \quad (2.36)$$

$$\frac{dH}{dt} = \Delta p + \Delta p_g - \Delta p_{fr} - \Delta p_{acc} \quad (2.37a)$$

$$H = \oint \rho u ds \quad (2.37b)$$

$$\Delta p = p_{in} - p_{out} \quad (2.37c)$$

$$\Delta p_g = \int \rho \bar{g} \cdot \hat{e}_s ds \quad (2.37d)$$

$$\Delta p_{fr} = \int \frac{\partial p_{fr}}{\partial s} ds \quad (2.37e)$$

$$\Delta p_{acc} = (\rho u^2)_{out} - (\rho u^2)_{in} \quad (2.37f)$$

The dynamic equilibrium point for velocity is given by:

$$\Delta p_g = \Delta p_{fr} + \Delta p_{acc} - \Delta p. \quad (2.38)$$

$\Delta p_g$  is interpreted as a driving force, and the RHS as the sum of resisting forces.

### 2.3.2 Two-phase loop equilibrium

We will proceed by finding the explicit expression of the terms in Eq. (2.38) in the case of a two-phase flow loop. Let us first describe the thermodynamic behavior of the fluid along the loop. The fluid enters the heated section in a subcooled condition and a certain amount of heat needs to be absorbed by the fluid before reaching its saturation point and starting boiling in the heated section. In Fig. 2.7, the length  $L_{sub}$  corresponds to the section over which the fluid is still in the subcooled condition. After saturation is reached, boiling starts and vapor starts populating the bulk of the fluid, reducing appreciably the average density on the cross section. This will produce the gravitational driving force<sup>2</sup>. Once the fluid leaves the heated section, no more vapor is added to the fluid particle, but on its way to the condenser the fluid conserves (approximately) its total enthalpy, which may be somewhere between that of saturated liquid and that of saturated vapor. Finally, the fluid particle arrives into the phase separator, the vapor goes to the free surface and the nearly saturated liquid can be recirculated. Vapor can be expelled from the loop, in order to avoid pressurization by energy accumulation. In that sense we say that the loop is *open*.

Some assumptions are made in order to simplify the analysis:

- density of the liquid phase is assumed constant, not depending on temperature or pressure;
- no boiling is accepted in subcooled region;
- differential pressure effects on fluid properties are neglected;
- kinetic and potential energy contributions are neglected in the energy balance.

Under this description of the problem, the energy conservation in the heated section yields

$$Q = \dot{m} C_p \Delta T_{sub} + \dot{m} h_{lg} x_{out}, \quad (2.39)$$

where

---

<sup>2</sup>Vapor production is not strictly required for having driving force, but a density gradient is needed, either in one-phase or two-phase flow. In the cases in which vapor is produced, the one-phase density variations are neglected.

- $Q$  is the total power injected in the heated section ( $W$ );
- $C_p$  is the specific heat capacity of the liquid phase ( $J kg^{-1} K^{-1}$ );
- $\Delta T_{sub}$  is the subcooling temperature difference ( $K$ );
- $h_{lg}$  is the latent heat of vaporization ( $J kg^{-1}$ );
- $x_{out}$  is the mass quality at the exit of the heated section (non-dimensional).

Moreover,

$$L_{sub} = \frac{\dot{m} C_p \Delta T_{sub}}{Q} L_h \quad (2.40)$$

and

$$x_{out} = \frac{Q - \dot{m} C_p \Delta T_{sub}}{\dot{m} h_{lg}}. \quad (2.41)$$

Furthermore, the heat balance from the entrance of the heated section to an arbitrary point of the ascending branch gives

$$x(z) = \begin{cases} 0 & \text{if } z \leq L_{sub} \\ \frac{z - L_{sub}}{L_h - L_{sub}} x_{out} & \text{if } L_{sub} < z \leq L_h \\ x_{out} & \text{if } z \geq L_h \end{cases} \quad (2.42)$$

A closure equation is necessary to link the thermodynamic variables of the system of equations. It is convenient to note that density depends on the value of local mass quality. If the HEM is considered:

$$\rho = \left[ \frac{x}{\rho_g} + \frac{1-x}{\rho_l} \right]^{-1}. \quad (2.43)$$

Taking into account Eqs. (2.42) and (2.43), the LHS of Eq. (2.38) can be written as

$$\begin{aligned} \Delta p_g &= \int_{L_{sub}}^{L_h} [\rho_l - \rho(x(z))] g dz + L_1 g (\rho_l - \rho(x_{out})) \\ &= g \rho_l (L_h - L_{sub}) \left[ 1 - \frac{\ln(1 + \rho_l v_{lg} x_{out})}{\rho_l v_{lg} x_{out}} \right] + L_1 g (\rho_l - \rho(x_{out})), \end{aligned} \quad (2.44)$$

where  $v_{lg} = \frac{1}{\rho_g} - \frac{1}{\rho_l}$ .

The friction contribution can be calculated for turbulent flow using friction factor correlations, for example (see section 2.2.2). For educational purpose only, we will assume that an overall friction factor  $K$  can be calculated for the one-phase and two-phase sections of the loop, taking into account all the lengths and the nature of flow in each section and the concentrated head losses:

$$\Delta p_{fr,total} = K_{1\phi}(\dot{m}) \dot{m}^2 + K_{2\phi}(\dot{m}, x_{out}) \dot{m}^2 (1 + \rho_l v_{lg} x_{out}) \quad (2.45)$$

We will just point out that  $K_{1\phi}$  and  $K_{2\phi}$  are weakly varying functions of  $\dot{m}$  and  $x_{out}$ . This dependence can be ignored as a first approximation for a simple qualitative result. The appearance of the last term on the RHS becomes clearer in the light of Eq. (2.33).

The mass conservation imposes  $\rho u A = \dot{m}$ . Thus, using Eq. (2.43), the acceleration term (Eq. (2.37f)) can be obtained as:

$$\Delta p_{acc} = \frac{\dot{m}^2}{A^2} x_{out} v_{lg}. \quad (2.46)$$

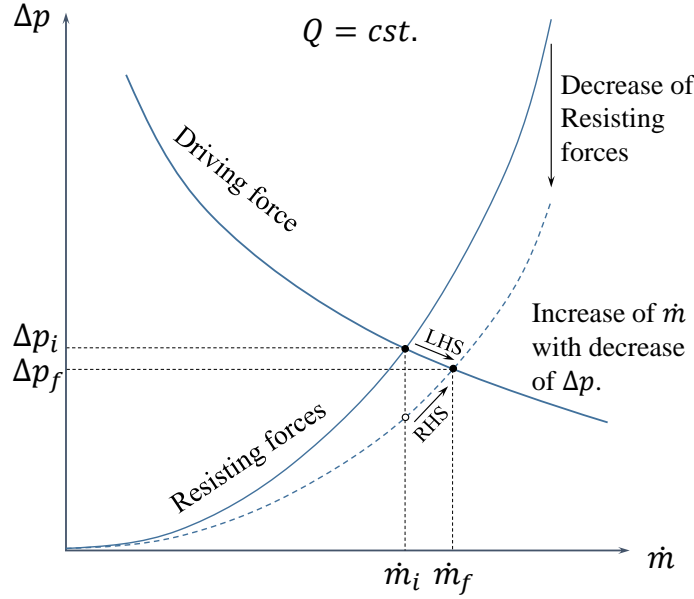


**Figure 2.8.** Response of the equilibrium point to the overall friction coefficient change in a natural circulation loop.

Finally, if we assume that in the discharge at the exit, the internal pressure is equal to that at the bottom of the phase separator,  $\Delta p$  (Eq. (2.37c)) is only due to the acceleration of the fluid at the entrance and the eventual concentrated head loss at this point that produce a decrease of  $p_{in}$ :

$$\Delta p = -\frac{\dot{m}^2}{2A^2\rho_l} - K_{entry}\dot{m}^2. \quad (2.47)$$

All the terms of Eq. (2.38) can be expressed in terms of  $\dot{m}$  and  $Q$  and a set of physical and geometrical constants. Thus, Eq. (2.38) provides  $\dot{m}$  as a function of  $Q$ . Explicitly,

$$\Delta p_g = K_{1\phi}\dot{m}^2 + K_{2\phi}\dot{m}^2(1 + \rho_l v_{lg} x_{out}) + \frac{\dot{m}^2}{A^2} x_{out} v_{lg} + \left( \frac{1}{2A^2\rho_l} + K_{entry} \right) \dot{m}^2. \quad (2.48)$$

Let us note that, for a fixed value of power, the LHS of Eq. (2.48) decreases as  $\dot{m}$  increases, while the RHS terms increase.

The dependence of  $\Delta p_g$  on  $x_{out}$  plays a significant role in the response of the equilibrium  $\dot{m}$  to  $Q$ . In general,  $\Delta p_g$  is a fast increasing function of  $x_{out}$  at low  $x_{out}$ , but for higher quality, even if the increasing trend is kept, the function saturates. This is a consequence of the two-phase density as a function of quality. Thus, the increase in mass flow rate is steep at low power (with an approximate power law  $\dot{m} \propto Q^{1/3}$  [56]), but it reaches saturation at a given value of power. It can even happen that the terms in the RHS (especially friction and acceleration contributions) be more responsive to power changes than the LHS, if power is sufficiently high. In that situation, mass flow rate diminishes as power increases. This has been measured in the case of helium natural circulation loops [9, 13].

Equation (2.48) also allows appreciating the effect of the constants of the system in the equilibrium mass flow rate. This situation is illustrated in Fig. 2.8. If, for example, the friction coefficients decreased in a given factor keeping constant  $Q$  and  $\dot{m}$ , the RHS would decrease (blank point in the figure). Thus, the driving force of the loop would exceed the resisting forces. This unbalance of opposing forces tends to produce an increase of  $\dot{m}$ . For the equilibrium to be restored if  $Q$  is still kept constant,  $\dot{m}$  needs to increase in order to lower the LHS and increase

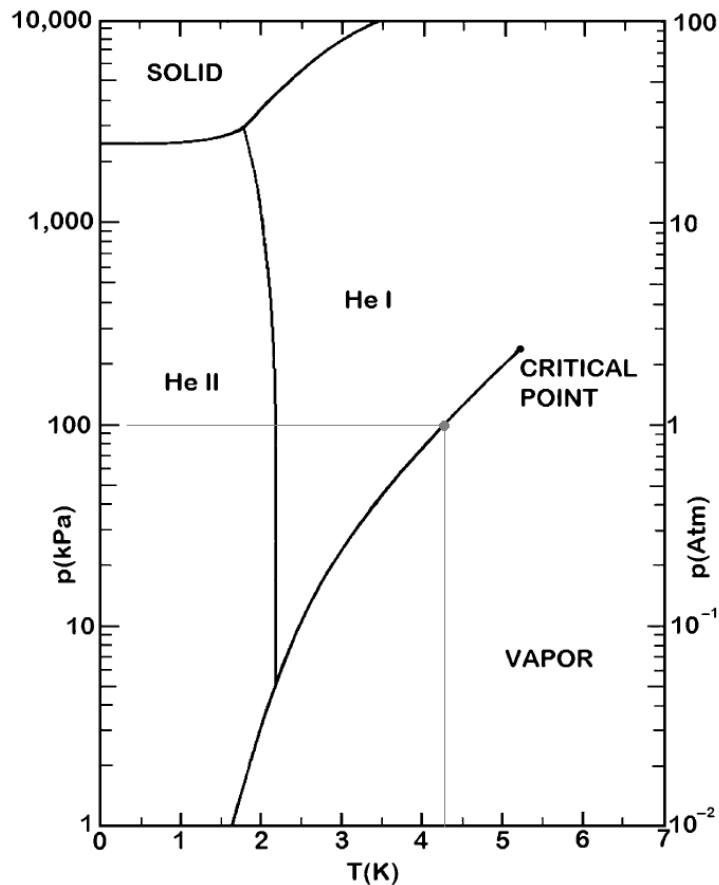


**Figure 2.9.** Helium phase diagram. The outlined point corresponds to the atmospheric pressure condition, the working point in this work.

the RHS, until equality is reached. The direct consequence of this is that the equilibrium value of the friction term decreases with respect to the initial equilibrium at the initial friction factor, even if the equilibrium mass flow rate increases, in response to a decrease of the friction factor.

## 2.4 Helium flows

Helium is the fluid which in its natural isotopic abundance has the lowest boiling point at atmospheric pressure, at 4.2 K. This feature makes it a very important fluid in extremely low temperature applications, especially superconductor cooling. Furthermore, the physical properties of helium differ enormously qualitatively and quantitatively from other well known coolants, such as water and nitrogen. In this section we expose some of the most relevant characteristics of helium in two-phase flows.

### 2.4.1 Phase diagram

Helium can be found in the three well-known states of matter: solid, liquid and gaseous. However, the phase diagram of this substance, shown in Fig. 2.9, presents a very singular particularity: there is no triple point between these three states. As a result of its quantum properties, solid states cannot exist below a pressure of 2.5 MPa, no matter how low the temperature is.

Within the liquid phase, there is a particular state that liquid helium can take only at very low temperature: the *superfluid state*. The line separating the two liquid phases is called

**Table 2.1.** Saturation properties of water, nitrogen and helium at atmospheric pressure.

Fluid	$T_{sat}$ K	$\rho_l$ kg/m <sup>3</sup>	$\rho_g$ kg/m <sup>3</sup>	$\rho_l/\rho_g$	$h_{lg}$ kJ/kg	$\mu_l \times 10^6$ kg/(m s)	$\mu_g \times 10^6$ kg/(m s)	$C_{pl}$ kJ/(kg K)	$\sigma \times 10^3$ N/m
Water	373	960	0.6	1600	2250	283	12.06	4.22	730.5
Nitrogen	77	807	4.56	177	200	141	5	2.03	8.85
Helium	4.2	125	16.6	7.53	20	3.17	1.25	4.48	$88.77 \times 10^{-3}$

the  $\lambda$ -line but it does not represent the same type of phase transformation as the passage from liquid to gas or solid. There is no latent heat necessary for the transformation. When crossing this boundary, the liquid loses completely its viscosity and the physical behavior of the fluid can no longer be described by classical fluid dynamics. Thus, when talking about liquid helium, we make a difference between *Helium-I* (or normal helium) and *Helium-II* (or superfluid helium). The properties of He-II are surprising, as is its high thermal conductivity, which can be orders of magnitude higher than that of conducting solids. This anomalous behavior can only be explained through complex quantum models. On the other hand, He-I, despite its low intermolecular interaction and viscosity, can be treated as a classical fluid.

The liquid-vapor saturation line has a positive slope in the plane p-T and there exists a *critical point* (5.1953 K, 0.22746 MPa) beyond which there is no longer a sharp transition between two phases with different densities. This is similar to what happens in other fluids.

The present study involves helium at near-atmospheric, near-saturation conditions. Consequently, as can be seen in Fig. 2.9, our attention will be directed to boiling He-I phenomena.

### 2.4.2 Physical properties at saturation

The physical properties of the coexisting liquid and vapor at the saturation point are determinant in all the boiling and two-phase flow phenomena observed. A comparison with other widely used fluids can be useful in order to know to what extent already known results for other fluids are applicable to helium. Table 2.1 exposes the most relevant saturation properties of water, nitrogen and helium at atmospheric pressure.

The most striking observations when comparing He to other fluids are:

- The density ratio between the two phases is quite close to unity;
- Surface tension is extremely low;
- The latent heat of vaporization is extremely low;
- The dynamic viscosity of liquid is two orders of magnitude lower.
- The gas to liquid dynamic viscosity ratio is one order of magnitude lower.
- Specific heat is the same order as for the other fluids.

The result of these characteristics is that helium flows are usually much more turbulent than in other fluids, because of low viscosity, and vapor structures can be more easily atomized, because of low surface tension. Small vapor structures are predominant. Evaporation takes place at low power given the low value of latent heat, but the comparatively high heat capacity allows for low overheating in wall boiling regimes. Furthermore, the low density ratio makes bubbles to have a relatively low limit velocity of ascension. This combined with easy atomization makes that a homogeneity assumption for two-phase flow modeling be appropriate in a wider range of situations than for other fluids. Furthermore, void fraction, as predicted by the homogeneous assumption, is a less violently varying function of mass fraction than in other fluids at low quality.

### 2.4.3 Flow Patterns

Two-phase flows of helium have been studied in many different configurations, especially those present in superconducting machines. The two more simple configurations of our interest are internal flows in horizontal and vertical channels. As we said in section 2.4.2, helium may have a two-phase flow behavior quite different to other well studied fluids. Among our main concerns, we want to know what the flow pattern is at a given flow condition and what is the right model to estimate pressure drop and heat transfer coefficients, in consequence.

Previous studies on vertical helium flows have had as an objective the construction of flow-pattern charts. These researches, to our knowledge, are not really extensive. The most important work in this area is that of Zust and Bald [79]. Their main result is a chart on the plane mass quality - total mass flux for *adiabatic flows*. In this chart only four flow patterns are present, as only those have been observed for the helium flows in their experiments:

- bubbly flow,
- slug or big bubble regime,
- churn turbulent flow,
- annular flow.

The chart they draw is shown in Fig. 2.10. These results have been qualitatively confirmed by Augyron [3] although the limits between patterns observed by her are quantitatively different from those in [79]. This could be a consequence of channel diameter, which can play a role even at fixed  $x$  and  $G$ . The limitation of these researches is that the mass fluxes are more than one order of magnitude too low compared with the values observed in our work. We will refer to them only in an informative manner as there is no experimental evidence that the equations provided for the limits are still valid at high mass flux. Furthermore, all these measurements were performed on adiabatic tube sections. The local behavior in heated sections can be different from that predicted by the chart due to the non-constant mass fraction along the tube.

The work by Augyron [3] provides the following rules for transition between regimes, which fit correctly their experimental observations:

- from bubbly to agglomerated flow, void fraction equal to 0.1;
- from agglomerated slug flow to churn flow a formula is given linking mass quality and mass flux:

$$x = \frac{\rho_g}{\rho_l - \rho_g} + \frac{0.05}{G} \left( \frac{g D \rho_g \rho_l^2}{\rho_l - \rho_g} \right)^{1/2}. \quad (2.49)$$

A theoretical estimation for transition to annular accepted in the work by Zust and Bald is the formula given by Wallis [74]:

$$x = \frac{0.9 [g D \rho_g (\rho_l - \rho_g)]^{1/2}}{G}. \quad (2.50)$$

This formula could not be properly tested in the cited works as the annular regime could not be observed properly in their experiments, except for very particular cases where  $x > 0.8$ . The mass fluxes they used are too low to observe this regime. Furthermore, the formula has been obtained from regular fluids, such as water, which calls into question its applicability to helium.

It has been observed that, given the high level of turbulence in helium flows and the low values of surface tension, in *heated tubes* regular big structures as those in slug regime are very rare when the mass flux is raised beyond the limits of the presented chart. The slug regime is

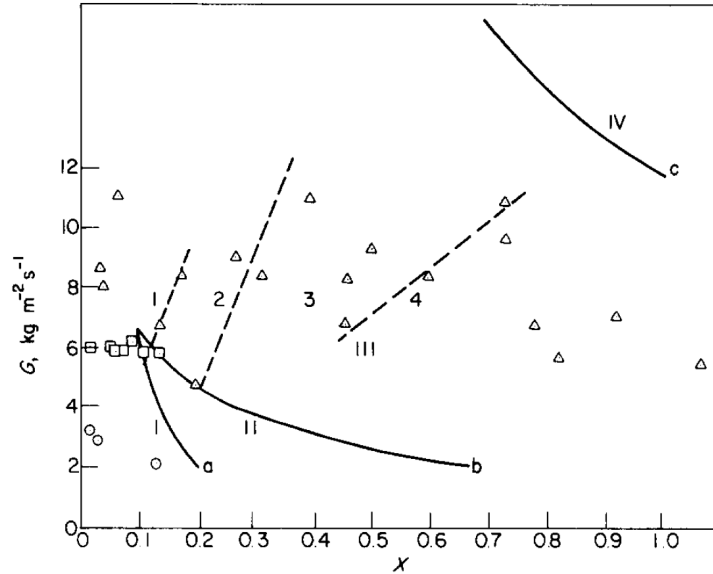


**Figure 2.10.** Two-phase flow pattern chart for helium in vertical channels by Bald and Züst [79]. The solid lines denote theoretically predicted flow regime boundaries: *a* – the transition to slug flow  $\alpha = 0.3$ ; *b* – the upper limit for slug flow; *c* – the transition to pure annular flow. These lines sub-divide the map into the following areas: I – bubble flow; II – slug flow; III – churn turbulent flow; IV – pure annular flow. The broken lines describe four areas with the following bubble velocity patterns. 1 – bubble rise velocity is regular; 2 – bubbles rise at different velocities; 3 – stagnant bubbles close to the tube wall, fast flow in core; 4 – fully developed back-flow close to the tube wall.

very hard to observe in helium, the predominant regimes are bubbly, churn turbulent and droplet flow, as observed by Züst and Bald [79].

To our present knowledge, there are no other significant works in the literature on helium two-phase flow patterns in vertical ducts at higher mass flow rates. As visualization is not part of the scope of our work, we will limit to the extrapolation of these empirical results and infer the flow pattern from other observed behavior apart from the local parameters in the charts.

#### 2.4.4 Void fraction

There are some studies that address the problem of void fraction and friction in helium flow, both vertical and horizontal.

One of the main references in void fraction measurements in helium vertical flow is the work by Khalil et al. [50]. They tested several well known two-phase void fraction correlations in order to evaluate their applicability range in terms of pressure and mass velocity. The major conclusion is that near atmospheric pressure, at low mass velocity it is Levy's correlation which predicts rather well the data, while at high mass flux, the homogeneous model is quite satisfactory at all values of quality. In accordance with this, the slip ratio (ratio of phases velocities) approaches unity as the mass flux increases.

Concerning horizontal flow, the work by Filippov [26] presents as one of the main results a correlation for void fraction, which qualitatively matches the criteria for vertical flow in the sense that at high mass flow rate it becomes the homogeneous model:

$$\alpha = \left[ 1 + \frac{1-x}{x} \left( \frac{\rho_g}{\rho_l} \right)^{1-y} \right]^{-1} \quad (2.51)$$

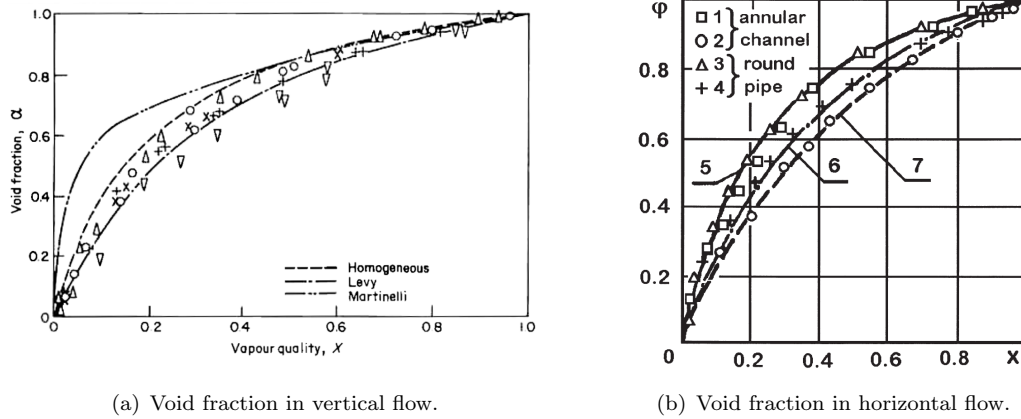


**Figure 2.11.** Void fraction data in vertical and horizontal flow as a function of quality. (a) Results by Khalil.  $P = 1.2 \text{ atm}$ , each data series has a different value of  $G$  (values not specified in the reference). (b) Results by Filippov. 1, 2, 3 and 4: data at different values of  $G$ :  $110, 34, 71$  and  $21.5 \text{ kg m}^{-2} \text{ s}^{-1}$  respectively; 5: homogeneous model; 6 and 7: analytical results by Filippov for low  $G$ .

where

$$y = \begin{cases} 0 & \text{if } G \geq 200 \text{ kg m}^{-2} \text{ s}^{-1} \\ 0.457 \times G^{-0.16} & \text{if } 10 \leq G \leq 200 \text{ kg m}^{-2} \text{ s}^{-1} \end{cases} \quad (2.52)$$

with  $G$  in  $\text{kg m}^{-2} \text{ s}^{-1}$ .

Figure 2.11 summarizes the main results for void fraction in helium, and the normally used correlations.

### 2.4.5 Review on two-phase friction estimation

Previous experimental research on the problem of two-phase flow friction pressure drop in vertical upward flow with several fluids, helium in particular, exists. There are two main groups of works: those focused on adiabatic flow and those that consider the effects of the presence of a heat flux on the wall. The latter are more poorly present in the literature, especially for post-CHF regimes.

Helium adiabatic two-phase flow pressure drop has been studied by a few authors [23, 27, 72, 79] who point out the effect of flow pattern on friction pressure drop. At low quality  $x$ , the homogeneous model prediction gives quite reasonable results. The friction factor  $f$  can be calculated using the regular correlations, for example the Blasius law:

$$f_{2\phi} = \frac{2 \frac{\partial P_{fr}}{\partial z} D \rho_l}{G^2 (1 + \rho_l v_{lg} x)} = 0.316 \left( \frac{GD}{\mu_{2\phi}} \right)^{-1/4}. \quad (2.53)$$

The two-phase viscosity  $\mu_{2\phi}$  [20] is generally given by

$$\frac{1}{\mu_{2\phi}} = \frac{x}{\mu_g} + \frac{1-x}{\mu_l}. \quad (2.54)$$

Subbotin et al. [72] published a regularly cited work about friction pressure drop with helium in vertical circular channels. Observing their plots for data at atmospheric pressure, shown in Fig. 2.12, the conclusion is that the homogeneous model gives a good prediction of the pressure drop up to qualities of around 0.35. At higher quality values they describe what they call the hydraulic resistance crisis phenomenon, characterized by a significant decrease of the slope of  $\frac{\Delta p}{\Delta \rho_l}$ . This could be the result of the fact that, even if the two phases have similar values of

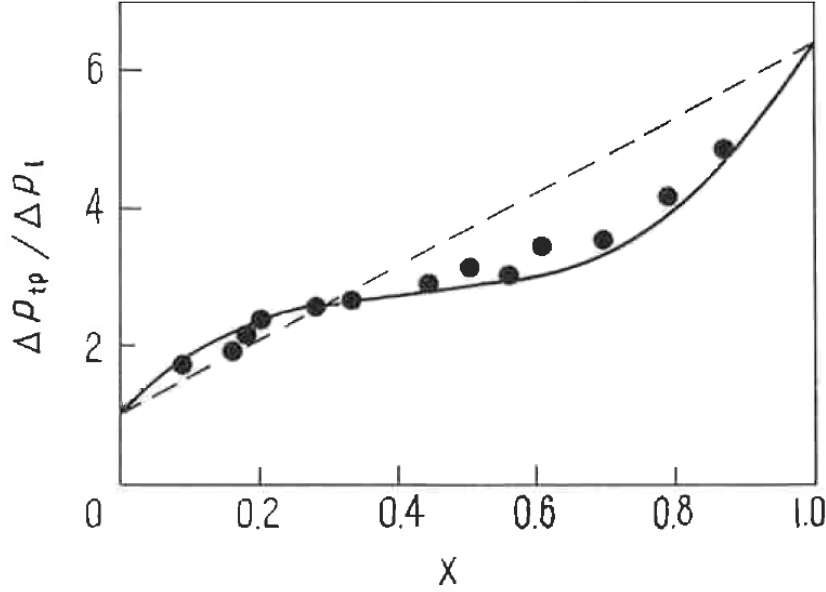


**Figure 2.12.** Two-phase friction factor in helium for vertical tubes by Subbotin et al.  $P=101 \text{ kN/m}^2$ ,  $G=115 \text{ kg m}^{-2} \text{ s}^{-1}$ ,  $D=1.63 \text{ mm}$ . --- Homogeneous model; — Subbotin's formula.

velocity, the flow pattern, i.e. the distribution of the phases in the cross section, affects the wall friction phenomena.

Reported data by Subbotin [72] shows that from  $x \approx 0.3$  the measured values of friction pressure drop are below the prediction of the homogeneous model. They propose to estimate the friction pressure drop gradient from the following formula:

$$\frac{\partial P_{fr}}{\partial z} = f_l \frac{G^2}{2D\rho_l} \left( 1 + F(x) \left( \frac{f_g \rho_l}{f_l \rho_g} - 1 \right) \right), \quad (2.55)$$

with the function  $F$  given by a table. We performed the best third order polynomial fit to data in order to have a tool easier to handle. The function  $F$  can be calculated as:

$$F(x) = 3.357x^3 - 4.336x^2 + 1.9837x. \quad (2.56)$$

Heated pipe flow pressure drop experiments have been conducted on non-cryogenic and cryogenic fluids. Beattie [11] gives a table with different calculation methods depending on the flow and heat transfer regime. In the low quality pre-CHF regime he proposes the bubbly flow model, in which the friction factor is defined as in Eq. (2.53) but  $\mu_{2\phi}$  is given by

$$\frac{1}{\mu_{2\phi}} = \frac{1}{\mu_l} \frac{1 + x \left( \frac{\rho_l}{\rho_g} - 1 \right)}{1 + x \left( \frac{\rho_l}{\rho_g} \frac{3.5\mu_g + 2\mu_l}{\mu_g + \mu_l} - 1 \right)}. \quad (2.57)$$

This definition provides a slightly higher prediction of friction pressure drop that fits better heated wall data, probably because it takes into account the non homogeneity of the vapor concentration profile on the cross section.

Pressure drop measurements on the heated section of a helium natural circulation loop have already been done but only in the low quality ( $<0.15$ ), NB regime [6]. These experiments show that in the NB regime, the homogeneous flow model gives very satisfying result for total pressure drop estimation. This indirectly implies that the void fraction estimation given by the homogeneous model is adequate for helium flows in large channels ( $\approx 10 \text{ mm}$  i. d.). However,

no record of measurements of friction pressure drop in the post-CHF regime in such systems is available.

We recall that in the post-CHF region two main situations can take place [20, 40, 57, 59]: either the flow is in the IAFB regime or in the DFFB regime (defined in section 2.1.2). If the IAFB is present, it occupies the region near the entrance of the heated section and can eventually, if the section is long enough, be followed by a region in DFFB regime.

Beattie proposes the simplest approach for the estimation of friction pressure drop in post-CHF regimes, by using the following definitions for  $f_{2\phi}$  and  $\mu_{2\phi}$ :

$$f_{2\phi} = \frac{2 \frac{\partial P_{fr}}{\partial z} D \rho_l^2}{\rho_g G^2 (1 + x v_{lg} \rho_l)^2} = 0.316 \left( \frac{GD}{\mu_{2\phi}} \right)^{-1/4}, \quad (2.58a)$$

$$\frac{1}{\mu_{2\phi}} = \frac{\rho_g}{\mu_g \rho_l} \left\{ 1 + x \left( \frac{\rho_l}{\rho_g} - 1 \right) \right\}. \quad (2.58b)$$

It is possible to show that this choice comes from the assumption that

- there is a saturated vapor layer close to the wall, responsible for the wall shear stress;
- the turbulent velocity profile is fully developed in the radial direction within the vapor layer.

Under this hypothesis the friction pressure drop can be calculated as if the whole section was fully occupied with saturated vapor that moves at the same *mean velocity* as the mixture. Naturally, this approach seems more reliable in the case of DFFB, where no veritable boundary exists between the vapor film and the bulk. However, these assumptions may not be appropriate in the IAFB regime when the viscosity and/or density of the two phases are comparable, or the vapor film too thin.

More complex models for estimating friction pressure drop in IAFB can be found in the literature. Models that intend to estimate heat transfer coefficients, as those presented in Refs. [38, 54], indirectly estimate the wall shear stress  $\tau_w$  and the thickness of the vapor film  $\delta$ . They do this by assuming a given, detailed nature for the velocity profile (turbulent or laminar profiles) in the radial direction and two independent constraints (e.g. boundary conditions at the edge of the film, total mass flow rate, vapor mass flow rate) that allow solving a system of equations for a unique pair  $(\tau_w, \delta)$  at each position along the heated section. Unfortunately, these authors treat exclusively the problem of subcooled or extremely low quality IAFB with no bubbles in the bulk.

## 2.5 Review on transient boiling heat transfer in helium

If boiling in steady state conditions involves very complex phenomena, not exhaustively studied up to date, boiling in transient conditions is still more complex and the literature on the subject less abundant, not to mention specific work on cryogenics. However, a selection of very interesting works treating transient boiling heat transfer in helium, that expose different aspects of the problem and regimes, is presented here. Most of the works were motivated by the problem of superconducting magnet cooling and thus, the experimental setups respond to the design choices in what respects geometry, heating configuration, flow regimes, values and wave function of power, etc..

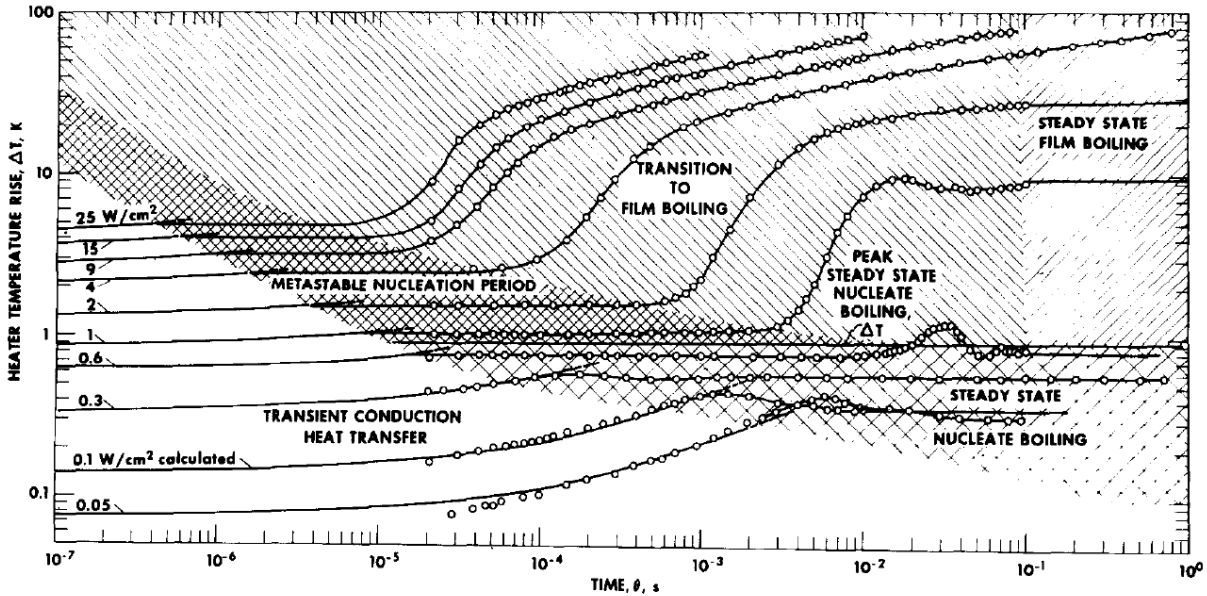


Figure 2.13. Heater temperature evolutions for different heat flux values, measured by Steward [71] in pool boiling from a vertical flat plate in a helium bath at  $4K$ .

### 2.5.1 The findings of pool boiling experiments

One of the aspects that interest us is the evolution of surface heat transfer during the very initial instants after a sudden increase in power or wall heat flux. A few authors have performed experiments of pool boiling under transient heat load.

Steward [71] performed one of the first experiments of transient heat transfer with helium on flat vertical surfaces in an initially static saturated liquid bath. He observed that during the very first instants after power injection the only available heat transfer mechanism is solid conduction in the heater and in the fluid close to it. He pointed out the importance of the effect of the heater heat capacity on these transients and the predominance of Kapitza resistance in the  $\mu s$  time range (especially for power close to and higher than steady state CHF). He also highlighted, for power higher than steady state CHF, the existence of a meta-stable nucleate boiling stage right before the sudden and intense temperature excursion typical of boiling crisis. The measured temperature evolutions that lead them to all these observations are shown in Fig. 2.13. These works provides a wide view of the phenomenology that can be expected. On the other hand, the applicability of the results was limited, because of the small size of the heating system, the non existence of a convective flow at the initial condition and the non-confinement feature of pool boiling.

With the purpose of clarifying the boiling helium superheating limits, Sinha et al. [69, 70] performed stepwise power injection experiments on a bismuth crystal in pool boiling configuration, and measured the temperature of the sample by a magnetic technique [16]. Their experimental data is shown in Fig. 2.14. The waveform of the time evolution of surface temperature depended on the level of power applied. For low power (curves a, b and c), the response presented a rounded peak above the finally attained temperature; above a given power (from curve d on), this peak became very sharp and its intensity was limited to a fixed temperature value. This allowed them to infer the *homogeneous nucleation limit* of helium, only attainable in such a transient regime given its meta-stable feature with a fast decay kinetics. They point out that this limit is somehow lower than the spinodal derived from Van der Waals theory. For helium at atmospheric pressure, this limit is  $0.35 K$ ; when reached by the liquid, nucleation takes place and puts end to the pure conduction transient described in the previous paragraph. Additionally,

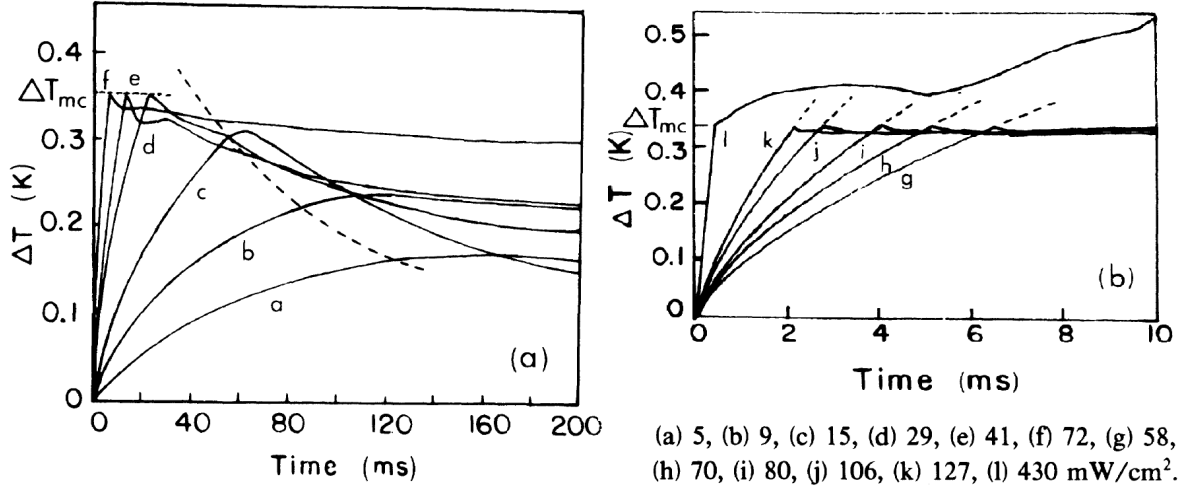


**Figure 2.14.** Heater temperature evolutions for different heat flux values, measured by Sinha et al. [69] in pool boiling in a helium bath.

these authors affirm and justify the possibility of having higher *wall superheat* than this value in the case nucleate boiling and elevated heat flux, given that the measured temperature is not the liquid's temperature but the time-space-averaged heater temperature, affected by the fraction of the surface covered by vapor. As a result, their experiments were highly illuminating on the difference between liquid and wall superheat in transient and steady state conditions but show that nucleate boiling temperature limits are highly dependent of each situation.

There is a group of Japanese authors that found interest in the lifetime of the meta-stable nucleate boiling regime before the transition to crisis identified by Steward. They performed experiments [63, 67] with horizontal cylinders in helium baths in which they measure this lifetime  $t_L$  as a function of a stepwise applied surface heat flux  $q$ , always higher than the steady state CHF. They identified two distinct regimes. From CHF to a higher power (30% higher),  $t_L$  decreased very steeply with the increase of  $q$  ( $t_L \propto q^{-12.5}$ ); for higher  $q$  the trend was still decreasing but less steeply ( $t_L \propto q^{-2.5}$ ). The effect of the heat input waveform was studied too. They concluded that their correlation could be generalized for functions monotonically increasing and saturating to a final value if the total amount of energy  $\int_0^{t_L} q dt$  was considered for its definition. Furthermore, they confirmed that the meta-stable regime is of nucleate boiling nature, as the measured temperature values were the natural prolongation of the nucleate boiling curve  $\Delta T$  vs.  $q$  beyond steady state CHF. These two valuable results are illustrated in Fig. 2.15.

Another interesting point of transient boiling is that heat transfer conducting to the formation and collapse of the vapor film during film boiling. A semi-empirical model was presented by Iwasa and Apgar [43]. They performed experiments on a flat copper surface ( $20 \times 20 \text{ mm}^2$ ) in a liquid helium bath on which they applied stepwise power pulses. They performed a detailed analysis of the temperature transient measured on the surface of the plate, taking into account the heat capacity of the wall material, which allowed them to estimate the instantaneous heating power transfer to the fluid. Data reduction allowed them to find an equivalent heat capacity of the vapor film that depends on temperature only, and that takes into account the vapor specific heat, as well as of the latent heat for film thickness change. Thus, the transient evolution of wall superheat  $\Delta T$  is:

$$q_t(t) = q_s(\Delta T) + a(\Delta T) \frac{\partial \Delta T}{\partial t}, \quad (2.59)$$

where  $q_t(t)$  is the instantaneous value of power transferred to the fluid,  $q_s(\Delta T)$  is the steady state heat flux transferred at a given superheat and  $a(\Delta T)$  is the film's heat capacity. The functions  $q_s$  and  $a$  are given in their article. Two unknowns ( $q_t$  and  $\Delta T$ ) are present; the equation needs

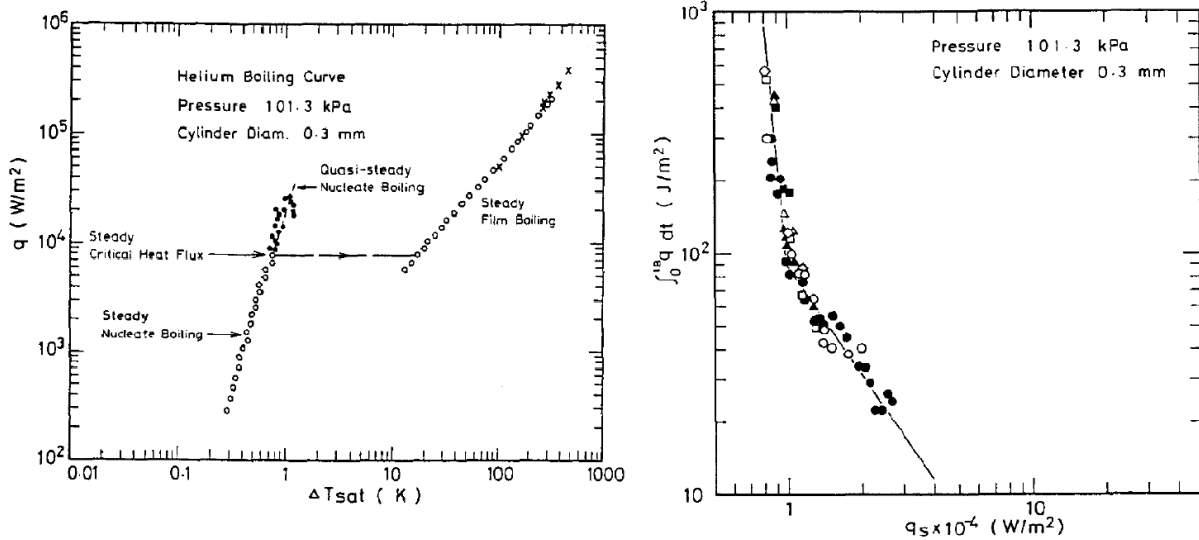


**Figure 2.15.** Results on nature and duration of quasi-steady nucleate boiling by Sakurai et al. [63]. Left: Helium boiling curve for a horizontal cylinder, with steady and quasi-steady data. Right: Experimental power laws of critical energy as a function of heat flux.

to be solved simultaneously to the heater's heat balance<sup>3</sup>.

A last experiment that is worth mentioning, although the fluid is not helium but nitrogen, is that conducted by Sinha et al. [68]. They placed vertical 10 cm long wires (diameter  $<0.25$  mm) inside a 5 cm i.d. dewar filled with liquid nitrogen. The most striking finding was that the sudden injection of a stable heat flux could induce a permanent transition to film boiling even if the final heat flux was as low as only 40% of the CHF obtained increasing power quasi-steadily. They attributed this to the time lag between the accumulation of energy near the heater and the full development of the natural convection currents. They verified indirectly this hypothesis by repeating the experiments in the presence of a convective current produced by a second flat heater placed under the vertical wire. They observed that the increase of the secondary heater's power produced an increase of the transient CHF.

Thus the transient pool boiling experiments allowed getting a full picture of the phenomenology involved in transient boiling regarding the initial pure conduction phase, its limitation by the onset of nucleation, the nucleate boiling phase, and eventually, for sufficiently high power a departure from this state in the case of boiling crisis after a certain amount of time that depends on the accumulated energy transferred to the fluid.

## 2.5.2 Transient boiling in channels

The problem of transient boiling in internal flow deserves a particular treatment as the phenomenology can be substantially affected with respect to that of open flow due to both confinement and elevated near-surface flow velocity.

A pioneer experiment that showed a wide view of the phenomenology of transient boiling in rectangular vertical channels is that by Schmidt and Turowski [64]. They injected power on the two walls of a 10 cm length channel formed by the gap between two vertical plates separated by 0.2 to 3 mm, immersed completely in a helium bath. The flow is thus produced by natural circulation. They measured the evolution of the system in quasi-steady power progressions and in the case of stepwise and periodical power wave functions. The steady state experiments showed

<sup>3</sup>If the heater has a small heat capacity, it is possible to assume that  $q_t$  is identical to the injected power.

that the values of CHF in channels (2000 to 5000 W/m<sup>2</sup>) are lower than those for pool boiling vertical walls (>6000 W/m<sup>2</sup>). The transient heat load experiments with stepwise power revealed that significant temporary temperature excursions (2 K degrees), presumably due to boiling crisis, can take place *at heat flux appreciably lower than the steady state CHF* at the same channel position. These excursions have the aspect of a fast temperature increase, followed by a more gradual decrease back to the nucleate boiling typical values. Permanent boiling crisis was only observed for final power values superior to steady state CHF. If this work shed light on phenomena that seem specific to channel flow, no detailed information is available on the time evolution of the flow inside the channel.

Iwasa and Apgar [43] have also performed narrow channel experiments with their apparatus. They intended to analyze the influence of the channel gap (0.25, 0.5 and 1 mm) in the transient film boiling phenomena. They determined that if during the evolution the temperature does not reach values high enough to have a vapor film thickness comparable to the gap (50% of it) the heat transfer characteristics are identical to those in open flow. For this they provided a third order polynomial function  $\lambda(\Delta T)$  that gives the expected film thickness at a given superheat derived from their semi-empirical model.

Boiling transients in channel flow in circular cross section pipes has been studied both in forced and natural circulation by Russian authors in small diameter (<2.8 mm i.d.) short (15 cm long) vertical channels. Some of these authors are Pavlov and Babitch [4, 61], who conducted experiments on an externally insulated 2.8 mm i.d., 15 cm long brass channel immersed in a helium bath (free circulation). They applied ramps of power on the wall while measuring the temperature at 8 equidistant axial positions. They noticed that for low power increasing rate, the value of heat flux at the moment of DNB is a strictly decreasing function of the position measured from the inlet, identical to that in steady state. However, for sufficiently high power increase rates (above 2000 W m<sup>-2</sup> s<sup>-1</sup>), a given segment length of the channel measured from the exit simultaneously faces a DNB transition at a higher instantaneous heating power than in the slower cases. This put into evidence a different mechanism favoring DNB only present for fast input power transients. They attribute this feature to the fact that during violent power injection, the increase of void fraction in the cross section expels fluid from the channel into the bath and natural circulation takes a given amount of time to establish; during this period the transition to crisis cannot be like in steady state because of the absence of flow. Based on this and some additional assumptions on mass exchange between the boundary layer and the bulk of the tube, they proposed a model for predicting the time of occurrence of burn-out as a function of the heat flux history in this bulk dominated regime. In the case of a stepwise rise of heat flux, the model predicts the following relation between the applied power  $q$  and the critical time  $t_c$ :

$$\frac{q}{q_s} \left[ 1 - \exp \left( -\frac{t_c q_s}{h_{lg} \rho_g d_d} \right) \right] + \frac{\rho_l}{\rho_l - \rho_g} \left\{ 1 - \exp \left( -\frac{t_c q_s}{h_{lg} \rho_g d_d} \right) - \left[ \exp \left( -\frac{4q v_{lg} t_c}{D h_{lg}} \right) - \exp \left( -\frac{t_c q_s}{h_{lg} \rho_g d_d} \right) \right] \left( 1 - \frac{4q d_d}{q_s D} \left( 1 - \frac{\rho_g}{\rho_l} \right) \right)^{-1} \right\} = 1. \quad (2.60)$$

In this expression,  $q_s$  is the steady state CHF for vertical surfaces in pool boiling (typically 6000 W/m<sup>2</sup>), included in the model to represent the capability of the liquid bulk of removing vapor from the near-wall region, and  $d_d$  is the bubble departure diameter. The 1 on the RHS is the void fraction assumed necessary in the near-wall region (of thickness  $d_d$ ) for DNB to take place. The model has only been tested in small diameter systems as the channel described. However, no quantitative criterion was established to determine the existence or not of bulk-induced DNB transition, i.e. the minimum heat flux at which such a transition, either temporary or permanent, can happen.

Other Russian authors who worked on transient boiling in channels are Yarmak and Zhukov [77]. They performed stepwise heat pulse experiments during forced flow in extremely narrow channels (0.8 mm i.d.) with an imposed known value of mass flux. In this case it became evident that the pressure transients taking place in such a confined space are highly significant, conducting even to supercritical conditions. According to Pavlov [61], based on his 2.8 mm channel, for tubes with  $L/D < 200$  and  $q < 10000 \text{ W/m}^2$  the pressure pulse can be neglected.

## 2.6 The contribution of this work

The literature available on the subject of transient boiling heat transfer in liquid helium has allowed the identification of the different stages present in the transient response to a stepwise power injection:

- pure conduction;
- onset of nucleate boiling;
- stabilization of nucleate boiling;
- eventual onset of boiling crisis after a finite time.

The experiments in channel flow have allowed to observe the particularities that arise from the confinement of the flow and from the possibility of natural circulation. Premature DNB (at lower heat flux than steady state CHF) can happen temporarily. For very intense power injections, it has been identified that the sudden rise of bulk void fraction can induce boiling crisis transition mechanism substantially different from that present in steady state. In particular quantitative laws have been proposed for predicting the nucleate boiling lifetime, also called critical time.

Nevertheless, all the available literature is focused on the study of small systems, both in diameter and length, with a degree of confinement much higher than the tubes that interest us particularly in this work. Furthermore, the experiments presented served to study quite thoroughly heat transfer but they are unable to link it to the evolution of the flow in the cases of natural circulation, since this physical quantity was not measured. Additionally, in the case of the bulk-induced DNB mechanism, no criterion was produced for the determination of its occurrence. It becomes evident when looking at the ensemble of experiments that the identification of this regime is not evident in all the cases and it is clear that it does not take place at sufficiently low power. We also pose the following questions: is there a link between the temporary, premature boiling crisis and the bulk-induced DNB transition? The answer to this question may be the key to finding an incipience criterion for this regime. Is it possible to induce permanent boiling crisis at values of heat flux below steady state CHF in helium channel flow?

For all the reasons stated above we see the necessity of studying larger systems (1 m long,  $> 5 \text{ mm}$  i.d.) in a natural circulation loop configuration<sup>4</sup>. This would allow us to have more accurate information on the problem of magnet cooling by natural circulation. Our scientific and technical objectives are

- to identify the different transient boiling heat transfer regimes present in such systems and determine their boundaries in terms of time during the evolution and heat flux;
- in particular, to determine transient boiling crisis limits and compare them to steady state boiling crisis (eventually, identify premature crisis);

---

<sup>4</sup>Not simply an open tube immersed in a bath

- to determine the validity of the existing models or empirical rules for the determination of critical heat flux and critical time;
- to complete the analysis of boiling crisis transients by counting with mass flow rate evolution data;
- to determine the nature of the mechanisms conducting to boiling crisis that can take place in these systems and their zones of dominance.
- to provide criteria or calculation tools that can be applied for future design of passive cooling systems.

To pursue these goals,

- experiments are to be conducted in a 2-m high natural circulation loop, in which transient boiling and thermohydraulic phenomena will be induced by time-varying power applied on the hot leg.
- numerical modeling possibilities for the simulation of these systems need to be explored and compared to experiments.



## Chapter 3

# The experimental facility

In order to study the transient behavior of a two-phase helium natural circulation loop, experiments were conducted in a cryogenic loop. In this chapter, we will describe the experimental facility regarding the cryostat, the elements of the hydraulic loop, the instrumentation, the data acquisition chain and the preparation of experimental sessions.

The experimental facility consists mainly of a natural circulation cryogenic loop inside a cryostat. The *cryostat* is a recipient in charge of reducing the heat transfer from the outside room temperature environment to the inside liquid helium temperature environment. The ensemble of the elements of the loop constitutes the *insert*, which can be removed from or placed into the cryostat. Schematic drawings of the insert and the cryostat are shown in Fig. 3.1. In the following sections we will describe the elements constituting these two main parts of the facility and all the instrumentation involved in our experiments.

### 3.1 The cryostat

Given the dimensions of the loop, the cryostat cavity is a cylindrical well in the ground, around 2 m deep and with a diameter of 70 cm. The following paragraphs describe the several measures that are taken in order to interpose heat transfer barriers between the outside and the inside of the cryostat.

The first barrier is a *nitrogen shield* set around the well. It consists of an annular cavity around it, that can store liquid nitrogen. The principle justifying this choice is that nitrogen has a saturation temperature of 77 K. When nitrogen intersects heat coming from outside it evaporates, keeping its temperature at its saturation point. The inside of the cryostat ‘sees’ the wall in contact with nitrogen at a constant temperature of 77 K. As this temperature is higher than that of the elements inside, radiation heat transfer takes place between this surface and the inner elements. This form of heat transfer, when considering the heat exchange between two surfaces at two different temperatures, follow the Boltzmann law:

$$Q = G\sigma\epsilon(T_h^4 - T_c^4) \quad (3.1)$$

where  $Q$  is the power from the hotter to the colder elements,  $G$  is a geometric factor,  $\sigma$  is Boltzmann constant,  $\epsilon$  is the emissivity (assumed equal for both surfaces) and  $T_h$  and  $T_c$  are the temperatures of the hot and cold surfaces respectively. Using this formula, we can compare power values at two different hot temperatures.

$$\frac{Q_{295K}}{Q_{77K}} = \frac{((295K)^4 - (4K)^4)}{((77K)^4 - (4K)^4)} \cong 215 \quad (3.2)$$

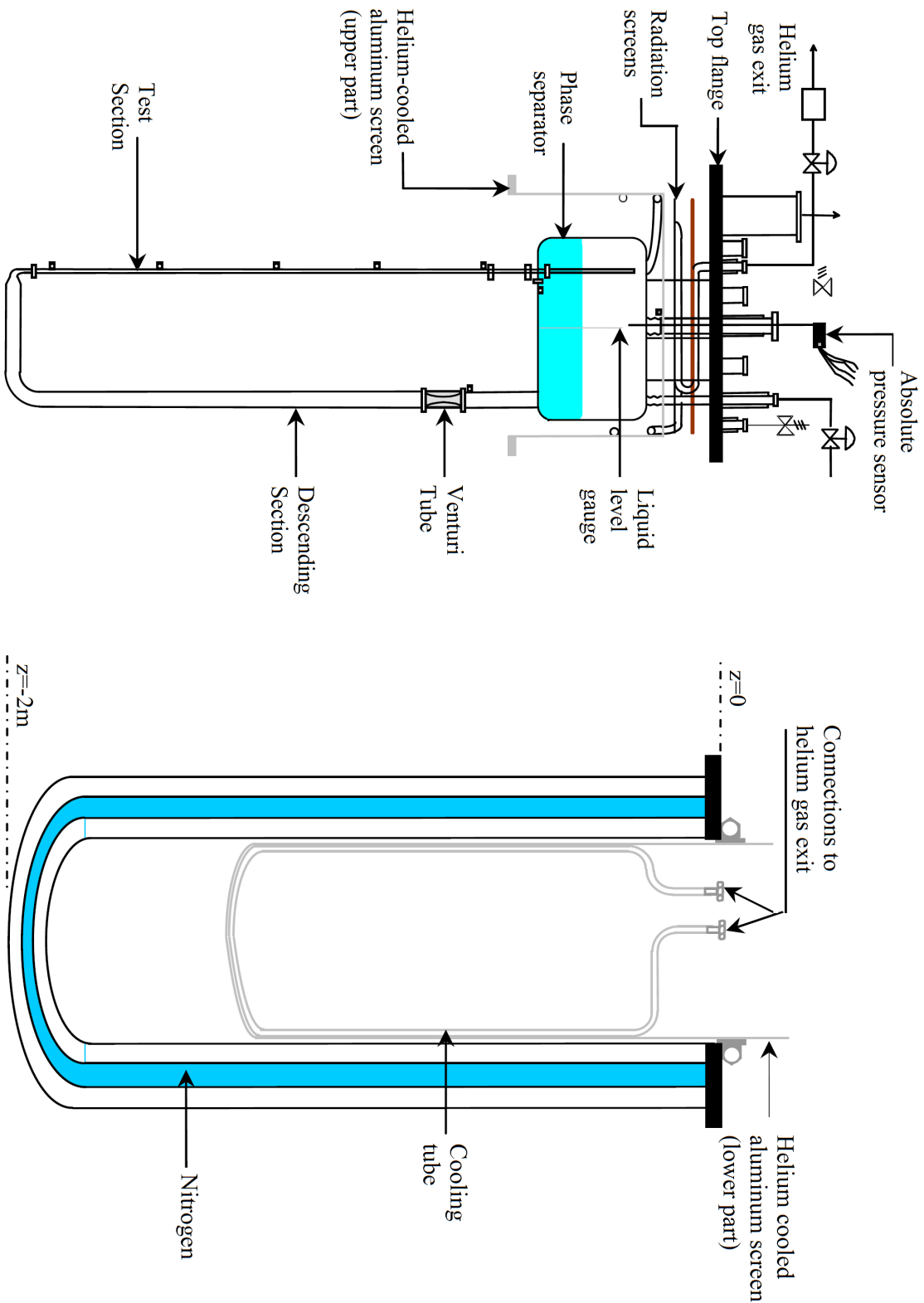


Figure 3.1. The experimental facility: (left) the insert and (right) the cryostat.

If the radiation heat exchange took place between the elements at 4 K and the cavity surface at 295 K (room temperature), the power exchanged would be approximately 215 times higher than it is between the same surfaces at 4 and 77 K, respectively. So adding the nitrogen shield reduces heat transfer to the inside by this factor. However it is necessary to keep in mind that nitrogen acts as a constant temperature body that *is consumed and refilled* continuously. It does not stop heat being transferred from outside, but it prevents it from entering the cryostat through evaporation and gas discharge to the atmosphere. Instrumentation linked to the nitrogen shield is presented in section 3.5.5.

The next thermal barrier is an *aluminum radiation screen* placed all around the loop. This screen is actively cooled by the helium gas, product of the evaporation that takes place in the loop during operation. Exhaust helium flows along a conduct glued on the screen, thus intersecting radiative (and eventually convective) power coming from the external wall at 77 K and keeping this screen at a temperature between 10 and 15 K.

Furthermore, *high vacuum* maintained inside the cryostat. By extremely reducing the density of the gas inside the cavity, conduction and convection heat exchange are drastically reduced. This is achieved through continuous pumping. Pressure values as low as  $10^{-4}$  Pa are achieved. In this condition, the gas inside the cryostat is in *molecular regime*, i.e. particle mean free path is much larger than the linear dimensions of the cavity; particles hardly interact with each other. Heat transfer takes place primarily through the transmission of energy during the collisions of gas molecules with the hot and cold surfaces (and radiation, of course).

These three barriers applied, if there are no other mechanisms for heat transfer, the total power would be inferior to 30  $\mu\text{W}$  [14]. However, there is another source of heat, which is conduction through insert supports. We will see this in section 3.2.

## 3.2 The insert

The insert is the part of the experimental facility that contains the loop that is studied in this work. The insert is separated in two parts by a circular flat steel-made flange. This flange constitutes the ‘roof’ of the cryostat and separates the interior and exterior.

The upper part of the insert consists mainly of tubes, valves and openings that enable access from the exterior to the interior of the loop and cryostat cavity. Some of them are in direct connection to the helium reservoir of the loop (see section 3.3), like the liquid helium inlet, the absolute pressure intake or the opening that allows the loop being purged; others connect to the interior of the cryostat cavity in order to provide the users with an electrical connection to the instrumentation. There are also openings in order to produce the vacuum in the cavity of the cryostat, over which a turbo pump has been permanently attached. When the insert is inside the cryostat, the flange is bolted to it.

The elements of the loop are at the inferior part of the insert, thus inside the cryostat during operation. However the inferior part of the insert contains some additional elements.

First of all, three circular-section epoxy glass supports are to attach the loop to the flange. They are designed to be able to resist the weight. Although the material is a bad heat conductor, these components connect thermally the flange and the loop elements, thus providing a way for conduction heat transfer to the thermosiphon. The power transferred to the loop has been estimated from the evaporation rate of helium, when the loop is not being used. Typical values between 1 and 2 Watts have been measured. This is, thus, the most significant heat contribution to the loop. It is necessary to emphasize that, since the heat enters the insert by the top, the power is deposited on the liquid inside the phase separator, not affecting the dynamics of the experiments.

Additionally, there are the reflective screens. They are to complete a closed surface when joined to the ones already described in section 3.1. There are two horizontal reflective screens right on top of the helium reservoir in order to reduce radiation coming from the flange, at room temperature. These screens have holes that let cables and penetration tubes pass through to the upper part of the insert. There is also an aluminum screen that surrounds by the top and the sides the helium reservoir and that is to be mechanically coupled (by means of screws) to the helium cooled screen inside the cryostat, described in section 3.1. Thus a closed-surface aluminum shield at temperatures between 10 and 15 K encloses the whole loop when in operation.

### 3.3 The elements of the loop

The natural convection loop on which the experiments were conducted is represented schematically in Fig. 3.2. It is formed by three main components:

- the phase separator;
- the descending section;
- the ascending section.

When the loop is in operation, liquid helium in the phase separator goes down the descending section and then passes to the ascending section, where it is heated and evaporation takes place. The descending section presents only liquid state, while the ascending section is under two-phase flow. Finally the liquid-vapor mixture reenters the phase separator, closing the circuit. Liquid is then recirculated, but vapor stays at the top and is finally expelled from the loop, as the gas is not re-condensed. The power that should be evacuated for a closed system operation would be too high to consider low temperature active cooling. This is the reason why the system is open and liquid helium is refilled to compensate the loss of mass.

The phase separator is a cylinder-shaped steel recipient of 45 cm of diameter and 30 cm tall. It also act as a reservoir storing liquid helium inside, in order to have an autonomy and not require continuous supply of helium through the inlet. It has four main openings related to fluid circulation:

- a *liquid helium inlet* through the top, that allows refilling it when the liquid inventory is too low;
- a *gas outlet* at the top, that allows the gas produced by boiling to quit the system and thus permit energy discharge and avoid pressure rise;
- a bottom opening for connection with the descending section;
- a bottom opening through which the ascending section riser penetrates in order to discharge the two-phase flow produced by heating.

There is another perforation, not used during operation, but for preparation of the experiments, which is the *purge conduct*. More will be said about it in section 3.7.

The descending section is a vertical steel tube of 4 cm of internal diameter and 130 cm long. It conduces liquid helium from the bottom of the reservoir to the bottom of the ascending section. It is connected to the latter by a 30 cm long horizontal tube of the same diameter and material. This way a U-shaped conduct is formed under the reservoir. The coupling between the vertical and horizontal tubes is made by a round elbow. Near the reservoir, the descending section is equipped with a Venturi tube, as will be seen in section 3.5.2.

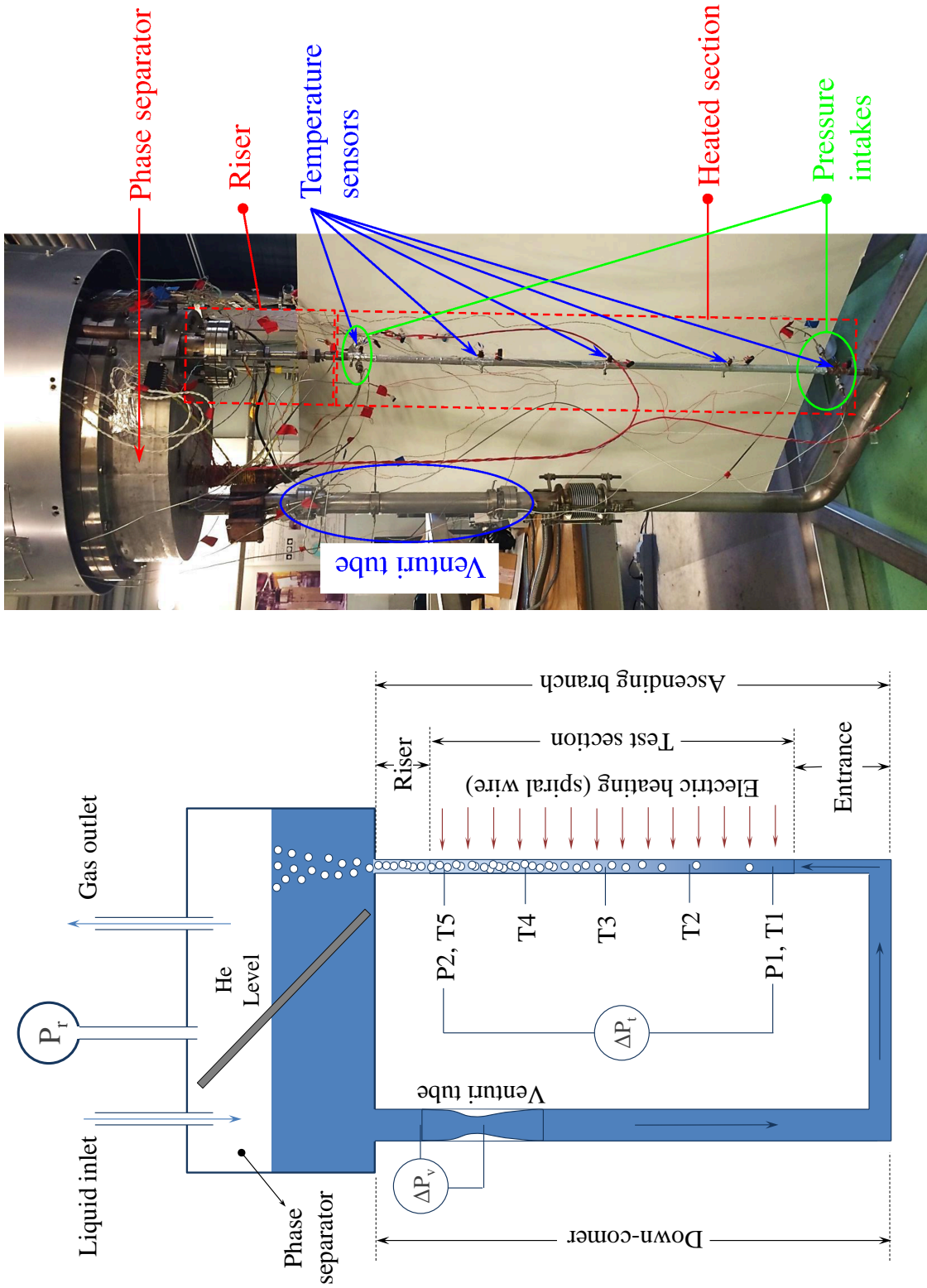


Figure 3.2. The loop elements and its instrumentation.

**Table 3.1.** *Heating configuration parameters. V10: Vertical section with 10 mm i.d.; V06: Vertical section with 6 mm i.d.. T1 to T5 indicate the positions of the temperature sensors from the entrance of the heated section, and P1 and P2 the position of the pressure taps measured from the entrance. The numbers in brackets are uncertainties on the last figure(s).*

Parameter	V10	V06
Heated length	0.950(5) m	1.050(5) m
Riser length	0.450(5) m	0.170(5) m
Internal diameter	9.85(10) mm	6.00(10) mm
T1	3.1(2) cm	3.0(2) mm
T2	24.3(2) cm	27.0(2) cm
T3	47.3(2) cm	52.0(2) cm
T4	71.3(2) cm	76.0(2) cm
T5	92.7(2) cm	101.0(2) cm
P1	2.5(2) cm	3.0(2) cm
P2	93.1(2) cm	101.0(2) cm

The ascending section is an element of the loop that can be modified in order to study different heating configurations. It is composed mainly of three items:

- A short entrance at the very bottom made of steel, mainly consisting of the coupling with the horizontal section described above, through a diameter reduction and a round elbow;
- The heated section, which can take different forms that we will describe in section 3.4;
- A non-heated riser: a steel tube of 1 cm diameter that connects the upper end of the heated section with the top reservoir. It can be considered adiabatic.

### 3.4 Heating configurations

As mentioned before, the heated section of the loop can be removed and changed in order to study the effect of the heating configuration. In this work, two types of heated sections have been used:

- a vertical heated section of 10 mm of i.d. (V10);
- a vertical heated section of 6 mm of i.d. (V06);

Both have a wall thickness of 1 mm and are made of oxygen free high thermal conductivity copper (OFHC) with RRR of 145, whose high conductivity ensures the uniformity of temperature in the tube material while heating. An electric Manganin wire is glued with an epoxy resin spirally around the tube with a regular step of 0.8 or 1 cm to exert ohmic heating on the wall.

Table 3.1 presents the most relevant parameters of each of the two heating configurations. Information about the riser is also included.

### 3.5 Instrumentation and measurements techniques

The instrumentation has been chosen in order not only to reach the low temperature requirement but also to respect the limited space available. Furthermore, non-intrusive measurement

techniques were preferred, in order not to perturb the flow. In the following sections, we will describe the instrumentation concerning:

- wall temperature on the heated section;
- inlet mass flow rate;
- heated section pressure drop;
- heating;
- other loop state variables.

### 3.5.1 Wall temperature

In order to study the heat transfer properties, wall temperature is measured at different positions all along the heated section. Five points were chosen for each test section (see T1 to T5 in Fig. 3.2) at the positions indicated in Table 3.1.

The material the heated section is made of, OFHC copper, has appreciably high values of conductivity and low specific heat (at loop operation temperatures). When taking into account the wall thickness and the maximum values of surface heat flux that would be applied on this tube, one realizes that the thermal diffusion time constant and the temperature gradient in the wall thickness are both small enough to accept the (useful) assumption that internal and external walls are at the same temperature at all times. This allows for temperature measurements to be made on the outer face of the copper heated section. Numerical simulations have already been made before by L. Benkheira [14] in order to evaluate the validity of these statements, giving positive results.

The chosen temperature sensors were Cernox<sup>TM</sup> temperature thermoresistors [53]. Cernox<sup>TM</sup> is a material developed by Lakeshore<sup>TM</sup>, used by this company to construct thin film resistance cryogenic temperature sensors. This material allows to make measurements up to 300 K too. This material changes appreciably its electric resistivity as temperature changes, especially at low temperatures, which allows constructing very sensitive cryogenic thermometers. Around 5 K, the rate of change for a typical sensor can be between 1000 $\Omega$ /K and 2000 $\Omega$ /K. It is thus possible to reach easily an absolute sensitivity of 0.5 mK.

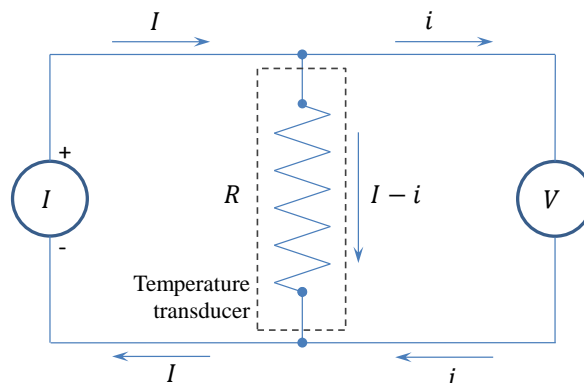


**Figure 3.3.** Diagram of a thermoresistor transducer. The current supply on the left delivers a current  $I$ . A negligible current  $i$  goes to the voltmeter on the data acquisition cards, thus the measured voltage  $V$  is essentially equal to  $IR$ .

The electric resistance  $R$  of the sensor is obtained from the electric tension  $U$  between its terminals, and the knowledge of the current  $I$  flowing through it:

$$R = \frac{U}{I}. \quad (3.3)$$

In practice, the current is supplied by a battery-fed continuous current source (Lakeshore<sup>TM</sup> 101 Current Source). This choice was made to avoid 50 Hz AC noise, by decoupling the powering of the sensors from the network. The current intensity was chosen at 10  $\mu\text{A}$ . This provides a  $U$  lecture in the tens of mV (appropriate for the acquisition system), having a good signal to noise relation (noise is in the order of 0.1 mV). The precision of the current sources is better than 1‰. In order to measure strictly the tension on the sensor, a 4-wire configuration is used, as shown in Fig. 3.3. This requires that two cables be soldered to each of the two terminals of the sensor. Consequently each temperature sensor has four contacts in the outside of the thermosiphon. Two of them are used for injecting current and the other 2 for measuring tension. Tension is measured using the acquisition system described in section 3.6.

There are two types of temperatures sensors that have been used for the measurements that are presented in this work:

- Cernox<sup>TM</sup> AA (CX-AA) temperature sensors;
- Cernox<sup>TM</sup> SD (CX-SD) temperature sensors.

Images of these two sensors are shown in Fig. 3.4. The two capital letters in the name of the model represent the packaging option of the sensor, i.e. the external shape of the sensor in which is embedded the Cernox<sup>TM</sup> component. In the following sections we will see the particular properties of each type.

### Cernox<sup>TM</sup> AA temperature sensors

As it is shown in Fig. 3.4, AA sensors have the external appearance of a cylindrical canister. A Cernox<sup>TM</sup> chip is lodged inside a gold-plated copper can with an internal atmosphere of  $^4\text{He}$ . The total mass of a sensor is of 390 mg. The sensor has four wires coming out of it, two of them for current injection and the other two for voltage measurement. Figure 3.5(a) shows the dimensions of the external packaging AA, as presented by the manufacturer.

It is necessary to have a good coupling between the temperature sensor and the surface whose temperature is to be measured. To do this for the AA sensors, specially conceived supports were brazed at the five chosen positions. These supports, illustrated in Fig. 3.6 are a copper cylindrical cavity open on one side, with internal diameter slightly bigger than the sensor, and a sharp cone on the other side, with an opening angle of  $60^\circ$ . To ensure a good positioning,  $90^\circ$ -angle cones are carved at each position on the OFHC tube, to which the supports are brazed, as shown in Fig. 3.6(b). As wires can conduct heat, the sensor could find itself at an intermediate temperature between the surface and the cables. That is why, the cables are coiled around and glued to the copper support with a mixture of varnish and copper, in order to set them to the same temperature as the surface.

To convert the electric resistance measurement into temperature, each of them is calibrated individually. The experimental observation is that, at least in the range from 4 K to 40 K, resistance decreases with increasing temperature in a strongly non-linear manner. An analytical expression that fits quite well the function between temperature  $T$  and resistance  $R$  is a rational polynomial function of logarithms of  $R$ :

$$\frac{1}{T} = \sum_{i=0}^N A_i (\log R)^i. \quad (3.4)$$

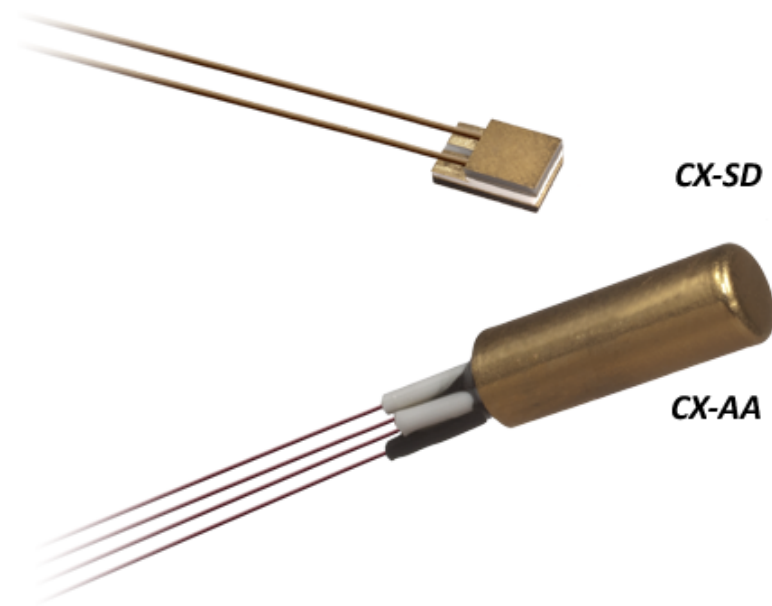


Figure 3.4. Cernox sensors used for wall temperature measurements [53].

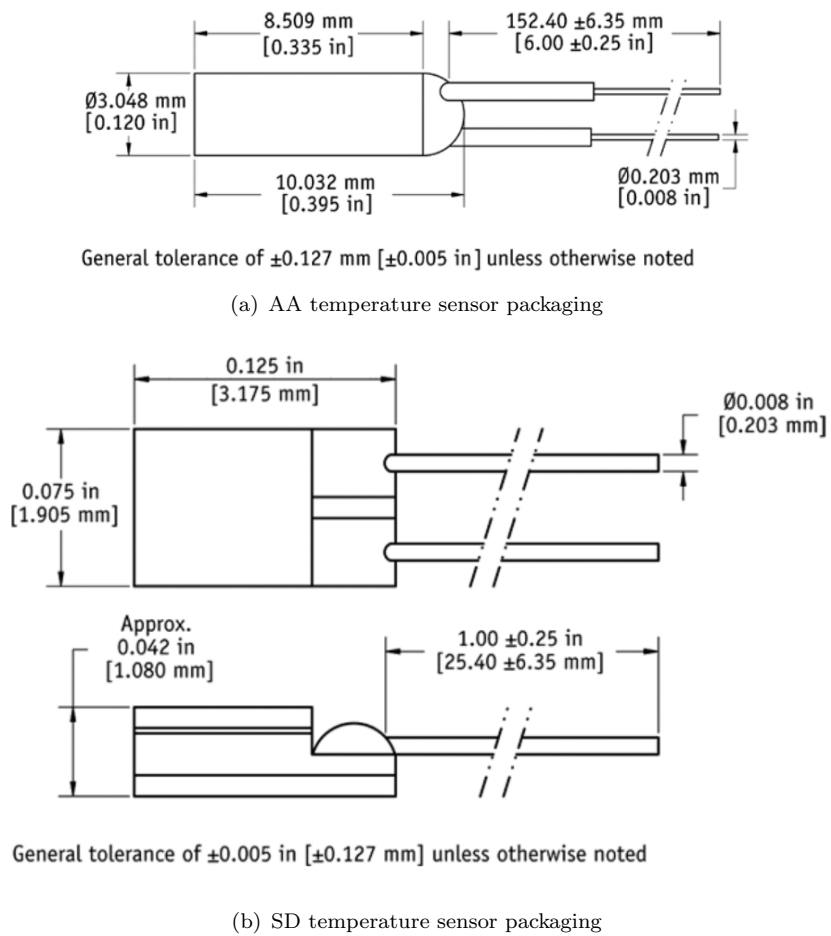
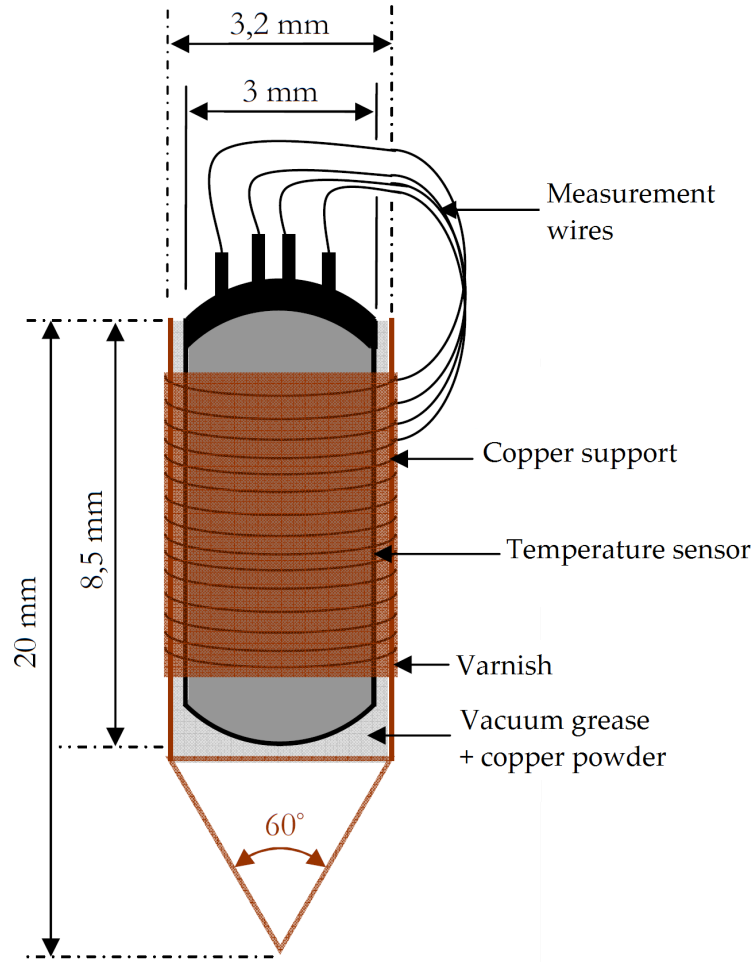
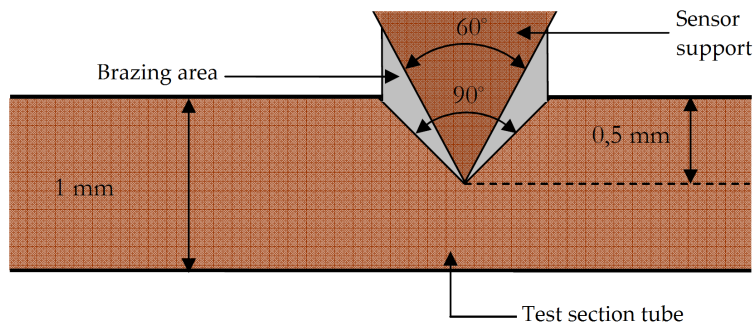


Figure 3.5. Dimensions of Cernox temperature transducers [53].



(a) The sensor in the support



(b) Diagram of the brazing for the support.

**Figure 3.6.** The support for AA sensors.

The calibration of a particular sensors is given as a particular set of coefficients  $A_i$ .

The time constant of this sensor, specified by the manufacturer is of 400 ms. This time could be higher than or of the same order as the characteristic time of the phenomena that we want to observe, which could give a distorted signal of the real temperature behavior.

### Cernox™ SD temperature sensors

Cernox™ SD temperature sensors have a hermetic ceramic packaging. They are appreciably smaller than the AA sensors in volume and mass, weighing only 40 mg. Their geometry is described by Fig. 3.5(b). Their small size grants them with a very shorter time response constant, of 15 ms as informed by the manufacturer, which makes them better suited for transient measurements.

This type of sensor has only two electric leads coming out of it, each of them at opposite sides of the resistance. So, for a 4-wire measurement it is necessary to solder two wires to each of the two contacts of the sensor.

Coupling of the sensor to the surface is done by gluing. In order to have a good contact, the gluing material needs to have a high thermal conductivity. It has been chosen to use silver paint for this purpose, after testing several methods and seeing how they affect the measurements in steady state compared to the results obtained with the AA sensors. Special attention has to be made in order to avoid short-circuits between the electric leads and the tube (silver paint solvent can dissolve varnish on the leads).

The calibration law for these sensors, provided by the manufacturer, is of the form:

$$T = \sum_{i=0}^N A_i \cos \left[ i \arccos \left( \frac{2 \log R - Z_u - Z_l}{Z_u - Z_l} \right) \right], \quad (3.5)$$

where  $Z_u$  and  $Z_l$  are constants defined for each particular sensor,  $N$  is the number of terms considered for the expansion (generally 8 or 9) and the  $A_i$  form a set of coefficients defined for each sensor.

### 3.5.2 Mass flow rate

The total mass flow rate at the inlet of the heated section is measured by using a Venturi tube in the descending section. As the fluid is in liquid phase in the whole descending section until the entrance of the heated section, density can be assumed to be uniform, as well as mass flow rate. In order to determine the mass flow rate through a Venturi tube, it is necessary to measure the pressure drop between the entrance of the tube and its throat. The methods for measuring the pressure drop in the Venturi tube are presented in section 3.5.3.

Once the pressure drop is known, a hydrodynamic model needs to be used in order to interpret it as a mass flow rate. For a Venturi tube, the Bernoulli equation is usually applied. For a vertical Venturi tube with point 1 at its large cross section entrance and point 2 at the narrow throat:

$$\frac{V_1^2}{2} + \frac{p_1}{\rho} + g z_1 = \frac{V_2^2}{2} + \frac{p_2}{\rho} + g z_2, \quad (3.6)$$

with the continuity equation:

$$\rho V_1 A_1 = \rho V_2 A_2 = \dot{m}. \quad (3.7)$$

$V$  is the average cross section velocity,  $p$  is the absolute pressure,  $g$  is gravity acceleration,  $A$  is the cross-sectional area and  $z$  the vertical position. The final formula for obtaining the mass

flow rate from measurements of  $p_2 - p_1$  is

$$\dot{m} = \varsigma \sqrt{\frac{\mathcal{P}}{C_1}} \quad (3.8)$$

with

$$C_1 = \frac{1}{2\rho} \left( \frac{1}{A_2^2} - \frac{1}{A_1^2} \right), \quad (3.9a)$$

$$\mathcal{P} = -[(p_2 - p_1) - \rho g (z_1 - z_2)], \quad (3.9b)$$

and  $\varsigma$  a experimental factor of 0.98 that accounts for friction losses in the Venturi tube (not considered in Eq. (3.6)).

This model is generally valid for steady state measurements. When the flow is unsteady the model needs to be adapted. Use can be made of the unsteady Bernoulli equation for the central streamline of the tube:

$$\frac{V_1^2}{2} + \frac{p_1}{\rho} + g z_1 = \frac{V_2^2}{2} + \frac{p_2}{\rho} + g z_2 + \int_{z_2}^{z_1} \frac{\partial V}{\partial t} dz. \quad (3.10)$$

$V$  has been assumed positive in the downward direction. This expression can be rewritten in a more compact form:

$$C_2 \frac{d\dot{m}}{dt} + C_1 \dot{m}^2 = \mathcal{P}(t). \quad (3.11)$$

with

$$C_2 = \int_{z_2}^{z_1} \frac{dz}{A(z)}, \quad (3.12a)$$

$$C_1 = \frac{1}{2\rho} \left( \frac{1}{A_2^2} - \frac{1}{A_1^2} \right) \quad (3.12b)$$

$$\mathcal{P}(t) = \rho g (z_1 - z_2) - (p_2 - p_1)(t) \quad (3.12c)$$

The quantity  $(p_2 - p_1)(t)$  is the measured pressure drop on the Venturi tube. Thus, this differential equation can be solved for  $\dot{m}(t)$  from known  $\mathcal{P}(t)$ .

### 3.5.3 Pressure drop

During our experiments, two differential pressure measurements are performed on the loop:

- Pressure difference between the two points on the Venturi tube.
- Pressure difference between entrance and exit of the heated section;

Two models of differential pressure transducer are used:

- Validyne<sup>TM</sup> DP10-20 pressure sensors are used for the Venturi tube;
- Validyne<sup>TM</sup> DP10-22 pressure sensors are used for the heated section.

The main difference between the two models is the range.

The pressure sensing element is a flat diaphragm of magnetic stainless steel, clamped between case halves of the same material, in a symmetrical assembly. Two pickup coils, excited with a 5 V rms at 3 kHz signal, one at each side of the diaphragm, sense its deflection by inductance

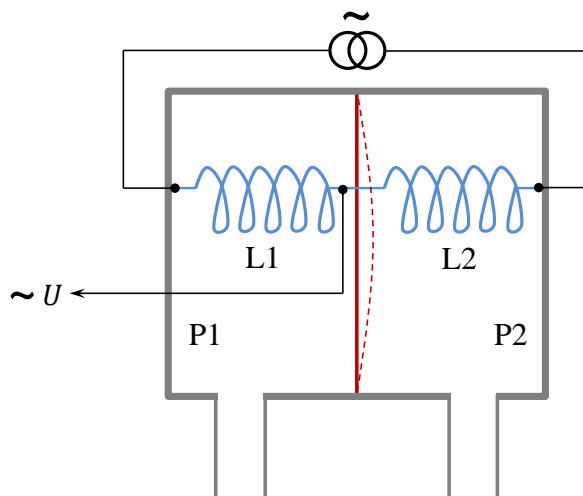


**Figure 3.7.** Working principle of a DP10 transducer.

change. The embedded coils are covered with a non-magnetic stainless steel exposure to the working media. These pressure chambers and the diaphragm utilize all-welded seals. A schematic view of the interior of the transducer is represented in Fig. 3.7. The unbalanced electric voltage of the coils circuit is demodulated by an electronic unit which is outside the cryostat. Thus, no electronic components involved with pressure measurements are inside the cryostat.

To have physical access to the measurement points, capillary tubes are brazed to holes on the walls of the Venturi tube and heated section and connected to the intakes of the transducers. The capillary pipes have an internal diameter of 1 mm and they are heated with a low amount of power; this ensures evaporation of any liquid that could go inside the capillary pipe, to minimize liquid column height pressure variations. The pressure drop intakes on the heated section are shown in Fig. 3.2 as P1 and P2 and the distance to the entrance of the test section is indicated in table 3.1.

The pressure transducers are placed inside the cryostat in order to minimize the length of the capillary pressure intakes and to eliminate strong temperature gradients in the gas column, that could affect the quality of the measurement. Although the manufacturer recommends the utilization of the sensor above a temperature of  $-50^{\circ}\text{C}$ , these pressure sensors have already been successfully used at cryogenic conditions [29].

### 3.5.4 Power supply and measurement

The power applied on the heated section is provided by an electrical DC source Agilent 6655A. This source can deliver up to 4 A in current and 120 V in voltage. This source is able to produce a step in delivered power in less than a millisecond, which is well-suited for studying the transient response of the system to power step pulses.

The source is controlled by the data acquisition program on the computer. Desired power is translated into a current requirement to be provided by the power supply control system. However, as there can be deviations from the demanded power and the really applied one, a measurement of the actual supplied power is necessary. A 4-wire method is applied on the heated section spirally glued cable as shown in Fig. 3.8. The voltage on the heater  $U$  is measured directly from the two tips of the spiral heater with a high tension acquisition board (National Instruments SCXI-1313). The current is supplied by low resistance, thick wires, in order to reduce losses anywhere else than on the heater. To measure the current, it needs to be transformed into

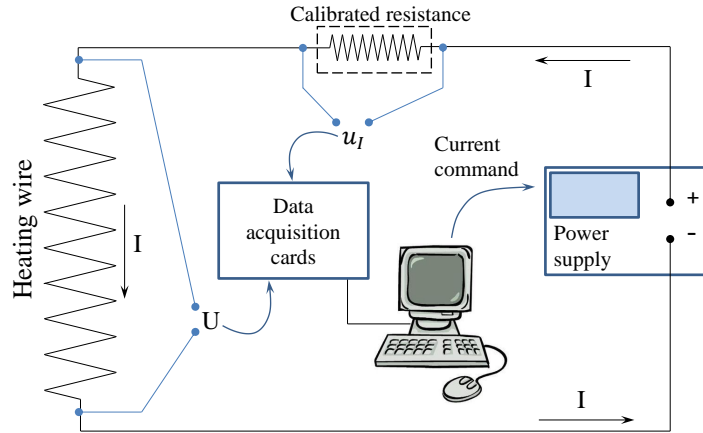


**Figure 3.8.** *The heating power control and measurement technique.*

voltage in order to have it measured by the acquisition system. To do this, a calibrated  $0.02 \Omega$  resistance is put in series in the heater circuit and the tension  $u_I$  on this resistance is measured by the acquisition system.

### 3.5.5 Other Instrumentation

#### Level monitors

Liquid helium level inside the phase separator is measured with a Cryomagnetcs, Inc. LM-500 superconducting liquid cryogen level monitor. As shown in Fig. 3.9(a), it is a straight cable made of a superconductor material with a critical temperature of around 9 K. When in use, a current circulates through it. If some of the superconductor is wetted by the liquid helium, its temperature goes under the critical value  $T_c$  and it becomes superconducting all along the wetted part. In fact, the superconducting zone would be above the liquid level due to thermal conduction; this effect is compensated by adding a small amount of electrical heating on the upper end. Since the superconducting state presents virtually zero resistivity, the total resistance of the gauge is a function of the wetted length. The result is that a conversion law can be established between the measured resistance and the wetted length. The total resistance of the instrument is directly proportional to  $x$  (see Fig. 3.9(a)), let us say through a proportionality constant  $a$ :

$$R = a x. \quad (3.13)$$

This allows us to calculate the liquid level  $y$  as

$$y = L - x = L - \frac{R}{a}, \quad (3.14)$$

where  $L$  is the total length of the gauge.

The volume of liquid nitrogen in the cryostat shield needs to be controlled in order to assure the thermal shield. An Air Liquide<sup>TM</sup> DMC RN24 level regulator is used. This device can start or stop a liquid nitrogen transfer from the laboratory's distribution line into the cryostat reservoir. A level detector of around 40 cm length, placed at the very top of the nitrogen reservoir, is used by the logic to know when a too high or too low nitrogen level has been achieved. The level gauge, schematized in Fig. 3.9(b), is a multiple punctual level detector. Four resistances are placed at different positions on a bar; the variation of its value allows determining if it is wet or not. Level is to be kept between the position of the two middle resistances (the other two work as 'alarming situation' detectors). When the lowest of the two middle indicators changes

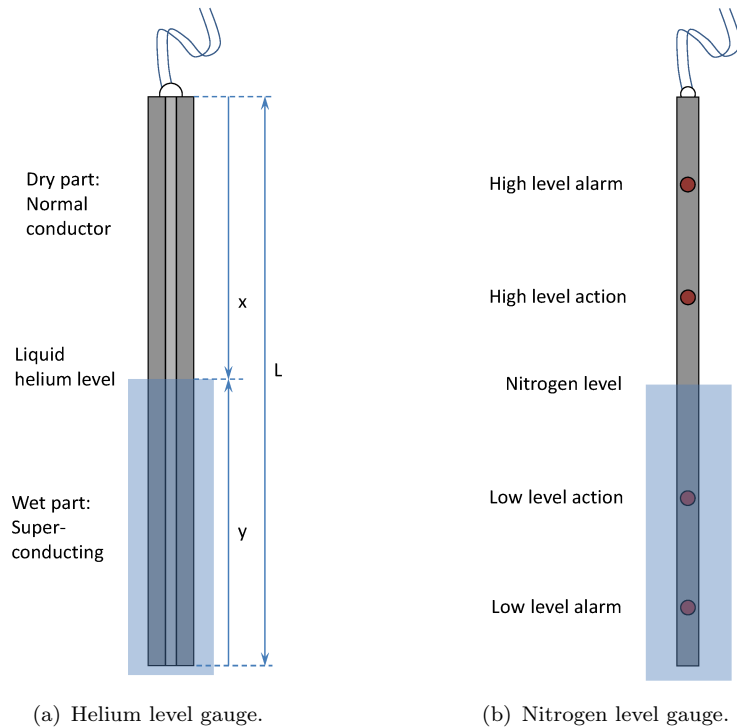


**Figure 3.9.** *Liquid level monitors.*

from ‘wet’ to ‘not wet’, the transfer is activated through the opening of a valve, and when the highest changes from ‘not wet’ to ‘wet’ this valve is closed to stop the level from becoming to high.

### Loop absolute pressure and saturation temperature

Absolute loop pressure is measured inside the phase separator using a Yokogawa™ EJA 310 A absolute pressure transducer. The pressure sensor is installed on the outside of the insert. It is connected to the interior of the reservoir through a capillary pipe of 3 mm internal diameter. The temperature of the fluid in the reservoir is measured with a Lakeshore™ Cernox™ AA sensor.

### Vapor mass flow rate

The exhaust vapor mass flow rate is measured at room temperature. After leaving the cryostat and passing through the heat exchanger, vapor mass flow rate is forced to pass through a manifold with two flow meters. These flow meters are Brooks Smart Flow Meters, model 5863S. They work by thermal principle: the gas is heated when passing through the instrument and the temperature difference between inlet and outlet is used to find the mass flow rate.

The vapor mass flow rate measurement accomplished like this cannot be considered during transient experiments; the time constant due to the need of the phase separator to pressurize in order to produce a flow along the long exhaust circuit is in the order of minutes, while the duration of a typical loop transient is in the order of a few seconds. Furthermore, when the vapor leaving the heated section is overheated, before leaving the phase separator it transfers enthalpy to the liquid and produces additional saturated vapor. Thus, in steady state operation the vapor mass flow rate is not representative of the vapor mass flow rate inside the heated section, but

rather of the total applied power on the loop.

### 3.6 Signal data acquisition

During the operation of the cryogenic loop, the acquisition and interpretation of the signals is centralized on a visual interface programmed in Labview<sup>TM</sup> and run on a desktop computer. National Instruments<sup>TM</sup> data acquisition cards (models SCXI-1320 and 1313) are used to convert the analogical voltages coming from the sensors into digital signals that are read by the visualization program. The program converts the raw voltages into the physical quantities they are supposed to represent by using calibration formulas. The main screen of the program presents several scrolling graphs that let the user see the time evolution of each quantity during the last few minutes. Also, on the same screen there is a command area, where the user can enter the parameters of the experiment, namely geometry and power commands.

A typical screen during an experiment looks like the one shown in Fig. 3.10. There are several scrolling graphs, showing the time evolution of wall temperatures, mass flow rate, test section pressure drop, exhaust vapor mass flow rate, phase separator pressure, heat flux and Venturi tube pressure drop. At the top left of the screen there is an indicator of the liquid level in the phase separator, in order to know when it is necessary to refill. At the top center of the screen there is a box in which all the command variables are concentrated, specially those used for defining the applied heating current at the initial condition and during the transient (geometry and desired heat flux). The big round button ‘acquisition on/off’ is used to record data.

Internally, the Labview<sup>TM</sup> program has three main blocks of actions:

- A command block.
- A visualization block.
- A data-file writing block.

The command block is responsible of giving the order to the main heating power source of delivering a certain amount of current. It uses the geometry of the heated section (diameter and length), the heater resistance, and the desired heat flux value (in  $\text{W}/\text{m}^2$ ) indicated by the user on the interface screen to calculate the current that makes it possible, using the equation:

$$I = \sqrt{\frac{q\pi DL}{R}} \quad (3.15)$$

The visualization block transforms the read voltages from each instrument into physical quantities using the calibration formula and displays the physical values on the scrolling plots on the screen in real time.

The data-file writing block stores in a file on the hard drive the raw voltage values read at each acquisition channel with a certain sampling frequency. The writing is only performed when the acquisition button is active. The format of the file is specific to National Instruments<sup>TM</sup> and is called TDMS. It is basically a binary file containing the values of the read voltages ordered consecutively by channels and then by time sampling step. The choice for this format is justified by the volume of information that needs to be stored; using text or Microsoft<sup>TM</sup> Excel formats, for example, would be too space consuming and slower, limiting the sampling frequency. An excel plug-in exists that can convert a TDMS file into an Excel worksheet, for data post-processing. The sampling frequency oscillates between 200 and 1000 Hz, trying to find an optimal between the time constant of the event of interest and the volume of data to store.

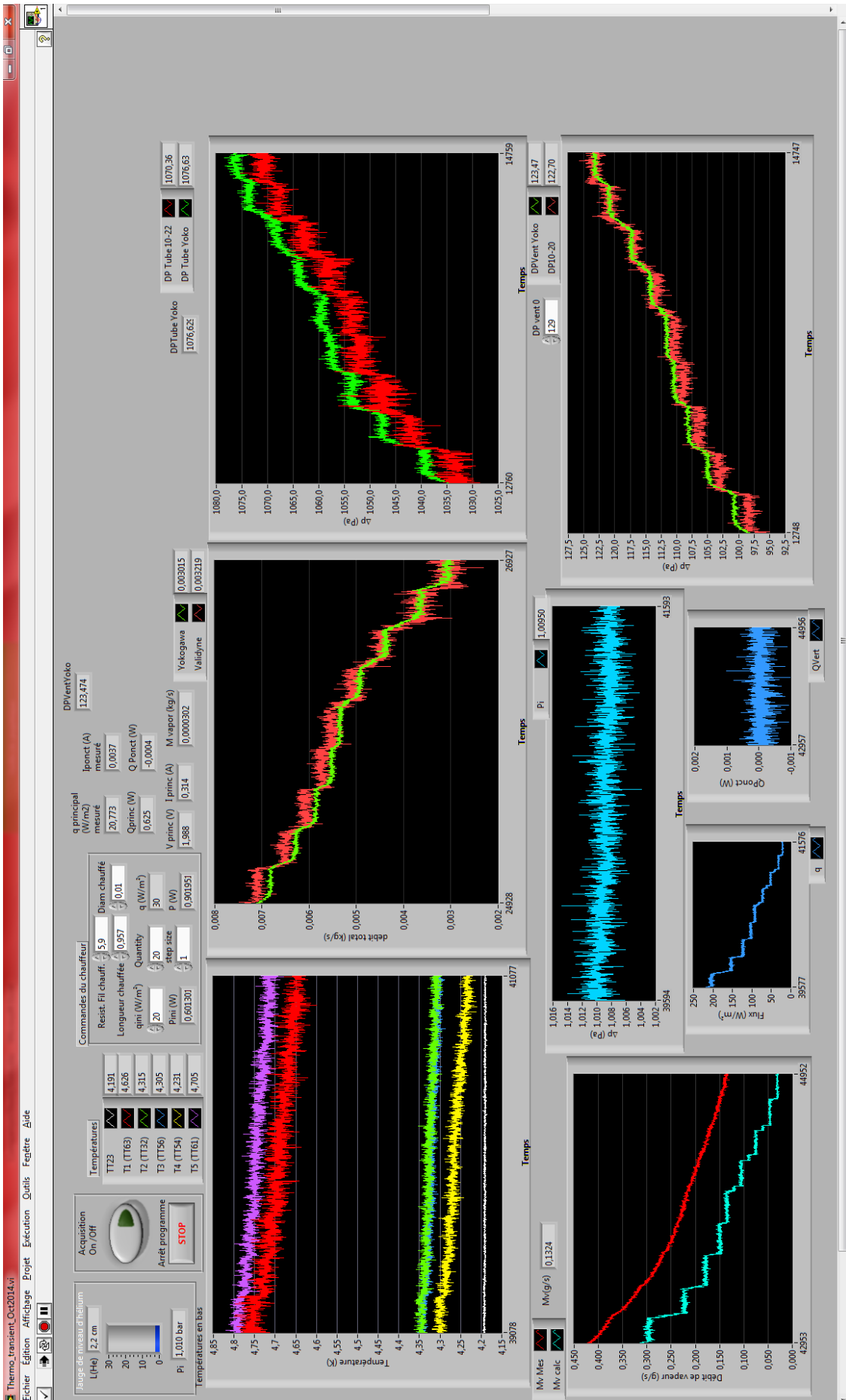
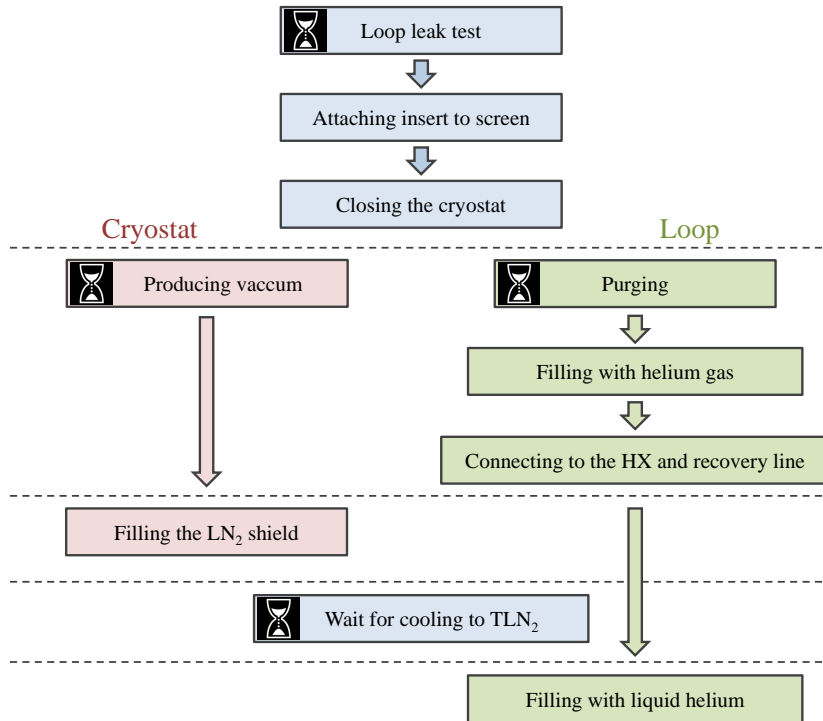


Figure 3.10. Typical Labview Screen.



**Figure 3.11.** Sequence of steps for the start up of an experimental session. The most time consuming actions are indicated with a clock symbol.

## 3.7 Preparation of the experiment

In order to start the experiments, there is a sequence of steps that need to be followed in the right order. These steps are summarized in Fig. 3.11. Two main type of actions can be distinguished:

- check-up actions:
  - electrical connections,
  - leak test;
- start up actions:
  - placing the loop in the cryostat,
  - vacuum and purging,
  - nitrogen cooling,
  - liquid helium cooling.

In the following paragraphs, these actions will be described.

### 3.7.1 Check-up actions

In order to be sure that good data acquisition will be possible, an *electrical test* of all the instruments, fully connected to the external electrical interface of the insert, needs to be done. The temperature transducers are tested by measuring their resistance on all possible pairs between the four wires. This allows detecting discontinuities or short-circuits. For the pressure transducers the control action is similar between the three terminals.

It is also necessary to perform a *leak test* on the loop components. It is important that the loop be hermetic, in order not to contaminate the vacuum of the cryostat with helium. Even if this test is time consuming, its importance is crucial because a leak threatens the thermal insulation of the loop. To perform the test, a *leak detector* is used. It consists of a vacuum pump coupled to a mass spectrometer tuned on helium. Vacuum is produced by the detector inside the loop. Gas helium, which has a great ability to penetrate small interstices, is sprayed near the points that are suspects of leakage (brazing points, tube connections, etc.) while pumping. If there is a leakage point, helium will enter the loop and be aspirated by the detector. The flow passes through the spectrometer, which ionizes the pumped gas particles and will eventually be able to ‘see’ the leaked helium.

### 3.7.2 Start up actions

Once all the tests are satisfactory, the insert is placed in the cryostat, attaching the lower part of the helium cooled screen of the cryostat to the upper part, which is part of the insert. It is also necessary to connect the two ends of the tube glued to the lower part of the thermal screen; one end to the exit of the reservoir and the other to the exit of the exhaust circuit that is meant to go to the heat exchanger.

Then, once the cryostat is closed, vacuum pumping is started in the interior of the cryostat with a duo of pumps in series: a turbo pump followed by a regular vacuum pump. Simultaneously, the purging of the interior of the loop is done. This operation consists of doing vacuum and refilling with helium, alternatively, a few times, in order to remove as much as possible the air, whose humidity would solidify at low temperatures. Once the purge is over, the loop is connected to the helium recovery line and kept filled with slightly pressurized helium by means of a helium gas supply line.

When the vacuum in the cryostat is good enough and purge is complete, cooling can start. The first stage consists of filling the nitrogen shield around the cryostat with liquid nitrogen. The cooling down of the loop after this is done will be slow, because the heat transfer is already diminished by the vacuum and the reflecting screen. It is necessary to wait a one or two days until the loop is near liquid nitrogen temperature.

The next stage is liquid helium cooling. Liquid helium is transferred from a 1000 l Dewar into the loop by the refilling opening on the top of the phase separator. An isolated transfer line is used for this purpose, in order to avoid helium evaporation before getting to the phase separator. When the liquid enters in contact with the inner surfaces of the loop, it will evaporate, cooling down the metallic surfaces. The vapors produced by this operation are evacuated through the exhaust that is used in normal operation and that conducts the vapor to the recuperation and liquefaction plant. Once the loop is cold enough, liquid will start to accumulate at the bottom of the tubes and slowly fills the whole volume up to the top of the reservoir. The whole helium cooling stage can take 3 hours. Still, after finished it is better to wait one day or two in order to assure the uniformity of temperature in the whole system and that residual heat transfer is at its minimum achievable.

## Final comments

In this chapter, a detailed description of the experimental set-up has been presented.

The experimental facility described in this chapter has been used for doing three types of experiments:

- Steady state experiments;

- Static initial condition transient experiments;
- Dynamic equilibrium initial condition transient experiments.

The *steady state experiments* correspond to the application on the system of a power progression, in order not to excite transient evolution modes. Power is increased from zero at small, slow steps and enough time is let go by in order to reach the steady state. The same experience is done too starting at high power in order to study the boiling crisis hysteresis properties of the loop, in analogy to the pool boiling experiment, described in section 2.1.1. This mode of exciting the system is the least violent solicitation conceivable.

On the other extreme, we have the *static initial condition transient experiments*. In this case, transients are produced in the system that is initially at rest, with *no power applied*, by setting the power to a positive value in a stepwise manner. This instantaneous onset of heating is the most violent solicitation conceivable of the system.

Finally, in order to approach the more realistic situation of a cooling system already in operation when a heat load incident takes place, *dynamic equilibrium initial condition transient experiments*. In this case, an initial value of heat flux is applied and the steady state reached. Thus, a mass flow rate with the corresponding thermohydraulic profile will be present before the transient starts. A stepwise increase of power will be exerted on the system, from which the transient behavior will result.

These studies will constitute the following three chapters.

## Chapter 4

# Study of the onset and hysteresis of boiling crisis in steady state

During the previous works addressing the problem of heat and mass transfer in two-phase helium natural circulation loops a very thorough experimental description of the pre-CHF regimes was achieved [5, 12–14]. Furthermore, a good description of the loop hydraulics and hydrodynamic models have been provided for the steady state in these regimes. However only preliminary results and analysis have been so far presented for the post-CHF regimes [10, 14].

It is necessary to count with a reference of the steady state behavior of the thermohydraulic loop to compare and comprehend the effects that can take place particularly in transient regime. This would allow us to identify to what extent the prediction methods for steady state regime are applicable in transient regime, and the differences; for example premature boiling crisis that could take place, as has been appreciated in other boiling systems [68] or other heat transfer regimes only accessible through transients.

In order to carry out a study of steady state regimes in a boiling helium natural circulation loop, experiments, described in section 4.1, were conducted. The analysis of the experimentally observed behavior of the system was done from two points of view. Firstly, the boiling heat transfer regimes and their limits were studied; this is presented in section 4.2. Secondly, the hydraulic effects of boiling crisis were analysed; this is presented in section 4.3.

### 4.1 Realization of experiments

For obtaining the data on steady state behavior, experiments were conducted on the cryogenic loop facility described in chapter 3 with the two vertical test sections: one with 9.85 mm internal diameter (hereafter V10) and another with 6 mm internal diameter (V06). The details about the geometry of the test sections are in table 3.1. The *modus operandi* for these experiments is described in section 4.1.1. The great volume of data required the development of data treatment tools, which are described in section 4.1.2. Finally, we obtained the evolution of the most significant thermohydraulic variables of the loop; this is presented in 4.1.3.

#### 4.1.1 Experimental protocol

The facility described in chapter 3 was used as the natural circulation loop of study. The control parameter of our study has been the *heat flux* applied on the wall of the heated section. The steady state study consisted of varying monotonously the applied heat flux on the system, sufficiently slowly to avoid transient effects. In this sense we can say that in fact we measured

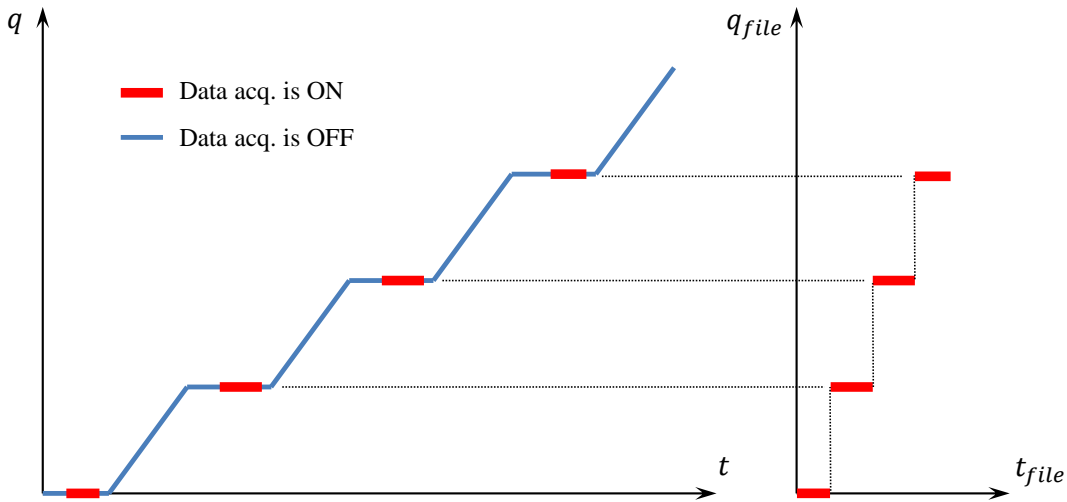


**Figure 4.1.** Power evolution during a steady state experiment.

the *quasi-steady* behavior of the loop, as all the variables do vary in time, though sufficiently slowly to consider that instantaneously the system is in equilibrium.

Two types of experiments were performed:

- increasing power: starting with no power applied, heat flux is increased gradually at small steps;
- decreasing power: analogously to the previous method, starting at a given (high) power value, heat flux is reduced gradually.

The increasing power experiments are meant to allow studying the onset of boiling crisis when the critical heat flux is reached, and the evolution of heat transfer regimes as the boiling crisis extends on the heated section. The decreasing power experiments are to provide information on the rewetting mechanisms once boiling crisis is already present in the system.

The power progression, either increasing or decreasing, were made at small steps. In general, the control up and down buttons next to the input field for heat flux in the Labview<sup>TM</sup> user interface (Fig. 3.10) were used to introduce power jumps of  $1 \text{ W m}^{-2}$  at a time. The continuous pressing of this button approximates quite well a ramp input and in all cases the rate of change was lower than  $3 \text{ W m}^{-2} \text{ s}^{-1}$ ). Thus, in order to obtain successive steady state points, power was increased from a value  $q_a$  to a value  $q_b$  using the approximate ramp method. Then, power was kept at  $q_b$  so that all variables stabilize, and only then the data acquisition was started. Only while acquisition is active, data was being added to the TDMS file. When a few seconds of data had been recorded for  $q_b$ , acquisition was turned off and a new ramp introduced for going to  $q_c$ , and so on. The power evolution is schematically represented at the left of Fig. 4.1. The produced file then contains consecutive blocks of statistically consistent data, one for each value of heat flux at which we stop. These blocks are separated by sudden jumps in the applied heat flux recorded signal, as can be appreciated at the right of Fig. 4.1.

#### 4.1.2 Data treatment

In order to produce data easier to handle and statistically significant, the mean values of all variables were calculated at each power step. Given that the duration of each step was not fixed, since the data were collected manually, it was necessary to develop a data analysis tool

for automating the process. This tool was developed in Visual Basic in Excel<sup>TM</sup>. The algorithm is capable of determining the power steps in the acquisition file, and for each distinct power it calculates the mean values of all variables. As a result a table with power as the main entry is produced hosting all the measured variables as a function of it.

### 4.1.3 Measured evolution of thermohydraulic variables

The data obtained from the experiments is presented in the form of a group of variables as a function of wall heat flux. These variables are the 5 wall temperatures measured (Fig. 4.2), the total mass flow rate (Fig. 4.3) and the pressure drop along the tube (Fig. 4.4). The results presented here were obtained by increasing and decreasing power methods. The decreasing power experiment was started at a heat flux value at which the whole test section was in the post-CHF regime.

Temperature is presented in the form of temperature rise, i.e.  $T - T(q = 0)$ . The difference is calculated with respect to the temperature measured by the sensor when no power is applied. This choice is made because of two reasons. First, there is a systematic error on the measurement (sensors do not give exactly the same value at zero heat flux, as they should theoretically). Secondly, the fluid temperature can vary along the section, as a result of pressure drop (mainly gravity) on the saturation point, but this effect is too small compared with the boiling crisis temperature jumps. For the sake of simplicity, it is assumed that subtracting the read temperature at zero power is a good approximation to subtracting the bulk temperature of the fluid.

## 4.2 Determination and characterization of flow boiling regimes

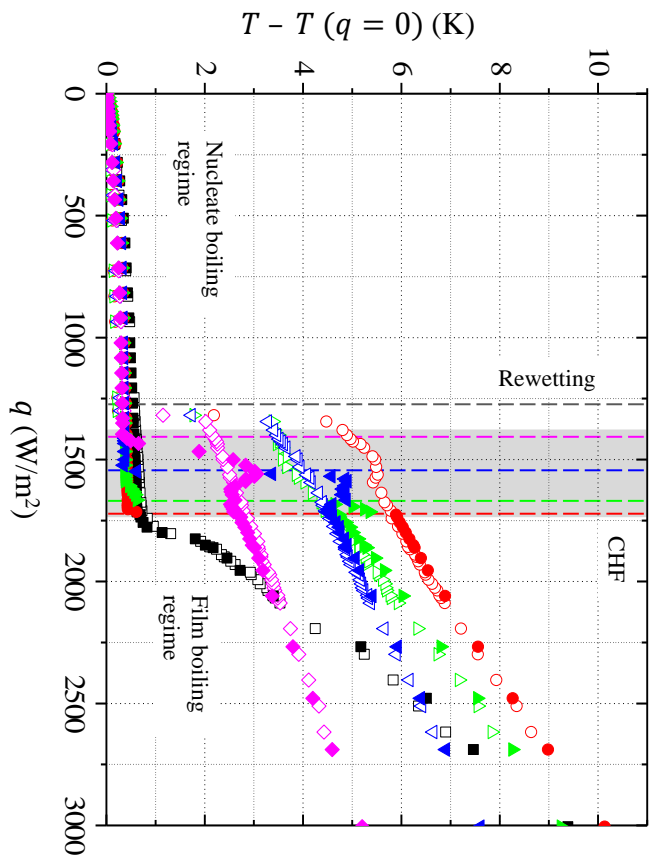
The first part of the analysis is from a thermal point of view; the *heat transfer regimes* were studied. The values of critical heat flux (CHF) were identified along the heated section (section 4.2.1). In order to evaluate the validity of existing prediction methods and observed the eventual existence of CHF anomalies [32, 35], the CHF data were compared to the values given by correlations found in the literature (section 4.2.2). The post-CHF temperature evolution was observed in order to infer the different boiling regimes that take place according to the position, heat flux and the position of the CHF boundary (section 4.2.3). Finally the boiling heat transfer hysteresis was analyzed (section 4.2.4), since this phenomenon introduces the possibility of multiple behavior at a given externally imposed heat flux, depending on the history of the system; this can play a role during transient system evolution.

### 4.2.1 Experimental observations on boiling crisis onset

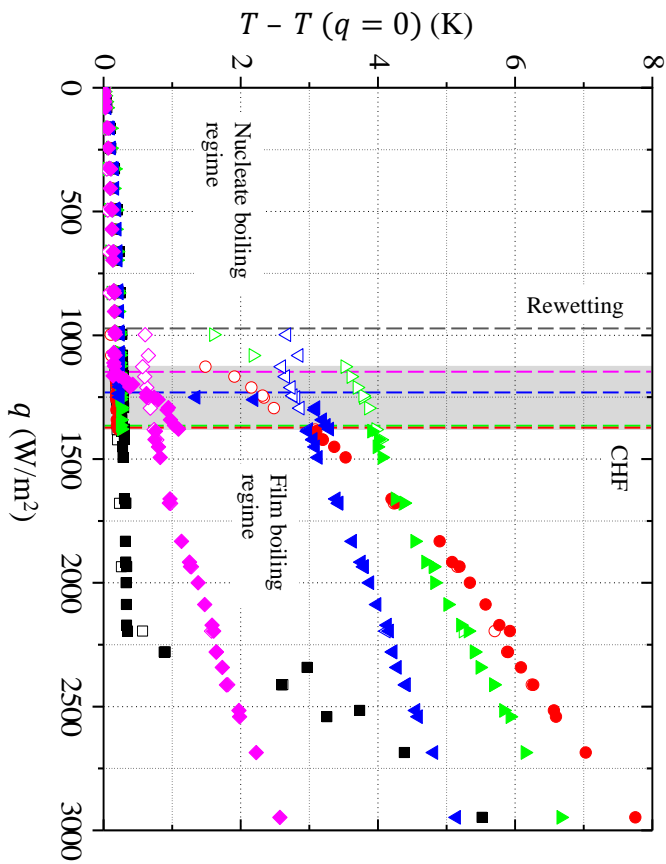
Looking at the wall temperature evolution during the increase of power (Fig. 4.2) we can identify very clearly two regions on the curve for each position:

- At low power, temperature increase is low, typically below 0.5 K; this is the nucleate boiling (NB) regime.
- Above a certain power value, the temperature increase becomes substantially higher; this is the post-critical regime.

The maximum possible value of heat flux at which the wall heat transfer can take place by the nucleate boiling mechanism is identified as the *critical heat flux* (CHF). Beyond the CHF, wall temperature increases abruptly due to the loss of liquid contact on the wall. The values of CHF

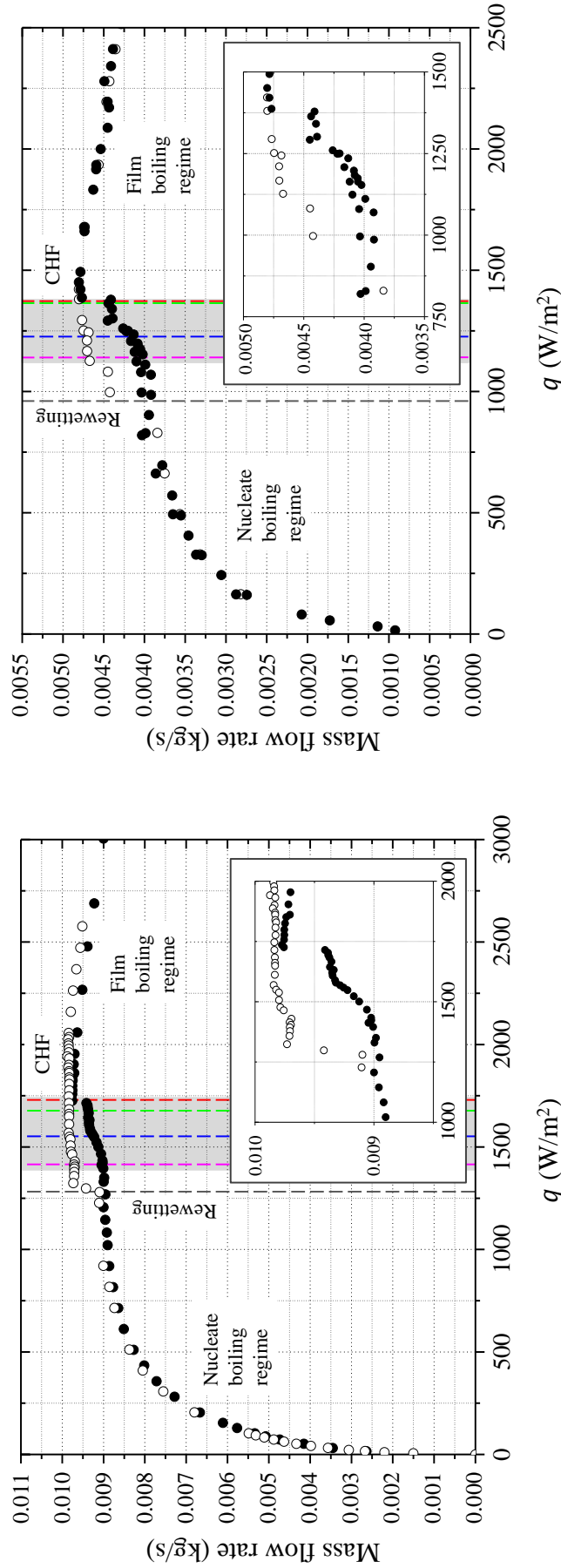


(a) Temperature increase vs. heat flux for V10.



(b) Temperature increase vs. heat flux for V06.

**Figure 4.2.** Thermal behavior of the heated sections in steady power regime. The gray area represents the power range of spatial development of boiling crisis when increasing power, and the vertical dotted lines show the CHF values at the temperature sensors' positions. ■ □ T1, ● ○ T2, ▲ ▼ T3, ◆ ◇ T4, ◆ ◇ T5. The solid points were obtained increasing power and the blank points decreasing power.



(a) Mass flow rate vs. heat flux for V10.

(b) Mass flow rate vs. heat flux for V06.

**Figure 4.3.** Experimentally observed total mass flow rate in steady power regime. Mass flow rate data  $\bullet$  increasing power and  $\circ$  decreasing power. The gray area represents the power range of spatial development of boiling crisis when increasing power. --- CHF at T1, - - - CHF at T2, - - - CHF at T3, - - - CHF at T4, - - - CHF at T5.

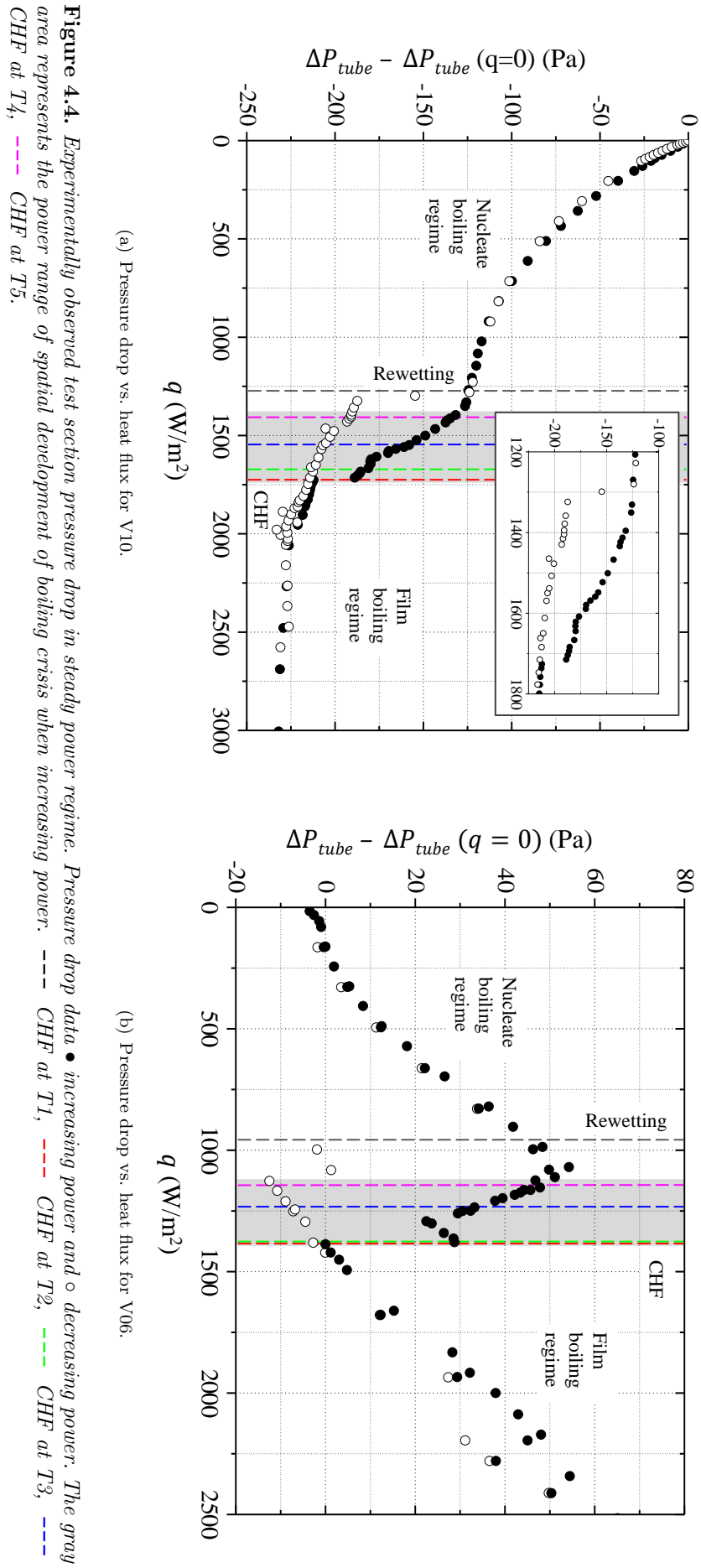


**Table 4.1.** CHF and RHF values found experimentally, in  $W/m^2$ . The numbers in brackets are uncertainties on the last figures.

Pos.	Section V10			Section V06		
	DNB min.	DNB perm.	RHF	DNB min.	DNB perm.	RHF
T1	1720(10)	1780(10)	1740(20)	2200(50)	2250(50)	2200(50)
T2	1720(10)	1720(10)	1300(20)	1380(10)	1380(10)	1100(20)
T3	1610(10)	1670(10)	1300(20)	1380(10)	1380(10)	950(50)
T4	1550(10)	1570(10)	1300(20)	1250(10)	1250(10)	950(50)
T5	1410(10)	1460(10)	1300(20)	1175(10)	1200(10)	950(50)

found in our experiments are presented in table 4.1 as a function of the position. In some cases, we distinguished two values:

- the lowest heat flux value at which a departure from nucleate boiling (DNB) was observed, materialized in a sudden, though maybe not permanent, intermittent or small, temperature increase from the nucleate boiling values.
- the lowest heat flux value at which the transition is permanent or the temperature appreciably higher.

In the cases of location T1 for the two test sections, the onset of crisis does not happen by a sudden jump to a high temperature value, but the increase of temperature is gradual, with a distinguishable change of slope. Patterns like these have been pointed out in other boiling regimes (at high qualities) in the discussion presented by Groeneveld [34]. It is argued that in those cases the boiling curve does not present a minimum heat flux point because the heat transfer deterioration in the transition regime is less severe; thus, when controlling power, no violent jump is observed. For our particular case, this can be a result of the fact that T1 is too close to the entrance of the heated section, and this means that in all cases the temperature sensor is very close to the edge of the film. In general the film starts only in the heated region. Thus, a strong axial wall temperature gradient is present in the sensor's zone (no discontinuities in the temperature profile are possible theoretically). The slow temperature increase at T1 as a function of  $q$  reflects the slow and short displacement of the film's edge towards the entrance.

When increasing the power gradually, at a first time, the region under boiling crisis takes over the test section gradually from its exit at the top towards the entrance at the bottom. This is evidenced by the fact that with V10, the CHF at T5 is lower than at T4, which is in time lower than at T3. However, there is a point at which the gradual extension of crisis is no longer possible and a slight increase in power produces the extension of the post-critical region up to a point very near to the entrance. This is seen by the apparition of crisis, or alternatively, the end of nucleate boiling, at T2 and T1 at practically the same heat flux value ( $\approx 1750 W/m^2$ ). This means that there is a particular point somewhere between T2 and T3 that separates the heated section in two regions:

- downstream, the crisis takes over the heated section gradually with power increase.
- upstream, the crisis extends instantaneously by an appreciable distance towards the entrance with a slight power increase.

In other words, it seems that the boundary between the pre and post-CHF regions cannot be inside a certain segment of the heated section. This segment is either entirely in NB regime, or entirely in post-CHF regime.

### 4.2.2 Prediction of the critical heat flux

Several correlations for predicting the CHF in vertical upward-flow in pipes exist [20, 40, 47]. However, only a few of these were obtained taking into account high vapor-liquid density ratio or helium data. One of the most universal description of the CHF mechanisms and values is given in the works by Katto [46, 48], which is presented in detail in section 2.1.3.

The boiling crisis transition mechanism map for atmospheric pressure saturated helium ( $\frac{\rho_g}{\rho_l} = 0.133$ ) predicted by Katto's criteria can be appreciated in Fig. 4.5. According to this chart, for the values of the dimensionless parameter couples ( $\frac{\sigma \rho_l}{G^2 z}, \frac{z}{D}$ ) that can be calculated for the experimental critical conditions determined in section 4.2.1 from table 4.1 and the measured mass flow rate values (around 10 g/s for V10 and 4.5 g/s for V06, see Fig. 4.3), all the experimental points lie far below the limit for the L-regime. In other words, at all positions on the two sections, the CHF transition predicted happens by *DNB to IAFB*. The points closest to the exit of the test section are quite close to the H-regime and the HP-H-N triple point.

The CHF values predicted by Katto's correlations were calculated for the two experiments and the results are summarized in table 4.2. We chose the three regimes N, H and HP because, although the points are in the N region, the ones corresponding to high  $z/D$  are near the zone corresponding to the other two.

The results show that the H-regime correlates very satisfactorily the results near the exit of the test section while better predictions are obtained by the N-regime assumption as we approach the entrance. Although for V10 all the points are in the N region, they are quite close to the N-H boundary, which could explain why the H-regime predicts well data near the exit (at T4 and T5). There are two points that need to be mentioned. The first is that the correlation does not comprise any helium data at such high diameter values as those used in the present work. The second is that a slight numerical change in the correlation coefficients or exponents, while not substantially changing the values of the CHF predictions, can have a great impact in the definition of the boundary. An example of the sensitivity of the boundaries to the coefficients is shown in the paper by Katto [46] for the HP-H transition, when he modified the correlation coefficients of different regimes to include helium data in the HP regime. For V06, on the other hand, the prediction that T5 should transit by H-mode and T3 and T4 by N-mode is found (the predictions are good to less than 5% error).

In summary, the CHF predictions by Katto's correlations for the positions that transit to boiling crisis gradually (downstream) for both test sections are satisfactory. On the other hand, for the positions near the entrance (T1 at V10; T1 and T2 for V06), the predictions are less accurate (more than 30% overestimation). This is in resonance with the fact that these positions are in the spatial region of the test section that transits to crisis by violent extension, as described in the previous sections.

One reason why this happens may be a consequence of the high thermal diffusivity in the copper of the tube. At the point that separates the wetted section from the dry-wall section, there is necessarily a very strong temperature gradient in the flow direction. Such a situation can be unstable if the wall-liquid heat transfer coefficient in the wetted region is too low. The conducted heat inside the tube wall will tend to heat the wetted part of the wall, upstream. If the temperature reaches temporarily a temperature higher than the Leidenfrost point, a vapor patch can form, insulating the wall otherwise wetted, and impeding rewetting. The film will survive even if the heat flux alone would not have been able to start the crisis locally, if the section had not been heated downstream. Thus, the vapor layer extends upstream thanks to this instability up to a point where the flow presents less favorable conditions (less bulk vapor available, better NB heat transfer coefficient), i.e. where the value of applied heat flux is not enough to destabilize the temperature gradient. From that point on, the increase of heat flux

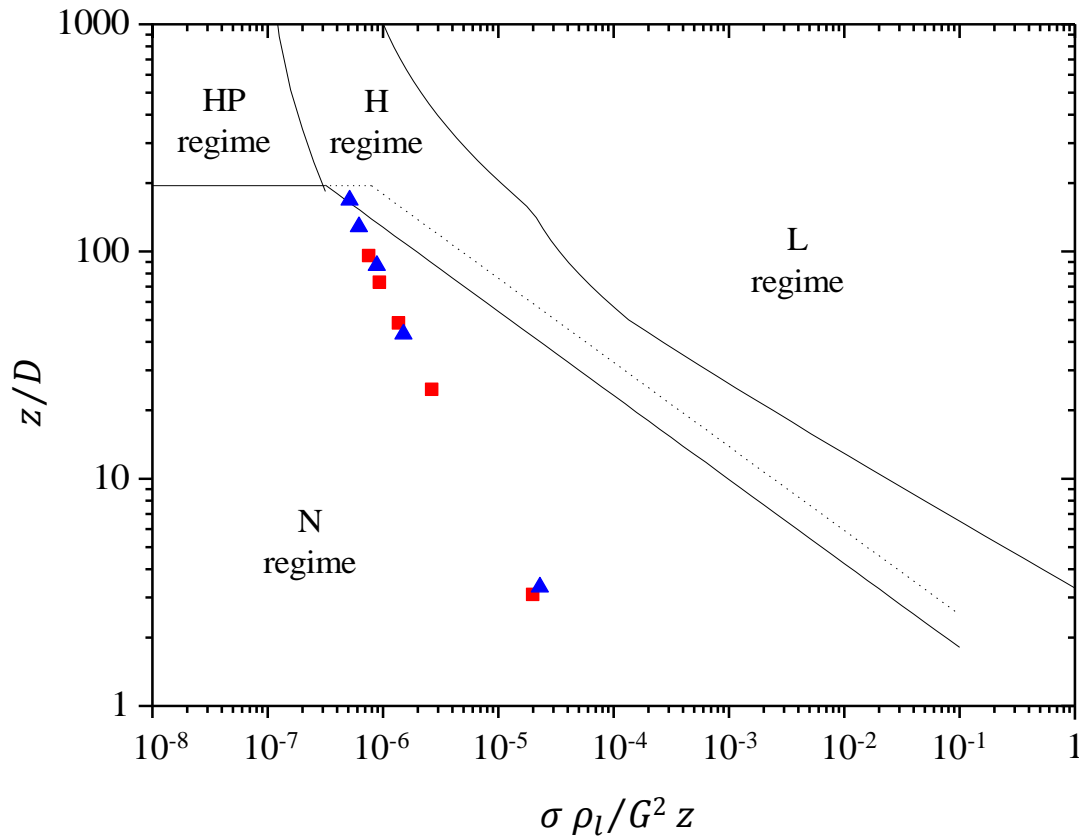


**Figure 4.5.** Katto's criteria for the CHF transition type [46] applied to our experimental data. ■ V10, ▲ V06.

Case	CHF predicted (W/m <sup>2</sup> )			Ratio prediction/experiment		
	HP-regime	N-regime	H-regime	HP-regime	N-regime	H-regime
T5 V10	1234	1113	1348	0.86	0.77	0.94
T4 V10	1453	1236	1577	0.93	0.79	1.00
T3 V10	1798	1413	1940	1.10	0.86	1.18
T2 V10	2376	1687	2597	1.38	0.98	1.51
T1 V10	4366	2615	5718	2.50	1.49	3.27
T5 V06	1046	1095	1187	0.88	0.92	1.00
T4 V06	1299	1261	1447	1.04	1.01	1.16
T3 V06	1642	1477	1815	1.17	1.05	1.30
T2 V06	2429	1853	2586	1.73	1.32	1.85
T1 V06	4727	3006	5993	2.12	1.35	2.69

**Table 4.2.** Values of CHF predicted by Katto's correlation [46], compared to the experimental results. The shaded values are the best predictions.

will continue to extend the post-CHF region towards the entrance at lower power values than expected. That may explain why at T1 for V10, and at T1 and T2 for V06 there are CHF values lower than predicted by the correlation and why there exists a violent extension of DNB for a considerably long part of the test section (of maybe 30 cm). We think it is quite possible that carrying out this experiment with tubes made of a less conductive material, such as regular steel, would not show this event. The choice for OFHC copper lies on the necessity of measuring precisely the internal wall temperature at the exterior of the tube, i.e. non-intrusively, and on the fact that it provides a homogeneous heat distribution over the surface.

Another reason to explain this behavior could be linked to CHF anomalies already observed before in other fluids [35]. In some cases CHF in upstream positions can be equal or lower than at the exit of a heated section, for high values of mass velocities, as shown experimentally in reference [32]. At intermediate mass velocities it is possible to have a region of the section where the CHF is practically uniform. In the cited works, it is pointed out that two different regimes of DNB can be identified:

- entrainment controlled: at low qualities, the liquid in the bulk of the section removes the vapor from the wall;
- deposition controlled: at high qualities, the bulk deposits vapor on the wall layer, lowering the CHF.

Near the boundary between the two regimes a negative change of slope or even a discontinuity in the relation CHF vs mass quality can be observed. This implies that the rate of spatial extension of the post-CHF regime with respect to heat flux may decrease right below the heat flux value at which the violent extension takes place in a flat ‘CHF vs.  $x$ ’ region. This effect is not evident when looking at the temperature evolution, but is observed when analyzing pressure drop evolution (see section 4.3).

### 4.2.3 Description of post-CHF heat transfer features

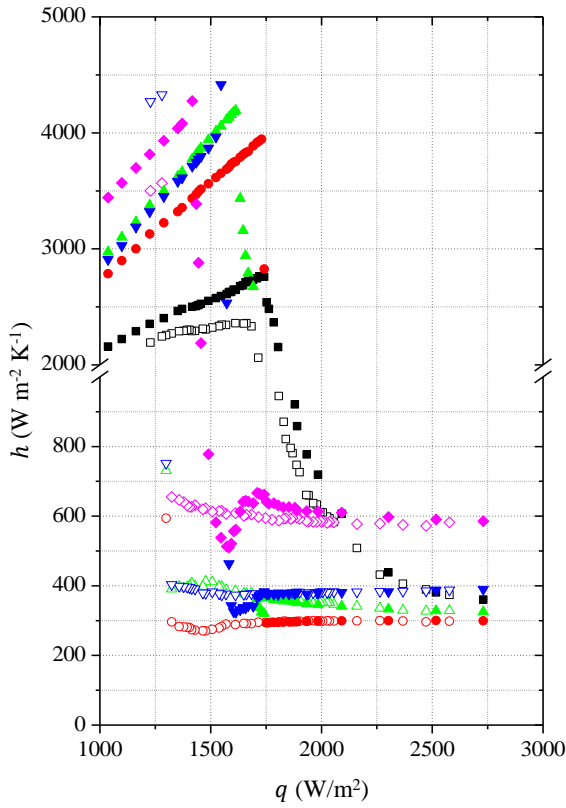
The analysis of heat transfer coefficients in steady state can give an insight of the flow patterns in film boiling, which could not be observed experimentally. The heat transfer coefficient  $h$  has been calculated assuming that at all time the bulk of the heated section is at the saturation point. Based on the arguments presented in section 4.1.3 concerning the calculation of temperature differences,  $h$  is calculated as:

$$h = \frac{q}{T - T(q=0)}. \quad (4.1)$$

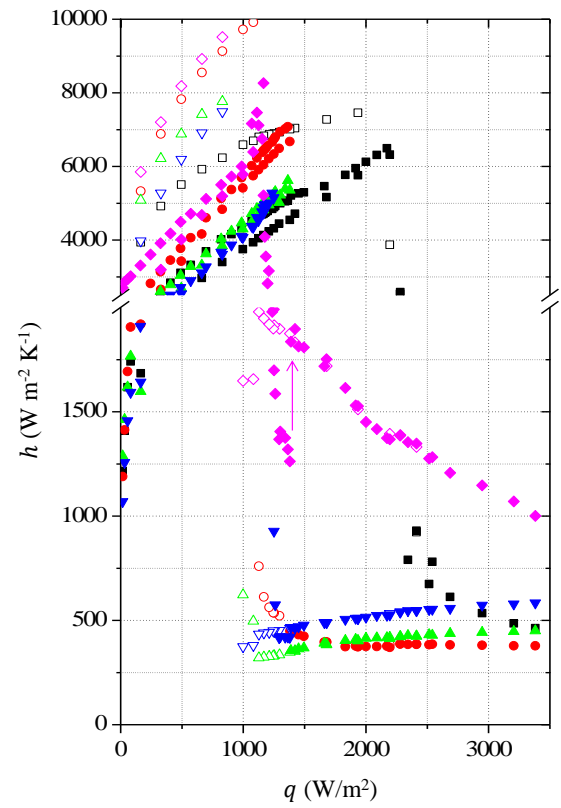
In the following paragraphs we observe the evolution of  $h$  vs.  $q$  in order to infer different heat transfer regimes, their dependence with position along the section and with respect to the position of the boiling crisis boundary.

For heat flux higher than 1850 W/m<sup>2</sup> the temperature evolution from T2 to T5 are quite close to a straight line going through the origin, suggesting that the heat transfer coefficient is constant at a given position for post-CHF regime in the whole section. This is verified by Fig. 4.6(a), which shows the heat transfer coefficients in the post-CHF regime. This is expected as the CHF boundary has practically reached the entrance and cannot advance any farther.

On the contrary, when the boundary between pre and post-CHF regions is gradually advancing towards the entrance, i.e. between 1400 and 1750 W/m<sup>2</sup>, the heat transfer coefficient presents a non monotonous evolution (see the temperature and heat transfer coefficient in this power range). Heat transfer is deteriorated with the onset of boiling crisis, the heat transfer coefficient drops to low values, but later, with power increase, it increases to reach the final asymptotic value.



(a) Heat transfer coefficients vs. heat flux. Section V10.



(b) Heat transfer coefficients vs. heat flux. Section V06.

**Figure 4.6.** Heat transfer coefficient for steady power. ■ □ T1, ● ○ T2, ▲ △ T3, ▼ ▽ T4, ◆ ◇ T5. The solid points were obtained increasing power and the blank points decreasing power.

Furthermore, when the boiling crisis extends violently to the upstream positions, a sudden change in the temperature profile downstream is observed, with more or less evident discontinuities in the temperature evolution at positions T3, T4 and T5 at  $1750 \text{ W/m}^2$ . The discontinuities are more evident at T3, less at T4 and barely observable at T5. This must be the effect of the CHF boundary suddenly getting farther from each sensor's position, which makes the points T3 and T4 pass from the 'head' of the post-dryout region to the fully developed region.

This shows that as the post-CHF region takes over, at a fixed point in the section, heat transfer is appreciably worse when the point is very close to the CHF boundary than when the boundary is located farther upstream. This must be linked to the transition between laminar or wavy vapor layer at the head of the film, and turbulent layer at the tail, as has been observed in other experiments in other fluids [36, 37, 57]. This effect is more pronounced the closer the point is to the exit of the section (compare this effect for T5 to T4 and T3 in Figs. 4.2(a) and 4.6(a)). For T2 this is not observed at all, given that when T2 becomes part of the post-CHF region, the violent extension of the boundary to the entrance, leaves it immediately in a position already in the fully developed region of the film. Furthermore, when the violent extension of boiling crisis takes place, a discontinuity is observed in the temperature evolution of T3 and T4 (less pronounced). As these two positions were relatively close to the boundary before the event, they were very sensitive to the change in the wall flow pattern upstream.

The comparison of the increasing heat flux experiment to that with decreasing heat flux shows that the heat transfer coefficient in the post-CHF regime is not only a function of the heat flux. In the range between  $1400$  and  $1750 \text{ W/m}^2$  the values of  $h$  obtained are lower when increasing than decreasing the power. The main difference between the two situations is the position of the head of the post-CHF region with respect to the measurement point at a given heat flux: when decreasing power, the post-CHF boundary is constantly somewhere between the entrance and T2 due to the hysteresis of boiling crisis (treated in section 4.2.4); thus, T3, T4 and T5 are all the time in the fully developed post-CHF region, the turbulent film zone, with  $h$  near the asymptotic value. For heat flux higher than  $1850 \text{ W/m}^2$ , no difference is observed between the two experiments since in both cases the temperature sensors are in the downstream part of the post-CHF region.

As for the asymptotic value of the heat transfer coefficient, it increases towards the exit of the test section, probably due to the increase of turbulence and mixing induced by the increase of vapor fraction and velocity. This trend is observed in post-CHF regimes with other fluids at different conditions [20, 36] and is suggested too in many experimental heat transfer correlations in the literature [33], where the Nusselt number increases with increasing quality, holding constant mass flux and diameter.

The analogous analysis on section V06 shows that positions T3 and T2 transit to the post-CHF regime at the same heat flux value ( $1380 \text{ W/m}^2$ ), which means that the CHF boundary moves from some point above T3 to some point below T2 instantaneously. The character of decreasing temperature along the section was also observed at a fixed heat flux value. The calculated heat transfer coefficient at T5 is significantly higher than at the other positions, indicating an enhanced heat transfer regime, probably dispersed flow film boiling (DFFB) [1, 33]. When the violent extension of the CHF boundary takes place, a discontinuity in the temperature evolution at T5 is observed; this manifests again that a change in the heat transfer conditions downstream is induced by the displacement of the CHF boundary as in the case of V10. In this case, T5 may be passing from partially to fully developed DFFB regime. The calculated heat transfer coefficient at T5 as a function of heat flux presents a strong decreasing trend, probably linked to both the decrease of mass flow rate in the loop at high heat flux (see mass flow rate evolution in Fig. 4.3) and the increase of local quality with  $q$ , which reduces the evaporation heat sink in the bulk. However, for the calculation of  $h$  at T5 considering the thermal non-equilibrium of the two phases (vapor super-heat) may need to be considered [36]; for this reason, the decrease

in  $h$  may be overestimated. We need to mention that the equilibrium exit quality is over 1 for heat flux values above  $3600 \text{ W/m}^2$ .

#### 4.2.4 Observations on rewetting during the decreasing power experiment

It is a general trend that, once the boiling crisis takes place on a surface, going back to the nucleate boiling regime requires decreasing heat flux far below the value of CHF [20, 58]. To study the transition back to nucleate boiling regime, measurements were performed decreasing power from a high power value at which post-CHF regime exists all over the test section. The values of temperature during this operation appear as blank points in Fig. 4.2. The value of power at which the mentioned transition takes place is in most cases much lower than CHF for any position, as shown in table 4.1.

Baudouy [7] and Benkheira [14] have pointed out the occurrence of boiling crisis hysteresis in the same natural circulation loop as ours, but with a greater internal diameter test section (14 mm). Furthermore, this phenomenon seems to be dependent on the position along the heated section.

Understanding the nature of the rewetting of the surface after boiling crisis can be useful for the comprehension of rewetting during boiling crisis transients, on which we will focus in the following chapters. In the following paragraphs we will point out our observations during the rewetting experiments.

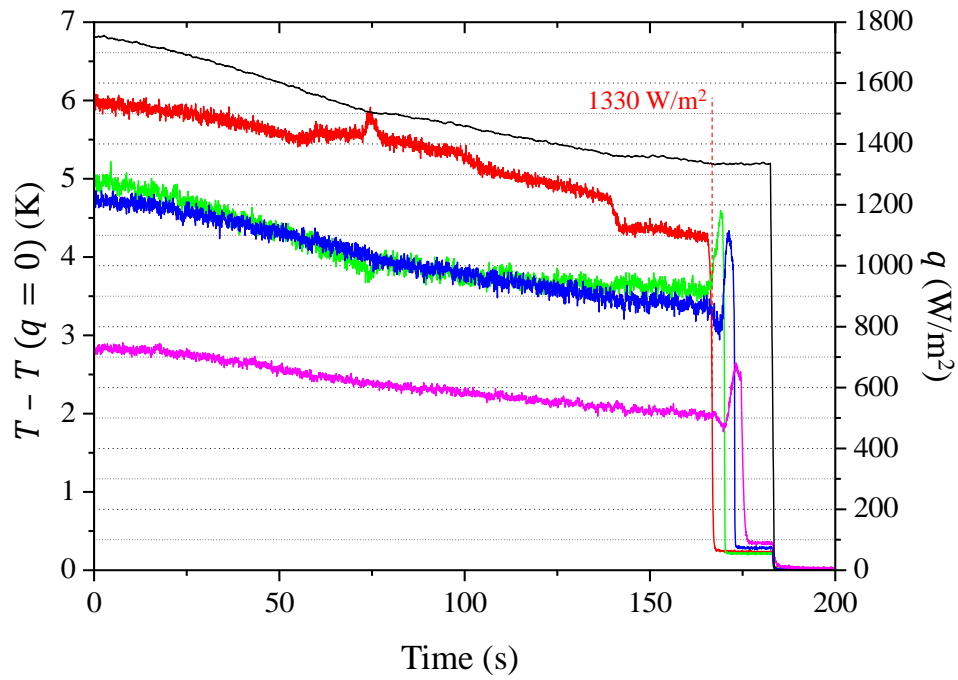
At T1, the closest to the entrance, no hysteresis effect was observed; practically the CHF and RHF values are the same. The temperature increase and decrease at this position is gradual; we cannot distinguish the two evolutions. This confirms the hypothesis that the boiling curve ' $q$  vs.  $T$ ' for T1 does not present a minimum in the transition boiling heat transfer regime.

Surprisingly, for T2 to T5 with V10 and T3 to T5 with V06, the RHF is the same: the transition to nucleate boiling is simultaneous for all the mentioned positions. In other words, the retreat of the post-crisis regime is not gradual as a function of decreasing heat flux. This is similar to the phenomenon described before, by which the transition to boiling crisis was simultaneous for all the upstream region of the section. T2 with V10 and T3 with V06 were the positions that transitioned to dryout in the violent spatial extension of dryout to upstream positions.

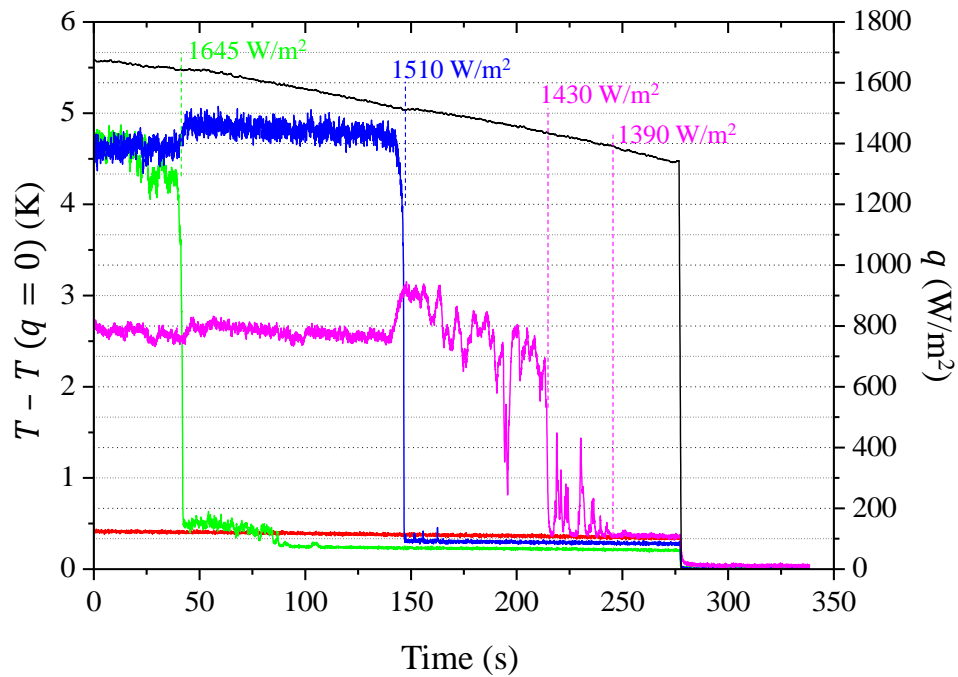
In order to study the phenomenon a new experiment was made (only for section V10). A sufficiently high power value was applied in order to establish boiling crisis only on the downstream region where the advancement of the CHF boundary is gradual, i.e. below  $1720 \text{ W/m}^2$ . In this situation positions T1 and T2 are in the nucleate boiling regime and T3, T4 and T5 are in the post-CHF regime. Then, power was decreased slowly in order to attain the rewetting transition for T3, T4 and T5. This time, the transition happened at appreciably higher heat flux values than the RHF in table 4.1. The values are slightly lower than CHF, and depend on the position: the transition is not simultaneous but gradual.

These experiments, depicted in Fig. 4.7, reveal that when the upstream (near-entrance) region of the section is in post-CHF regime after the violent spatial extension, the transition back to nucleate boiling happens at a definite power value simultaneously for the whole segment section downstream. When only the downstream region is in post-CHF regime, the transition back to nucleate boiling is gradual with heat flux as a function of position and at higher values than in the first case.

It is worth to point out that the wall temperature transient from boiling crisis to nucleate boiling in the first case has a finite duration, as can be appreciated in Fig. 4.7(a). The rewetting at T5 takes place 10 seconds later than at T2. Furthermore, right before the pronounced de-



(a) Power decrease with T2 initially in post-CHF regime.



(b) Power decrease with T2 initially in nucleate boiling regime.

**Figure 4.7.** Temperature evolutions in transition from post-CHF to nucleate boiling regime. —  $T_2$ , —  $T_3$ , —  $T_4$ , —  $T_5$ , —  $q$  (scale on the right).

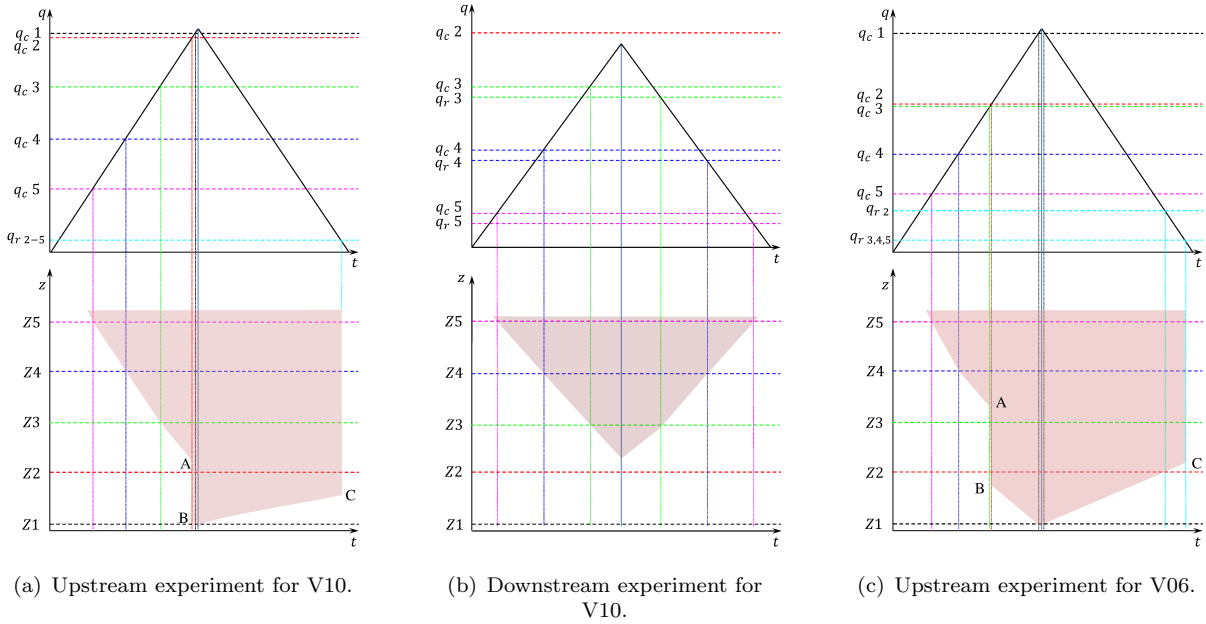


**Figure 4.8.** Schematic observed crisis evolution during rewetting experiments.  $q_c$  is the measured CHF,  $q_r$  is the RHF. The axis are not to scale. The shaded area represents the portion of the heated section in post-CHF regime.

crease of temperature indicating the transition, T3, T4 and T5 show an increase in temperature. This can be associated with the bad heat transfer near the boundary of the post-CHF region already identified when increasing heat flux gradually (see figure 4.2.3). As the boundary moves downstream during the transition transient, it approaches each temperature sensor, making the temperature rise right before the nucleate boiling regime takes over.

To summarize the observed phenomena, Fig. 4.8 shows the three boiling crisis hysteresis experiments. Figures 4.8(a) and 4.8(c) show the experiment in which the post-CHF regime was completely developed on the whole section; Fig. 4.8(b) shows the observations of the experiment in which the boiling crisis has only been attained in the gradual CHF downstream region. The plot on top represents a hypothetical slow power evolution and the shaded area in the plots at the bottom represents the portion of the heated section in post-CHF regime. When increasing power, the CHF-boundary instantaneously jumps from point A to B if CHF at A is attained, and the simultaneous rewetting takes place beyond point C, which is somewhere between A and B.

### 4.3 Study of the hydraulic effects of boiling crisis

The second part of the analysis consists of the *hydraulic* aspects of the loop. In order to identify particular hydraulic effects of boiling crisis, the evolution of the mass flow rate and the test section pressure drop were observed in the developing and post-CHF power ranges (section 4.3.1). In order to identify the mechanism responsible for the observed behavior, different models existing in the literature were evaluated and compared to the data (section 4.3.2). Finally, in order to improve the prediction of friction pressure drop, a new practical model was developed using a two-fluid approach and previous knowledge of heat transfer coefficients (section 4.3.3).

### 4.3.1 Experimental observations on pressure drop and mass flow rate during crisis development

In this opportunity, we focus on the evolution of mass flow rate ( $\dot{m}$ ) and pressure drop on the heated section ( $\Delta P_{tube}$ ). The latter is calculated as  $P1 - P2$ . In order to eliminate possible systematic offset, we subtracted the measured value of pressure drop at zero power ( $\Delta P_{tube}(q = 0)$ ), theoretically equal to  $\rho_l g (z_2 - z_1)$ .

When we look at Fig. 4.3, the description presented at the end of section 2.3.2 is quite accurate for the pre-CHF part of the curves. The fast increase of void fraction as quality increases, at very low quality, results in a very fast increase of mass flow rate at low power. Then, at moderate power values a mass flow rate plateau is reached, which reflects the plateau of void fraction as a function of quality for higher quality values. However, when temperature evolution indicates the transition to FB,  $\dot{m}$  increases gradually more than can be extrapolated from the pre-crisis behavior and it shows a strong correlation with the advancement of post-CHF region along the section. In fact, when the violent extension of FB to T2 and T1 takes place, a discontinuity is observed in  $\dot{m}$ , with an instantaneous increase.

Similar observations can be made about the evolution of the pressure drop variation, shown in Fig. 4.4. In the pre-CHF power region, the pressure drop on the section evolves differently according to the diameter of the section. For V10, the increase in power produces a decrease of the pressure difference. This means that the loss of density (negative) contribution is more important than the friction (and eventually acceleration) contribution(s). On the other hand, for V06, the increase of power produces positive pressure drop variation, indicating the predominance of friction on density change effects.

The trend suggested by the pre-CHF region does not apply once boiling crisis takes over the section. In both experiments, the pressure drop is lower than expected with an important slope break at sensibly the same heat flux at which the temperature sensor near the exit (T5) starts ‘firing’. In the case of V10 the slope before and after CHF are both negative, with the one above CHF being more pronounced. In the case of V06 the slope was positive before CHF and negative afterwards. At the point where the violent extension of the post-CHF region takes place, both pressure drop and  $\dot{m}$  show a discontinuity.

During the rewetting experiment (decreasing heat flux), the low values of pressure drop in the post-CHF regime show a continuous trend until the rewetting heat flux (RHF) is reached. As soon as the whole section goes back to NB regime, a discontinuity is observed in the pressure drop and the mass flow rate, returning exactly to the same values as when increasing power from zero. In other words, the increasing and decreasing power evolutions give the same pressure drop and mass flow rate values only below RHF or above the CHF for the upstream anomalous region (recall the last paragraph of section 4.2.1). In between, the evolution is different for increasing or decreasing power, given the boiling crisis region spatial extension is too.

It becomes evident that a strong relation exists between the hydraulic forces equilibrium and the wall heat transfer conditions. The apparition of boiling crisis produces an *increase of mass flow rate* and a *pressure drop lessening effect* which appears to be proportional to the extension of the post-CHF region. The last affirmation could mean that *wall friction is significantly reduced by the apparition of the near-wall vapor layer, acting as a ‘thermal insulator’ and a ‘hydraulic lubricant’*. In the light of a force balance similar to that in Eq. (2.48), as explained at the end of section 2.3.2 and depicted in Fig. 2.8, the decrease of the friction proportionality constant in the heated section would lead to a RHS terms lower than the LHS term if  $\dot{m}$  and  $q$  are not allowed to change. Thus, to reach equilibrium with a lower friction factor in the heated section,  $\dot{m}$  needs to increase, so that the gravity driving term diminishes and the RHS term increases until they meet at a new equilibrium point.

The lessening of the friction forces due to boiling crisis has been observed before on other fluids but the extent of the effect is variable. In the case of water, the effect is not as pronounced as in our case, but still appreciable. Leung *et al.* [55], report a drop of the two-phase multiplier from 2 to 1.5 with CHF on steam water systems. In the case of hydrogen, as reported by Graham and *et al.* [31], the friction forces practically disappear.

### 4.3.2 Evaluation of pressure drop prediction methods during boiling crisis

The two-phase pressure drop in a vertical *uniformly heated* tube with upward flow and saturated liquid at the inlet can be described by a simple pipe friction model. The pressure gradient is composed of three contributions:

$$\frac{\partial P_{2\phi}}{\partial z} = - \underbrace{\frac{\partial P_{fr,2\phi}}{\partial z}}_{\text{friction}} - \underbrace{G^2 v_{lg} \frac{\partial x}{\partial z}}_{\text{acceleration}} - \underbrace{\frac{g}{v_l + v_{lg} x(z)}}_{\text{gravity}}, \quad (4.2)$$

where, taking into account that the liquid at the inlet of the test section is subcooled (due to mainly the hydrostatic pressure in the down-comer) and neglecting potential and kinetic energy terms, the local quality  $x$  in the two-phase region is approximately given by

$$x(z) = \frac{q\pi D}{\dot{m}h_{lg}} (z - L_{1\phi}) \implies \frac{\partial x}{\partial z} = \frac{q\pi D}{\dot{m}h_{lg}}. \quad (4.3)$$

Assuming no subcooled wall boiling, a reasonable approximation for the one-phase subcooled length is:

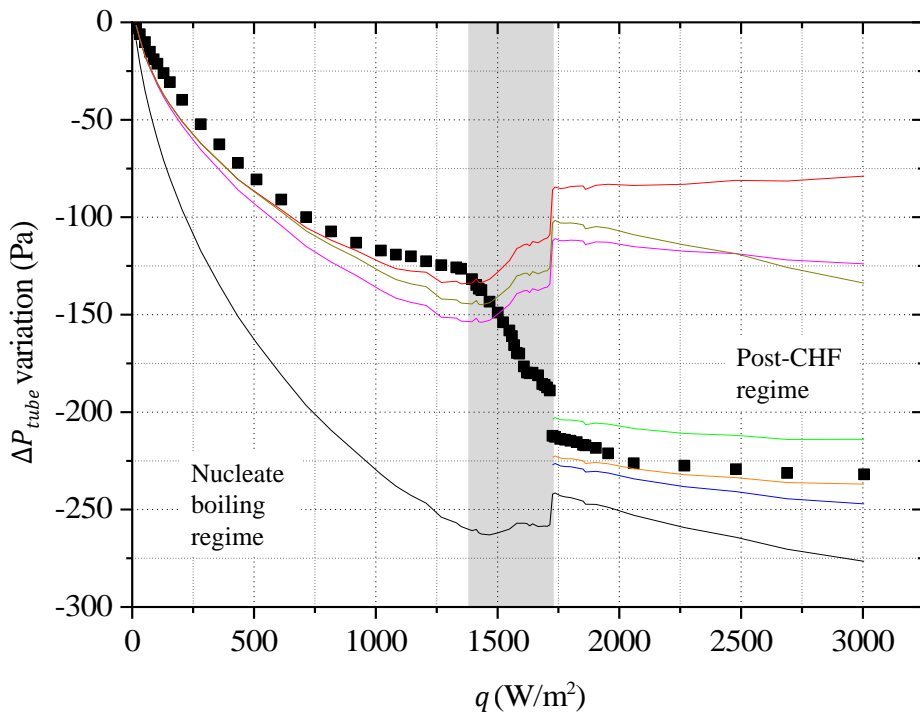
$$L_{1\phi} = \frac{\dot{m}C_l\Delta T_{sub}}{q\pi D}. \quad (4.4)$$

In Eq. (4.2) it has been assumed that the phase distribution is homogeneous over the cross section and the two phases velocities are equal for the acceleration and gravity terms (i.e. the homogeneous model assumptions). The friction term is to be calculated with the corresponding model from those exposed in section 2.4.5.

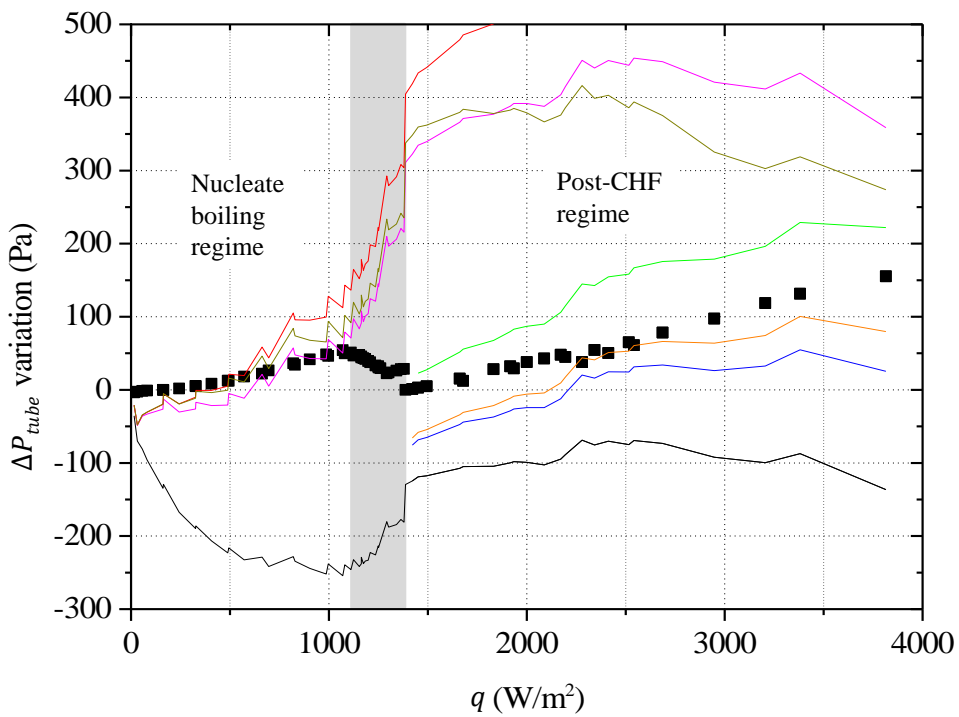
The pressure drop on the heated section, between positions P1 and P2, was estimated taking into account the friction models presented in section 2.4.5. The input parameters for the calculation are the measured values of  $q$  and  $\dot{m}$ , presented in Fig. 4.3. The predictions are compared to the data in Fig. 4.9.

The total pressure drops predicted for V10 by the homogeneous model, bubbly flow model and the formula given by Subbotin [72] are in very good agreement with the measurements in the nucleate boiling (NB) regime. However, in the crisis development region the predictions and the data diverge. This shows that the two-phase multiplier decrease presumably due to flow pattern change (considered by Subbotin's formula) does not explain the lessening of friction observed at CHF. Thus, we conclude that it is veritably the presence of a vapor film on the wall that produces this drop on the friction coefficient. In order to test the hypothesis that friction pressure drop vanishes completely as reported in [31] for hydrogen, the calculation of the pressure drop without friction contribution is also presented on Fig. 4.9 (black curve). It is assumed that the flow is still homogeneous in the bulk of the section for calculating the gravity and acceleration pressure drop components. The experimental points at high power seem to follow a similar trend to those obtained this way, suggesting that a friction component is present but small.

For section V06, the total pressure drop predicted in the NB regime differs from data. This is due to the fact that the measured values are close to zero and in the model, the total pressure drop is the result of an addition of friction and acceleration (positive contributions) minus gravity (negative contribution). The opposed contributions are approximately as high, and the difference

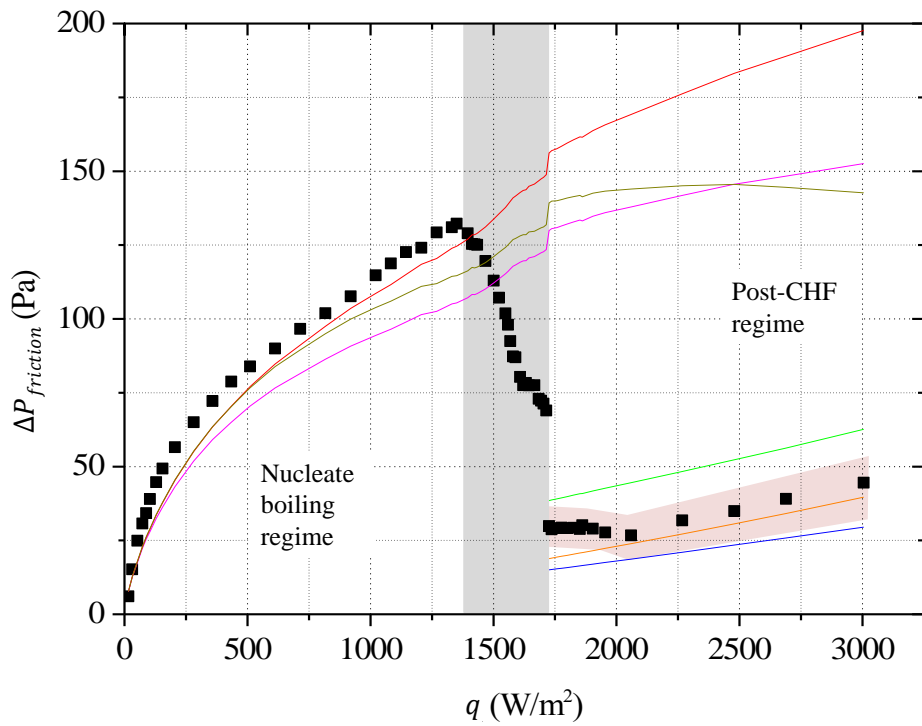


(a) Section V10.

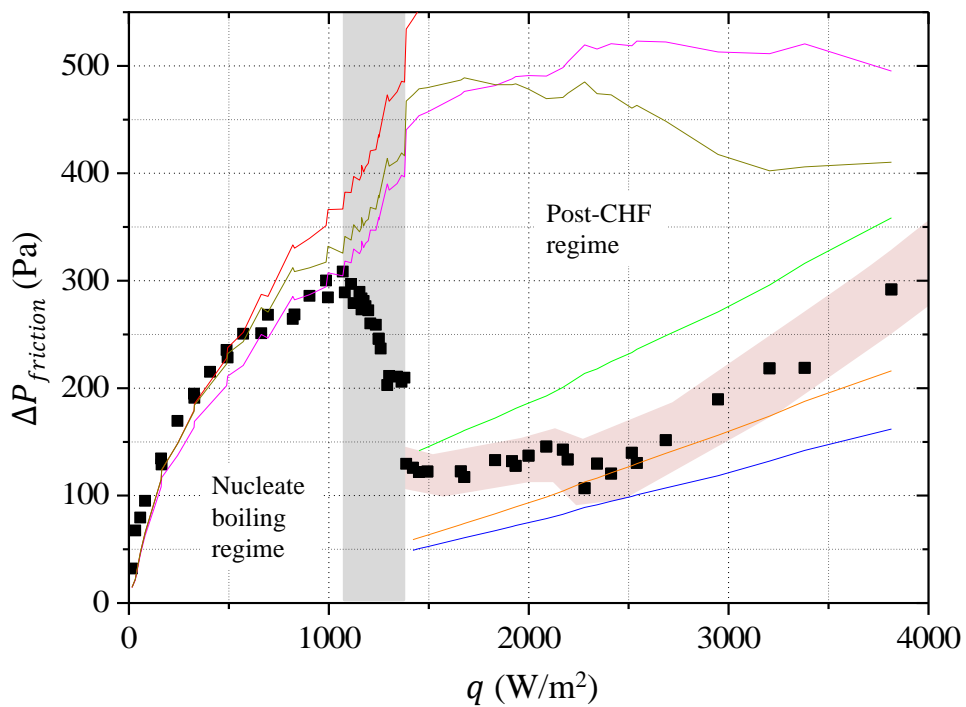


(b) Section V06.

**Figure 4.9.** Pressured drop prediction. ■ Experimental data ( $\Delta P_{measured} - \Delta P_{gr} - \Delta P_{acc}$ ), — homogeneous model, — bubbly flow model, — Subbotin's model [72], — post-dryout correlation [11], — laminar equivalent smooth moving wall model, — laminar equivalent fully turbulent bulk model, — homogeneous model without friction (only gravity and acceleration contributions). The vertical gray rectangle shows CHF development range.



(a) Section V10.



(b) Section V06.

**Figure 4.10.** Friction pressure drop. ■ Experimental data ( $\Delta P_{measured} - \Delta P_{gr} - \Delta P_{acc}$ ), — homogeneous model, — bubbly flow model, — Subbotin's model [72], — post-dryout correlation [11], — laminar equivalent smooth moving wall model, — laminar equivalent fully turbulent bulk model. The vertical gray rectangle shows CHF development range, the pink area around data in post-CHF regime illustrates 1% parametric impact of internal diameter.

has an uncertainty naturally higher than zero. In any case, although the predictions and measured data present a similar trend in the NB region, a larger difference appears when boiling crisis starts near the exit of the section. Again, the flow pattern influence present in Subbotin's prediction does not explain the measured evolution. When the boiling crisis is present along the whole section, the model without friction predicts a pressure drop parallel to the measured one, but the difference is higher than in the V10 case.

An experimental friction contribution to the pressure drop was calculated: the acceleration and gravity contributions calculated as in Eq. (4.2) were subtracted from the total measured pressure drop. This quantity and the friction contribution according to the models are plotted as a function of heat flux in Fig. 4.10.

These plots show how the homogeneous, bubbly flow, and Subbotin's models' predictions for friction pressure drop are good in the NB regime. For V10 the friction pressure drop is less significant than for V06, as is to be expected for similar mass velocities, given the difference in diameter. The bubbly flow model seems to be the more adequate for V10, while the homogeneous flow is for V06. This may be a result of the fact that a better homogeneity in vapor cross-sectional distribution is easier to achieve for a smaller diameter.

As soon as the boiling crisis takes over, the three models predict an increase in the friction pressure drop, mainly because experimentally a significant increase in  $\dot{m}$  has been found. The  $\dot{m}$  relative variation is higher for the V06 case, which in time makes the two models' prediction increase dramatically between 1200 and 1500 W/m<sup>2</sup>. This effect is smaller in the V10 case. The difference between the two cases is due to the fact that in V06 most of the friction in the whole loop originates in the test section, because it is the component with the smallest diameter along a significant length. For V10, the fraction of the total friction produced in the test section is much lower. A change in the friction factor in the test section for unchanged gravity and acceleration contributions needs to be compensated by a given increase in total  $\dot{m}$  up to a new equilibrium value. The change in  $\dot{m}$  needs to be more significant if the relative friction contribution of the test section to the whole loop is too.

In the fully developed post-CHF regime, the friction pressure drop presents a slightly increasing trend, probably due to the considerable bulk velocity increase near the exit of the heated section. For the V10 section, the lessening of friction due to boiling crisis is dramatic (5 times lower than the maximum), while for V06, although a clear lessening is observed, the values of total friction pressure drop are still high (half of the maximum, 150 Pa). This shows that for small diameters, the friction in the vapor film is still considerable, although appreciably lower than in the NB regime. As the diameter increases, the friction in the vapor film is less significant.

Predictions of the pressure drop in the post-dryout region were made using Beattie's dry wall model [11], shown as a green curve in Figs. 4.9 and 4.10. It has been assumed for the calculation that the test section is under boiling crisis from the very entrance. The trend obtained by this prediction method reflects the behavior of the experimental data in the fully developed post-dryout zone, especially the rate of growth with respect to heat flux. On the other hand, it seems to overestimate the actual value of the friction contribution.

It should be mentioned that the diameter of the test section has a considerable impact on the calculation of the measured friction pressure drop. In the figures the pink shaded area around the data in the post CHF regime reflects the effect of a  $\pm 1\%$  variation in the diameter. The percentage of variation of the friction pressure drop predicted can be as high as 25% for V10 and 15% for V06.

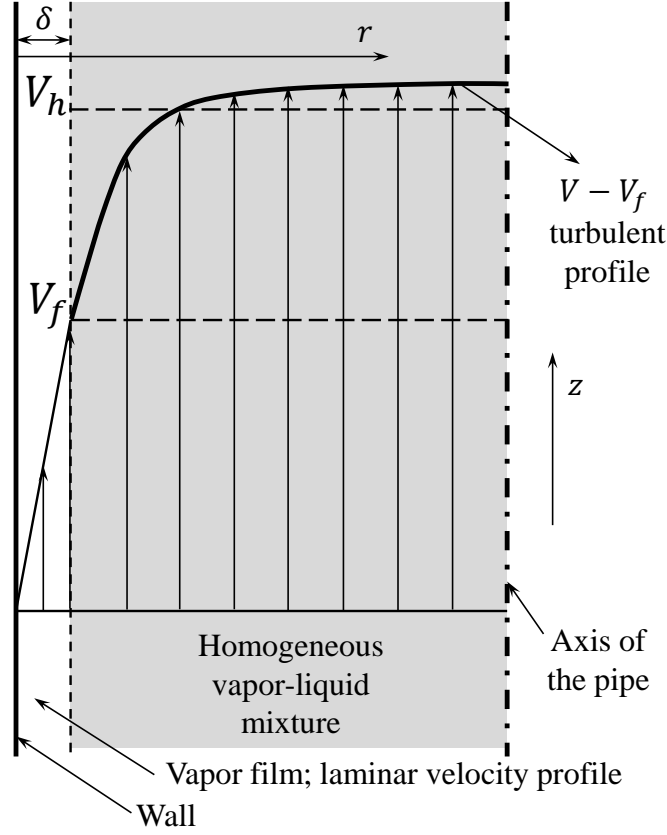


Figure 4.11. Schematic velocity profile assumed for the FB model study.

### 4.3.3 Creation of a new film boiling pressure drop prediction model

The post-dryout friction model by Beattie assumes that the turbulence is completely developed in the vapor film, to the point that the velocity at the interface is equal to the bulk average velocity  $V_h$ . In fact, it can be shown that the model is based on the following equations:

$$\frac{\partial P_{fr}}{\partial z} = \frac{f_g \rho_g V_h^2}{D \cdot 2}, \quad (4.5a)$$

$$\text{with } f_g = 0.316 \left( \frac{\rho_g V_h D}{\mu_g} \right)^{-1/4}. \quad (4.5b)$$

The value of the velocity at the boundary of the film plays a very important role on the near wall velocity profile, not only as a proportionality constant of its derivative at the wall, but also because it affects the typical laminar sublayer length.

In an attempt to make a prediction of the friction pressure drop in FB regime that takes into account the fact that the interface velocity can be lower than the bulk velocity, we propose the model that we expose in the following paragraphs.

We consider, as is illustrated in Fig. 4.11, that the channel flow can be separated in two distinct regions:

- The near-wall vapor film of thickness  $\delta$ , where the flow is assumed laminar;
- The bulk flow, a mixture of liquid and gas with a given value of mass vapor fraction and resulting properties (viscosity, density).

The wall shear stress, that will eventually originate the friction pressure drop is

$$\tau_w = \frac{D}{4} \frac{\partial P}{\partial z} = \mu_w \frac{\partial V}{\partial r}. \quad (4.6)$$

We will assume that the film thickness can be neglected face to the diameter, thus the problem can be assumed locally 1D in the radial direction at each value of  $z$ . In the following equations, the dependence on  $z$  will not be explicitly expressed to simplify the notation.

To solve the velocity field in the film in the radial direction, we need boundary conditions. We consider that turbulence at the interface with the bulk produces a great amount of mixing, both of energy, velocity and mass. The intensity of turbulence may be high enough at some point to detach bubbles from the film, especially if the fluid has a very low surface tension, as is the case of helium. Thus, statistically, there is a near wall layer with only vapor present, followed by a fully turbulent region where the two phases are present. It is at this point where the pure vapor layer ends that we define the actual effective interface with the bulk. Furthermore the bulk is assumed to be in saturated thermal equilibrium; thus, the temperature is uniform in the axial direction, and we can neglect the convective term in the energy equation inside the film. As a result, the temperature only varies in the direction perpendicular to the wall as a result of the conductive uniform heat flux:

$$\frac{\partial T}{\partial r} = -\frac{q}{k(T)}, \quad (4.7a)$$

$$\text{with } T(r=0) = T_w \text{ and } T(r=\delta) = T_{sat}. \quad (4.7b)$$

The laminar velocity profile is given by

$$\frac{\partial V}{\partial r} = \frac{\tau}{\mu(T)}, \quad (4.8a)$$

$$\text{with } V(r=0) = 0 \text{ and } V(r=\delta) = V_f. \quad (4.8b)$$

For very thin films, the value of  $\tau$  can be considered uniform in the radial direction inside the film (curvature is neglected) and equal to  $\tau_w$ :

$$\tau(r) = \tau_w = \tau_f. \quad (4.9)$$

The simultaneous solution of Eqs. (4.7) and (4.8) gives:

$$\tau_w \int_{T_{sat}}^{T_w} \frac{k}{\mu} dT = qV_f. \quad (4.10)$$

For helium, the ratio  $\frac{k}{\mu}$  is almost constant with respect to the vapor temperature. Between 4.2 and 10 K the variations of this ratio is lower than 2%. Thus, it is valid to say

$$\tau_w = \frac{qV_f\mu_g}{(T_w - T_{sat})k_g} = V_f \frac{\mu_g h}{k_g}. \quad (4.11)$$

We can define an effective thickness, the *laminar equivalent* thickness as:

$$\delta_{eff} = \frac{k_g}{h}. \quad (4.12)$$

Thus, the values for  $\delta_{eff}$  can be obtained from the heat transfer coefficient of the surface, for example from using a  $Nu$  number correlation. Note that in general  $\delta \neq \delta_{eff}$ . From Eq. (4.7):

$$\delta = \delta_{eff} \frac{\int_{T_{sat}}^{T_w} k(T) dT}{k_g (T_w - T_{sat})}. \quad (4.13)$$

They are equal if  $k$  does not depend on  $T$ .

For a very thin film, the geometry and the mass balance for the bulk are simplified as:

$$D_h = D, \quad A_h = A, \quad \dot{m}_h = \dot{m}, \quad G_h = G. \quad (4.14)$$

The bulk of the fluid has an average density  $\rho_h$  and velocity  $V_h$  depending on  $z$ , due to the increase of the mass vapor fraction  $x$  along the heated section (Eq. (4.3)). If a homogeneous flow is assumed together with Eq. (4.14), then

$$\rho_h = \frac{\rho_l}{(1 + x\rho_l v_{lg})}, \quad (4.15a)$$

$$V_h = \frac{\dot{m}}{\rho_h A} = G(xv_{lg} + v_l). \quad (4.15b)$$

One way to couple the bulk with the film is to consider it as an internal flow with an effective velocity equal to  $V_h - V_f$ , as if the wall (the film-bulk interface) was a *moving smooth wall* with velocity  $V_f$ . We assume for the calculation of friction in the bulk that the film-bulk interface is perfectly cylindrical, with no waving due to shear. Then the friction forces acting on the bulk can be obtained as:

$$\frac{\partial P_{fr}}{\partial z} = \frac{4}{D} \tau_f = \frac{f_h \rho_h (V_h - V_f)^2}{2 D_h}, \quad (4.16)$$

where the friction factor can be obtained from the friction correlations for a smooth tube. For simplicity, we consider the Blasius equation,

$$f_h = 0.316 \left( \frac{\rho_h (V_h - V_f) D_h}{\mu_h} \right)^{-1/4}, \quad (4.17)$$

with a definition of  $\mu_h$  according to either the homogeneous model (Eq. (2.35)) or the bubbly flow model (Eq. (2.57)). From Eqs. (4.16), (4.17) and (4.14) we obtain:

$$\tau_w = \frac{0.316}{8} D^{-1/4} \rho_h^{3/4} \mu_h^{1/4} (V_h - V_f)^{7/4}. \quad (4.18)$$

The association of Eqs. (4.11), (4.12) and (4.18) gives:

$$\left( \frac{8}{0.316} \frac{\mu_g}{\delta_{eff}} D^{1/4} \rho_h^{-3/4} \mu_h^{-1/4} \right)^{4/7} V_f^{4/7} + V_f = V_h. \quad (4.19)$$

Note that this result is valid for each point  $z$  of the section, which has its own particular values of  $V_h$ ,  $\mu_h$ ,  $\rho_h$  and  $\delta_{eff}$ . In appendix B we give some advice to solve Eq. (4.19). Finally, the shear stress is calculated as:

$$\tau_w = \frac{4\mu_g V_f}{D\delta_{eff}}. \quad (4.20)$$

A more realistic alternative, is to consider that on the bulk side at the interface the turbulence is completely developed and that the velocity profile takes the *fully-turbulent* self-similar form [65]:

$$V(r) = V_f + \frac{1}{\kappa} \sqrt{\frac{\tau_w}{\rho_h}} \ln \left( \frac{r}{\delta} \right) \quad \text{for } r > \delta. \quad (4.21)$$

For a very thin film,  $R/\delta \gg 1$  and the average velocity obtained by integration of the profile on the cross section can be approximated as:

$$V_h \approx V_f + \frac{1}{\kappa} \sqrt{\frac{\tau_w}{\rho_h}} \left[ \ln \left( \frac{D}{2\delta} \right) - 1 \right]. \quad (4.22)$$

The association of Eqs. (4.11), (4.12) and (4.22), with the elimination of  $V_f$  gives

$$\tau_w = \frac{\mu_g}{\delta_{eff}} \left\{ V_h - \frac{1}{\kappa} \sqrt{\frac{\tau_w}{\rho_h}} \left[ \ln \left( \frac{D}{2\delta} \right) - 1 \right] \right\}. \quad (4.23)$$

Equation (4.23) can be solved as a quadratic equation of  $\sqrt{\tau_w}$  at each position:

$$\tau_w = \frac{V_h \mu_g}{\delta_{eff}} + \frac{\mu_g^2 U^2}{2\delta_{eff}^2} \left( 1 - \sqrt{1 + \frac{4V_h \delta_{eff}}{\mu_g U^2}} \right), \quad (4.24a)$$

$$\text{with } U = \frac{1}{\kappa \sqrt{\rho_h}} \left( \ln \left( \frac{D}{2\delta} \right) - 1 \right). \quad (4.24b)$$

It has been found that substituting  $\delta_{eff}$  for  $\delta$  in the definition of  $U$  has a very slight effect on  $\tau$ . For an experimental case with wall temperature of around 10 K,  $\delta \approx 1.5 \delta_{eff}$ , the substitution  $\delta \leftarrow \delta_{eff}$  provokes an underestimation of  $\tau_w$  of around 2 or 3%. For  $T_w = 20$  K the error is less than 5%. Thus, for a simple application of the model, only  $\delta_{eff}$  is determined and substituted for  $\delta$ .

Once the solution to either of Eqs. (4.19) or (4.24) is known, the pressure gradient can be calculated along the section, and the total pressure drop can be found as:

$$\Delta P_{fr} = \int_{z_1}^{z_2} \frac{4\tau_w(z)}{D} dz. \quad (4.25)$$

In summary, for the utilization of these models, the steps to follow are:

- from a couple of  $q$  and  $\dot{m}$ , determine the value of  $x(z)$  (Eq. (4.3)),  $\rho_h(z)$  (Eq. (4.15a)) and  $V_h(z)$  (Eq. (4.15b));
- determine the local value of  $\delta_{eff}(z)$  from heat transfer coefficient data or correlations.
- solve Eq. (4.19) or Eq. (4.24) to find  $\tau_w$ ;
- integrate Eq. (4.25) on the heated section.

These models were compared to our experimental results in Figs. 4.9 and 4.10, blue and orange curves. For the calculation of  $\delta_{eff}$  the experimental asymptotic values of the heat transfer coefficient (presented in section 4.2.3) were used and a linear approximation of the profile  $h(z)$  was assumed between the temperature measurement positions.

It is found that in all cases, the data lies in between the prediction of our smooth moving wall model and Beattie's post-dryout correlation. The fully turbulent model is the one that gives the best prediction of the data. The results are very satisfying for section V10. For V06, the data approaches the closest the fully-turbulent model for the CHF at T1 (2300 W/m<sup>2</sup>). However, for  $q$  beyond 3000 W/m<sup>2</sup>, the prediction underestimates data. This may be explained by the high void fractions that take place in V06 in most of the section at such high powers (in fact, the last point in Fig. 4.10 has exit quality higher than 1). With a bulk flow that resembles more a foam, or even a mist flow, than a liquid bubbly flow, the assumptions of our model lose validity. Furthermore, the fact that the critical transition at a given position is from NB to IAFB at local CHF does not necessarily imply that, at higher heat fluxes, the flow pattern at the same position cannot change to DFFB. In the part of the section that transits to DFFB, Beattie's model should be more appropriate, thus increasing the integrated friction pressure drop.

## Summary

Experiments were conducted in a two-phase helium natural circulation loop with the objective of studying the transition to boiling crisis in quasi-steady state. The measured temperature evolutions increasing gradually heat flux have allowed determining the critical heat flux at different points on the heated section as well as the evolution of the local temperature before and after the transition as a function of heat flux.

Based on the Katto's CHF transition criteria, we determined that the dryout transition for our experiments is of N or H type, according to the position on the section (H closest to the exit). We conclude that the dryout by liquid deficiency was not observed in our experiments. The mass flux for all CHF events is between 120 to 160 kg m<sup>-2</sup> s<sup>-1</sup>.

The values of CHF predicted by Katto's correlation are in agreement only with the results found for a downstream segment of the heated section. The near entrance region of the heated section presents a CHF anomaly, as a segment of around 30 cm transits to film boiling simultaneously and observed CHF values at the near entrance positions are lower than predicted. This divides the section in three regions according to the CHF behavior (see Fig. 4.8):

- the downstream region: CHF is a function of position between point A and the exit, in agreement with correlations.
- the inaccessible region: the region between points A and B cannot contain the CHF boundary, it is either completely in post-CHF regime or in NB regime and transits to crisis instantaneously with slowly increasing power.
- the upstream region: CHF seems to be gradual again between the entrance and point B.

The multiple behavior could be a consequence of the level of dominance of vapor deposition or liquid entrainment in each segment. Another hypothesis to explain this is the fact that the high conductivity of the tube could make the wall temperature profile spatially unstable, with propagation of the hot zone towards the entrance.

The rewetting experiment revealed that, in resonance with the existence of two CHF behavior zones, there are two different rewetting behaviors:

- If only the downstream region has transited to the post-CHF regime, there is almost no rewetting hysteresis, i.e., the local RHF is only slightly lower than the local CHF and depends on the position, as CHF.
- On the other hand, if the violent post-CHF regime extension has taken place, the rewetting is simultaneous for the inaccessible and downstream regions, and at a lower power than CHF for any position. It is possible that if the test sections were longer, the values of CHF near the exit would be lower than the simultaneous RHF, with which the post-CHF regime would still persist near the exit.

In any case, this means that the presence of film boiling in the upstream region can render stable the post-dryout regime in the downstream region for lower heat flux values.

Measurements of loop mass flow rate and heated section pressure drop simultaneous to boiling crisis onset brought to light a pressure drop lessening effect of the vapor film: a gradual but pronounced decrease in the total friction pressure drop was observed in the heated section with the advancement of the CHF boundary along the section. The natural circulation loop responds to this by increasing appreciably the mass flow rate (between 10 and 15%). The effect

is greater as the dominance of the heated section's friction is higher, thus the highest relative mass flow rate increases were observed for the 6 mm i. d. test section.

The lessening of friction cannot be explained by the already known two-phase multipliers observations in adiabatic helium flow. In a heated tube in IAFB flow regime, the thin vapor film on the wall acts as a very thin layer of lubricant.

A *laminar-equivalent* model based on this idea was conceived and compared to the experimental data, giving satisfactory results for both test sections. The model should be valid as long as the flow pattern corresponds to that of IAFB. Naturally validity is lost at high quality values, where the DFFB regime takes over.

The diameter has a remarkable effect on the behavior of the different contributions of pressure drop. With 10 mm internal diameter, the dominating effect is the reduction of the gravity term with the appearance of vapor, over the increase of friction and acceleration components. With a diameter of 6 mm, the friction force is the dominating term when the system is in the nucleate boiling regime. In NB regime, the predictions of simple traditional models (homogeneous or bubbly flow) have proved to be very satisfactory.

The excitation of the natural circulation loop with a slowly increasing power is the closest possible experimental case to the quasi-static evolution of the system; it constitutes the extreme case where no transient takes place at all. The objective of this work is understanding how the system behaves when the heat load is more dynamic. To bound the universe of possible behavior, it is convenient to study first the response of the system to the most violent excitation (in contrast to the least violent given by the quasi-static evolution). The most violent solicitation possible on such a system is the injection of a sudden power step on the heated section parting from a static initial condition (no power applied). This kind of situation constitutes the object of study of Chapter 5. Later, in Chapter 6, a study of intermediate, more realistic situation will be presented: that on transients initiated by a power step and with non-zero initial heat flux.

## Chapter 5

# Study of stepwise heat load induced transients with static initial condition

The experimental study of the transient response of a system requires applying an excitation and measuring the system response. In order to be able to have an insight of the dynamical properties of the system it is necessary to choose some canonical excitation function. Generally, time functions used for this purpose are step-pulses, ramps, monomial functions, sinusoidal functions or exponential functions, among others. In our study we chose to excite the system with step-pulse functions. This choice is justified from two points of view; first, there is the simplicity to produce the signal experimentally and to analyze the response of the system *a posteriori*, specially for a non-linear system; second, the fact that this function is quite representative of actual heat load incidents in a cooling system.

The steady state experiments described in chapter 4, with very gradual increasing power steps can be regarded as the limiting case of step-pulse induced transients where the initial and final conditions are too close. In this chapter we describe the experiments that represent the opposite extreme: the most violent possible solicitation on the system, that one produced by a heat load step-pulse from an initial static condition to a given final power.

In section 5.1 we present the experimental protocol and an overview of the measured response of the system to excitations of the kind described above of different intensity. In section 5.2 our attention is directed at the initiation of the heat transfer and circulation immediately after the power injection. Subsequently, in section 5.3, attention is concentrated on the analysis of the onset of the boiling crisis, with an accent on the time characteristics of the response. Finally in section 5.4 a detailed study of the identified boiling crisis initiation regimes is put forward and in the case of the most frequently observed regime a criteria to predict its occurrence (incipience and critical time) is defined.

### 5.1 Realization of experiments

The experiments that are object of this chapter were conducted on the natural circulation loop described in chapter 3 using the two vertical test sections V10 and V06. In section 5.1.1 we expose the experimental protocol followed in order to produce the stepwise heat load induced transient. In section 5.1.2 we present several examples of measured time evolution of the system to show an overview of all the phenomena that takes place in different experimental conditions.

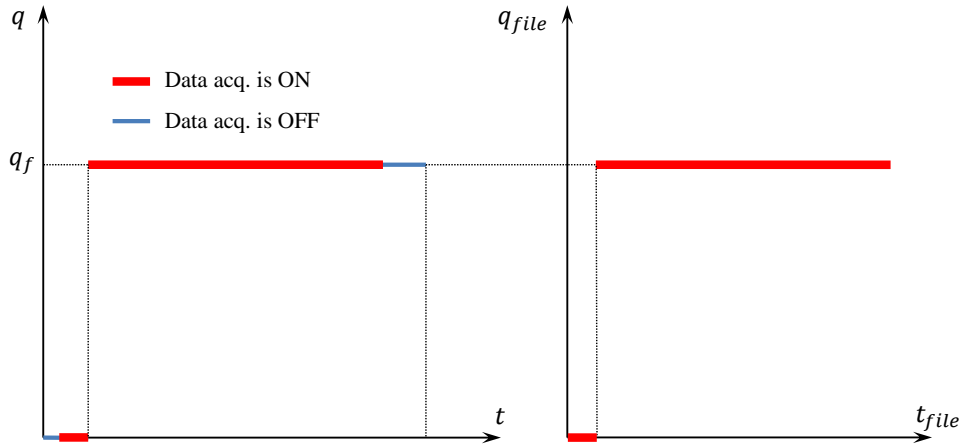


Figure 5.1. Schematic time evolution of heat flux in static initial condition transient experiments.

### 5.1.1 Experimental protocol

As stated above, a choice was made for a stepwise heat load excitation. Thus, a transient will be defined by two parameters: the initial and the final heat fluxes,  $q_i$  and  $q_f$ . In this chapter we are going to consider only cases where the system is *initially at rest*, i.e.  $q_i = 0$ . Thus,  $q_f$  is the *only parameter* defining a transient.

For the measurement of one transient:

1. the system is made to reach steady equilibrium at  $q = 0$ ;
2. data acquisition is started;
3. suddenly  $q = q_f$  is applied in a stepwise manner;
4. a new steady state is reached and data acquisition is stopped;
5. power is reset to 0;

Enough time is let go by (at least 2 minutes) before coming back to step 1 if we want to continue by measuring a new transient. The recording of the initial condition at  $q = 0$  was extremely important in order to correct any systematic offset of the instruments. The time history of heat flux and its acquisition is represented in Fig. 5.1.

The data acquisition chain is the same used for the experiments in steady state, as well as the routines for converting the data files into physical variables (temperature, pressure, mass flow rate, etc.) time evolution files. All further analysis specific to transients is described in this chapter.

The measurements are organized in series formed by transients measured successively. Within each series, the final heat flux at each transient is either increased monotonously, decreased monotonously or neither; this was with the objective of seeing if the history and order of the measurements has an effect on the evolution of the system.

The values of  $q_f$  have been chosen from 0 to as high as  $3000 \text{ W m}^{-2}$  for V10 and  $4000 \text{ W m}^{-2}$  for V06 every  $50 \text{ W m}^{-2}$ . In the ranges where interesting variations of behavior were observed two successive heat flux values can differ by only  $20 \text{ W m}^{-2}$ .

### 5.1.2 Measured time evolution overview

Some examples of measured time evolution of wall temperature and mass flow rate for different values of  $q_f$  is presented in Figs. 5.2 through 5.5. The plots in the figures are organized grouping the temperature evolutions at a given position for different final values of heat flux.

As  $q_f$  increases, substantial changes can be observed in the time evolution of local wall temperature. We can classify the transients according to their behavior regarding boiling crisis. For sufficiently low power, during the whole transient the temperature increase stays in the range that corresponds to the NB regime, typically less than 0.5 K. It is the cases of all the transients represented in Fig. 5.2. We are going to say in this case that the transient is of type ‘*Stable Nucleate Boiling*’ (SNB). At some positions, at a given heat flux, we start to see temperature excursions, where the temperature increase abruptly takes off from the NB values and can go up to several Kelvin. Eventually if power is not high enough, after a certain period of time, the value of temperature falls back to those of NB. The temperature excursion is showing that only temporarily the wall is dry or badly cooled but finally rewetted. In this case, we will talk about a transient of type ‘*Temporary Boiling Crisis*’ (TBC). Finally, if heat flux is high enough, temperature excursions take place without coming back to NB, i.e. the boiling crisis stays in the new steady state regime. These transients will be referred to as of type ‘*Stable Boiling Crisis*’ (SBC).

In the following sections we present the characterization of the different aspects of the transient response in all the regimes.

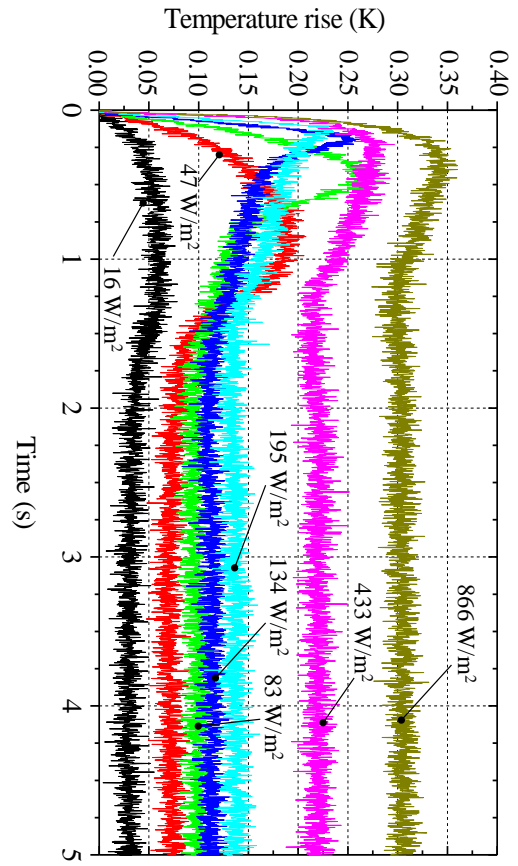
## 5.2 Characterization of the initiation of the transient

Characterizing the behavior of heat transfer and hydraulics immediately after the sudden injection of heat is important in view of the protection of the cooled component. It will determine the detectability of an event and the time scale in which an action needs to be taken. In this section we will analyze how the system responds during the very initial instants of time, trying to identify different heat transfer regimes, what determines them, their interaction and the hydraulic response of the loop to power step pulses. In this analysis we will not consider those cases where there is boiling crisis; that will be the subject of the next section.

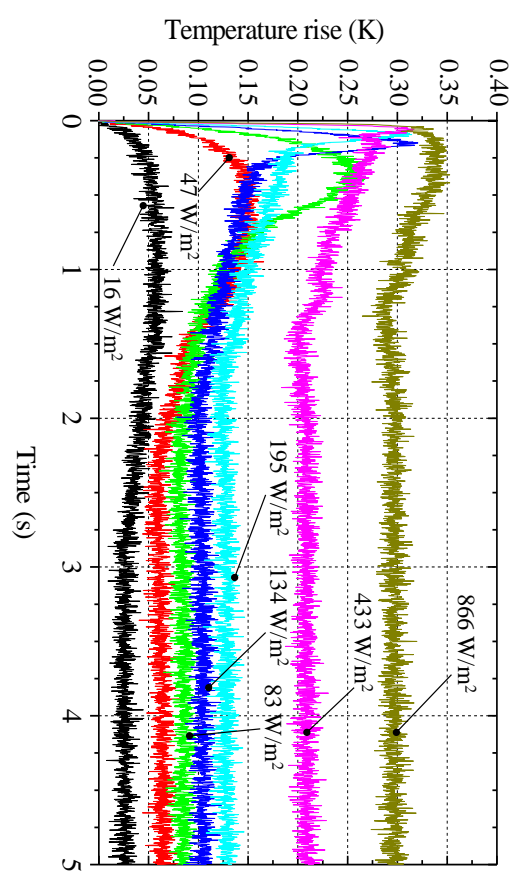
### 5.2.1 Study of the effect of heat flux on time evolution

The typical response of wall temperature to the injection of power at different wall heat flux values for SNB cases is presented Fig. 5.2. The immediate observations that we can make are:

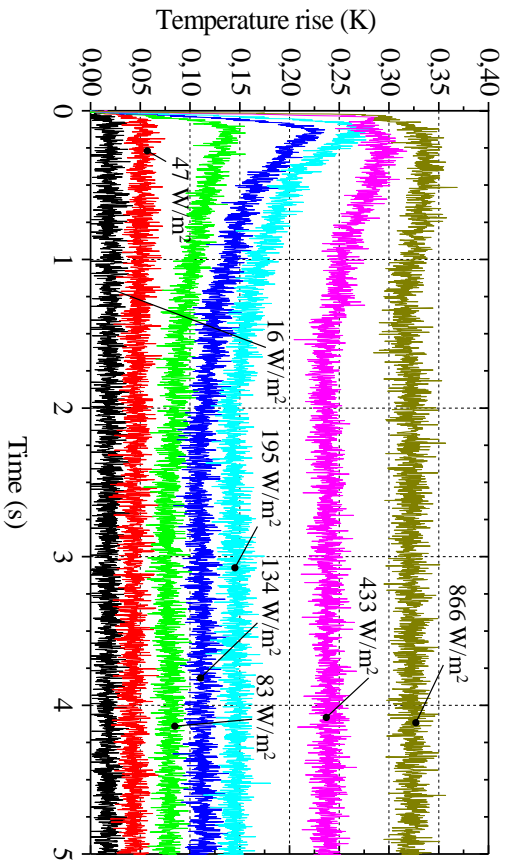
1. the rate of variation of temperature at the initial instant of time increases with increasing heat flux;
2. the final temperature and mass flow rate attained increases with increasing heat flux;
3. the mass flow rate evolution presents damped oscillatory behavior and overshoot;
4. the rise time (duration of the increasing mass flow rate phase) diminishes with increasing heat flux;
5. not only duration and amplitude, but also the shape of the temperature evolution changes with increasing heat flux.



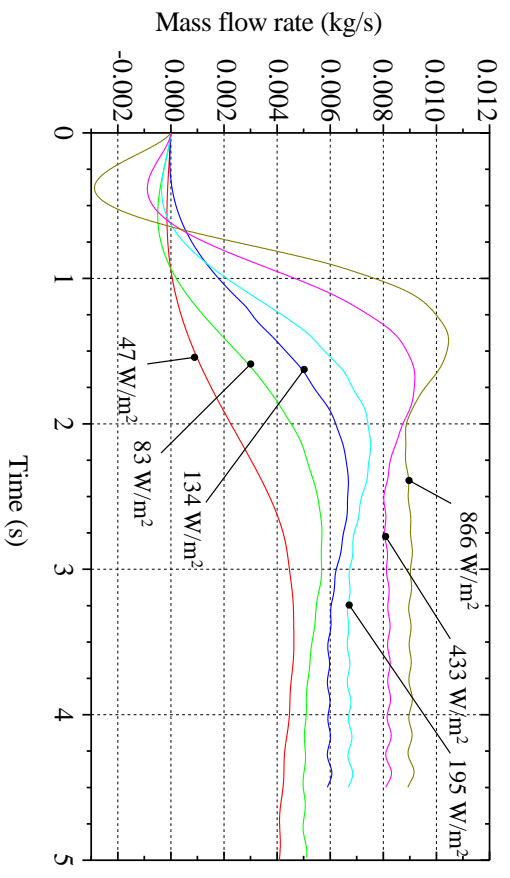
(a) T2 in V10.



(b) T3 in V10.

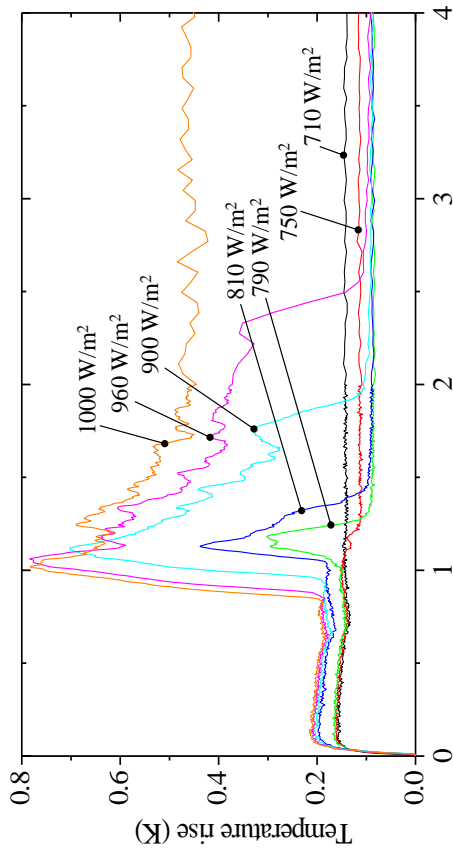


(c) T4 in V10.

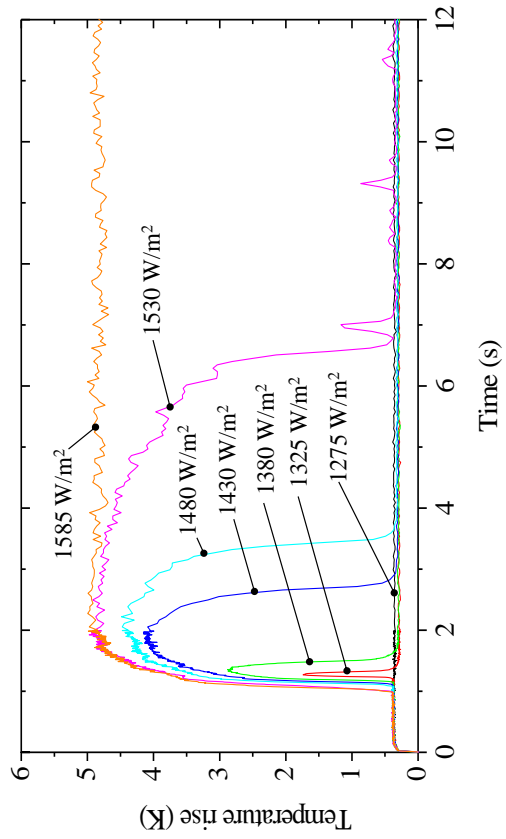


(d) MFR in V10.

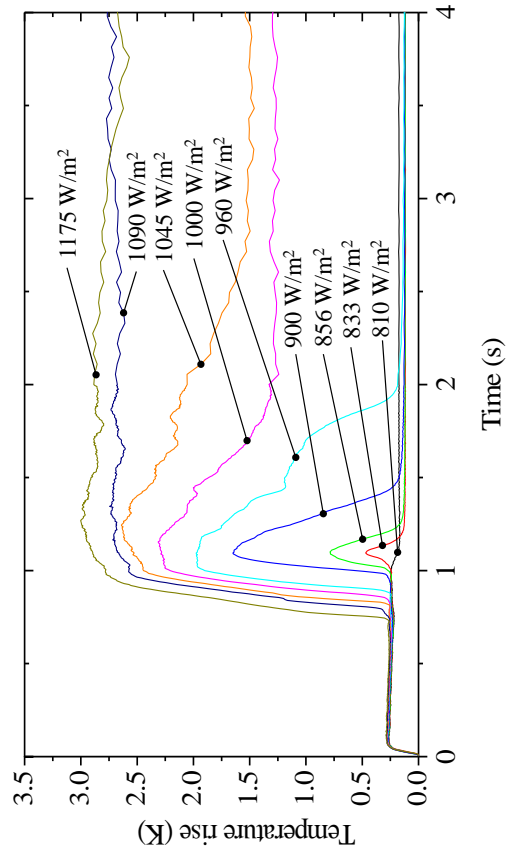
Figure 5.2. Time evolution in static initial condition transients at different values of  $q_f$  (part I).



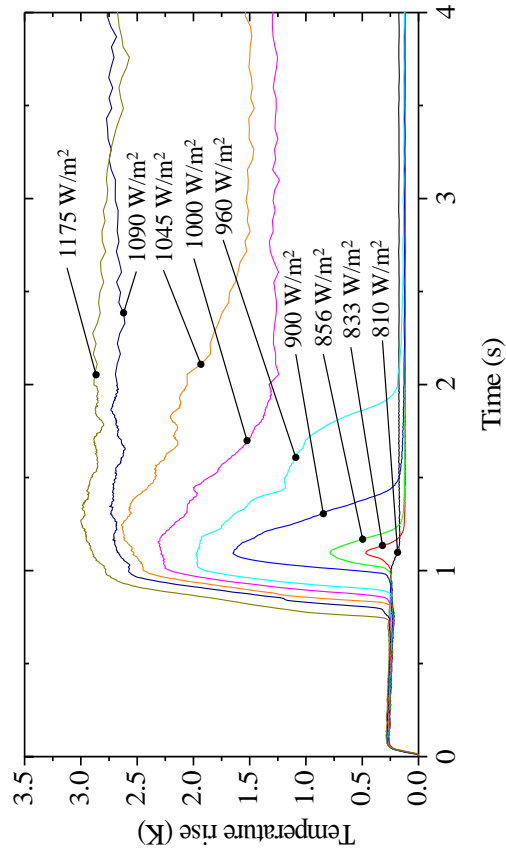
(a) T5 in V10.



(b) T5 in V06.



(c) T4 in V10.



(d) T4 in V06.

**Figure 5.3.** Time evolution in static initial condition transients at different values of  $q_f$  (part 2).

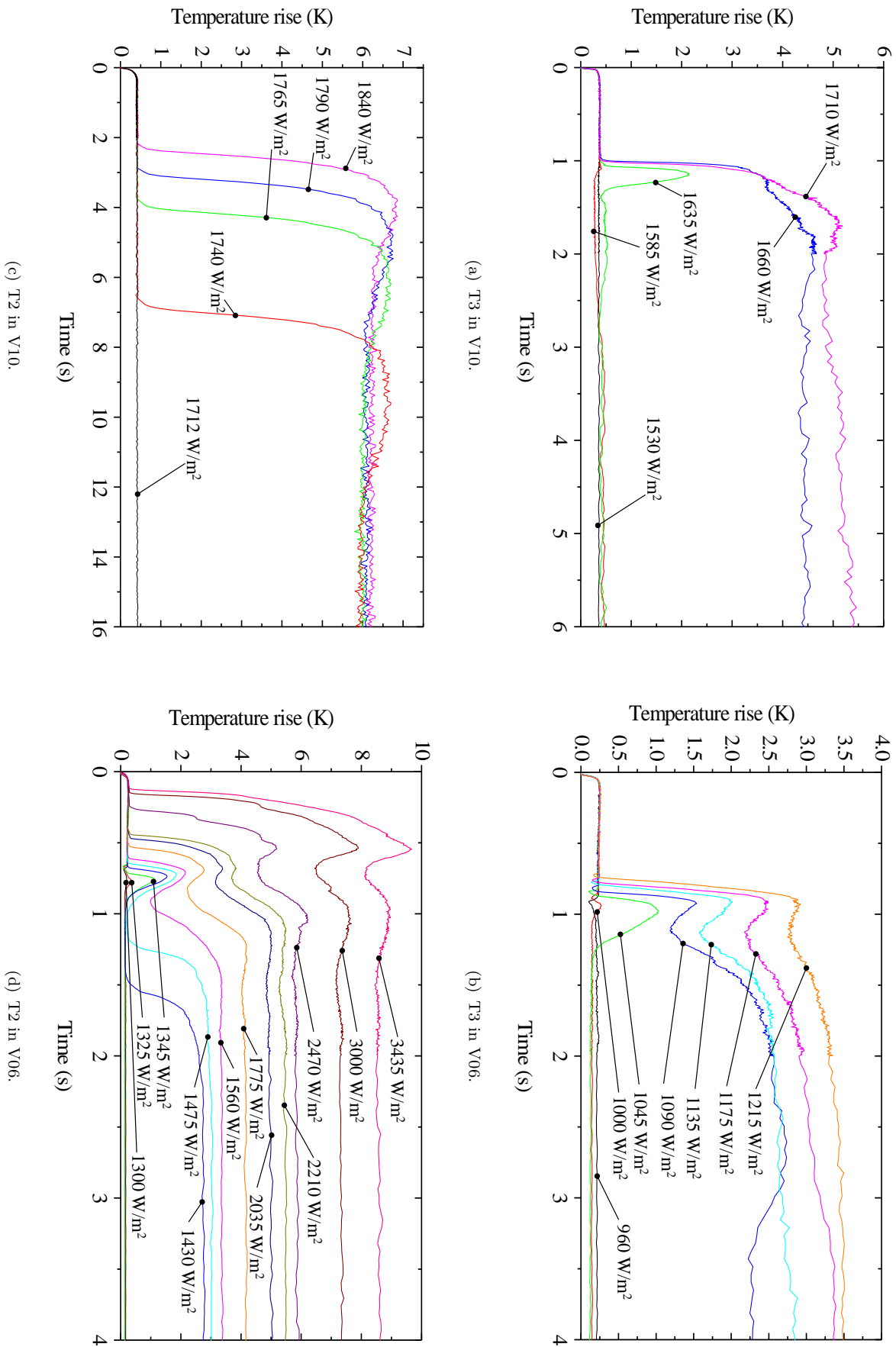
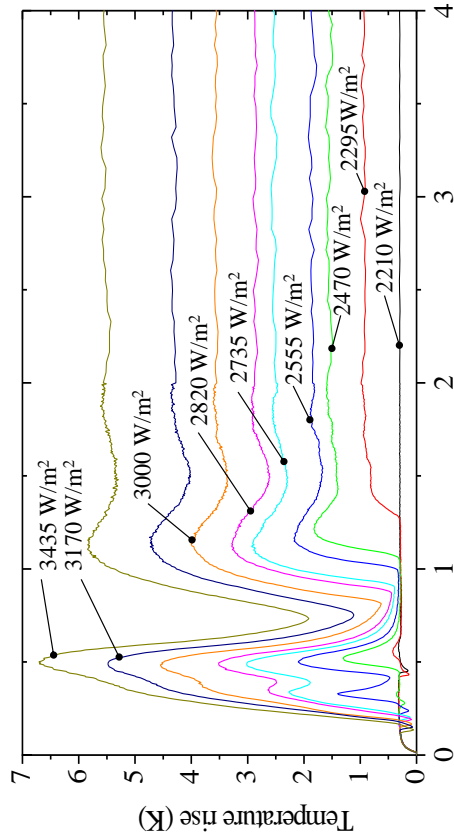
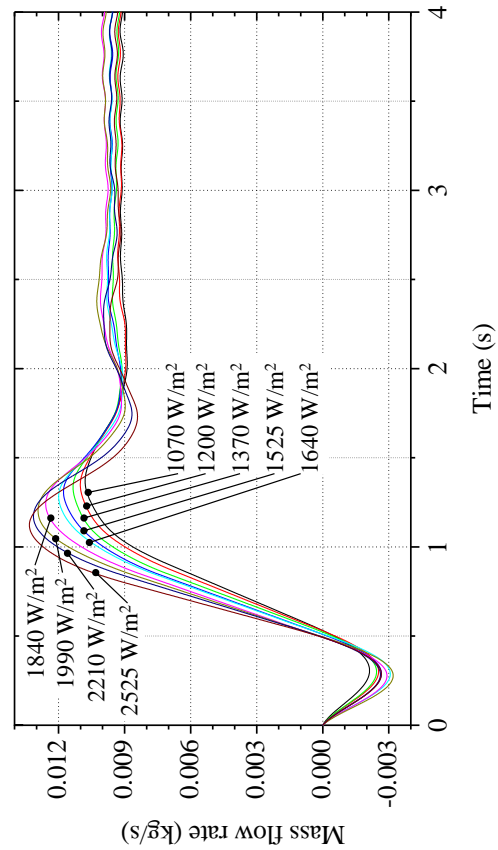


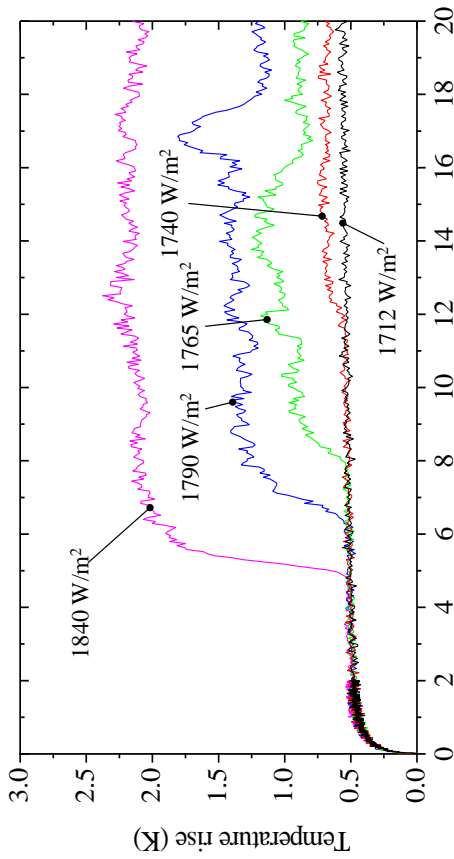
Figure 5.4. Time evolution in static initial condition transients at different values of  $q_f$  (part 3).



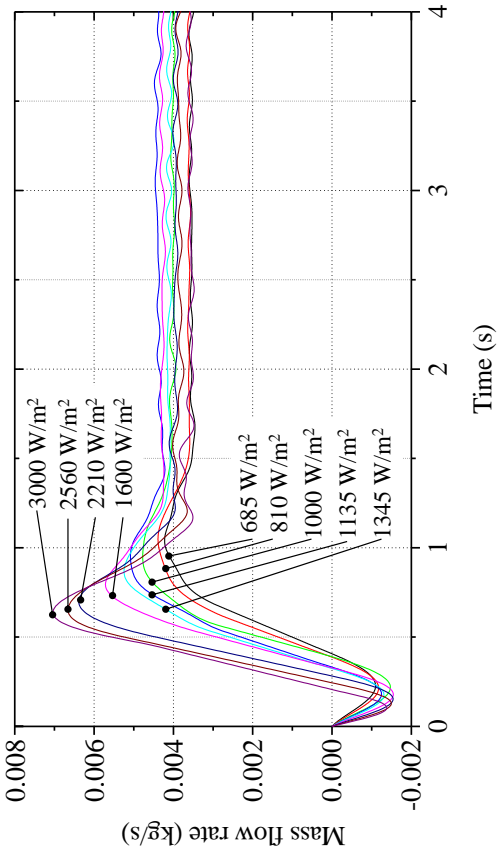
(a) T1 in V10.



(b) Mass flow rate in V10.



(c) T1 in V06.



(d) Mass flow rate in V06.

**Figure 5.5.** Time evolution in static initial condition transients at different values of  $q_f$  (part 4).

The first two points are expected. However, the other points reveal the nature of the dynamic system. The oscillatory feature of the mass flow rate shows that, during the very initial phase, friction is not dominant among all the forces acting on the fluid of the loop. The fact that the time constants of the system (rise time, damping rate, oscillation frequency, etc.) depend on the applied power highlights the strong non-linearity of the dynamics<sup>1</sup>. This non-linearity has two origins:

- The non-linearity of the friction and acceleration pressure gradients with velocity and density (and other properties);
- The transport terms (terms of the form  $u \frac{\partial \cdot}{\partial s}$ ).

The non linearity of the equilibrium mass flow rate with power is a direct consequence of the first point. The second point is particularly influential on the time response parameters. The quantitative analysis of the mass flow rate evolution is the object of section 5.2.2.

Regarding the temperature evolution, the evolutions at very low power ( $q < 100 \text{ W/m}^2$ ) present a rounded maximum followed by a slight valley before reaching an intermediate final value. At intermediate power ( $100 \text{ W/m}^2 < q < 500 \text{ W/m}^2$ ), a quite fast temperature increase is suddenly interrupted, followed by a sudden decrease of temperature, a slight valley and a settling at intermediate temperature. At high power ( $q > 500 \text{ W/m}^2$ ), the evolution is very fast at the beginning and suddenly a plateau is attained with no appreciable diminution. This behavior brings to light the existence of competing time-dependent heat transfer regimes that react differently to the power value increase. This will be the object of study of section 5.2.3.

### 5.2.2 Characterization of the mass flow rate evolution

One of the objectives of this work is to test to which extent the predictions that can be made for such a system in steady state can give information about the transient behavior. Thus, it is natural that we compare the typical values of variables during the transient regime with those measured in the (quasi-)steady state. Figure 5.6 presents plots of the maximal and the final value of  $\dot{m}$  during the transient and of the quasi-steady values, as a function of heat flux.

The final values, determined as the mean of the mass flow rate signal during one second after all the variables reached a stable value, are essentially the same as those measured in steady state when increasing power. The only range of power where some qualitative differences were observed is the region between 900 and 1400  $\text{W/m}^2$  for V06. In the insert in Fig. 5.6(b) we can appreciate this region in more detail. We recall that the difference in quasi-steady state between the increasing and decreasing power curves was explained by the boiling crisis hysteresis combined with the friction pressure drop lessening produced by film boiling. The final values of the transient seem to indicate that the final state of the test section corresponds to that of boiling crisis. This will be confirmed in section 5.3, where the temperature evolutions are analyzed. The several discontinuities of the  $\dot{m}_f$  curve (at 950, 1025 and 1400  $\text{W/m}^2$ ) may indicate that the boiling crisis spatial extension in the final state is a discontinuous function of heat flux.

The maximal values become appreciably higher than the final value as  $q$  increases. What is remarkable is that even if the final mass flow rate stagnates and decreases, the maximum always increases. This highlights that the forces that limit the growth of stable mass flow rate do not have the same importance during the initial transient stage. In the following paragraphs we will analyze this stage.

---

<sup>1</sup>In a linear system those time response parameters are constants of the system and the response is proportional to the excitation.

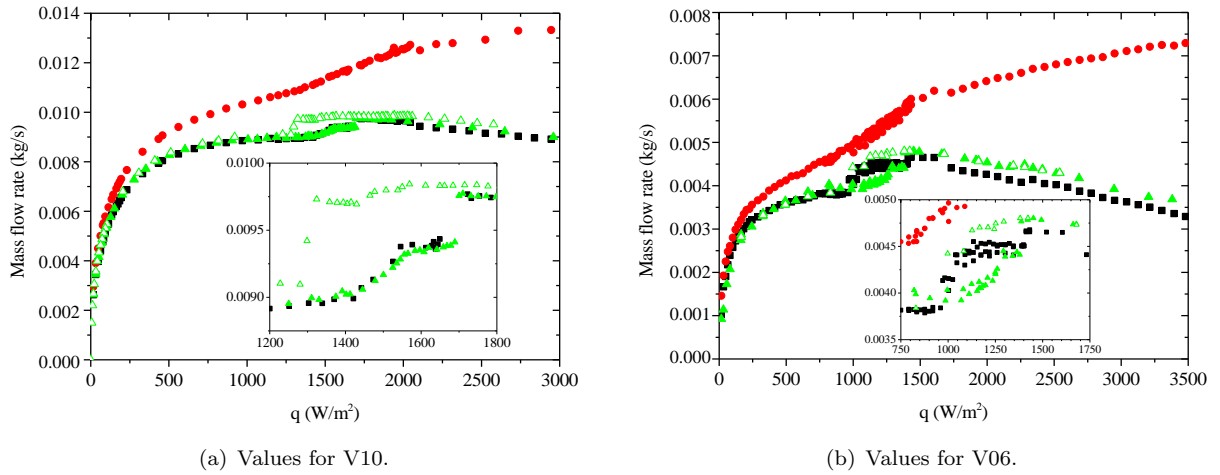


**Figure 5.6.** ■ *Final value*; ● *maximum*; ▲ *quasi-steady increasing power*; ▽ *quasi-steady decreasing power*.

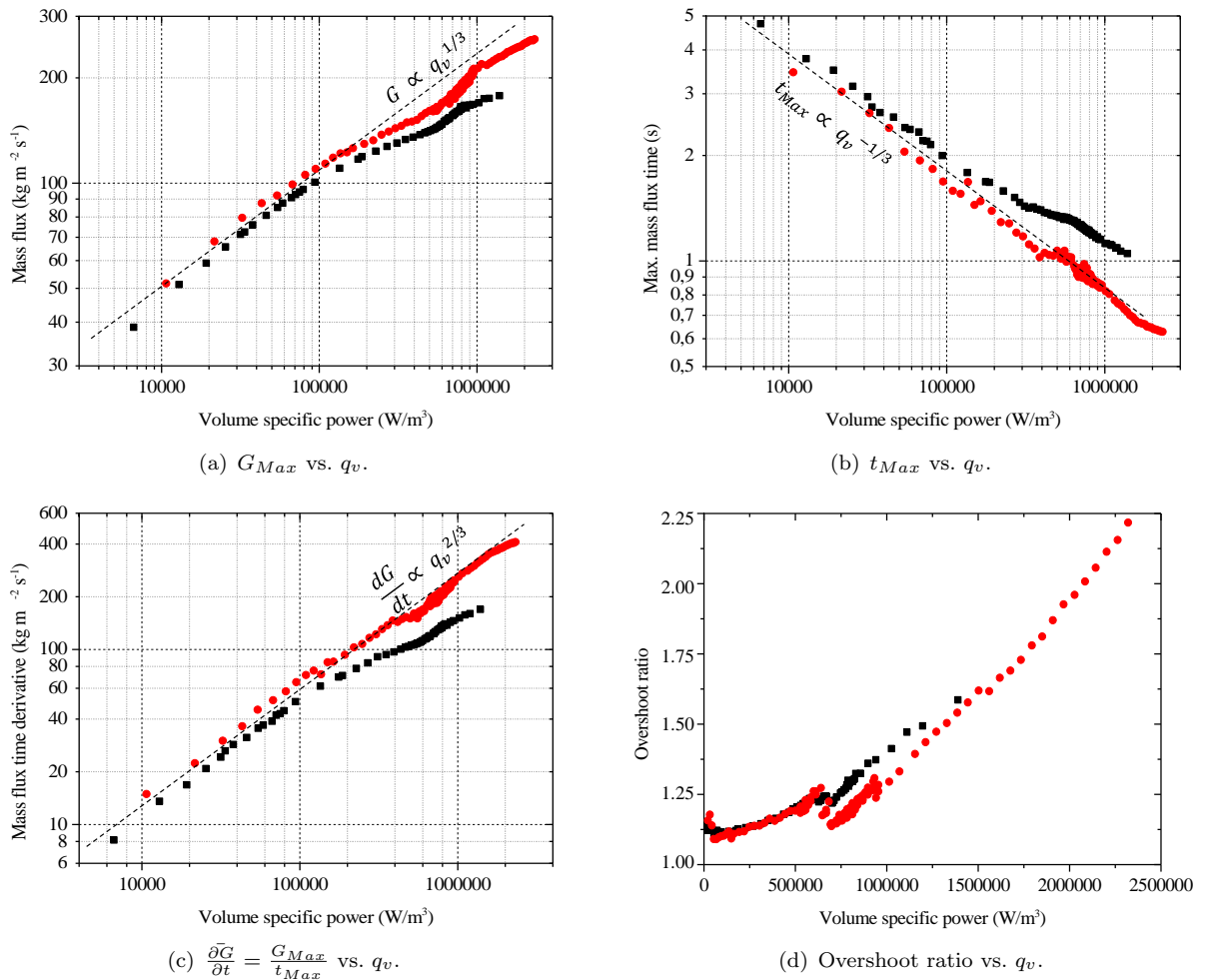


**Figure 5.7.** Quantitative analysis of the instantaneous hydraulic response. ■ V10; ● V06.

It has been noted that the hydraulic response of the system is faster when the applied power increases. The overshooting response of the system is a consequence of the competition of two phenomena with different time lags:

- the diminution of density on the heated section, which produces a gradual acceleration of the system;
- the transport of vapor towards the exit and the entrance cold liquid through the inlet, which increases the mean density, thus, reducing the driving force.

The time lag of the first process is ruled by the system's mass and the buoyant forces; the time lag of the second, by the transport time of the particles to the exit of the system.

During a stepwise power injection transient on a pipe filled with a saturated liquid, the first response of the system is a sudden pressurization due to the instantaneous internal energy ramp at constant specific volume. If the ends of the pipe are open, this will finally result in the expulsion of mass through the ends and a depressurization and fluid expansion wave will travel from the ends to the center of the pipe. After this phase, lasting approximately the transit time of the sound wave, the fluid is at saturation again and changing of phase; a stable expansion (with the consequent density diminution) ruled by the amount of power and the latent heat takes place. During this phase the fluid is going out of the pipe by both ends. In this condition, the evolution of the thermodynamic properties is spatially uniform inside the heated section. We will call this stage *uniform-quality*. If gravity is present and the pipe is vertical, a continuous diminution of the column weight will be observed. In a natural circulation loop, this will accelerate the flow upwards. This will produce the entrance of particles that are below, outside the heated section, and thus with lower thermodynamic quality than those that were previously there. This stage will be referred to as *non-uniform-quality* or *cold front stage*. We can divide the particles present in the heated section into three categories:

- those that have been in the section since the beginning and never left it;
- those that were in the section at the beginning, but have been expelled by the bottom before the flow was established, after which they went through the section again.
- those that were not in the section at the beginning, but below it.

The particle that was exactly at the entrance (let us call it particle 1) at the beginning separates the last two categories. The first two categories are separated by the particle that was at the inlet of the section at the instant when the inlet velocity becomes positive (let us call it particle 2). During the period of time before particle 1 reenters the section, the particles in the first category have been heated (with the consequent expansion), while the ones in the last category have not at all. Thus, the entrance of particles in the third category represents a cold front, in the sense that these particles have a significantly lower amount of internal energy, and a significantly higher density, than those in the first category. Furthermore, all the particles in the first category have been inside the section the same amount of time, while those in the third category have not. Thus, the region occupied by the first category presents uniform density, while that occupied by the third category presents a density that decreases towards the exit but higher than in the other region. The traveling of this front towards the exit, moving at the local velocity of particle 1, produces a gradual diminution of the buoyant force.

To simplify the analysis, let us assume that the mass flow rate reaches its maximum approximately at the moment when the particle 1 exits the riser. This choice is founded on the fact that at this moment the uniform-quality stage is certainly over; the density profile does not present anymore the low uniform density region and, as a result, the driving force of the flow diminishes abruptly. Additionally, we assume that during this period of time:

- the velocity of the two-phase mixture can be represented by a uniform value on the whole section;
- the impact of friction and acceleration forces is negligible;
- the density variations can be approximated as a linear function of mass quality (defined as the mass fraction of vapor in the two-phase mixture);
- the mass quality is uniform along the section and evolves linearly in time.

The first three assumptions increase their validity as heat flux approaches 0. The uniformity of mass quality is not exact because of the cold front entering the bottom of the test section, but is quite accurate for the segment of the section that has not been reached by this cold front. We will see below that the cold front will not move significantly along the section until velocity reaches significant values, thus the uniform quality assumption will remain accurate for a considerable period of time.

The evolution of the inlet mass flux  $G$ , which is ruled by the buoyant term in the absence of the other forces, can then be approximated as:

$$\frac{\partial G}{\partial t} = C_{G,x} x(t) = C_{G,q} q t. \quad (5.1)$$

The constants  $C_{G,x}$  and  $C_{G,q}$  contain all the geometrical and fluid properties information that ensures the validity of the equation. Thus,

$$G = \frac{C_{G,q}}{2} q t^2. \quad (5.2)$$

The transit time  $\tau$  of a particle from the inlet of the heated section to the exit of the riser is given by:

$$L = \int_0^\tau u(t) dt, \quad (5.3)$$

where  $L$  is the distance between the two points. As  $G = \rho u$ ,

$$\begin{aligned} \rho L &= \int_0^\tau G(t) dt = \frac{C_{G,q}}{6} q \tau^3 \\ \tau &= \left( \frac{6\rho L}{C_{G,q}} \right)^{1/3} q^{-1/3} \end{aligned} \quad (5.4)$$

Thus, from our assumption, the rise time of the transient diminishes with  $q$  with a  $-1/3$  power law. The fact that the position of this particle evolves as  $t^3$  reinforces the validity of assuming a uniform quality profile. The particle will stay close to the exit for a significant amount of time before traveling very fast to the exit. The non-uniform quality stage will be comparatively short. The maximal value of mass flux attained is

$$\begin{aligned} G_{Max} &= \frac{C_{G,q}}{2} q \tau^2 \\ G_{Max} &= \frac{C_{G,q}}{2} q \left[ \left( \frac{6\rho L}{C_{G,q}} \right)^{1/3} q^{-1/3} \right]^2 \propto q^{1/3}. \end{aligned} \quad (5.5)$$

The mean value of the time derivative of  $G$  is

$$\left\langle \frac{\partial G}{\partial t} \right\rangle = \frac{G_{Max}}{\tau} = C_{G,q} q \frac{\tau}{2} \propto q^{2/3}. \quad (5.6)$$

In summary, with the increase of power the diminution of density is faster and more notorious, the mean velocity increases faster, but that reduces the transport time of any point of the loop towards the exit of the riser. As a result, the density effects are more intense but over a shorter period of time.

We have determined from the experimental data the maximum value of the mass flux,  $G_{Max}$ , and the time at which it happens,  $t_{Max}$ . Figure 5.7 shows plots of these quantities as a function of the volume specific power,  $q_v = \frac{4q}{D}$ . Despite all the simplifications of our previous analysis, the power laws presented in Eqs. (5.4) through (5.6) have been found. This confirms that the sudden and significant reduction of density, suddenly wiped away by colder particles, explains the observed overshoot. Furthermore a plot of the overshoot ratio, defined as  $\frac{G_{Max}}{G_f}$  is included too. Not only do we see that the power laws are quite accurate, but also we can appreciate that the plotted parameters depend little on the diameter of the test section when the independent variable is  $q_v$ . This indicates that this phenomenon is highly dominated by the evolution of cross section bulk properties. We attribute the small difference between the two test sections to the fact that section V06 is 11% longer than V10, which produces a higher buoyant drive. There is a slight depart of the data from the derived law when the heat flux starts being considerable. At this point, the homogeneity of  $G$  along the section and the linear relation between density drop, quality and time are lost, or the friction and acceleration forces start to be considerable even in this phase of the transient due to the high velocities reached. Very marked inflections of the curves are observed at the onset of boiling crisis, presumably due to the friction effects of the wall vapor film discussed in chapter 4.

A more detailed, mathematically accurate and complete description of these two initial stages will be given in the oncoming sections, as it will be necessary for the understanding of the transient onset of boiling crisis.

### 5.2.3 Characterization of heat transfer during the initiation of boiling

Previous research on transient boiling has highlighted the different stages that the wall temperature evolution goes through in the case of a sudden power injection. As stated and experimentally shown in Ref. [71], it is expected that at the very beginning of the transient, if the coolant is static, the only heat transfer mechanism available is solid conduction into the liquid. The time evolution of wall temperature results from the thermal coupling of the heater and the fluid. As long as convection currents or boiling are not available, the wall temperature should behave as predicted by the solution of the conduction equations.

In order to know at what point the enhanced heat transfer mechanisms (convection and boiling) set on, it is necessary to model the conduction transient. Fortunately, it is not necessary to solve the problem for each specific heat flux, given the linearity of the system of equations. The solution is determined except for a multiplicative constant, the heat flux.

#### Modeling of the conduction heat transfer stage

The dynamics of temperature distribution in each material responds to the Fourier equation

$$\frac{dT}{dt} = -\alpha \nabla^2 T, \quad (5.7)$$

where  $\alpha$  is the thermal diffusivity of the material and  $T$  the local temperature.

The value of thermal diffusivity of a material can give us an idea of the time it can take to a certain input of punctual energy to diffuse a certain distance. Usually,

$$\alpha = \frac{L^2}{\tau}, \quad (5.8)$$

where  $L$  is the distance and  $\tau$  the order of magnitude of the time it takes for this process to take place. Let us assume a fixed value of  $L$  in order to compare materials. Thus,

$$\frac{\tau_1}{\tau_2} = \frac{\alpha_2}{\alpha_1}, \quad (5.9)$$

with indexes corresponding to different materials to be compared.

In the system that interests us, there are three main components that draw our attention:

- the helium in the cross section of the heated tube;
- the copper composing the heated tube;
- the material for gluing the heating wire (some epoxy variety).

Typical values of thermal diffusivity for these three type of components near 4.2 K have been found to be [21] (in m<sup>2</sup>/s)

$$\alpha_{He} = 4.8 \times 10^{-8}, \quad \alpha_{Cu} = 1.07, \quad \alpha_{Epoxy} = 10^{-5}. \quad (5.10)$$

Diffusion times, as compared to those in helium, are:

$$\frac{\tau_{He}}{\tau_{Cu}} \approx 2 \times 10^7, \quad \frac{\tau_{He}}{\tau_{Epoxy}} \approx 2 \times 10^2. \quad (5.11)$$

These values tell us that temperature inhomogeneities in copper and epoxy fade away in a time scale a few orders of magnitude smaller than that in helium. This consideration is very useful for simplifying the model. We can consider a conduction model where the temperature in copper and epoxy is uniform (lumped capacitance model), while it has a spatial distribution in helium in accordance to Eq. (5.7).

The lumped capacitance model is a 0-D model of the time evolution of the temperature of a body. The whole body is assumed to have a uniform temperature at all times. The internal source is the heat produced by the electric heater and the sink is the heat transferred to the fluid. If we represent the epoxy glue with index  $g$  and copper with index  $Cu$ :

$$(M'_g C_g + M'_{Cu} C_{Cu}) \frac{dT_w}{dt} = \left( q'' - \underbrace{k_{He} \frac{\partial T}{\partial r} \Big|_{r=D/2}}_{\text{heat flux to He}} \right) \mathcal{P} \quad (5.12)$$

$$\frac{\partial T}{\partial t} = -k_{He} \frac{1}{r} \frac{\partial}{\partial r} \left( r \frac{\partial T}{\partial r} \right) \quad (5.13)$$

where  $M'$  is the mass per unit length of tube,  $C$  is the specific heat of each material and  $T$  gives the temperature profile in the liquid. The appropriate boundary conditions are:

$$\text{at } r = D/2 \quad T = T_w, \quad (5.14a)$$

$$\text{at } r = 0 \quad \frac{\partial T}{\partial r} = 0. \quad (5.14b)$$

It is possible to show by solving a case that the solution  $T_w$  of this problem has a behavior in two stages:

- At the beginning of the transient,  $k_{He} \frac{\partial T}{\partial r} \Big|_{r=D/2}$  is negligible on the RHS, thus  $T_w$  is a linear function of time.

- At a certain point, the previously neglected term becomes comparable to  $q''$  and eventually dominant, and the evolution of  $T_w$  is dominated by the diffusion process in the liquid.

The second stage is well described by the problem of a semi-infinite solid with constant heat flux at the boundary, as long as the penetration depth stays much smaller than the internal radius of the tube. The wall temperature evolution in that case evolves proportionally to  $\sqrt{t}$  [42].

The amount of glue present on the external wall of the tube is an undetermined parameter. An analysis assuming that there is a 0.2 mm thick layer of glue on the wall, shows that the first stage of the transient should last around 1 or 2 ms. Even if the thickness of the layer were 1 mm, the duration of this stage would not exceed 10 ms.

Another aspect of the temperature measurement that needs to be taken into account is the time response constant of the temperature sensor. The manufacturer reports a 15 ms and 400 ms time constants for SD and AA sensors, typically. For this reason we should not expect that the measured signal to be able to follow a  $\sqrt{t}$  wave function at the very initial instants of time, given its extremely fast varying feature.

### Determination of the pure conduction phase

We inspected the temperature evolution curves presented in Fig. 5.2 in order to find segments of the temperature evolutions that grow as  $\sqrt{t}$ . In Fig. 5.8 the temperature evolutions are plotted in double logarithmic scale, and dashed lines show the identified segments. At the highest power values, this segment could not be observed, probably due to the slow response of the sensor in the tens of milliseconds range.

We consider that convection and boiling mechanism activate at the point where the measured evolution moves away from the  $\sqrt{t}$  trend line. Those points are signaled with an open circle in Fig. 5.8. It is possible to see that the end of the pure conduction stage happens in two ways:

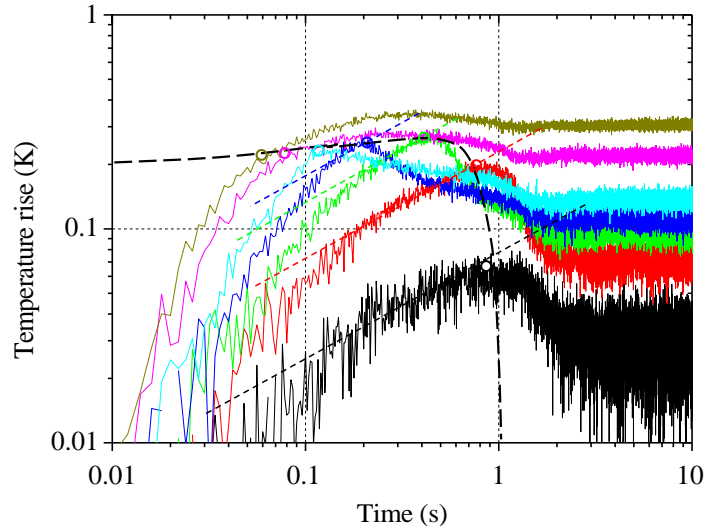
- when a temperature threshold of around 0.3 K is reached (horizontal limit);
- when enough time from the power step pulse has gone by (vertical limit).

The first limit is directly linked with the homogeneous nucleation limit of liquid helium ( $\approx 0.35$  K for helium at 1 atm) [69]. It was determined that in sufficiently fast transients, when this temperature is reached the kinetics of the homogeneous nucleation in the bulk of the liquid becomes practically instantaneous. The liquid cannot exist even in meta-stable state at more than 0.35 K above the saturation temperature. With the resulting appearance of vapor, a great number of the cavities on the surface are filled with vapor. This starts the nucleate boiling regime and stops the temperature increase.

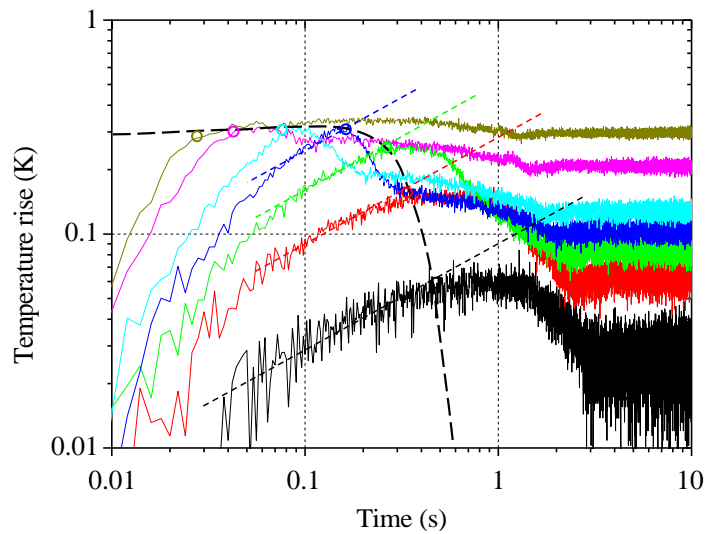
In the second case, as the temperature evolution is slower, the apparition of vapor is possible at lower temperatures, at which the kinetics of nucleation has a time scale comparable to that of the temperature evolution. In this case the amount of time required for the end of pure conduction seems to depend slightly on power or temperature, being longer for lower power or temperature. Furthermore there is a clear dependence of this boundary on the position along the section. The positions closer to the entrance show longer waiting times. This may be linked to subcooling.

### The effect of the onset of natural circulation flow

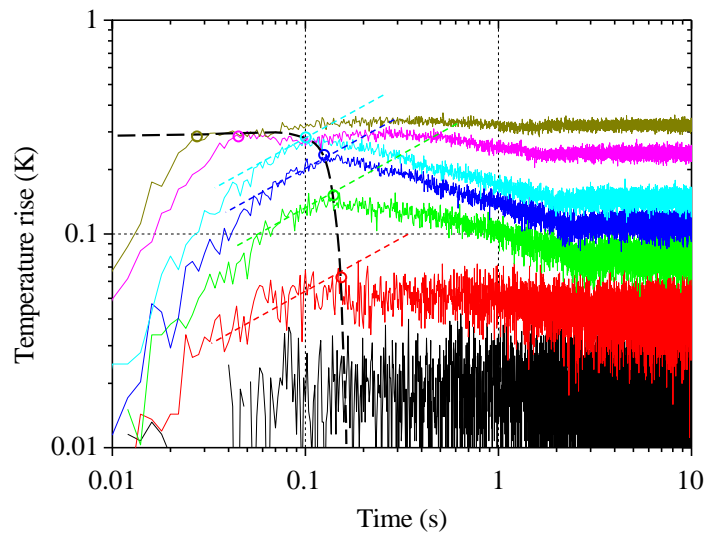
We noticed the existence of a valley on the temperature signals at a time appreciably higher than that corresponding to the end of the pure conduction phase. This valley is particularly visible,



(a) T2 on V10.

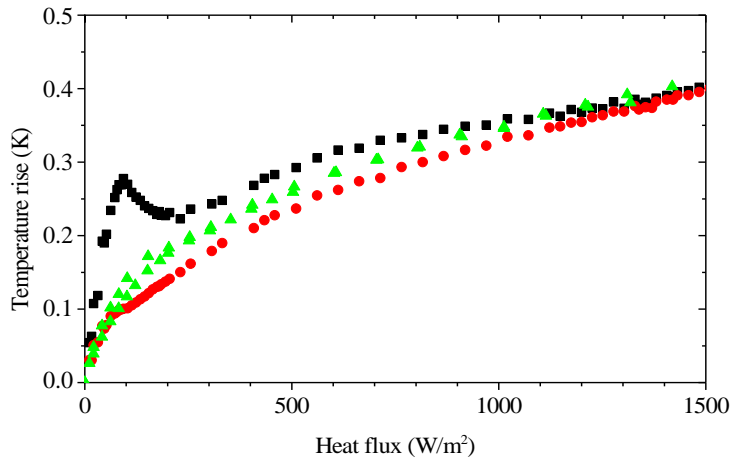


(b) T3 on V10.

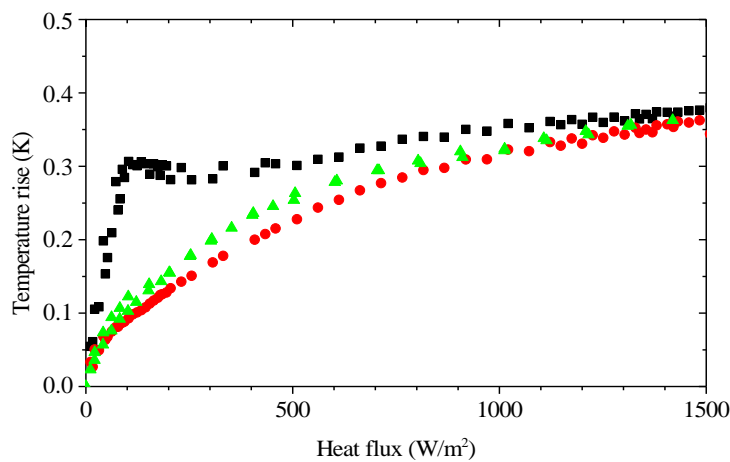


(c) T4 on V10.

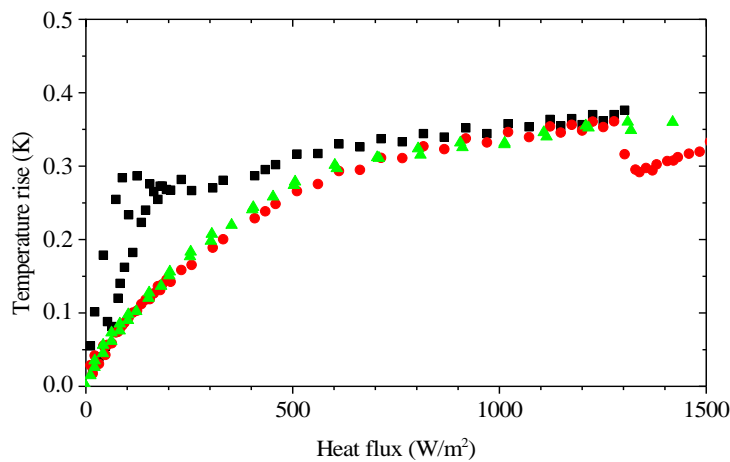
**Figure 5.8.** Determination of the end of the pure conduction phase.  $q_f =$  —  $q_f = 16 \text{ W/m}^2$ ; —  $q_f = 47 \text{ W/m}^2$ ; —  $q_f = 83 \text{ W/m}^2$ ; —  $q_f = 134 \text{ W/m}^2$ ; —  $q_f = 195 \text{ W/m}^2$ ; —  $q_f = 433 \text{ W/m}^2$ ; —  $q_f = 866 \text{ W/m}^2$ .



(a) T2 on V10.



(b) T3 on V10.



(c) T4 on V10.

**Figure 5.9.** Global temperature values during stepwise power transients as a function of the applied final heat flux. ■ Maximum temperature; ● final temperature; ▲ data measured in quasi-steady increasing power progression.

for example, at powers lower than  $134 \text{ W/m}^2$  and time of more than 2 s (see Fig. 5.8) but is present in all cases. The point identified as the end of the conduction stage represents in these curves a point after which a sudden temperature drop is observed, attributed to the activation of boiling. However, especially in the mentioned cases, a second temperature drop is observed in the time scale of the second. This temperature diminution is directly correlated with the apparition of significant values of mass flow rate (see the evolutions in Fig. 5.2(d)). The temperature drop is observed earlier at the bottom of the test section than at the top, which indicates that the effect is dominated by transport of a cold front from the entrance. This enhances heat transfer by wiping away the accumulation of vapor that takes place in the initial phase.

### Relation between transient and steady state temperatures in NB regime

In Ref. [70] it was argued that the homogeneous nucleation limits is by no means the wall superheat limit in nucleate boiling. The homogeneous nucleation imposes a temperature limit to the existence of the liquid phase. However, the wall in contact with that liquid is also partially covered by vapor, and its temperature fluctuates in time and space. The measured value is a time-space average. As vapor can be hotter than the nucleation limit, the stable nucleate boiling temperatures can be higher than the homogeneous nucleation temperature. Figure 5.9 shows the maximum and final measured temperatures during stepwise power transients as a function of the final heat flux as well as the stable temperatures measured in the quasi-steady power increase. The final temperature behaves much as the quasi-steady nucleate boiling temperatures, a trend which is quite close to  $T \propto q^{1/2}$ . On the other hand, the maximum temperature

- increases linearly with heat flux at low heat flux (lower than  $100 \text{ W/m}^2$ ),
- exhibits a clear plateau when the value of 0.3 K is attained (at around  $100 \text{ W/m}^2$ ),
- follows the trend of final temperature when final temperature becomes comparable to (and then higher than) 0.3 K.

The values of  $q$  at which the maximum temperature starts overcoming the plateau coincide naturally with those during which the reaching of 0.3 K does not produce a peak followed by a sudden decrease but just a sudden stop of the fast temperature growth immediately followed by a much slower increasing trend. At very high power the final value is substantially the same as the maximum value.

We draw the attention to the fact that the final temperature values measured in transients is somehow lower than the ones measured in quasi-steady power increase. This is the result of the temperature history: before becoming steady, wall temperature exhibits significantly higher values. This can produce additional activation with respect to the case in which temperature increases monotonically and slowly to its final value. The NB hysteresis has been observed before in many fluids and, in particular, in helium on normal metallic surfaces [64]. This effect is remarkably reinforced in the cases above  $1300 \text{ W/m}^2$  for T4; this is because, as it will be seen in the following section, boiling crisis takes place during the corresponding transients and the maximum overheating is in the order of a few K degrees.

## 5.3 Characterization of boiling crisis during transients

The description in section 5.1.2 highlights that there are key values of heat flux that limit the different types of behavior regarding transient boiling crisis (SNB, TBC and SBC), in the same manner as CHF in steady states separates nucleate and film boiling. In the following paragraphs

we will describe the experimental observations of the different type of transients at each position for each test section, define the heat flux limits at which the different regimes were observed, and describe quantitatively the time features of transient crisis onset.

### 5.3.1 Determination of transient critical heat flux

We are going to define the *transient CHF* as the heat flux necessary to observe any kind of boiling crisis during the transient. As observed in Figs. 5.3 through 5.5, for temperature sensor locations T3, T4 and T5 on both test sections and T2 in section V06 the three types of transient (SNB, TBC and SBC) have been observed. Thus, for these locations, the  $q_f$  scale can be divided into three segments, one corresponding to each of these types of behaviors. For  $q_f$  lower than a given value of heat flux that we are going to call  $q_{c,t}$  (temporary crisis transient CHF) the transient is of type SNB. For  $q_f$  between  $q_{c,t}$  and  $q_{c,p}$  (permanent crisis transient CHF), the transient is of type TBC. For  $q_f$  above  $q_{c,p}$ , the transient is of type SBC. In these cases, the transient CHF is  $q_{c,t}$ .

For positions T2 in V10 and T1 in both test sections, the type TBC has not been observed at all. In those cases we can only define one heat flux limit,  $q_{c,p}$ . When  $q_f < q_{c,p}$  the transient is of type SNB, otherwise it is of type SBC. In these cases, the transient CHF is  $q_{c,p}$ .

In table 5.1 we present the found values of  $q_{c,t}$  (when existent) and  $q_{c,p}$  for each test section.

The TBC power interval ( $q_{c,t} < q < q_{c,p}$ ) is greater near the exit of the test section. There is a theoretical point where  $q_{c,t} \rightarrow q_{c,p}$ . This point is between T2 and T3 for V10 and T1 and T2 for V06. It is remarkable that in some cases, the *transient CHF can be appreciably lower than the steady state CHF*. In the case of test section V10 this feature is only observed for  $q_{c,t}$ , but for V06 the SBC was prematurely attained in terms of heat flux ( $q_{c,p} < q_{c,s}$ ) for the downstream positions on the test section (T3 to T5).

Boiling crisis was stable *after a transient* on V06 at a heat flux 20 to 25 % lower than the CHF in the quasi-steady experiment. The reason why this happens on one of the test sections and not on the other is not evident. However, the simultaneous observation of tables 4.1 and 5.1, taking account of the nature of steady state boiling crisis hysteresis depending on to what extent boiling crisis was extended on the test section in the initial condition, can give some understanding.

Temporary boiling crisis is observed in the positions near the point of the sudden extension of boiling crisis in V06 (near T3, towards T2), but not for V10 (near T2, towards T1). We remind the reader that the boiling crisis hysteresis was not observed in quasi-steady state if this sudden extension of boiling crisis had not happened *a priori*. Transients of type SBC can exist prematurely at T3, T4 and T5 on V06 because the value of  $q_{c,t}$  at the sudden extension point is lower than the  $q_{c,s}$  at the downstream positions but higher than the simultaneous RHF.

Unfortunately, a detailed measurement of the rewetting in V06 with boiling crisis from below T2, with smaller power steps was not obtained. It is highly probable that the rewetting is not simultaneous like on V10 but in two simultaneous pipe segments. That would explain why T3 presents a higher  $q_{c,p}$  than T4 and T5. In any case, it is clear that the value of  $q_{c,p}$  at T3 is enough for producing TBC up to a point somewhere between T2 and T3, close to T3. The occurrence of boiling crisis at this point (presumably, the sudden extension point) stabilizes it all downstream, as in the quasi-steady experiment, because  $q_{c,p}$  at T3 (1065 W/m<sup>2</sup>) is higher than the RHF (950 W/m<sup>2</sup>). To confirm this, let us notice that the power values for the simultaneous rewetting of V06 segments, power is between 950 and 1100 W/m<sup>2</sup>, and the values of  $q_{c,p}$  at T3 through T5 are comprised in this range. For this to happen on V10 it would have been necessary that at 1300 W/m<sup>2</sup> (the simultaneous RHF) T2 showed at least TBC; which is not the case.

**Table 5.1.** Transient critical heat flux,  $q_{c,t}$  and  $q_{c,p}$  values in  $W/m^2$ . The numbers in brackets are uncertainties on the last figure(s).

Position	z (cm)	$q_{c,t}$	$q_{c,t}/q_{c,s}$	$q_{c,p}$	$q_{c,p}/q_{c,s}$
V10 T1	3.1	—	—	1730(20)	0.99(2)
V10 T2	24.3	—	—	1730(20)	1.01(2)
V10 T3	47.3	1600(20)	0.97(2)	1640(20)	0.99(2)
V10 T4	71.3	1320(20)	0.85(2)	1540(30)	0.99(2)
V10 T5	92.7	1190(20)	0.83(2)	1425(20)	0.99(2)
V06 T1	3.0	—	—	2270(30)	1.01(3)
V06 T2	27.0	1335(20)	0.97(2)	1400(20)	1.01(2)
V06 T3	52.0	1010(20)	0.73(2)	1065(30)	0.77(3)
V06 T4	76.0	840(20)	0.67(2)	990(30)	0.79(2)
V06 T5	101.0	760(20)	0.64(2)	990(30)	0.83(3)

Thus that premature SBC happens if the boundary of the sudden extension of boiling crisis can show TBC at a power lower than  $q_{c,s}$  in the whole segment of the section that rewets simultaneously. We want to emphasize the independence of the two events. On the one hand, there is a mechanism that allows boiling crisis during the transient at a heat flux  $q^*$  lower than the *local*  $q_{c,s}$  at the sudden extension point and, on the other hand, this value of  $q^*$  can or not be higher than the simultaneous RHF downstream.

### 5.3.2 Identification of interesting time response parameters of transient boiling crisis

In order to make a systematic study of the characteristics of the transient temperature evolution of the system it is necessary to define the most relevant numerical parameters whose variation needs to be analyzed.

As can be appreciated in Figs. 5.3, 5.4 and 5.5, whenever crisis was observed, before the start of the temperature excursion that indicates the drying of the wall, there is a certain period during which the temperature evolution is of the same nature as that of NB regime. During this stage, the system reaches a NB metastable state that lasts a given amount of time that we are going to call *critical time*,  $t_c$ . Once the boiling crisis takes place, the temperature increases to a certain maximum temperature value,  $T_{max}$ . If the transient is of type TBC, after a lapse of time  $t_d$  after  $t_c$ , the temperature decreases abruptly to reach a final value,  $T_f$ . If the the transient is of type SBC, then a parameter like  $t_d$  has no meaning and  $T_f$  is not very different from  $T_{max}$ .

These parameters, in the case of a TBC transient, are represented schematically on a measured temperature evolution in Fig. 5.10.

### 5.3.3 Data treatment for critical transients

Given the very large amount of data to treat (in the order of 400 files with 5 temperature histories each) an automatic approach for determining the transient boiling crisis parameters was developed. Given that the data was originally in TDMS format, the most practical approach was treating the files with an Excel<sup>TM</sup> interface and Visual Basic for Applications (VBA). The conversion from raw voltage data to physical variables has already been explained in chapter 4. Here we are going to focus on how we determined the transient boiling crisis parameters. We

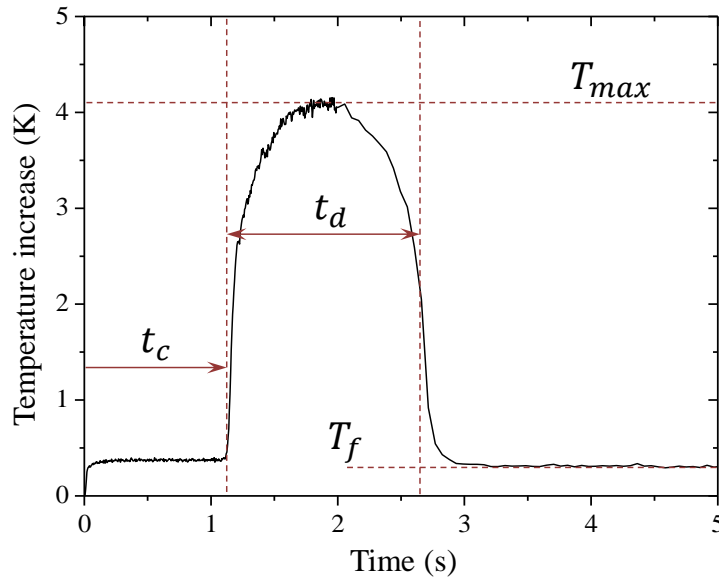


Figure 5.10. Parameters characterizing transient boiling crisis

are not going to give the internal details of the code in VBA, but to describe the algorithms used for determining the values of the parameters. On the five temperature histories the applied algorithm is identical.

### Maximum and final temperature

The search for the maximum temperature is a very simple one: the column containing the temperature history is scanned up to the end comparing each temperature value with the maximum stored so far; if the new read value is higher than the stored, it is substituted for the stored maximum. The final temperature is calculated as the arithmetic mean of the instantaneous values registered during a period of time determined by the user at the very end of the acquisition (or before turning power off). We have used a duration of 1 s for this period of time.

### Critical time and duration of TBC

The search for the critical time is based on a time derivative criteria. There are two stages in the determination of the critical time:

- the determination of a critical temperature excursion event;
- the determination of critical time, given there is an event.

For the first stage, it was required to detect the occurrence of a very rapidly increasing temperature time zone; this can be done by calculating the first time derivative of the signal. In order to determine the maximum derivative point, the numerical derivative was calculated with a centered scheme using a time step of 10 ms, in order to filter the noise of the signal when subtracting adjacent sampled values. The search for the maximum derivative is done with a simple algorithm (as the one explained above for maximum temperature). Once the maximum has been found, it is necessary that all the values in a certain interval around it be higher than a certain threshold value for it to be considered legitimately as indicator of a boiling crisis event. In order to determine the width of the interval and the height of the threshold, we performed tests

on a subset containing very diverse measured data (moderate and high power values), trying to minimize the false detection of events and the lack of detection of true events.

For the second stage, the previous determination of a maximum time derivative helps to limit the research area for the start of the temperature excursion: the takeoff needs to happen no long before it. Thus, the critical time was found as the point at which the second time derivative is maximum, as has been done before [77]. In order to avoid false detection of events, this maximum has to verify too that it be surrounded by an interval where the second time derivative is higher than a given threshold. Again, the interval width and threshold values were tuned by testing on measured data.

The finalization of the temperature excursion in a TBC transient is determined by finding the minimum (negative) time derivative of the temperature with an analogous method above (with a negative threshold).

A temperature threshold criteria was not applied to determine the occurrence of a crisis event because sometimes this temperature excursion can be quite small, and the maximum temperature values can be close to NB typical temperature values. However, the comparison of maximum temperature between successive experiments can help the user discern that the prediction of the algorithm is correct when post-analyzing. In any case, the risk of bad analysis is high only for the marginal cases, near the transient CHF. As there are not many files to analyze in that region, a manual verification of these individual cases is affordable.

### Massive data treatment

The procedure explained in the previous paragraphs is applied to each transient file individually. In order to accelerate the analysis of aggregated data, routines were written to automate

- the individual analysis of the time evolution parameters successively on a specified group of series of files;
- the production of summary files, which group the individual parameter information of each transient by series and contain plots of the evolution of these parameters as a function of some controlled variable (for example,  $q_f$ ).
- the production of comparison files, which group the time evolution of a given variable as a function of time for several cases, and plot it.

Thus the analysis of hundreds of files is reduced to the study of a few summary files. Whenever questions arise on specific case or series (suspicion of erroneous values, for example), the user can always refer to the comparison files or the individual files.

#### 5.3.4 Comparison of transient to quasi-steady temperatures in post-CHF regimes

In the same fashion as we did with the measurements in the NB regime, we present here plots of the maximum and final temperatures of transients as a function of  $q_f$  and we compare them to the values measured by quasi-steady increase and decrease of power. These results are shown in Figs. 5.11 and 5.12.

For both test sections, in the positions that have premature TBC, in the power region  $q_{c,t} < q < q_{c,p}$  the maximum temperature naturally exceeds significantly the final temperature, by an amount that represents the intensity of the temporary temperature excursion due to TBC. The final temperature values are in the NB region and are lower than the ones measured

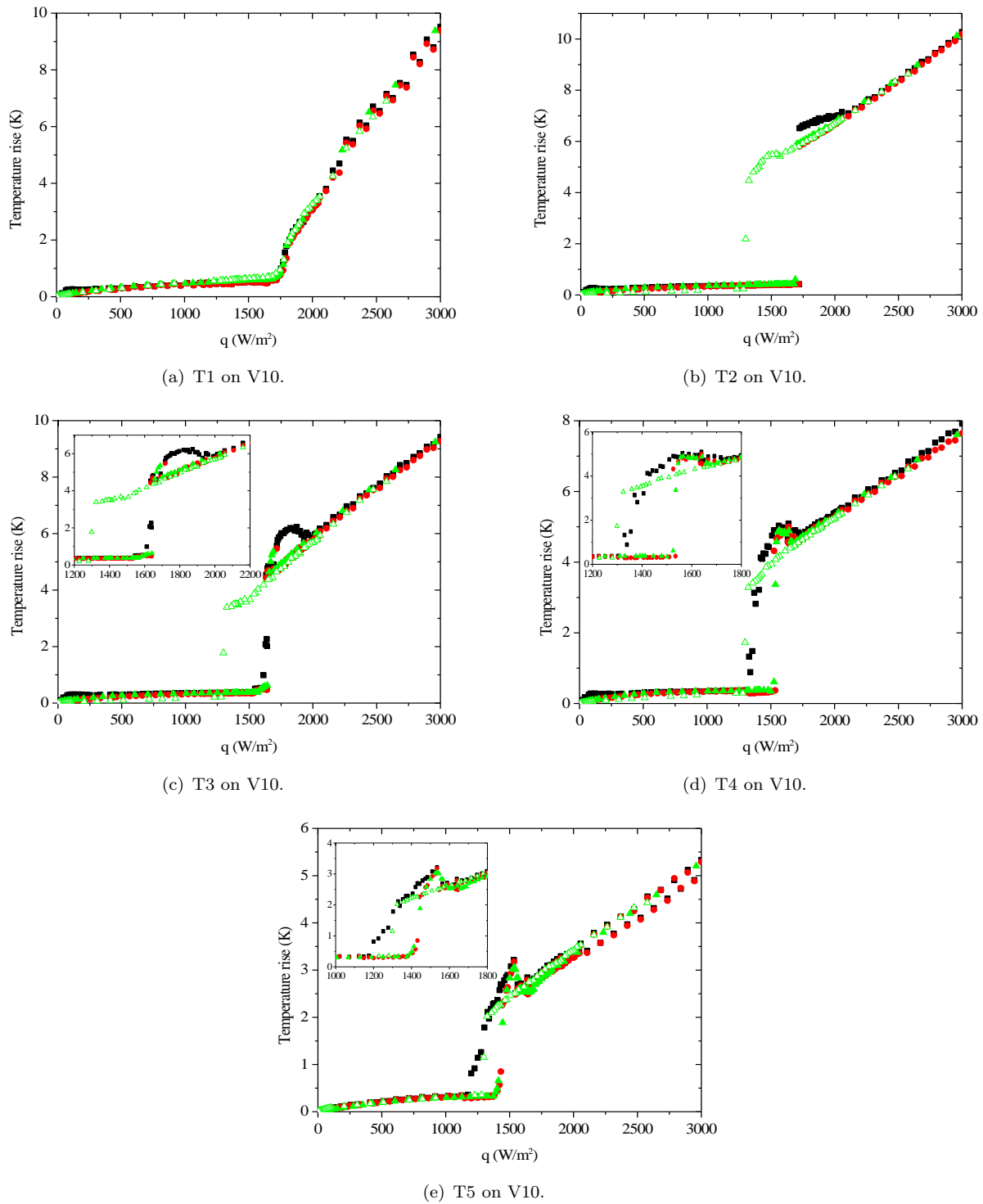


**Figure 5.11.** Temperature maximum and final values compared to those in quasi-steady state, as a function of heat flux for V10. ■ Maximal value; ● final value; ▲ quasi-steady increasing power; △ quasi-steady decreasing power.

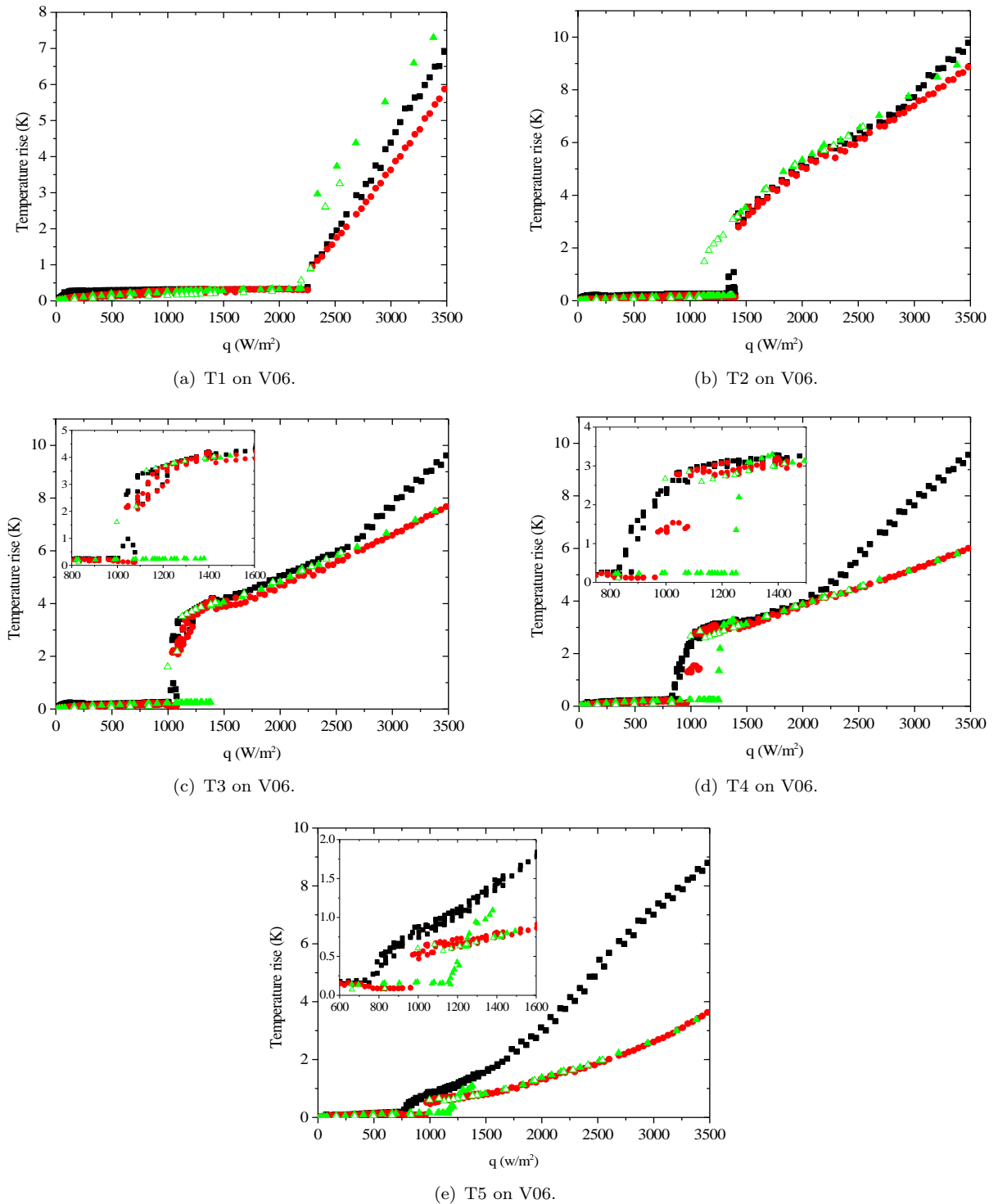


**Figure 5.12.** Temperature maximum and final values compared to those in quasi-steady state, as a function of heat flux for V06. ■ Maximal value; ● final value; ▲ quasi-steady increasing power; ▾ quasi-steady decreasing power.

in quasi-steady power increase. The fact that only momentarily the wall was completely covered with vapor and at high temperature activates, if not fully, to a further extent nucleation sites; thus, when NB takes over again the heat transfer coefficient has been significantly enhanced. This was observed even at the incipient cases, i.e. when  $q_f \approx q_{c,t}$ ; in these cases, even if no temperature excursion was observed, a decrease of the NB temperature was observed at around the same instant of time where the TBC appears visibly for slightly higher powers. It is possible that a non-detectable (fast and narrow) temperature peak is taking place in these cases, with the consecutive NB heat transfer enhancement.

The comparison of final temperature values in the case of SBC to the quasi-steady measurements highlights a fundamental difference in behavior between the two test sections. For V10  $T_f$  is practically equal to the values measured in the quasi-steady increasing power experiments. However, for V06,  $T_f$  is in agreement with the quasi-steady decreasing power experiment values. This observation is in full agreement with the fact that the SBC in V06 is heat-flux- premature for T3, T4 and T5, already discussed in section 5.3.1.

At powers higher than  $q_{c,p}$ , at all positions, the maximum and final values are practically identical for V10. For V06 this is true but only up to a certain power value that depends on the position. That power value is lower for the positions closer to the exit. From this power value on, a difference between maximum and final values starts growing continuously as  $q$  increases. This leads us to look at the temperature evolutions at the 5 positions simultaneously, to understand what happens. In Fig. 5.13 we can appreciate a few cases of how these temperature excursions evolve at increasing  $q_f$  values. In case (a), the temperature peak is only observed at T5<sup>2</sup>, in (b) and (c) we see it develops at T4, in (d) it appears already at T1, T2 and T3, but its value is not yet the absolute maximum of the evolution. In (e), finally, at all the positions this peak becomes the absolute maximum. This temperature excursion is associated with the complete evaporation of liquid in the section. During the initial phase of the transient, the sudden apparition of vapor in the section produces expansion and expels fluid out of it before the natural circulation starts. During this phase the evolution of the system is uniform along the section and the mass fraction of vapor evolves exponentially (as shown in section 5.4.3). When this fraction reaches the value 1, the saturation condition is lost, and significant bulk overheating becomes possible<sup>3</sup>. The time to reach total evaporation has been calculated and it coincides with the instant of initiation of the temperature rise immediately before the peak. On the other hand, the peak is the result of the end of this phase. When circulation starts, fluid particles that have spent less or no time in the heated section during the initial phase can reach the different positions of the section, and as their vapor mass fraction are low, they cool down the wall. A detailed look at the peak times confirms this, as the temperature decrease arrives earlier for the near entrance positions than for those closer to the exit.

### 5.3.5 Determination of the dependence of critical time on heat flux

The existence of a metastable NB stage before crisis has already been observed in other type of boiling experiments [61, 63, 68, 71, 77]. The cited works have shown that its duration  $t_c$  is highly dependent on heat flux, and it is this dependence that we intend to study for channel flow in natural circulation loops.

The critical time data obtained by the algorithms presented in section 5.3.3 is plotted as a function of final heat flux in Fig. 5.14.

---

<sup>2</sup>The peak at T2 is not associated with the phenomenon we are studying here, but with the onset of bulk-dominated boiling crisis, exposed in upcoming sections.

<sup>3</sup>In fact, when liquid is present vapor can be at a higher temperature (non-equilibrium boiling), but difficultly this difference can be of several K.

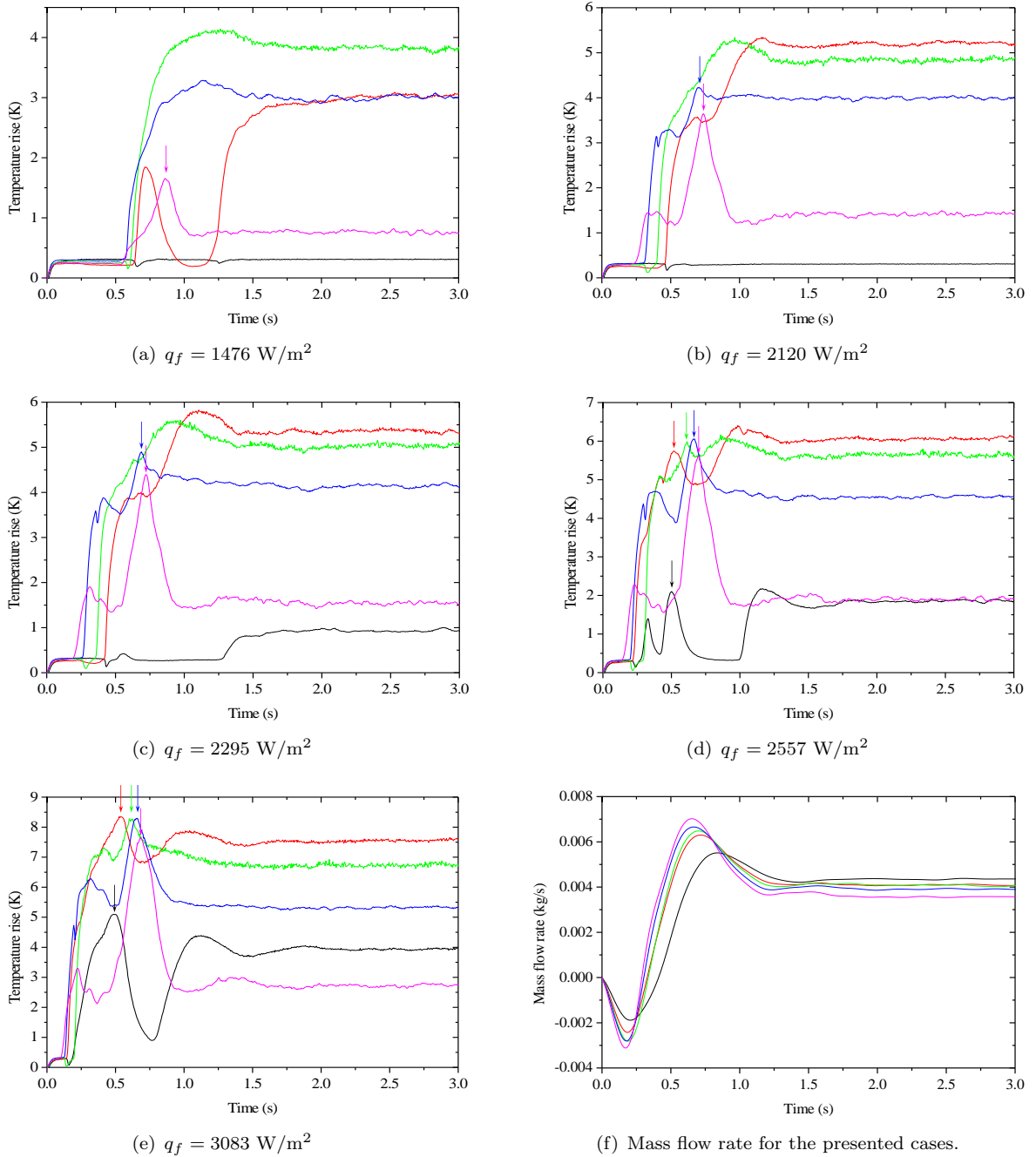
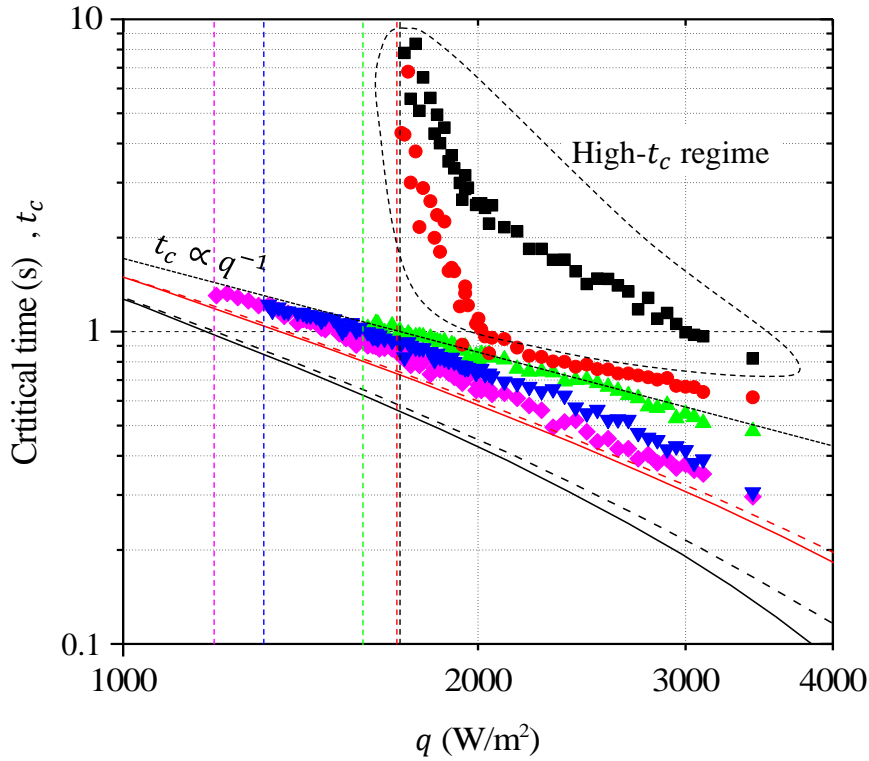
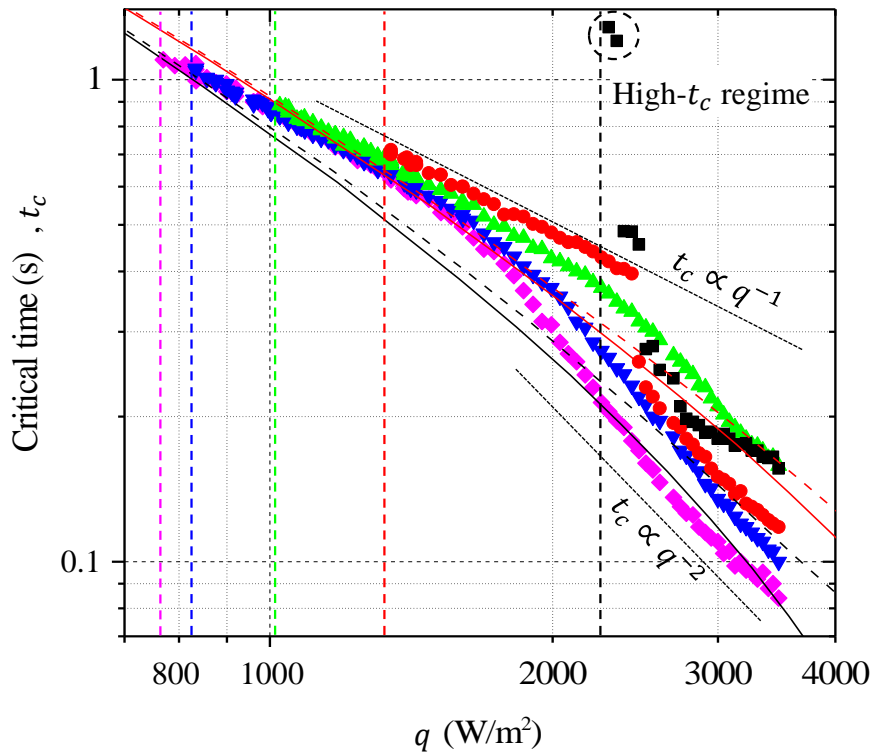


**Figure 5.13.** Simultaneous temperature evolutions for V06. In (a) through (e): —  $T1$ ; —  $T2$ ; —  $T3$ ; —  $T4$ ; —  $T5$ . In (f): —  $q = 1476 \text{ W/m}^2$ ; —  $q = 2120 \text{ W/m}^2$ ; —  $q = 2295 \text{ W/m}^2$ ; —  $q = 2257 \text{ W/m}^2$ ; —  $q = 3083 \text{ W/m}^2$ .



(a) V10.



(b) V06.

**Figure 5.14.** Critical time vs. final wall heat flux. ■ T1, ● T2, ▲ T3, ▼ T4, ◆ T5. The vertical dashed lines show the transient CHF limits of each position (same color code as symbols). The other lines represent: — Pavlov’s model [61] with  $q_s = 6000 \text{ W/m}^2$ ,  $d_d = 0.00009 \text{ mm}$ ; - - -  $q_s = 6000 \text{ W/m}^2$ ,  $d_d = 0.0005 \text{ mm}$ ; —  $q_s = 10000 \text{ W/m}^2$ ,  $d_d = 0.00009 \text{ mm}$ ; - - -  $q_s = 10000 \text{ W/m}^2$ ,  $d_d = 0.0005 \text{ mm}$ .

We will analyze first the case of test section V10. For the positions that are closer to the exit,  $t_c$  seems to respond to a power law, quite close to  $t_c \propto q^{-1}$ . Hereafter, we will refer to this dependence as the *linear regime*. The curves are quite close to each other, and in order: the critical time increases slightly as we move away from the exit. This is the case of the curves for T5, T4, T3 and the power range above 2000 W/m<sup>2</sup> for T2. This indicates that the boiling crisis propagates like a wave from the exit of the heated section towards the entrance. Nevertheless, the situation is different for the positions upstream. For T1 at any power and T2 below 2000 W/m<sup>2</sup>, the points are not in the linear regime. For simplicity, we are going to call this regime the *high- $t_c$  regime*. This difference in behavior according to the position and heat flux lets us infer that there are two different mechanisms at the origin of transient boiling crisis.

For the experiment with test section V06, T5, T4, T3 and T2 are in the linear regime from the lowest values of  $q_f$  at which transient boiling crisis takes place. At higher power, however, T5, T4 and T3, show a gradual change of behavior; the relation becomes  $t_c \propto q^{-2}$ , called hereafter the *quadratic regime*. The power at which this transition takes place is lower for T5 than for T4, and lower for T4 than for T3. At T2 the critical time presents a discontinuity at 2450 W/m<sup>2</sup>. For heat flux higher than this,  $t_c$  at T2 is lower than at T3, showing that the boiling crisis at T2 starts independently from the crisis front moving upstream from the exit; there must be a dry patch appearing locally somewhere near T2 during the negative inlet velocity stage of the transient. It is possible that the reversed flow stops bubbles from moving upwards, which favors its accumulation in the near entrance region. For T1 a rather complex behavior is observed. Though every transient conducting to crisis at T1 produces SBC at the end, we can see in Fig.5.5(b) that there is an initial phase where a TBC temperature excursion takes place, after which, later, the SBC appears. This happens too at T2 for power higher than 1400 W/m<sup>2</sup> (see Fig. 5.4(d)). In these cases, the SBC is not initiated by the first event that conduces to crisis. The critical time determined corresponds to the first temperature excursion, which is temporary. In the incipient cases, this excursion is completely over (the temperature comes back to NB levels, probably due to the apparition of intense flow) before the permanent boiling crisis appears with a second excursion. The latter is triggered presumably by the mechanism corresponding to the high- $t_c$  regime. However, as power increases, the onset of SBC happens earlier, the two events get closer on the time scale and the valley between the two temperature excursions disappears.

From all the observed above, we can conclude that there are different mechanisms that initiate transient boiling crisis. These mechanisms in most cases have different time scales. When the linear regime happens below  $q_{c,s}$ , the temperature excursion can be only temporary if no boiling crisis hysteresis effects are triggered. In some other cases, above  $q_{c,s}$ , a TBC event, activated by the linear mechanism, can be totally or partially inhibited and followed by SBC, activated later by the high- $t_c$  mechanism. Thus, the origin of boiling crisis and its ability to survive at the end of the transient are independent.

## 5.4 Study of transient boiling crisis initiation regimes

In the previous section we have identified three main mechanisms that started boiling crisis in our transient experiments:

- the one corresponding to the linear regime;
- the one corresponding to the quadratic regime;
- the one present at the high- $t_c$  regime.

In the following sections, our attention will be devoted mostly to the linear regime:

**Table 5.2.** Values of the product  $t_c \times q_v$ , in  $\text{kJ}/\text{m}^3$ . The numbers in brackets are uncertainties on the last figure(s).

Position	Section V10	Section V06
T5	575(75)	580(20)
T4	630(30)	580(20)
T3	680(30)	600(20)
T2	800(50)	640(20)
T1	—	800(30)

- in most of the cases it is the mechanism dominating at the *incipience* of transient crisis, i.e. at  $q_f = q_{c,t}$  or  $q_f = q_{c,p}$  when only SBC was observed;
- it can produce power-premature boiling crisis in most of the heated section.

The other two mechanisms are regarded as secondary because more particular conditions are necessary to observe them and they are less critical (in the sense that their occurrence comes at higher power than the linear regime). Very high heat flux is necessary for the quadratic regime and, as we will discuss later, its nature is similar to that of the linear regime. The high- $t_c$  regime is only present near the entrance of the heated section and its incipience is ruled by the steady state CHF (thus, not specific to transient response of the loop).

#### 5.4.1 The linear regime

In general the critical times observed for a given value of wall heat flux are lower for V06 than for the equivalent position on test section V10; the crisis originates faster on V06 than on V10 for equal wall heating conditions, presumably due to the smaller diameter. The dependence  $t_c \propto q^{-1}$ , or alternatively  $t_c \times q = \text{cst.}$  suggests that the mechanism producing crisis is linked to the total amount of energy transferred to the fluid. However the value of the constant seems to be highly dependent on the diameter of the section. That is why in Fig. 5.15  $t_c$  is represented as a function of the volumetric heat input homogenized on the cross section:

$$q_v = \frac{4q}{D}. \quad (5.15)$$

This representation shows that for the equivalent positions, in the  $t_c \propto q^{-1}$  region, the diameter effect is less pronounced (difficult to observe for T4 and T5 and slightly increasing for T3 and T2). We can conclude from this analysis that the  $t_c \propto q^{-1}$  regime is governed mainly by the bulk specific energy content of the cross section. The transition to boiling crisis takes place when a certain amount of energy per unit volume has been transferred to the fluid in the cross section. Table 5.2 presents the proportionality constants  $t_c \times q_v$  that can be found from experimental data with their uncertainty for the different positions and test sections in the linear regime. No results are presented for T1 as this regime has not been clearly observed there. Except for T2 on V10 and T1 on V06, the values of  $t_c \times q_v$  are contained between 575 and 690  $\text{kJ}/\text{m}^3$ , i.e. 10% dispersion around 630  $\text{kJ}/\text{m}^3$ . However, the dispersion is not random, but depending on the position on the section; positions farther from the entrance present lower products. Figure 5.16 shows the product  $t_c \times q_v$  as a function of the non-dimensional position  $z/D$ , where  $z$  is the distance from the entrance. For  $z/D$  large enough (larger than  $\approx 80$ ), the asymptotic value is attained, but below, larger amounts of energy are necessary for reaching boiling crisis.

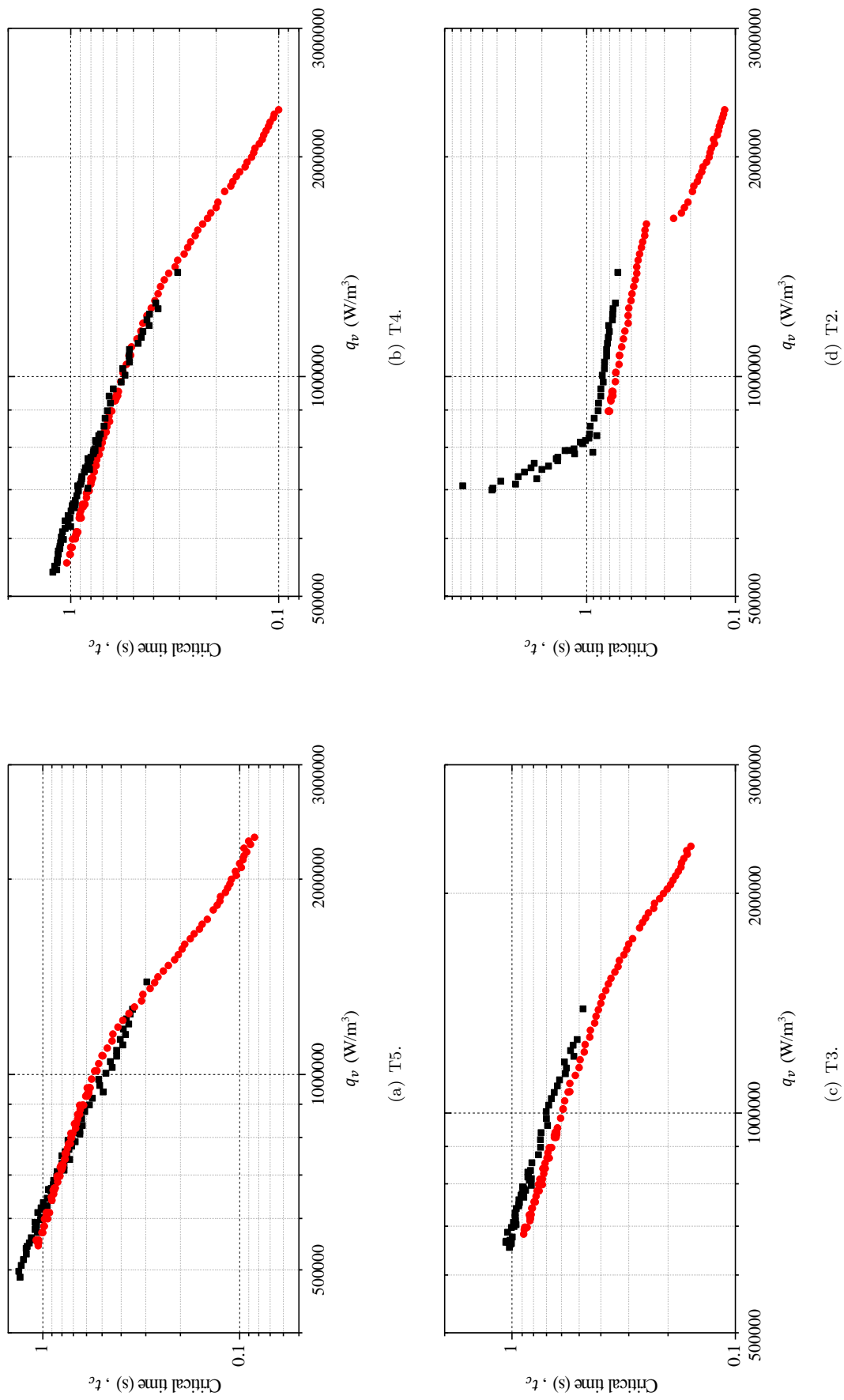


Figure 5.15.  $t_c$  vs.  $q_v$ . ■ V10; ● V06.

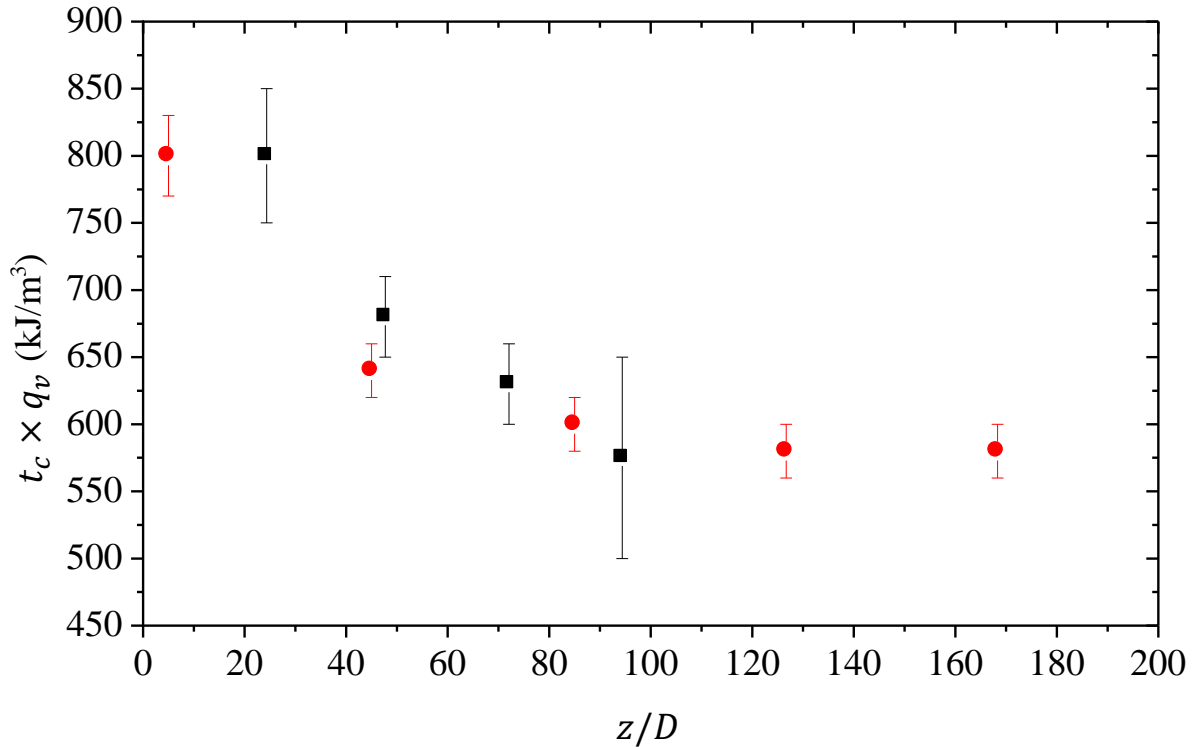


Figure 5.16. Spatial dependence of  $t_c \times q_v$ . ■ V10 data, ● V06 data.

#### 5.4.2 Comparison of critical time data with models

In section 2.5 we presented previous research on the problem of transient boiling crisis and the meta-stable NB stage preceding it. Researchers that did boiling experiments in different pool boiling configurations determined empirical power laws followed by their data. On the other hand, a few works on boiling in upward flow vertical channels show that the correlations of critical time and power are not the same as in pool boiling, and deserve a separate treatment.

The work by Yarmak [77] showed that in the case of narrow channels with forced convection there exists an empirical relation  $q \times t_c = \text{cst.}$  if power is sufficiently high. This relation has been observed in our data with some limitations.

Pavlov and Babitch [4, 61] studied a channel immersed in a pool and determined the existence of a transient boiling crisis regime dominated by the void fraction evolution of the bulk of the heated section. They proposed a model to predict critical time as a function of heat flux. This model is represented by Eq. (2.60). In Fig. 5.14 the predictions of critical time are included next to data, and in Fig. 5.17 the data for the product  $q_v \times t_c$  is presented as function of  $q_v$ , along with the predictions of the Pavlov model.

If the model predicts acceptably the order of magnitude of the measured critical time and the overall shape of  $q_v \times t_c$  as function of  $q_v$  as a function of heat flux, we need to point out its limitations. In the first place, according to the model, all the positions should have the same critical time at a given heat flux, because of the assumed uniformity of the vapor mass transfer mechanisms and of void fraction evolution during the phase with no natural circulation. The prediction of the model is quite sensitive to its parameters, namely  $q_s$ ,  $d_d$  and the void fraction in the wall region necessary for the transition. It is possible to show that the model predicts:

- at very low power, an asymptotic value of

$$q_v \times t_c = -\frac{h_{lg}}{v_{lg}} \ln \left( 1 - \frac{\alpha_w^* (\rho_l - \rho_g)}{\rho_l} \right) \quad (5.16)$$

- at very high power, an asymptotic value of

$$q_v \times t_c = \frac{4h_{lg}d_d}{v_{lg}D} \quad (5.17)$$

or alternatively

$$q \times t_c = \frac{h_{lg}d_d}{v_{lg}} \quad (5.18)$$

In Eq. (5.16),  $\alpha_w^*$  is the void fraction at the wall layer assumed necessary for the onset of crisis ( $\alpha_w^* = 1$  in Eq. (2.60)). The low power asymptote corresponds to a regime that is fully dominated by the evolution of void fraction in the bulk (bulk-dominated), while the high power asymptote corresponds to a regime where the power is so high that the vapor cannot get removed from the near-wall layer before the boiling crisis takes place (wall-dominated).

The low power asymptotic value seems to be too high compared to the experimental data. In the case of V06 it is possible to see very clearly the limiting values of  $q \times t_c$  on the horizontal curve they describe for T2 through T4 at sufficiently low power. They are the values in Table 5.2. When taking  $\alpha_w^* = 1$ , as suggested in Pavlov's paper, the obtained value is  $q_v \times t_c \approx 815200$  J/m<sup>3</sup>. The RHS of Eq. (5.16) is very responsive to  $\alpha_w^*$  near  $\alpha_w^* = 1$ . Thus assuming that the necessary values of void fraction in the near-wall layer is 0.9, we get  $q_v \times t_c \approx 600000$  J/m<sup>3</sup>, which is closer to our data. It is reasonable that not exactly the whole volume in the near-wall layer, but most of it, is required to be occupied by vapor for boiling crisis to happen. The asymptotic value being lower for V06 may indicate that the curvature of the wall may have an effect on bubble coalescence.

The bubble departure diameter is highly influential on the asymptote at high power. An increasing the asymptotic value of  $q_v \times t_c$  naturally modifies the values in the transition power range too. This can also be appreciated in Fig. 5.17. It is reasonable to assume that the departure diameter is not the same on the whole section because the bulk velocity can play a role on the microscopic process of bubble growth and detachment. This could be the result for example of the convective effect on the thermal boundary layer.

In deducing their model, Pavlov made the assumption that vapor is removed from the near-wall layer by a term of the form

$$\frac{q_s}{h_{lg}} (\alpha_w - \alpha_e), \quad (5.19)$$

where  $q_s$  is the CHF in pool boiling for a vertical surface, and  $\alpha_w$  and  $\alpha_e$  are the void fraction in the wall layer and at the channel bulk, respectively. With this choice, they are assuming that the bubble detachment mechanism inside the channel is of the same intensity as in pool boiling. This is probably not the case, given that in the presence of external flow, the detachment should be enhanced. As we see in Fig. 5.17, the model fits better the data when the constant  $q_s$  is increased from the suggested 6000 W/m<sup>2</sup> to 10000 W/m<sup>2</sup>. The increase of this parameter displaces the transition between the bulk-dominated to the wall-dominated regimes to higher values of power. In the case of V10, the model seem to predict correctly the trend of the critical time at T5 and T4. For V06, apparently the experimental data show the transition to the wall-dominated regime, but it is later and more abruptly than predicted by the model.

In conclusion, we can see that Pavlov's model for predicting  $t_c$  gives a reasonable approximation of the order of magnitude especially in the low power regime. However, the wall-dominated

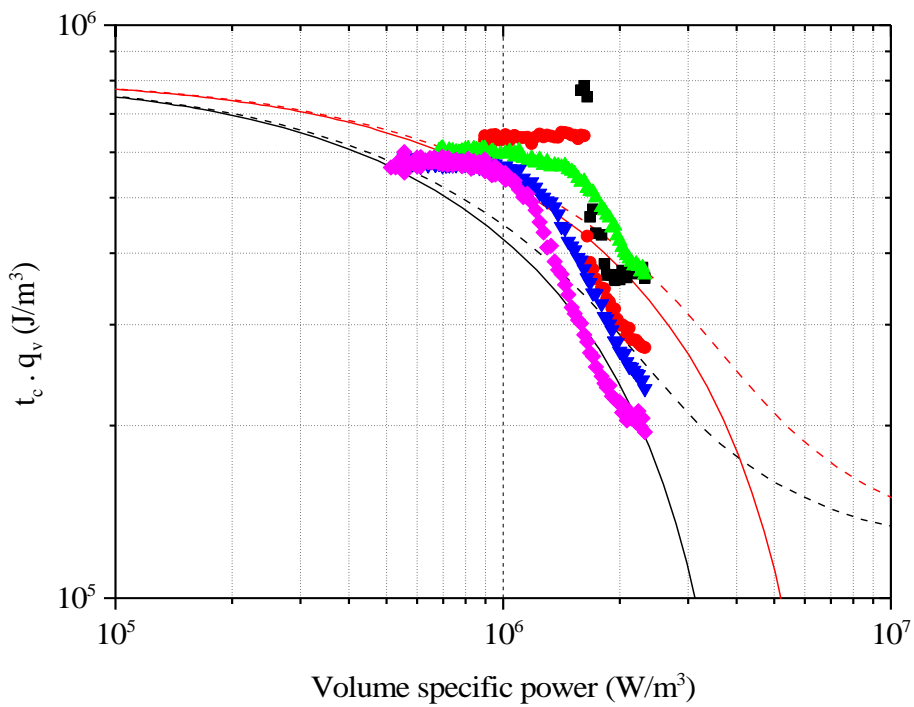
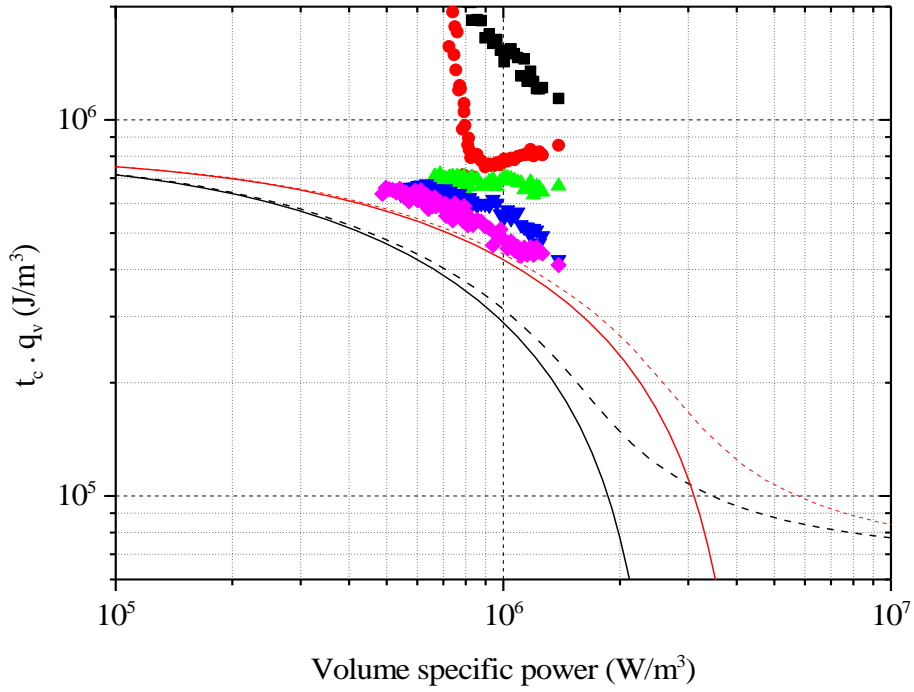


**Figure 5.17.** Critical product  $t_c \times q_v$  vs. final volume specific power. ■  $T1$ , ●  $T2$ , ▲  $T3$ , ▼  $T4$ , ◆  $T5$ .  
 — Pavlov's model [61] with  $q_s = 6000 \text{ W/m}^2$ ,  $d_d = 0.00009 \text{ mm}$ ; ---  $q_s = 6000 \text{ W/m}^2$ ,  $d_d = 0.0005 \text{ mm}$ ;  
 —  $q_s = 10000 \text{ W/m}^2$ ,  $d_d = 0.00009 \text{ mm}$ ; ---  $q_s = 10000 \text{ W/m}^2$ ,  $d_d = 0.0005 \text{ mm}$ .

regime and the transition to it are highly dependent on parameters that can have a great variability (they may depend on flow velocity, wall condition, etc.). For that reason, they may fail to predict experimental results in these power regions.

### 5.4.3 Study of incipience of the linear-regime

Although the previous analysis of data gives a satisfying explanation for the quantification of the critical time, it does not explain the incipience of transient boiling crisis, i.e. it does not predict  $q_{c,t}$  or  $q_{c,p}$ . In their paper, Pavlov does not mention this question, but he points out the fact that the origin of this type of transition to crisis is due to happen in the stage of the transient where natural circulation is not yet established.

In order to find an answer to the question of transient boiling crisis incipience it is necessary to take into account the transient evolution of the thermohydraulic variables in the loop, namely the velocity field and the mass quality.

#### Modeling of the evolution of a fluid particle

After the step injection of a heat flux on the initially static system, there are two distinct phases. At the beginning, the production of vapor in the test section creates a volume expansion of the heated fluid, thus, the fluid is expelled through the two ends of the heated section. During the lapse of time before the natural circulation develops and produces a global positive movement of the loop, the local velocity is negative at the inlet and positive at the exit of the heated section. If the thermal equilibrium homogeneous model is adopted, the thermodynamic quality inside the section is uniform in space but increasing in time. Later, in a second stage, the reduction of weight of the heated branch has accelerated the mass of the whole loop, and this movement inverts the velocity sign at the entrance of the section. From that moment on, ‘fresh’ liquid is entering the heated section by the bottom for the first time since the transient started. The velocity evolves during time, and the cold front travels from the entrance to a given position on the test section in a finite time. Thus, the first stage of the transient is longer the farther the position is placed from the entrance. The following formulae describes the dynamics of these two distinct stages. During the uniform expansion phase, the local value of the specific enthalpy evolves according to

$$\frac{dh}{dt} = \frac{q_v}{\rho(h)}, \quad (5.20)$$

with the homogeneous density defined as

$$\frac{1}{\rho} = \frac{1}{\rho_g} \frac{h - h_l}{h_{lg}} + \frac{1}{\rho_l} \left( 1 - \frac{h - h_l}{h_{lg}} \right). \quad (5.21)$$

The pressure, gravity and kinetic energy effects have been neglected in the energy equation (5.20), as in this system the diameters are quite big and the friction should not produce such a resistance to the evacuation of fluid during the expansion (thus originating high expansion pressure gradients). Also, any subcooling of the fluid has been neglected, in view of the great heat flux values that conduce to boiling crisis. The integration of Eq. (5.20) gives

$$x(t) = \frac{h - h_l}{h_{lg}} = \frac{v_l}{v_{lg}} (e^{\Omega t} - 1), \quad (5.22)$$

with the expansion rate  $\Omega$  defined as

$$\Omega = \frac{v_{lg} q_v}{h_{lg}}. \quad (5.23)$$

It can be shown (see app. C.1) that under the homogeneous model assumption, at all times, the velocity in the heated section presents a linear profile as a function of position:

$$u(z, t) = u_0(t) + \Omega z. \quad (5.24)$$

The evolution of  $u_0$ , the velocity at the entrance of the heated section, is ruled by the momentum balance. If  $u_0(t)$  is known, it is possible to integrate the trajectory of any fluid particle, given its position at an initial time, by solving the equation

$$\frac{dz}{dt} = u_0(t) + \Omega z \implies \frac{dz}{dt} - \Omega z = u_0(t). \quad (5.25)$$

We will be especially interested by the particle that at the instant of time when  $u_0$  becomes positive, denominated  $t_0$ , is at the entrance of the section. That one is the particle that has marginally not left the heated section during the uniform expansion period. The solution to Eq. (5.25) is

$$z(t) = e^{\Omega(t-t_0)} \int_{t_0}^t e^{-\Omega(t'-t_0)} u_0(t') dt'. \quad (5.26)$$

The first particle that arrives from below the entrance to a given point has necessarily spent less time inside the heated section than the particles that never left the section, thus their energy content per unit mass is lower. In consequence, the maximum local quality attained happens when the particle described by Eq. (5.26) arrives to the position of interest.

### Determination of a criterion for the critical condition and boiling crisis incipience

The hypothesis that we propose for explaining the incipience of transient boiling crisis is the following: there will be transient boiling crisis at a given position only if, before the moment the cold front arrives there, a certain value of local thermodynamic quality has been exceeded. This statement will be the most valid in the lower power region, near the incipience points, where the measured critical times respect closely the relation  $q_v \times t_c = \text{cst.}$

Using the experimental data we tested the validity of this hypothesis. We chose the limiting cases for each position and test section, i.e. experiments with  $q_f$  slightly below and above the values of heat flux presented in table 5.1 and where the crisis onset takes place in the linear regime. For each case, Eq. (5.26) was applied using the data for mass flow rate  $\dot{m}$  to estimate  $u_0(t)$ :

$$u_0(t) = \frac{\dot{m}}{\rho_l A}. \quad (5.27)$$

The mass flow rate measurements needed to be interpreted taking into account the time dependent Bernoulli equation of the Venturi tubes (Eq. (3.11)). The pressure difference  $\Delta P$  signal was filtered with a perfect low-pass filter at 25 rad/s cutoff frequency, and the best time function  $\dot{m}$  compatible with the Venturi pressure drop time evolution was found.

The transit time  $t_r$ , at which the particle that is at the inlet at  $t_0$  reaches the position of interest, was found by means of Eq. (5.26), for all the temperature sensor locations, for each transient experiment. Moreover, the maximum value of local mass quality attained was calculated using Eq. (5.22), evaluating  $x(t_r)$ .

The analyzed cases are presented in table 5.3 with the results of the analysis. Furthermore, Fig. 5.18 shows the measured critical times (only when transient boiling crisis takes place in the linear regime) vs. the obtained transit times  $t_r$ . It can be appreciated that:

- the critical times for the incipient cases are very close to  $t_r$ ;

**Table 5.3.** *Transit time and quality analysis applied to incipient linear regime boiling crisis cases. The SBC cases for V10 T2, are distinguished between non-linear (NL) and linear (L) and the value in column  $q_{c,t}$  is in fact the transition power value from the near-entrance regime to the linear regime. The numbers in brackets are uncertainties on the last figures.*

Position	$q_{c,t}$ (W/m <sup>2</sup> )	Case $q_f$ (W/m <sup>2</sup> )	type	$t_0, t_{r,pos.}$ (s)	$q_v t_{r,pos.}$ (J/m <sup>3</sup> )	max. $x$ at pos.
V10 T5	1190(20)	1175	SNB	0.612, 1.414	674560	0.687
V10 T5	1190(20)	1200	TBC	0.530, 1.368	666660	0.670
V10 T4	1320(20)	1300	SNB	0.520, 1.229	650540	0.638
V10 T4	1320(20)	1330	TBC	0.534, 1.219	657940	0.653
V10 T3	1600(20)	1590	SNB	0.510, 1.049	676750	0.692
V10 T3	1600(20)	1610	TBC	0.503, 1.049	686590	0.713
V10 T2	2050(50)	1990	SBC(L)	0.496, 0.869	703460	0.751
V10 T2	2050(50)	2030	SBC(NL)	0.498, 0.868	714630	0.776
V06 T5	760(20)	750	SNB	0,399, 1,146	572690	0,497
V06 T5	760(20)	770	TBC	0.403, 1.148	589300	0.524
V06 T4	840(20)	830	SNB	0.406, 1.008	555870	0.470
V06 T4	840(20)	850	TBC	0.380, 1.014	579520	0.508
V06 T3	1010(20)	1000	SNB	0.357, 0.833	556800	0.471
V06 T3	1010(20)	1025	TBC	0.398, 0.837	570680	0.493
V06 T2	1335(20)	1325	SNB	0.324, 0.646	570160	0.492
V06 T2	1335(20)	1345	TBC	0.327, 0.642	575840	0.502

- critical times for higher heat fluxes are lower than  $t_r$ ;
- for each of the test sections the maximum quality attained in the incipient cases has a well defined value, compatible (through Eqs. (5.22) and (5.23)) with the values of  $t_c \times q_v$  found before (Table 5.2).

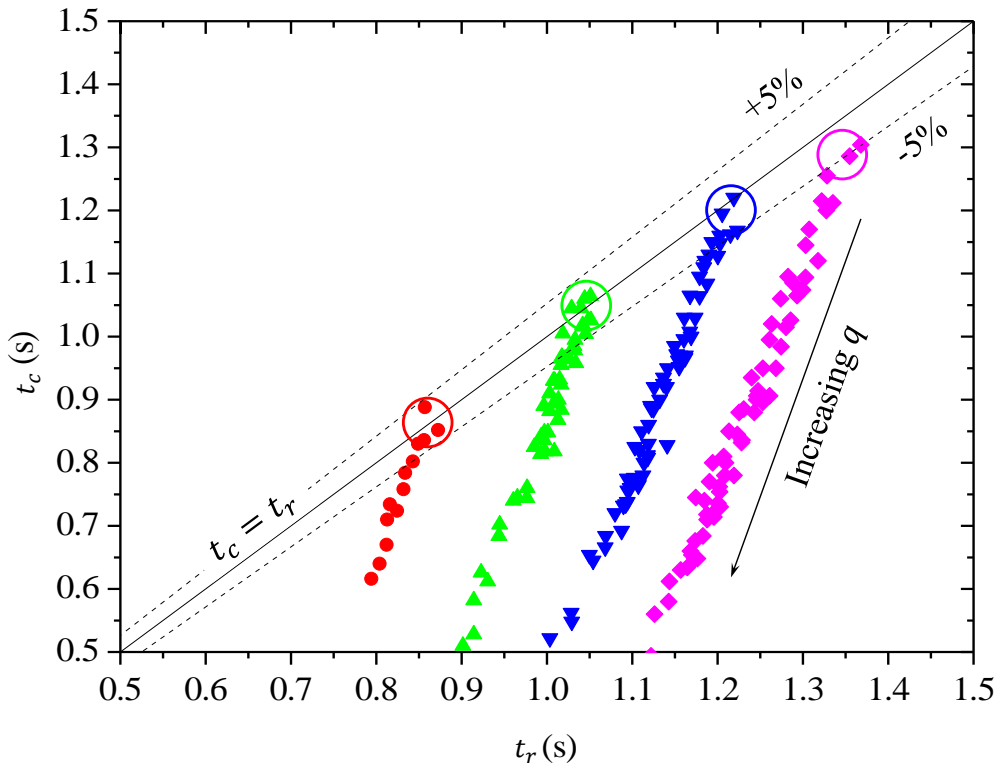
This results suggests that boiling crisis in the linear regime cannot happen during the transient if a specific amount of energy accumulated in the bulk of the heated section is not reached. The possibility to reach this value in a natural circulation loop is ruled by the mass flow rate evolution: the competition between the initial stage of uniform evaporation and the second phase of transport of the cold front from the entrance. If the critical time required is higher than the instant of time at which the cold front reaches the surface, crisis cannot take place.

During the uniform stage the vapor quality increases as an exponential function of the product  $q \times t_c$ . Thus the required time to reach a given value of quality is  $t_x \propto q^{-1}$ . However, the duration of the uniform stage, i.e. the transit time  $t_r$  of the cold front to a given point of the section, should follow a law similar to the inlet velocity overshooting time:  $t_r \propto q^{-1/3} z^{1/3}$ , where  $z$  is the distance from the entrance to the point of interest<sup>4</sup>. The fact that  $t_x$  decreases faster than  $t_r$  as a function of  $q$ , makes it possible to have  $t_x < t_r$  above a given value of heat flux. Furthermore, the power laws in this paragraph lead us to the prediction that the bulk-dominated boiling crisis incipience heat flux should follow a rule  $q \propto z^{-1/2}$ . This description is surprisingly accurate.

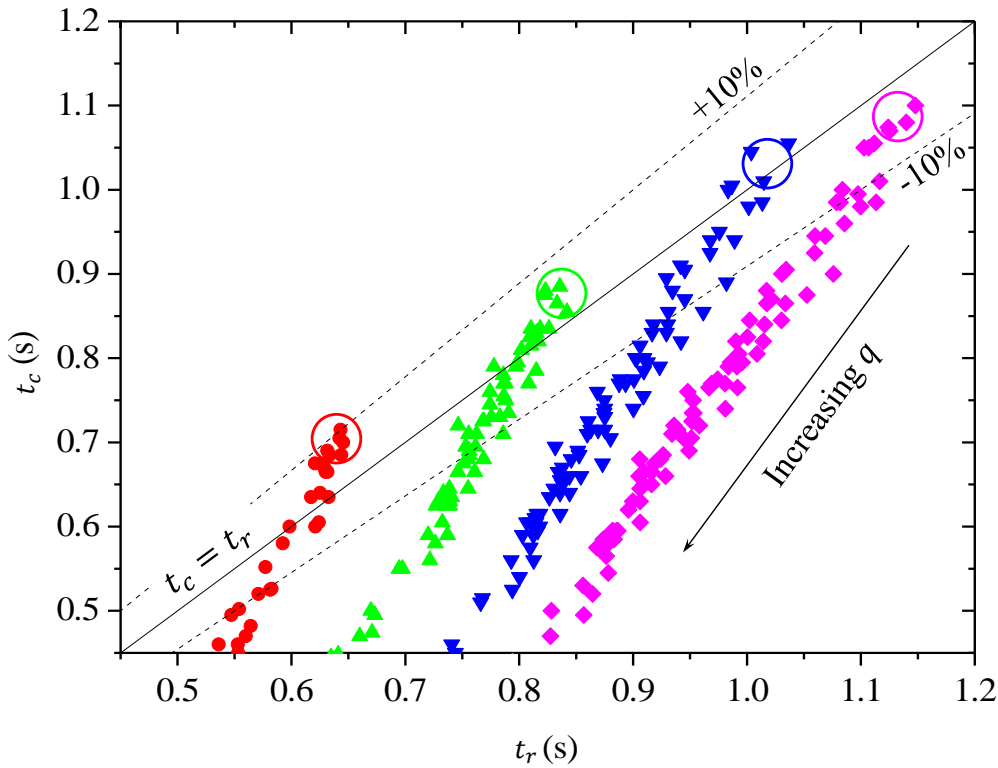
#### 5.4.4 The quadratic regime

The quadratic regime has only been observed at very high values of volumetric power on V06. In all the cases, the onset of this regime means shorter critical times that would have been predicted by the extrapolation of the linear regime to higher power values. This suggests that at high power less total bulk energy is necessary for reaching the critical condition. The reason

<sup>4</sup>The dependence on  $z$  is only approximate and can be induced from Eq. (5.4).



(a) V10



(b) V06

**Figure 5.18.** Evaluation of the transient boiling crisis incipience criterion in the linear regime by the ‘uniform expansion-transit time’ model. ● T2, ▲ T3, ▼ T4, ◆ T5. All points identified in the linear regime or quadratic regime are included, specially those near the incipience, marked with a big circle.

to this is that the transient vapor concentration profile is much less uniform on the cross section for the cases with high power. This could be the case if, for example, vapor transport in the radial direction has a diffusive nature. There are two competing contributions with different time constants. On the one side, there is the increase of average cross section mixture specific enthalpy, with a time constant proportional to  $q^{-1}$ . On the other side, there is a diffusion time for the vapor to travel a distance  $R$  from the wall to the bulk, and the time constant associated to this is not linked to the heat flux directly. Thus for high heat flux, the two time constants may become comparable and the impact of the diffusion process becomes visible. We will show that a dependence  $t_c \propto q^{-2}$  can be the consequence of a diffusive process.

Let us assume that during the transient, and only for short times after the power step pulse, vapor is preferably accumulated near the wall with a profile that decreases towards the center of the section. By analogy with a diffusion problem in a semi-infinite solid, we will approximate the solution by a linear profile:

$$\alpha(r, t) = \begin{cases} \alpha_w(t) \left(1 - \frac{r}{L(t)}\right) & \text{if } r < L \\ 0 & \text{if } r \geq L \end{cases} \quad (5.28)$$

with  $L(t)$  given by a diffusion model,

$$L(t) = \mathcal{C} \sqrt{\gamma t}, \quad (5.29)$$

where  $\mathcal{C}$  is a numerical constant and  $\gamma$  is the diffusion coefficient of void fraction.

The region of non-zero void fraction will grow so that the cross section average void fraction verifies Eq. (5.22):

$$\langle \alpha \rangle (t) = \frac{\alpha_w}{2} \left[ \left( \frac{L}{R} \right) - \frac{1}{2} \left( \frac{L}{R} \right)^2 \right] = \frac{v_g}{v_{lg}} (1 - e^{-\Omega t}). \quad (5.30)$$

For low values of time at which  $\Omega t \ll 1$  and  $\frac{L}{R} \ll 1$ , Eq. (5.30) simplifies to

$$\frac{\alpha_w}{2} \left( \frac{L}{R} \right) = \frac{v_g}{v_{lg}} \Omega t. \quad (5.31)$$

Taking into account Eq. (5.29), and the definition of  $\Omega$ ,

$$\begin{aligned} \frac{\alpha_w}{2} \frac{\mathcal{C} \sqrt{\gamma t}}{R} &= \frac{v_g}{h_{lg}} \frac{2q}{R} t, \\ \frac{h_{lg}}{v_g} \frac{\alpha_w}{4} \mathcal{C} \sqrt{\gamma} &= q \sqrt{t}. \end{aligned} \quad (5.32)$$

If it is assumed that boiling crisis requires that quality reaches a certain critical value  $\alpha_{w,c}$ , then

$$q^2 t_c \propto \alpha_{w,c}^2 \gamma, \quad (5.33)$$

which explains the behavior of critical time at high heat flux, when the diffusion time  $\frac{R^2}{\gamma}$  becomes comparable or greater than the time constant  $\frac{1}{\Omega}$ .

#### 5.4.5 The high- $t_c$ regime

The values of critical time in the positions near the entrance for relatively low heat flux values are significantly higher than those found in the other two regimes. We can make a few general

remarks about this regime. Our remarks are based on the experimental data for V10, given that it is in this case that we have a great number of points to make statistically relevant analysis.

Concerning the occurrence of boiling crisis by high- $t_c$  mechanism, it has been observed only at heat flux higher than the steady state local CHF; never at heat flux lower than  $q_{c,s}$ . When the temperature excursion takes place in this regime, in most of the cases, the most dynamic part of the transient, which lasts between two or three seconds and where the  $\dot{m}$  oscillations are present, has already ended and the system seems to have found a stable configuration. Thus, the onset of crisis by this mechanism takes place in what seems to be a *metastable* equilibrium state in the system, at least hydraulically speaking. The fact that this mechanism can take place in thermohydraulically stable conditions explains why no premature (at  $q < q_{c,s}$ ) boiling crisis is observed near the entrance of the heated section. In section 5.4.1 we showed that these positions' transient maximum vapor content does not reach the critical condition necessary for the linear or quadratic regime crisis to take place. However, in the steady phase, the existence or not of crisis is given by the value of  $q_{c,s}$ . If crisis is not started by the thermohydraulic transient, then it will eventually start by the same mechanism by which it does in a steady condition.

Experimentally, the critical time diverges as  $q - q_{c,s}$  approaches 0. The diminution of the critical time is quite fast as soon as  $q - q_{c,s}$  grows. Furthermore, the curve formed by the measured points presents a greater statistical dispersion in this regime than in the linear or quadratic ones. This puts forward that this regime is in nature based on stochastic mechanisms. The occurrence of DNB is a combination of many stochastic processes: the surface density and activation of boiling sites, the frequency of production and departure of bubbles in each site, the interaction of bubbles near the heated surface (either produced at contiguous sites or detached successively from the same site). The macroscopic result of the combination of these processes is a time probability distribution of reaching a given surface condition (e. g. vapor surface concentration, wall temperature, hot spot size, etc.) that triggers the DNB. The value of heat flux does naturally affect this distribution, since it produces the activation of sites and vapor in the sites; more heat flux means more active sites and more bubbling frequency. Below  $q_{c,s}$  the probability is 0 for all time. Above, the probability per time unit of reaching the critical condition at time  $t$  after the power injection increases with  $q$ , and the mean time of occurrence lowers. The factors that modulate the evolution of  $t_c$  vs.  $q$  are the relative bulk velocity, the bulk void fraction and quality, the surface condition, etc.. Probably, the higher contents of vapor at T2 than at T1 in V10, explain the higher probability at T2 of reaching the critical condition at a given  $q$  with respect to T1, where the bulk quality is near 0 in the metastable phase.

## Summary

We conducted experiments in which a stepwise power injection, the most violent possible solicitation on the cooling system, is exerted. These experiments allowed us to study the different stages of the loop hydraulics and of heat transfer on the wall of the heated section.

We observed that the hydraulic response of the loop presents an overshoot whose intensity and time of occurrence is a function of the power applied:  $G_{Max} \propto q^{1/3}$ ,  $t_{Max} \propto q^{-1/3}$ . This overshoot is the result of a time lag between the acceleration of the flow due to a density reduction, more severe than in the steady state, and the transport of cold particles into and through the heated section.

Concerning heat transfer, in all cases, with heat flux values up to 4000 W/m<sup>2</sup>, nucleate boiling was observed, either in a stable manner or before the onset of boiling crisis. The onset of NB was studied too by observing the temperature evolution at times shorter than 1 s. This showed that for moderate to high power, boiling is initiated by reaching the homogeneous nucleation temperature, while if power is too low, this limit is not reached and boiling starts after a certain

amount of time that decreases with heat flux or temperature and increases with subcooling. However, the final value of wall temperature can be higher than the homogeneous nucleation limit.

Transient boiling crisis could be observed for the two test sections used. In some cases boiling crisis is only temporary, and in others it is stable. The values of transient CHF were determined. Temporary boiling crisis was observed at power values 17% and 35% lower than steady state heat flux for the test sections of 10 mm and 6 mm i.d., respectively. Stable boiling crisis was observed at a power up to 23% lower than steady state CHF for the section with 6 mm i.d.. This highlights that transient boiling crisis needs to be considered differently than steady state boiling crisis.

The critical time was systematically calculated from data. Its dependence on heat flux allowed identifying different mechanisms that can initiate boiling crisis. We can mainly distinguish two of them.

One that is the same mechanism that causes crisis in steady state, when power is increased slowly. This mechanism relies on stochastic phenomena on the heated surface and produces rather long critical times. It is not observed at power below the steady state CHF.

The other is a mechanism directly linked to natural circulation loops. During the initial phase of the transient, the sudden injection of power produces the expansion of the fluid inside the section, having fluid expelled by the two ends of the section. As no cool liquid enters, the evolution in the heated section is uniform and high values of quality or void fraction can be attained. This prejudices the removal of vapor from the wall, with which crisis takes over. A model present in the literature was compared to the experimental results. Qualitatively, the model represents the phenomena observed, but quantitatively it needs to be adjusted to fit the data.

The incipience of boiling crisis cannot be explained if we do not take into account the stage of the transient in which the cool front enters and travels along the heated section. Experimentally we could verify that it is necessary that the critical condition, ruled by the bulk quality or the void fraction, be reached before the cold front reaches the position of interest.

The findings of this chapter arise two new problems:

- if the initial condition was not static, but that of an initially operating loop, how would the onset of boiling crisis be affected?
- it is necessary to know *a priori* the evolution of velocity in the heated section in order to determine the occurrence of transient induced boiling crisis.

These two issues are going to constitute the following two chapters of this study.



## Chapter 6

# Study of the effect of a dynamic equilibrium initial condition on stepwise heat load induced transients

During the operation of a natural circulation loop as cooling system, the sudden injection of power is supposed to represent an undesired incident. In normal operation, a (low) given value of power to be continuously extracted is permanently present; thus, to be more realistic, an applied initial power before the transient should be considered. The study of chapter 5 has shown that the application of a sudden heat load step-pulse on a boiling helium natural circulation loop can produce a premature occurrence of boiling crisis. Premature in comparison to the value of power needed to reach boiling crisis when increasing it gradually, as in the experiments of chapter 4. This arises the following observation: there must be an initial condition (characterized by an initial power value) at which the sudden application of the same final heat flux does not produce boiling crisis during the transient.

Based on these remarks, we have conducted an experimental study of the effect of the initial condition of the loop on the step-pulse heat load induced transient. In section 6.1 we present the experiments and an overview of the main qualitative effects of the initial condition are identified. In section 6.2, a quantitative analysis of data was conducted to characterize the different behaviors observed and define the boundaries between them. In section 6.3, the simplified model presented in section 5.4.3 is extended to consider the effect of non-static initial condition in the thermohydraulic evolution of the system. Finally, from the analysis of the incipient crisis cases, a general boiling crisis initiation criterion is proposed in section 6.4.

### 6.1 Realization of experiments

The experiments that are object of this chapter were conducted on the natural circulation loop described in chapter 3 using the two vertical test sections, V10 and V06. In section 6.1.1 we expose the experimental protocol followed in order to produce series of measurements with initial power as parameter. In section 6.1.2 we present the measured time response of the system, showing an overview of the effects induced by the initial condition on transient behavior.

#### 6.1.1 Experimental protocol

The experiments performed to study the effect of the initial condition are based on the same *modus operandi* as the ones object of chapter 5. Stepwise heat load excitation were applied,

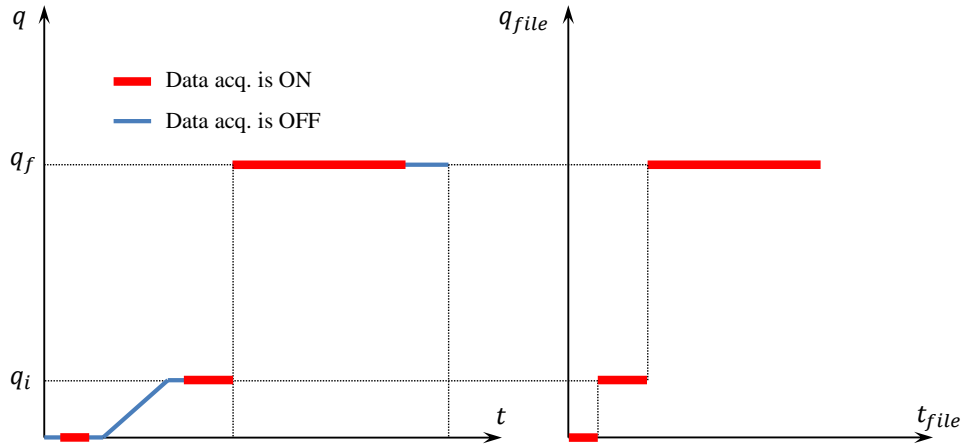


**Figure 6.1.** Schematic time evolution of heat flux in non-static initial condition transient experiments.

defined by two parameters: the initial and the final heat fluxes,  $q_i$  and  $q_f$ . In this chapter we are going to consider the effect of  $q_i \neq 0$ .

The procedure for the measurement of one transient consists of the following steps:

1. the system is made to reach steady equilibrium at  $q = 0$ ;
2. data acquisition is performed for a few seconds in this condition;
3. power is increased gradually up to  $q_i$ ;
4. when the system is steady, data acquisition starts;
5. suddenly  $q = q_f$  is applied in a stepwise manner;
6. a new steady state is reached and data acquisition is stopped;
7. power is reset to 0;

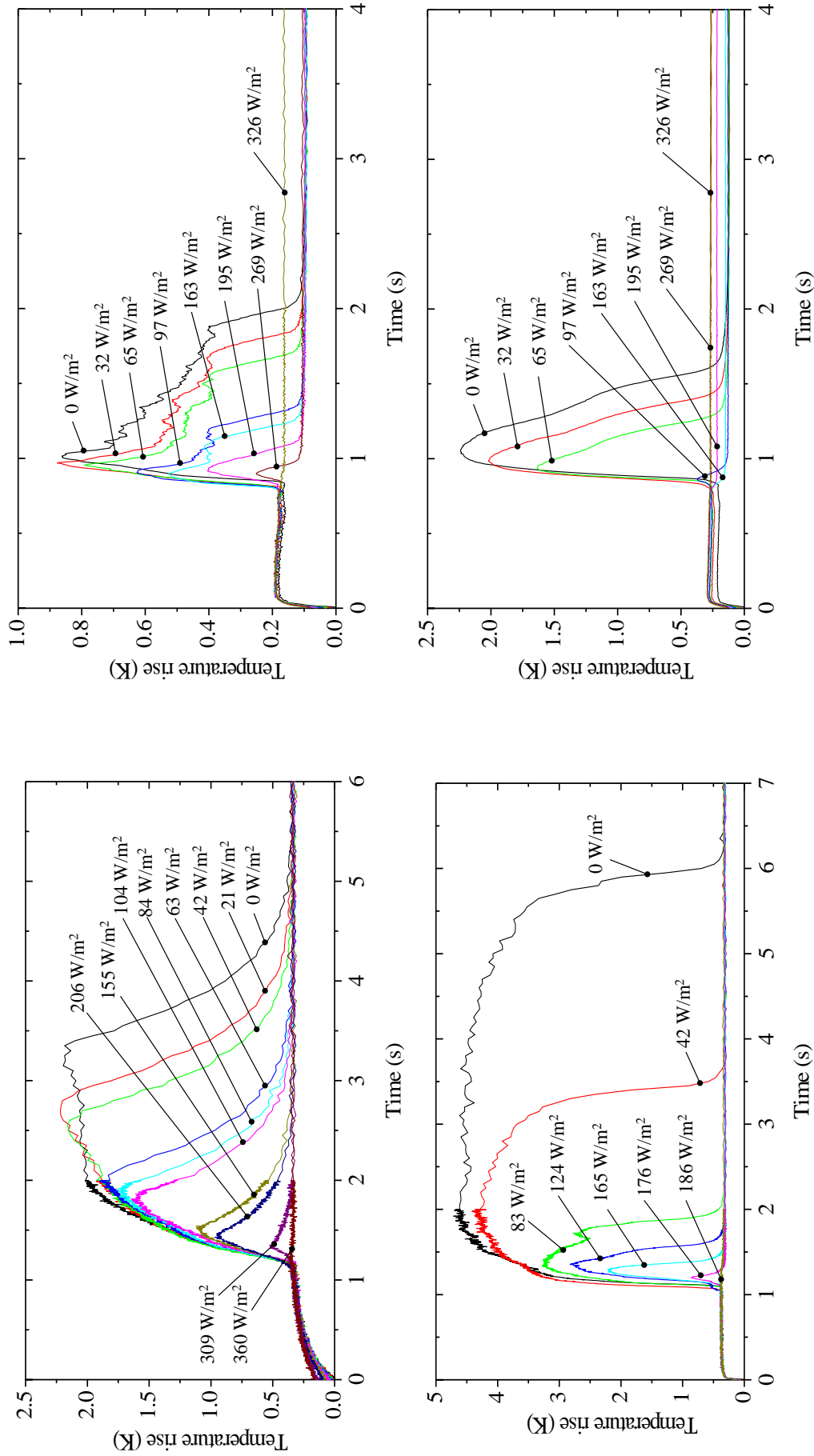
A waiting time of at least two minutes is set between two successive measurements, for the relaxation of the system. The time history of heat flux and its acquisition is represented in Fig. 6.1.

The measurements are organized in series formed by transients measured successively and with a given value of  $q_f$ . Within each series, at each transient  $q_i$  is either increased monotonously, decreased monotonously or neither; this was with the objective of seeing if the history and order of the measurements has an effect on the evolution of the system.

The values of  $q_i$  have been chosen from 0 to as high as  $1400 \text{ W/m}^2$ . In the ranges where interesting variations of behavior were observed two successive  $q_i$  values can differ in only 5 or  $10 \text{ W/m}^2$ .

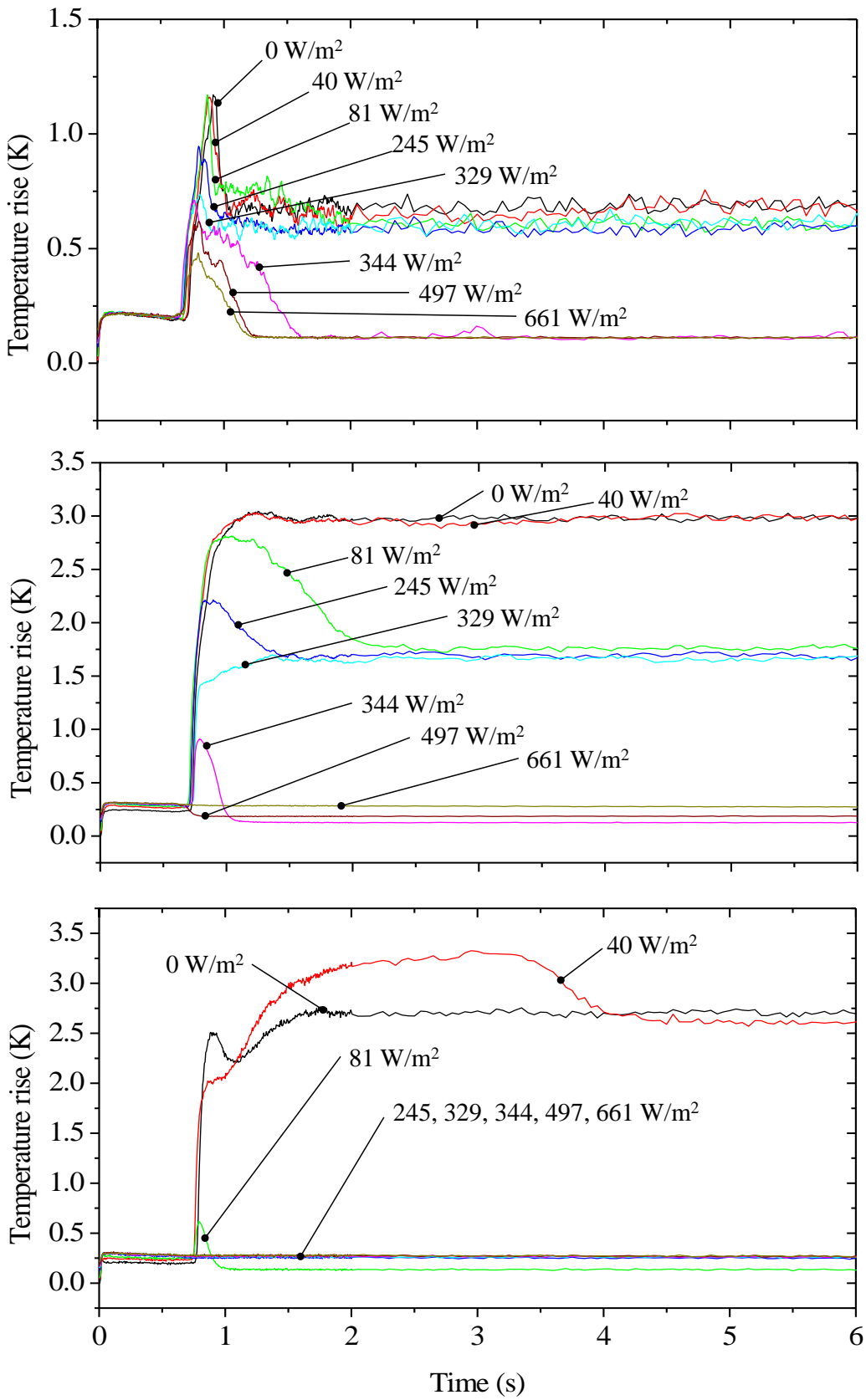
### 6.1.2 Measured time evolution

We selected a few examples of measured series that illustrate different aspects of the effects of initial conditions on the transient evolution. Their temperatures evolutions are presented in Figs. 6.2 to 6.6, and examples of the effect on mass flow rate are presented in Fig. 6.7. The plots have been grouped deliberately to highlight one particular effect at a time. These effects are enumerated and described in section 6.1.3.



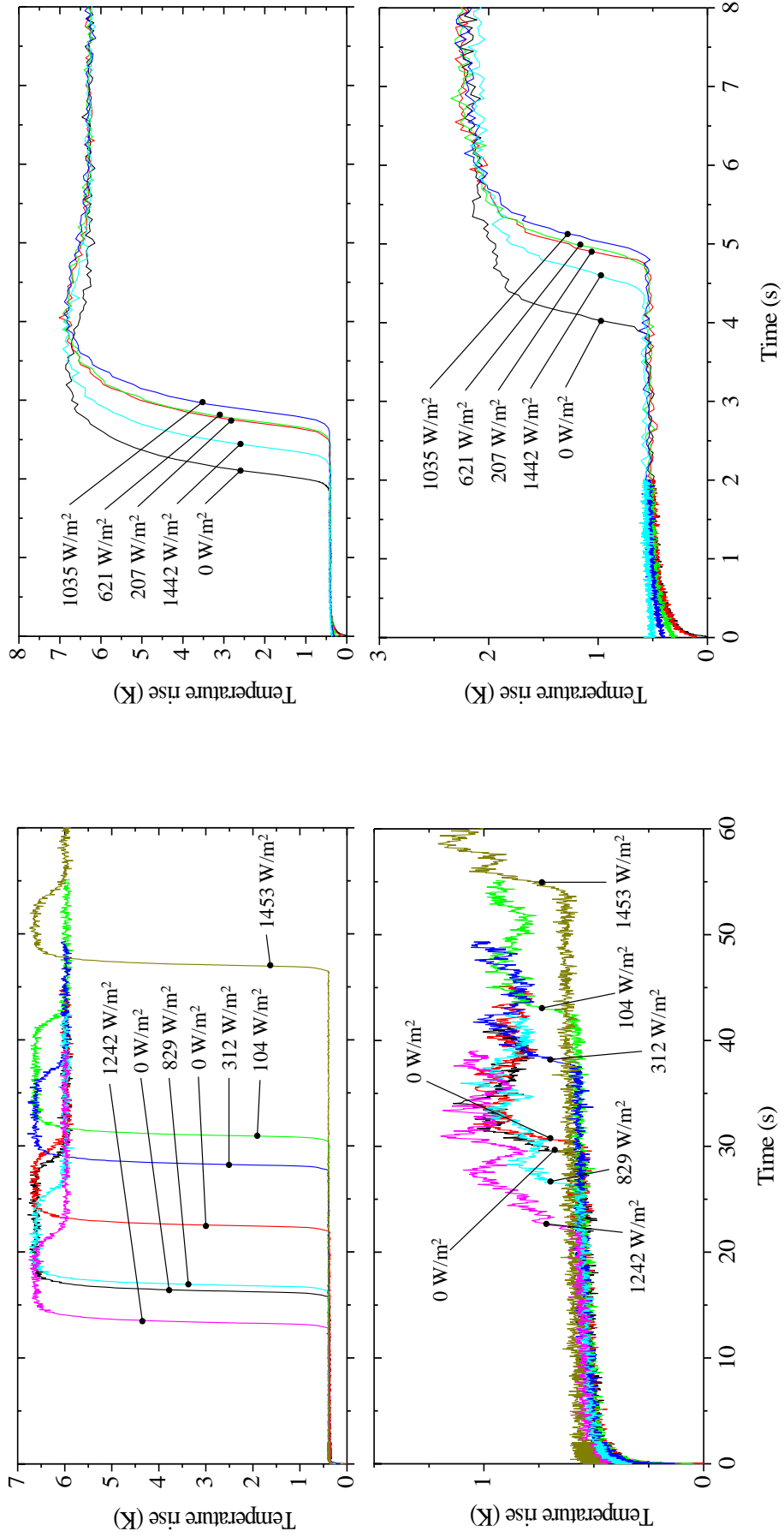
(a) Test section: V10. Top: T5 with  $q_f = 1365 \text{ W/m}^2$ ; bottom: T4 with  $q_f = 1495 \text{ W/m}^2$ . (b) Test section: V06. Top: T5 with  $q_f = 995 \text{ W/m}^2$ ; bottom: T4 with  $q_f = 995 \text{ W/m}^2$ .

**Figure 6.2.** The effect of initial heat flux on time evolution (Part 1). Inhibition of TBC. The parameter on the arrows is  $q_i$  for each case.



Section V06.  $q_f = 1165 \text{ W/m}^2$ . Top: T5; middle: T4; bottom: T3.

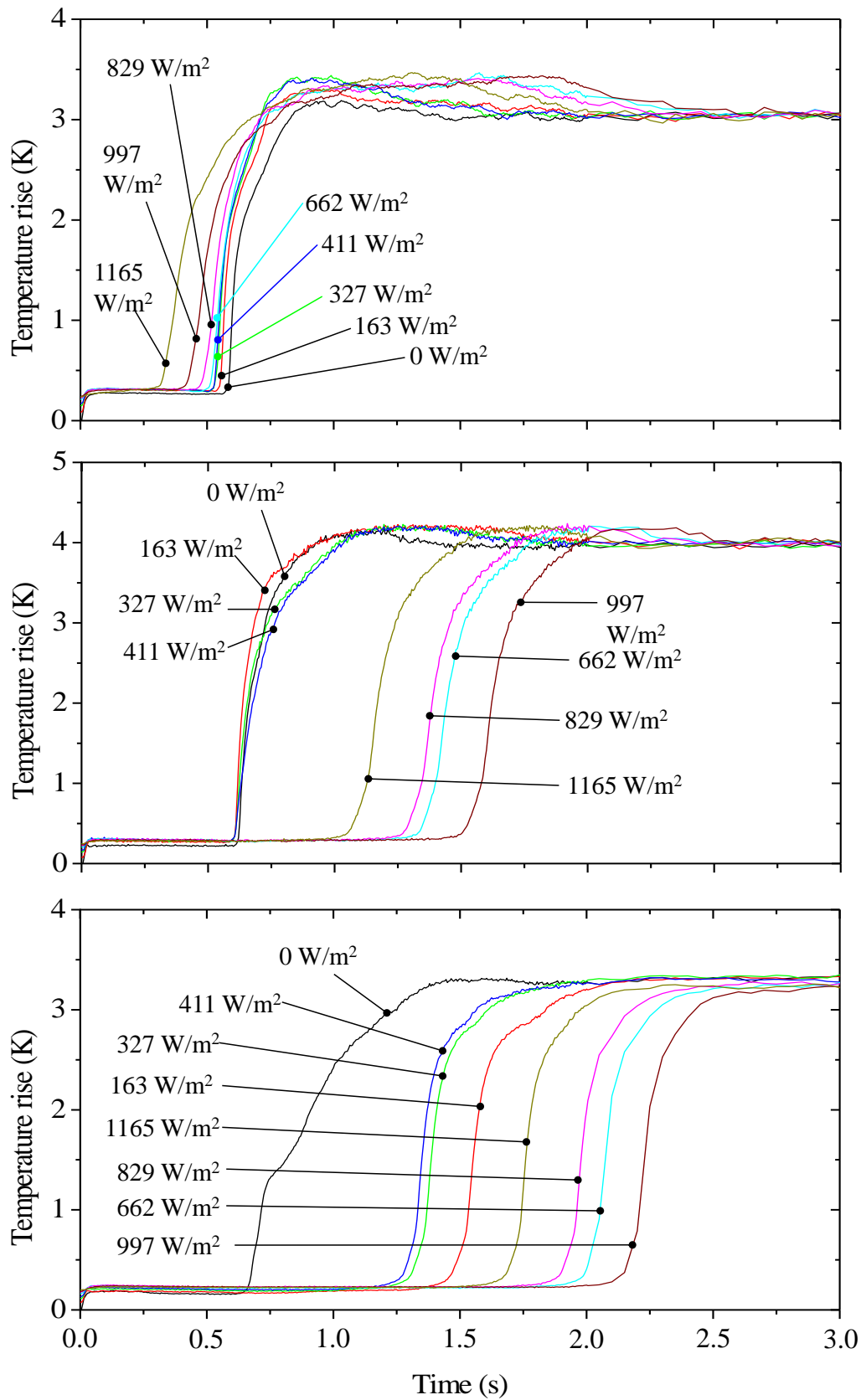
**Figure 6.3.** The effect of initial heat flux on time evolution (Part 2). Inhibition of SBC into TBC and finally into SNB. The parameter on the arrows is  $q_i$  for each case.



(a) Test section: V10.  $q_f = 1760 \text{ W/m}^2$ . Top: T2; bottom: T1.

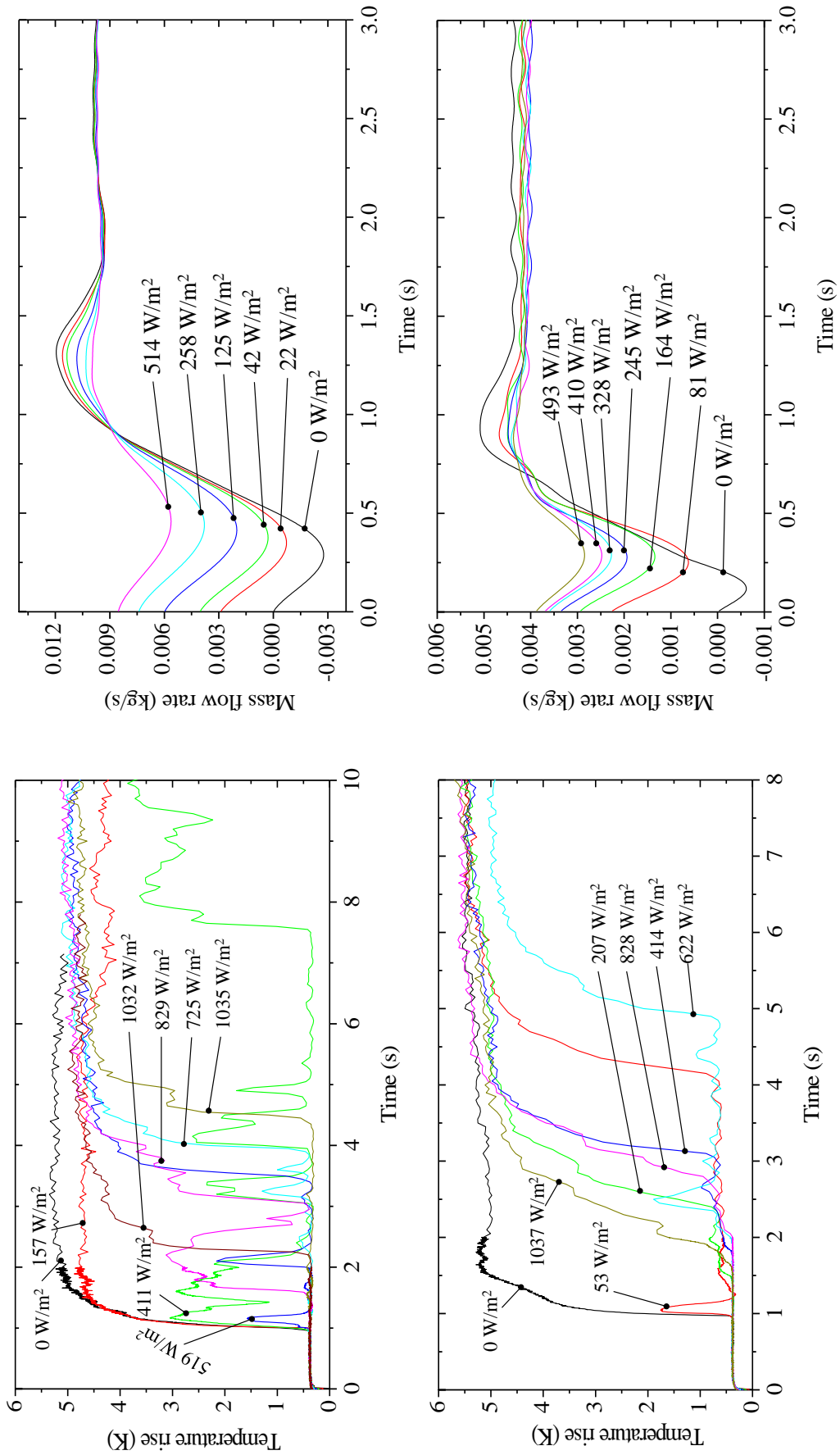
(b) Test section: V10.  $q_f = 1870 \text{ W/m}^2$ . Top: T2; bottom: T1.

**Figure 6.4.** The effect of initial heat flux on time evolution (Part 3). Impact on the high- $t_c$  regime. The parameter on the arrows is  $q_f$  for each case.



Section V06.  $q_f = 1420 \text{ W/m}^2$ . Top: T4; middle: T3; bottom: T2.

**Figure 6.5.** The effect of initial heat flux on time evolution (Part 4). Change of crisis initiation mechanism. The parameter on the arrows is  $q_i$  for each case.



Top: Section V10 with  $q_f = 1546 \text{ W/m}^2$ ; bottom: Section V06 with  $q_f = 1078 \text{ W/m}^2$ .

**Figure 6.7.** The effect of initial heat flux on time evolution (Part 6). Impact on mass flow rate evolution. The parameter on the arrows is  $q_i$  for each case.

Test section: V10. Top: T4 with  $q_f = 1660 \text{ W/m}^2$ ; bottom: T3 with  $q_f = 1760 \text{ W/m}^2$ .

**Figure 6.6.** The effect of initial heat flux on time evolution (Part 5). Change of crisis initiation mechanism. The parameter on the arrows is  $q_i$  for each case.

### 6.1.3 Identification of main effects of initial conditions on transients

The realization of experiments with fixed  $q_f$ , analyzed in terms of increasing  $q_i$ , brought into light the following phenomena:

- initial circulation can completely inhibit temporary boiling crisis (TBC);
- in cases where  $q_{c,p} < q_{c,s}$ , the initial circulation can turn the premature SBC into TBC and finally eliminate it;
- no particular influence on the high- $t_c$  regime could be clearly identified;
- in cases with  $q_f > q_{c,s}$  and initiating crisis by the linear regime at  $q_i = 0$ , the initial circulation can change the boiling initiation mechanism to that of high- $t_c$  regime.

#### Inhibition of temporary boiling crisis

Figure 6.2 shows typical temperature evolutions far from the entrance at  $q_f$  such that  $q_{c,t} < q_f < q_{c,p}$ , i.e. TBC transient type. If for  $q_i = 0$  the temperature evolution showed a stable temperature period before the NB takeover, the increase of  $q_i$  has initially a shortening effect on boiling crisis:  $t_d$  becomes shorter. At the point where the duration of crisis becomes comparable to the temperature increase time, the maximum temperature attained starts decreasing with the increase of  $q_i$ . There exists a value of  $q_i$  for which no longer TBC is observed at all (only NB). This value is going hereafter to be referred to as the *inhibition heat flux*,  $q_{inh}$ . A systematic search of this parameter is going to be presented in section 6.2.

#### Inhibition of permanent boiling crisis

We have already seen in section 5.3.1 that sufficiently far from the entrance, the static initial condition transients could start a permanent boiling crisis at final heat flux lower than  $q_{c,s}$  on V06. This justifies asking the question whether values of initial heat flux exist such that the transient for the same value of  $q_f$  becomes of type TBC or SNB.

Figure 6.3 exemplifies such a situation, which took place only in the experiments with test section V06. At  $q_i = 0$ , T5, T4 and T3 would exhibit premature SBC initiated by the linear mechanism. The increase in initial heat flux rapidly inhibits the occurrence of boiling crisis at T3, first by turning it into TBC, and finally SNB. When no longer SBC happens at T3, the final state downstream, though still in post-CHF regime, shows a visibly different final temperature value (especially for T4). This may indicate that the final position on the section of the CHF boundary has been displaced discontinuously with the continuous increase of  $q_i$ , which produces a non developed heat transfer regime at T4 (T4 contained in the head of the developing region of the vapor film). This could be linked to anomalous hysteresis properties of boiling crisis, already observed in the experiments of previous chapters (see sections 4.2.4 and 5.3.1). The transition from stable to temporary boiling crisis at T4 and T5 happens at the same value of  $q_i$  (between 329 and 344 W/m<sup>2</sup>). Again, this indicates that the hysteresis properties of boiling crisis depend on its spatial extent. The TBC is completely inhibited at T4 at lower  $q_i$  than at T5.

We can see then that the inhibition of SBC and TBC is not of the same nature.

- SBC inhibition is *spatially discreet*: finite length segments of the test section get SBC inhibited by a slight change in  $q_i$ .
- TBC inhibition is *spatially continuous*.

Furthermore, the fact that boiling crisis be stable after a transient seems to be linked with the fact that during the transient, boiling crisis appears at a given position sufficiently close to the entrance so as to *trigger* the hysteresis mechanism that allows it to survive on the downstream segment.

### The high- $t_c$ regime

In those cases where the transient with  $q_i = 0$  shows boiling crisis initiated in the high- $t_c$  regime, the effect of the presence of a non-zero initial heat flux was investigated. Examples of these experiments are presented in Fig. 6.4. No clear trend of the critical time as a function of the initial heat flux was observed. In this regime, the critical time presents a great random dispersion, and the mean value seems only to be linked to the final heat flux.

### Change of boiling crisis initiation mechanism

We have seen that in the case of static initial condition, a given position can exhibit two different boiling crisis initiation mechanism according to the applied  $q_f$ . This was the case of T2 on test section V10, for example (see section 5.3.5). There was a value of  $q_f > q_{c,s}$  such that below it boiling crisis was initiated by the high- $t_c$  regime, and above by the linear regime.

The examples shown in Figs. 6.5 and 6.6 present a related situation. At  $q_i = 0$ , the boiling crisis was initiated by the linear mechanism. When increasing  $q_i$ , in a first time the critical time stays at approximately the same value, however, above some value of  $q_i$ , crisis starts at critical times appreciably higher than the original one, and no correlation is clearly identified between the initial heat flux and the critical time, which fluctuates enormously (in comparison to the linear regime which does not). In the middle and bottom cases of Fig. 6.5 it can fluctuate of as much as 1 s above 500 W/m<sup>2</sup> and 100 W/m<sup>2</sup>, respectively. In Fig. 6.6, for the case at the top above 520 W/m<sup>2</sup> and for the case at the bottom above 100 W/m<sup>2</sup>, it fluctuates of several seconds.

The linear regime can be inhibited by the increase of initial heat flux, as was the case in the previous paragraph in this section; but as  $q_f > q_{c,s}$ , boiling crisis needs to appear eventually by the high- $t_c$  mechanism. Furthermore, the examples presented in Fig. 6.6 put forward the random character of the latter.

## 6.2 Experimental determination of behavior boundaries

The observation of different behavior according to the values of  $q_i$  and  $q_f$  leads us to idea that we can define boundaries on the  $(q_i, q_f)$  planes. Taking into account the experimental observations, the following are the boundaries that we would be searching for:

- *crisis inhibition heat flux*: value of  $q_i$  that separates the regions with and without crisis when at  $q_f < q_{c,s}$ .
- *linear regime boundary*: limits the region of the plane where boiling crisis is started due to the linear mechanism;
- *permanent boiling crisis boundary*: limits the region of the plane where boiling crisis stays at the end of the transient.
- *transient critical heat flux*: separates SNB transients from any other type of transient presenting boiling crisis;

### 6.2.1 Determination of the inhibition heat flux

The inhibition heat flux boundary was determined by observing simultaneously the evolution of maximum and final temperature as a function of  $q_i$  for a fixed  $q_f$  series. If  $q_f < q_{c,s}$ , at  $q_i$  sufficiently high, the final temperature presents low values, corresponding to the final state of nucleate boiling. The criterion considered for defining complete boiling crisis inhibition heat flux was to determine at what  $q_i$ , the maximum temperature curve intersects the final temperature curve at typical NB values. Figure 6.8 illustrates different cases where this criterion can be applied. As  $q_i$  increases and boiling crisis starts being inhibited, the maximum temperature diminishes. Eventually, when no crisis is observed at all, the maximum temperature is practically identical to the final temperature<sup>1</sup>. Thus, the analysis of each series with fixed  $q_f$  produces a point on the plane  $(q_i, q_f)$  that belongs to the searched boundary. The general trend is that as  $q_f$  increases,  $q_{inh}$  increases too. This is shown in Fig. 6.9.

### 6.2.2 Identification of transition between crisis initiation regimes

In order to identify the mechanism conducting to transient boiling crisis, we performed a systematic study of the critical time as a function of initial heat flux. This parameter was obtained from temperature evolutions by the method explained in section 5.3.3. The values we found are plotted for a given value of  $q_f$  value as a function of  $q_i$  with the position as parameter in Figs. 6.10 and 6.12 and for a given position as a function of  $q_i$  with  $q_f$  as parameter in Figs. 6.11 and 6.13.

The positions sufficiently far from the entrance undergo a transition to boiling crisis by the linear regime mechanism when  $q_i = 0$ . As long as a transition to boiling crisis in the linear regime is still possible at  $q_i \neq 0$ , there is a general decreasing trend of  $t_c$  vs.  $q_i$ , for unchanged final power. This is the case of T5 in V10 at all powers, T4 in V10 for  $q_f > 1700 \text{ W/m}^2$  and T3 in V10 for  $q_f > 1900 \text{ W/m}^2$ . However it has been observed that for  $q_f > q_{c,s}$  it can happen that above a given value of  $q_i$ , the  $t_c$  values break the trend and suddenly increase and their distribution becomes stochastic. This is the case of T4 in V10 for  $q_f < 1700 \text{ W/m}^2$  and T3 in V10 for  $q_f < 1900 \text{ W/m}^2$ . The transition by linear regime mechanism is inhibited by the increase of  $q_i$  and, in that case, as  $q_f > q_{c,s}$ , the boiling crisis will set on by the high- $t_c$  mechanism.

### 6.2.3 Identification of the link between the transition regimes and the inhibition of crisis

We have shown that the occurrence of crisis by the linear regime mechanism depends highly on the possibility of the local quality to reach a threshold during the transient; that possibility is ruled by the transit of cold particles from the entrance of the test section. The increase of  $q_i$ , increases the values of inlet velocity during evolution. At low  $q_i$ , inlet velocity is initially positive, it can become negative briefly and finally positive again; if  $q_i$  is high enough, inlet velocity will not be negative at any instant. The effect of this is that transit of the cold inlet front will occur sooner and that the maximum local quality attained at a given point will diminish, as well as its time of occurrence. If the quality value required for starting linear crisis is not reached, this crisis will not happen. The non-occurrence of linear crisis when  $q_f < q_{c,s}$  means the non-occurrence of transient crisis *at all*, since this is the only available mechanism for inducing crisis in this situation either TBC or premature SBC. Thus, the inhibition of transient premature boiling crisis is equivalent to the inhibition of the linear regime at a given position when  $q_f < q_{c,s}$ .

<sup>1</sup>It is slightly higher due to a combination of the initial nucleate boiling onset transient and the noise of the signal

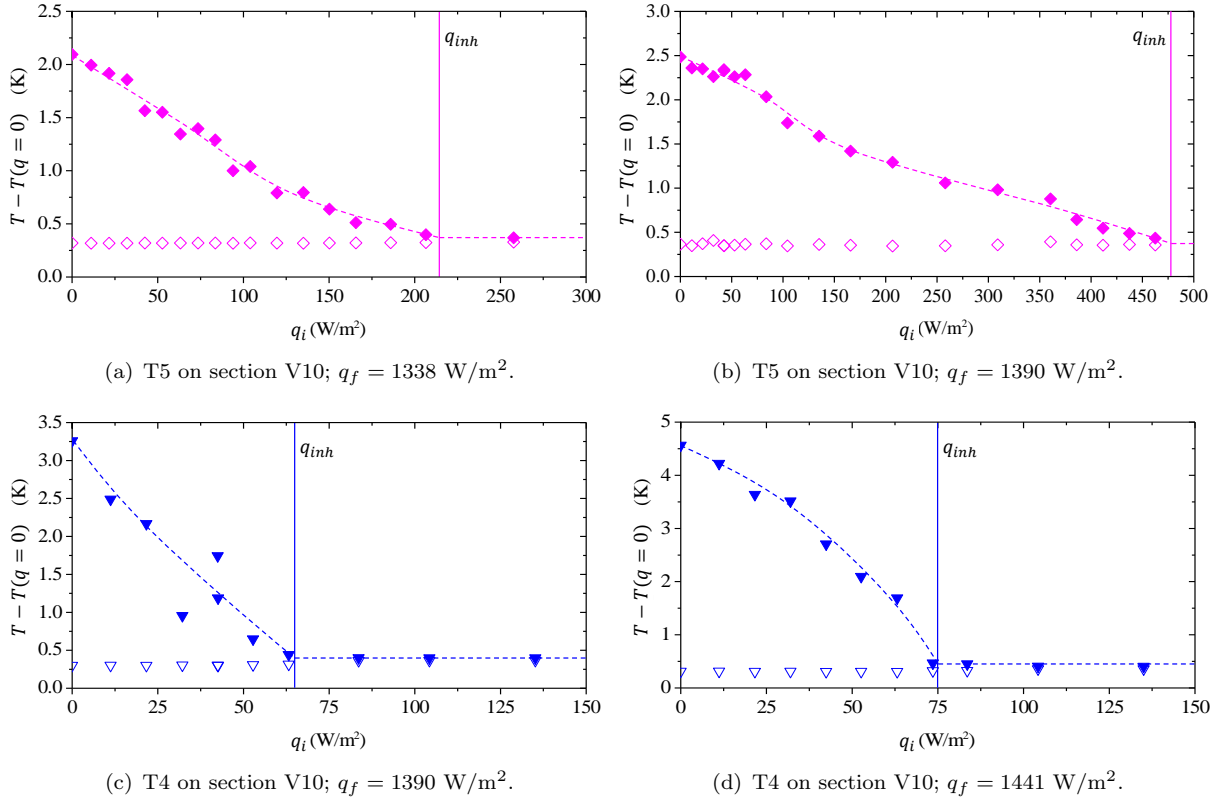


**Figure 6.8.** Criterion for finding the crisis inhibition heat flux.  $\blacklozenge$  T5 maximum;  $\diamond$  T5 final,  $\blacktriangledown$  T4 maximum;  $\triangledown$  T4 final.

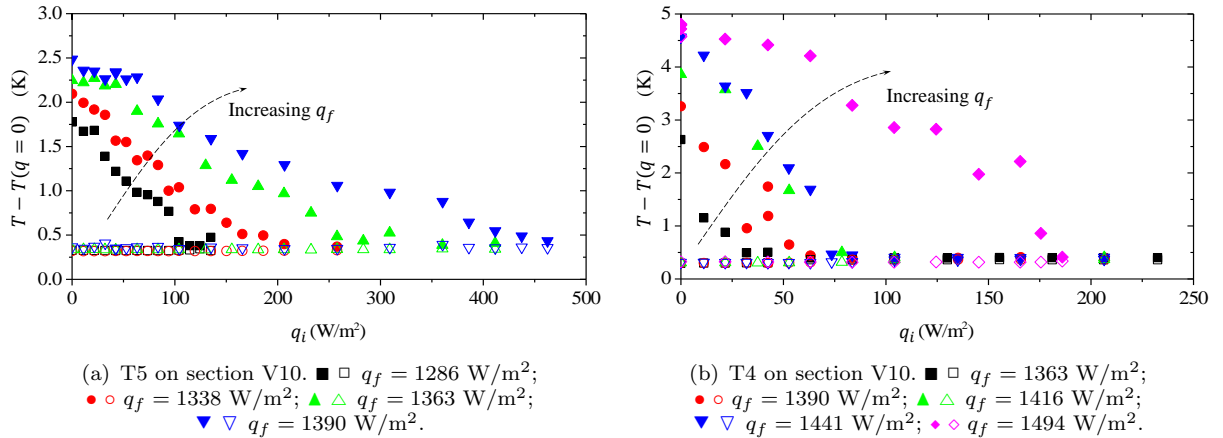


**Figure 6.9.** Effect of  $q_f$  on  $q_{inh}$ . The solid points show maximum temperature, the blank points show final temperature.

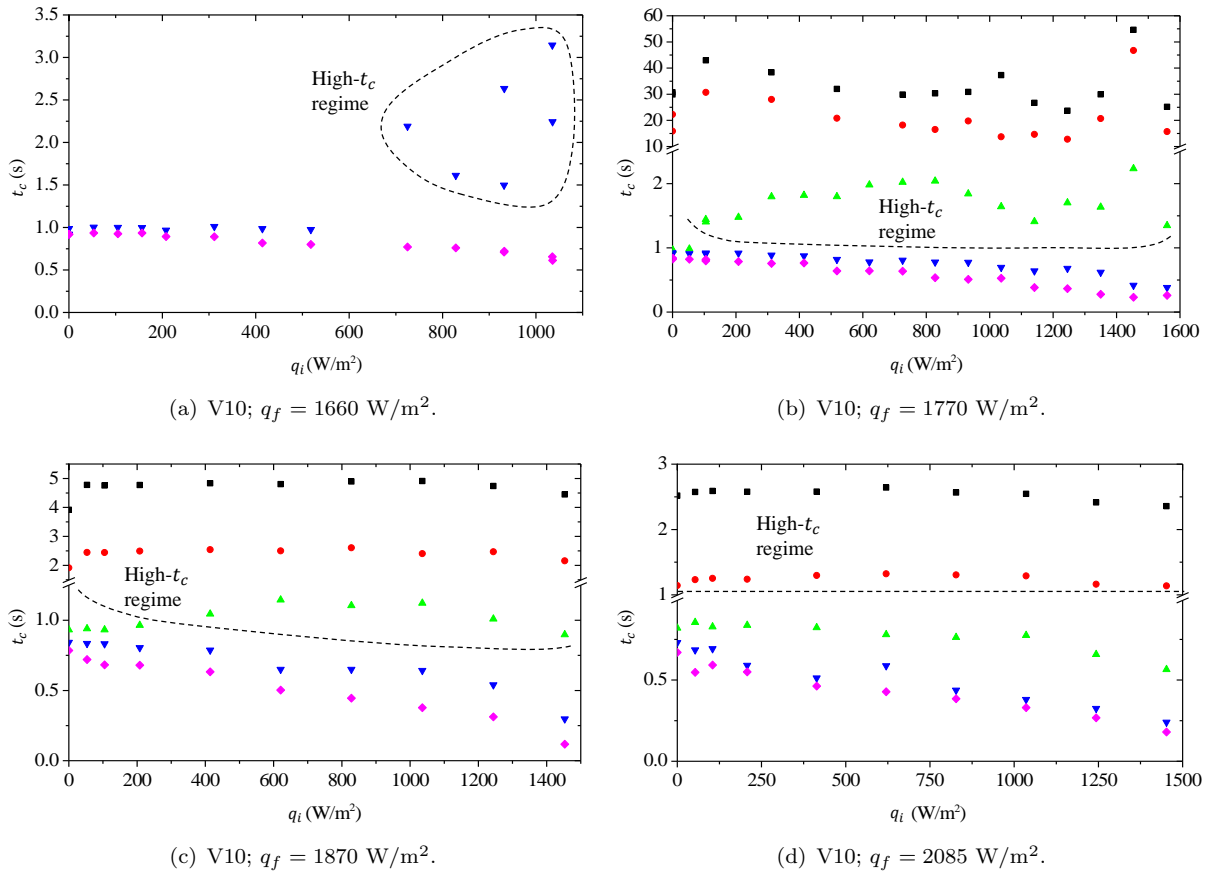


**Figure 6.10.** The effect of initial heat flux on critical time in V10. ■  $T_1$ , ●  $T_2$ , ▲  $T_3$ , ▼  $T_4$ , ◆  $T_5$ .

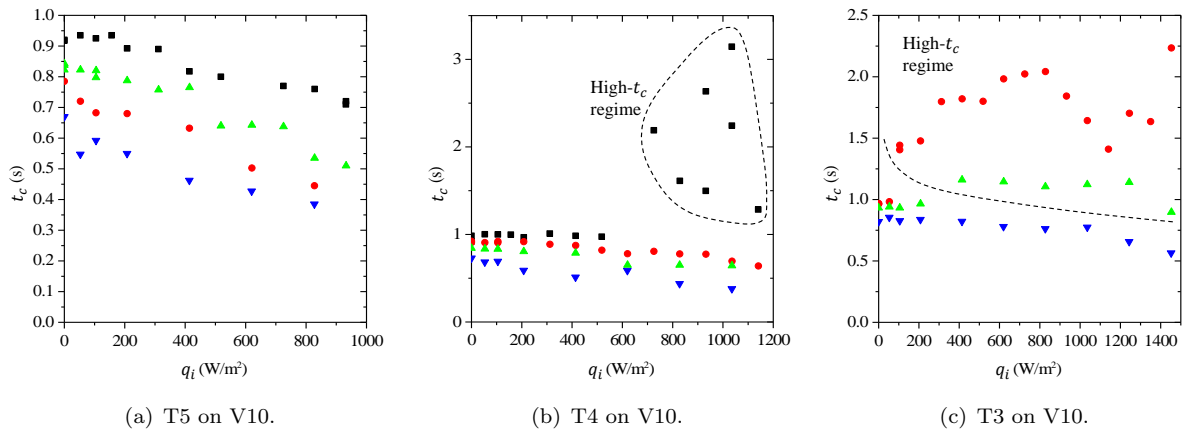


**Figure 6.11.** The effect of initial heat flux on critical time in V10 — linear regime life at a given position as a function of  $q_i$  and  $q_f$ . ■  $q_f = 1660 \text{ W/m}^2$ , ●  $q_f = 1760 \text{ W/m}^2$ , ▲  $q_f = 1870 \text{ W/m}^2$ , ▼  $q_f = 2085 \text{ W/m}^2$ .

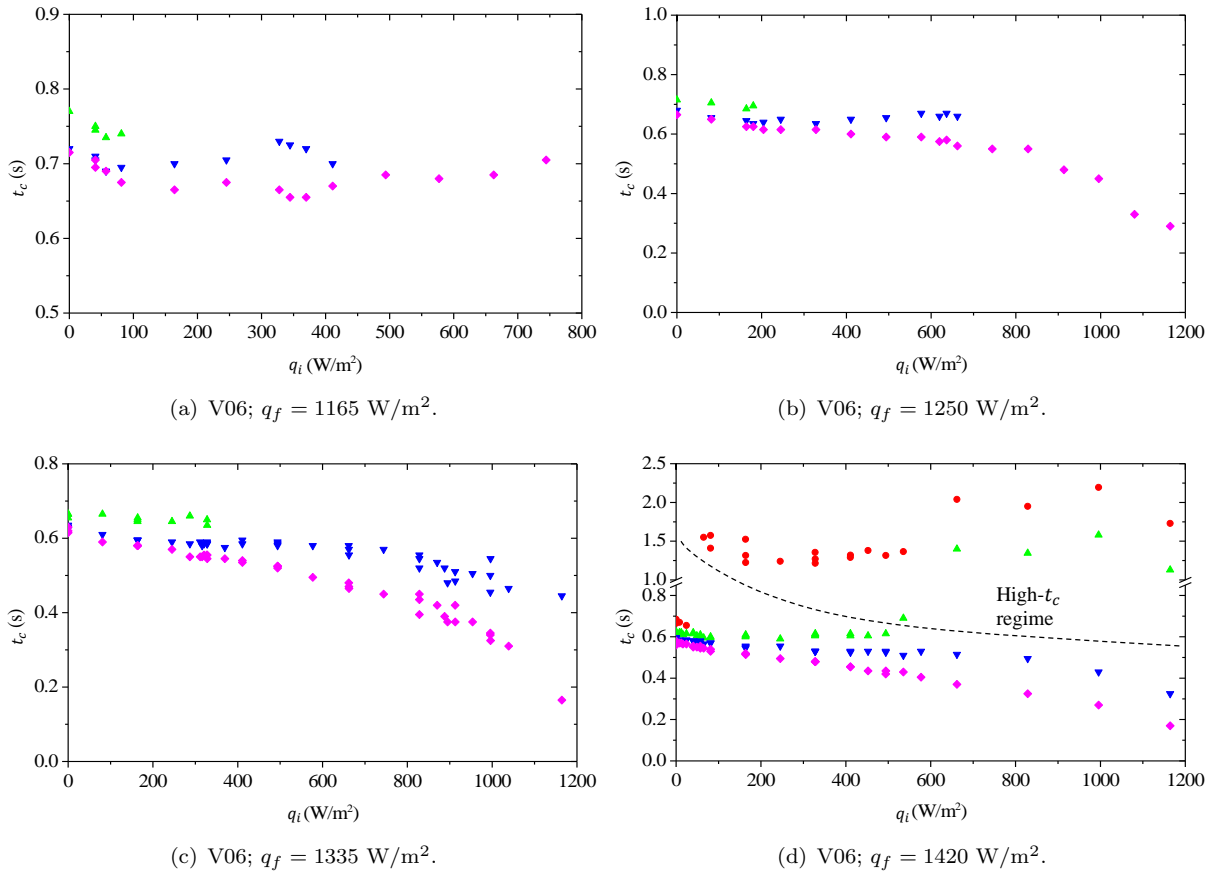


**Figure 6.12.** The effect of initial heat flux on critical time in V06. ■ T1, ● T2, ▲ T3, ▼ T4, ◆ T5.

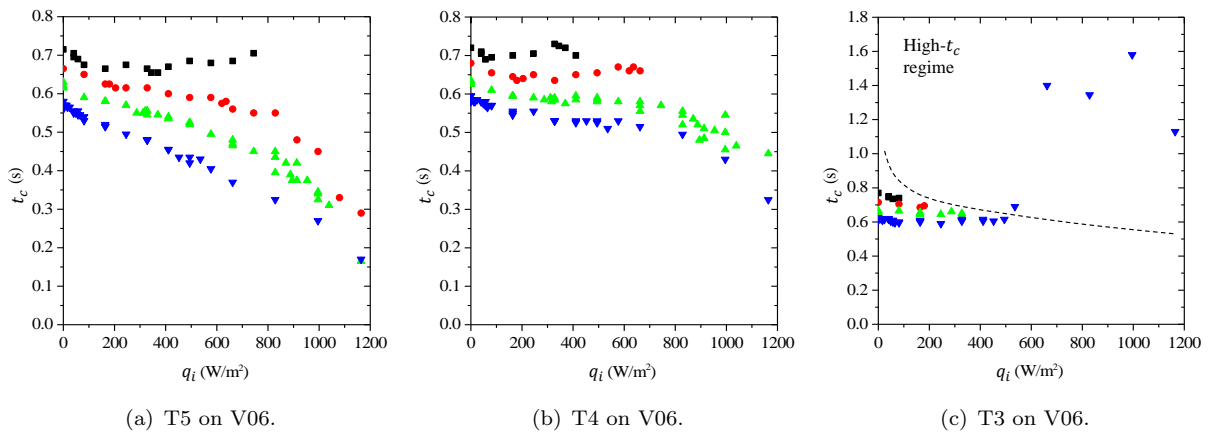


**Figure 6.13.** The effect of initial heat flux on critical time in V06 — linear regime life at a given position as a function of  $q_i$  and  $q_f$ . ■  $q_f = 1165 \text{ W/m}^2$ , ●  $q_f = 1250 \text{ W/m}^2$ , ▲  $q_f = 1335 \text{ W/m}^2$ , ▼  $q_f = 1420 \text{ W/m}^2$ .

The transition between crisis initiation mechanisms at  $q_f > q_{c,s}$  is a consequence of the inhibition of the linear regime too; necessarily boiling crisis needs to happen for  $q_f > q_{c,s}$ , and the elimination of the linear regime trigger leaves its place to the high- $t_c$  regime.

As a result of these two observations, we can only conclude that the two phenomena are of the same nature: they consist on the inhibition of the linear regime crisis initiation mechanism. Thus, there are only two veritable boundaries: that of SBC and that of the linear regime. Their crossing on the  $(q_i, q_f)$  plane can define up to four possible behaviors:

- SNB;
- TBC (always initiated in the linear regime);
- SBC initiated in the linear regime;
- SBC initiated in the high- $t_c$  regime.

If they do not intersect, only three of these will be observed. In the next section we will see the final aspect of these behavior regions in different cases.

#### 6.2.4 Drawing the experimental behavior maps

With the collected information on individual series behavior boundaries, we are in measure of drawing the behavior maps. The resulting maps for T3, T4 and T5 on both test sections, are presented in Fig. 6.14.

The first step was to identify the linear regime boundary. For that, we placed on the  $(q_i, q_f)$  plane the TBC inhibition (solid) and change of mechanism (cross) points determined in section 6.1.3. The linear regime boundary was sketched as a dotted line.

Then, the SBC boundary was determined. Outside the linear regime region, this boundary is given by  $q_f = q_{c,s}$ . Inside the linear regime regime, for V10 experiments showed that the same relation applies. However, for V06, we found SBC at  $q_f < q_{c,s}$  and its boundary is given by the points found in section 6.1.3 (blank points). A dashed line was used to represent the SBC boundary.

Finally a solid line was drawn without adding any new data, but to emphasize the border of the SNB behavior. It is in this region that the operation of the cooling system is safe, i.e. presenting no crisis.

As a general feature, we can see that keeping the heating length almost identical and reducing only the diameter of the heated section, reduces all the limits in terms of final surface heat flux, at a given distance from the entrance. Furthermore, when approaching to the entrance the linear boundary moves upward faster than the  $q_{c,s}$  boundary; this makes the crossing point of these two curves move to the left. In the case of V10, at T3 this point is almost  $q_i = 0$  and for T2 (not in the figure) this point does not exist. The behavior map of T2 in V10 must look like the one schematically represented in Fig. 6.15(a). In fact the point  $q_{lin}$  could be observed in Fig. 5.14(a) at around 2000 W/m<sup>2</sup>. Unfortunately, the amount of data at higher  $q_f$  with  $q_i \neq 0$  is insufficient for drawing the accurate behavior map. In Fig. 6.15(b) we present the opposite situation, in which the whole linear boundary lies below the  $q_{c,s}$  boundary. This situation is impossible, since it would mean that the initial heat flux can be arbitrarily close to the final heat flux and still produce a premature TBC event. The quasi-steady state progression, experimentally tested, contradicts this possibility.

We need to mention that the behavior maps obtained are particular to the natural configuration loop adopted in each experiment. They depend on the length of all the components of

the loop, their diameters, and their disposition. It is necessary to study what is the common denominator of all the cases on the boundary to define a criterion for the incipience of transient boiling crisis. This will occupy the rest of this chapter.

## 6.3 Theoretical study of the system with arbitrary initial condition

Based on the same ideas that gave origin to the analysis exposed in section 5.4.3, in this section a theoretical model is presented in order to simulate the behavior of the fluid system during the transient starting at an arbitrary initial condition.

### 6.3.1 Simplifying Assumptions

It will be assumed that the system is initially at a steady dynamic equilibrium, characterized by the initial mass flow rate  $\dot{m}_0$  and the initial uniform heat flux  $q_i$ . These two quantities define a quality and velocity profile. Once the heat flux changes in a stepwise manner, the mass flow rate will be considered known, and the evolution of quality and position of two-phase mixture fluid particles will be simulated from a simplified version of the mass and energy conservation laws. In this simplification we will ignore subcooling, local pressure variations and kinetic and potential energy changes. Furthermore, the two-phase mixture is assumed homogenous. In these conditions, the assumption of uniform expansion rate  $\Omega$  as in section 5.4.3 can be considered valid.

### 6.3.2 The equations

From the simplifications enunciated above, we obtain a set of differential equations that give a Lagrangian approach. The position  $z(t)$  and quality  $x(t)$  of the particle are given by

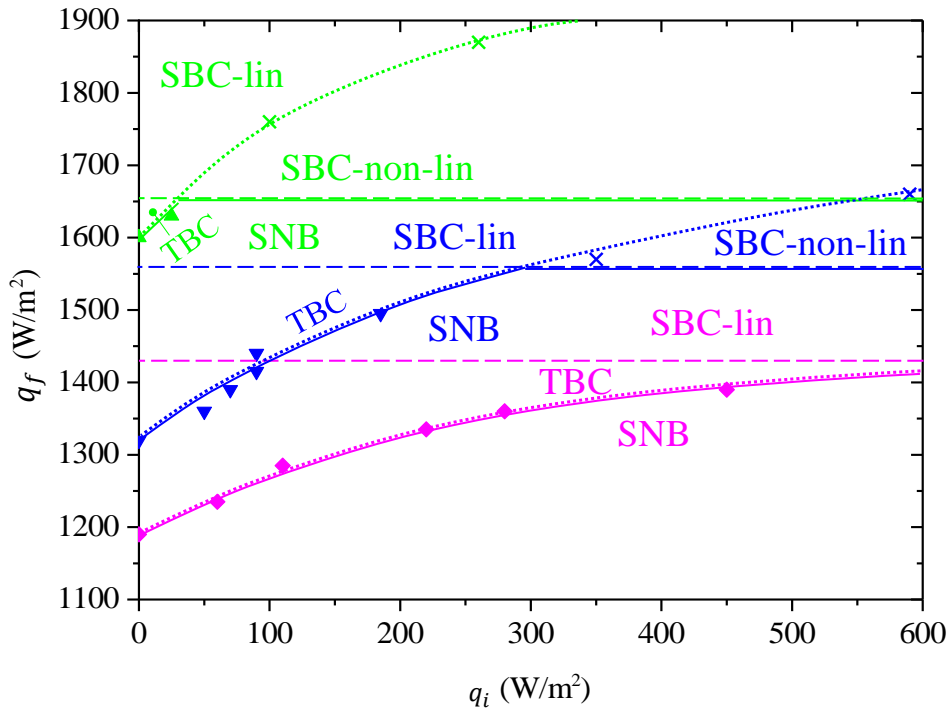
$$u(z, t) = \frac{dz}{dt} = u_0(t) + \int_0^{z(t)} \Omega(z') dz' \quad (6.1a)$$

$$\frac{1}{h_{lg}} \frac{dh}{dt} = \frac{q_v(z)}{\rho(t) h_{lg}} = \frac{dx}{dt} = \frac{q_v(z) v_l}{h_{lg}} + \Omega(z)x(t) \quad (6.1b)$$

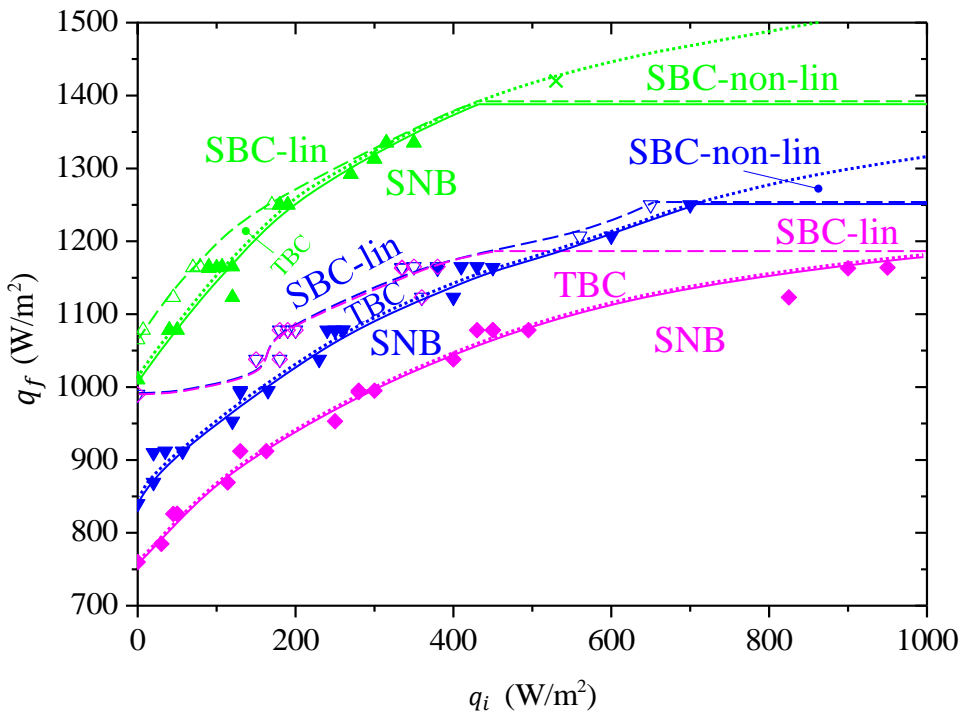
with the following observations:

- The dependence of  $q_v$  and  $\Omega$  on  $z$  comes from the fact that the heating power is non-zero only inside the heated section.  $q_v$  and  $\Omega$  are 0 outside the heated section and have a constant positive value inside (i.e. when  $0 < z < L$ ). This introduces non-linearity in the problem. We remind the reader that  $\Omega = \frac{q_v v_{lg}}{h_{lg}} = \frac{\partial u}{\partial z}$  (demonstrated in app. C.1).
- A particle is chosen with an initial position  $z(0) = z_i$ . Equation (6.1a) can be solved independently of Eq. (6.1b) because no dependence on the quality is present in Eq. (6.1a).
- The choice of  $z_i$  fixes the initial quality  $x_i$  by the equilibrium condition:

$$x_i = \frac{\pi D^2}{4 h_{lg} \dot{m}_i} \int_0^{z_i} q_{v,i}(z') dz'. \quad (6.2)$$



(a) V10.



(b) V06.

**Figure 6.14.** Experimental boiling crisis transient behavior maps.  $\blacktriangle \triangle \times$  T3,  $\blacktriangledown \triangledown \times$  T4,  $\blacklozenge \lozenge$  T5. Solid symbols and solid lines — indicate the boundary for SNB; blank symbols and dashed lines ---, the boundary for SBC; cross symbols and dotted line ·····, delimit the linear regime initiated boiling crisis.

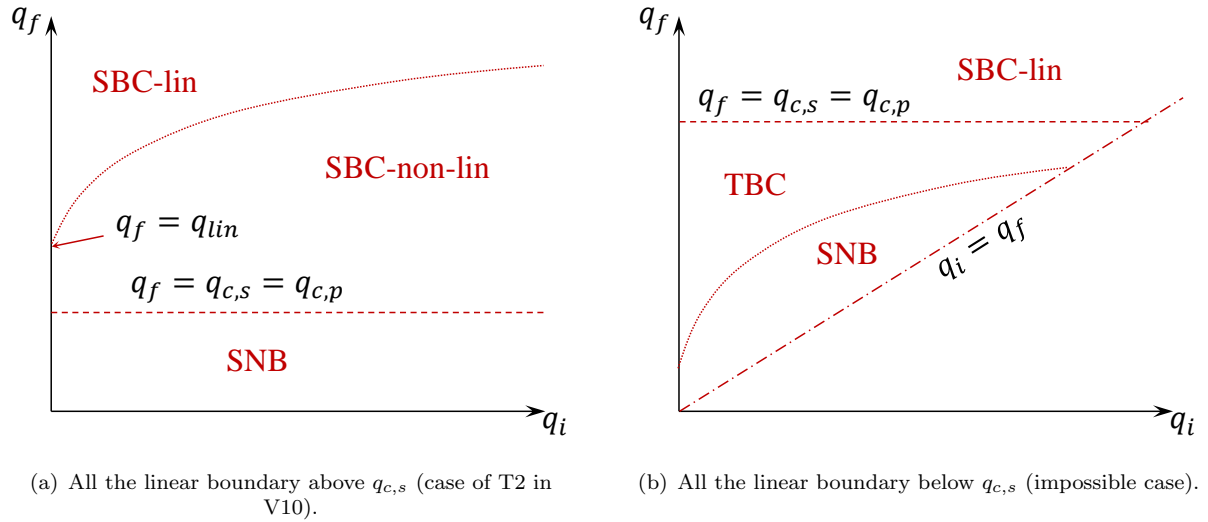


**Figure 6.15.** Behavior maps in which the linear boundary does not intersect the  $q_{c,s}$  boundary.

### 6.3.3 Numerical approach

Even though an analytical solution can be found for the system given by Eq. (6.1) if a mathematical expression of  $u_0(t)$  is known, the discontinuity of heating makes it complicated to analyze all possible cases of initial conditions and evolutions. It was chosen to perform an analysis by solving the equations numerically.

A great number of particles were simulated, with initial conditions inside and outside the heated section. The initial conditions were chosen uniformly spaced on the  $z$  direction. The time advancement of the equations was made by the explicit Euler method.

In order to obtain the dependent variable profiles on a fixed grid, the position of the successive particles was interpreted as a time-variable grid, and the values of the dependent variable were interpolated.

### 6.3.4 Observation of the effect of initial condition on quality evolution

To identify the effects of initial heat flux on the local quality evolution, we solved the equations of the model in section 6.3.2. We used the measured mass flow rate evolution to estimate  $u_0(t)$ , as an input for the model. The measured initial heat flux and mass flow rate allowed calculating the initial conditions of the particles to be simulated. The measured final heat flux was used to evaluate the time derivatives of Eq. (6.1) during the transient. As a result of the simulation it was possible to obtain the time evolution of the quality as a function of position, i.e.  $x(z, t)$ , for experimental cases measured. Some examples of this are presented in Fig. 6.16. The color map represents the quality intensity, the green lines show constant quality level contours, and the white lines the trajectory of some of the individual particles simulated.

A general feature of the obtained quality profiles is the presence of an abrupt spatial slope front (the “cold” front) that travels along the section on a characteristic line on the  $(t, z)$  plane. This front is strongly associated to the particles that are initially slightly upstream from the entrance, given they spend, during the transient, significantly less time in the heated region than those whose initial position was inside. Downstream from this front, the local quality increases exponentially at a given position, and as soon as the cold front reaches the position, the local quality diminishes suddenly.

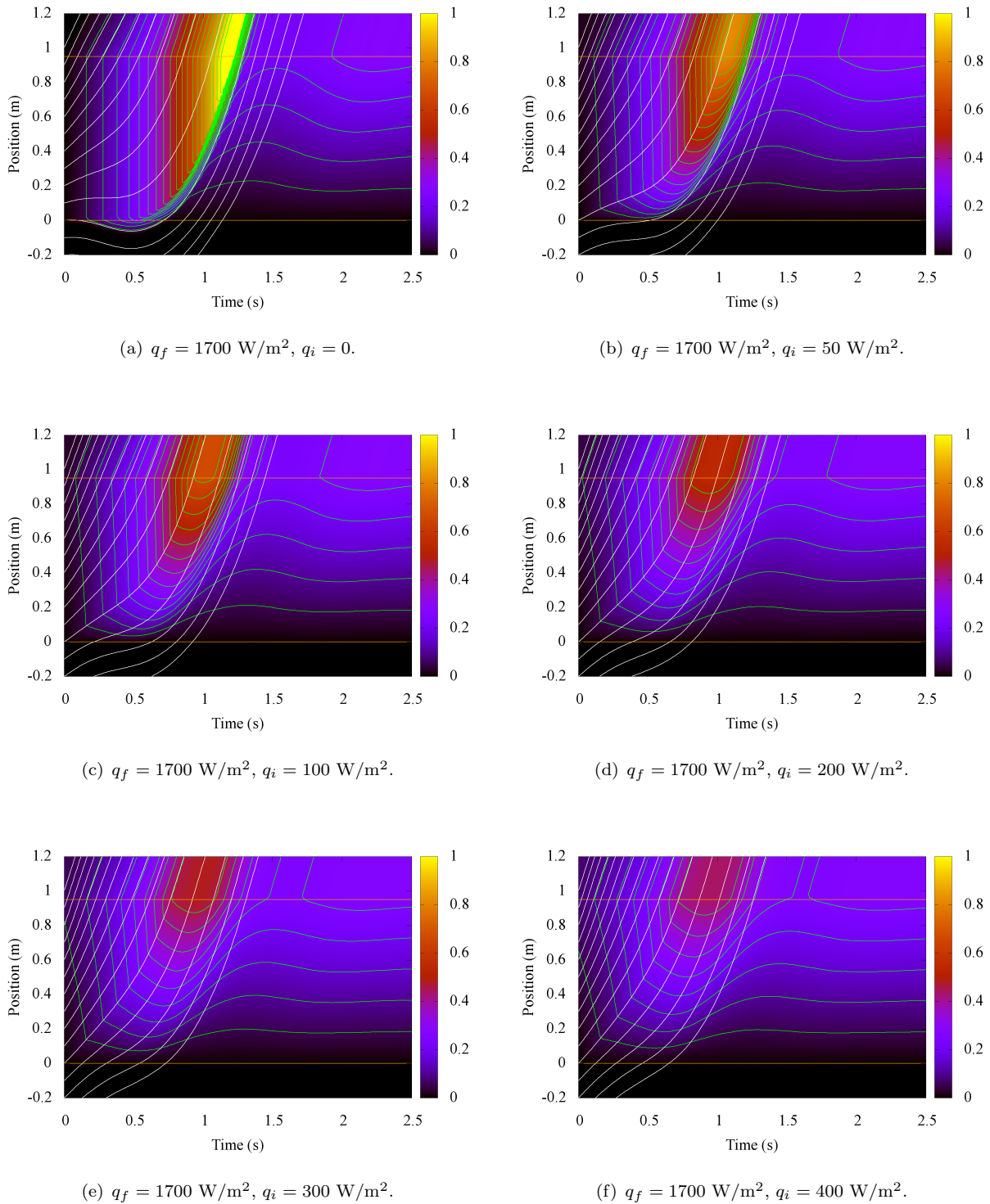


**Figure 6.16.** Simulation of thermodynamic quality for non-static initial condition for V10. White lines: particle trajectories; green lines: level contours of quality.

The intensity of the quality excursion that takes place before the arrival of the cold front is very sensitive to the initial condition of the flow. The existence of a non-zero velocity from the very beginning of the transient both shortens the stay of particles inside the heated section and accelerates the arrival of the cold front to any point of the cross section. As a result, the maximum quality attained at any point of the section is lower as the initial heat flux increases. It could have been argued that the increase of initial heat flux would increase the maximum quality attained because the initial quality increases. The fact is that at low power, the initial mass flow rate responds to power as  $q^{1/3}$  and the values of initial quality are too small to produce any appreciable effect. As the fluid velocity is highly responsive to  $q_i$ , it is this effect that prevails. Nevertheless, at high initial heat flux, the variations of power produce only slight variations of initial mass flow rate; in that case, the increase of initial quality, particularly significant far from the inlet, can have an effect in anticipating the occurrence of crisis, as has been experimentally observed in section 6.1.3, in which Figs. 6.10 through 6.13 show the decreasing trend of  $t_c$  as a function of  $q_i$  for position or  $q_f$  fixed.

We want to point out the fact the overshoot of local quality at a fixed position is the consequence of the diminution of mass flow rate below its initial value, as this has the effect of increasing the transit time of particles from the entrance of the section to a given position. Notice how the contour lines of quality, interpreted as curves  $z = f(t)$ , reflect the shape of the inlet mass flow rate at the right of the trajectory of the particle that initially was at the inlet. If inlet velocity, initially positive, stayed constant (or increased monotonically to a higher value) when power increases, local quality would increase monotonically to the new value in a finite time; a time lapse equal to the transit time of the particle that was initially at the inlet to the position that one is looking at.

## 6.4 Determination of a criterion for boiling crisis initiation

In section 5.4.3 we have shown that for zero initial heat flux there is a threshold quality value that needs to be surpassed during the transient in order to trigger boiling crisis. This had been determined by simulating the evolution of quality from the mass flow rate measurements.

We performed an analogous study for the transients with arbitrary initial condition presented in this chapter. With the model of section 6.3.2 we simulated the quality profile evolution for the cases close to the linear regime boundary presented in fig. 6.14. We observed and compared the simulated quality evolutions between the different experimental cases, paying particular attention at the position at which the boiling crisis is incipient (T3, T4 or T5).

Tables 6.1 and 6.2 summarize all the cases observed and their most relevant parameters: initial and final heat flux, initial mass flow rate, initial and maximal simulated quality, time-averaged simulated quality (Eq. (6.3), see below), measured critical time and time of occurrence of the simulated quality maximum.

Looking at the maximal quality values as the value of  $q_i$  and  $q_f$  increase when moving along the linear crisis boundary line, we realize that the quality threshold for boiling crisis incipience presents a decreasing trend as a function of initial power, as depicted in Fig. 6.17(a). This means that the simple empirical criteria of crisis being triggered by an instantaneous value of quality is not enough. The presence of initial heat flux seems to favor boiling crisis, as it lowers the required maximum quality to obtain it. It is remarkable that the points  $x_{Max}$  vs.  $q_i$  corresponding to different positions lie on the same curve, for a given heated section. Thus a maximal quality criterion for the onset of linear crisis is independent of position, but still depends slightly on  $D$  and  $q_i$ , at low  $q_i$ .

Still guided by the intuitive idea that the vapor exchange between the near-wall region and

**Table 6.1.** *Quality analysis of linear boundary cases for transients with  $q_i \neq 0$ , section V06.*

Position	$q_i$ (W m <sup>-2</sup> )	$q_f$ (W m <sup>-2</sup> )	$\dot{m}_i$ (kg s <sup>-1</sup> )	$x_i$	$x_{max}$	$\langle x \rangle$	$t_c$ (s)	$t_{Max}$ (s)
V10, T3	0	1588	0.00000	0.0000	0.680	0.252	1.07	1.05
V10, T3	0	1612	0.00000	0.0000	0.688	0.255	1.05	1.04
V10, T3	0	1639	0.00000	0.0000	0.698	0.258	1.04	1.03
V10, T3	0	1662	0.00000	0.0000	0.690	0.256	1.02	1.01
V10, T3	0	1664	0.00000	0.0000	0.705	0.260	1.03	1.02
V10, T3	105	1768	0.00556	0.0133	0.395	0.198	0.99	0.83
V10, T3	105	1772	0.00584	0.0126	0.383	0.193	0.98	0.82
V10, T3	208	1769	0.00690	0.0212	0.308	0.174	0.98	0.8
V10, T3	208	1874	0.00686	0.0213	0.342	0.188	0.95	0.79
V10, T3	414	1874	0.00807	0.0361	0.265	0.164	0.95	0.76
V10, T4	0	1303	0.00000	0.0000	0.619	0.233	1.21	1.22
V10, T4	0	1329	0.00000	0.0000	0.623	0.234	1.2	1.2
V10, T4	0	1339	0.00000	0.0000	0.633	0.240	1.19	1.21
V10, T4	11	1338	0.00208	0.0057	0.632	0.241	1.2	1.2
V10, T4	32	1363	0.00352	0.0096	0.520	0.209	1.15	1.07
V10, T4	53	1391	0.00438	0.0128	0.475	0.196	1.13	1
V10, T4	78	1416	0.00519	0.0161	0.434	0.192	1.11	0.97
V10, T4	84	1442	0.00504	0.0176	0.450	0.199	1.1	0.97
V10, T4	176	1495	0.00656	0.0284	0.367	0.188	1.08	0.91
V10, T4	311	1609	0.00783	0.0422	0.320	0.186	1.03	0.86
V10, T4	412	1546	0.00829	0.0527	0.283	0.174	1.05	0.85
V10, T4	518	1663	0.00863	0.0637	0.285	0.185	0.98	0.84
V10, T5	0	1175	0.00000	0.0000	0.634	0.237	1.33	1.37
V10, T5	53	1234	0.00442	0.0164	0.481	0.201	1.28	1.14
V10, T5	104	1286	0.00562	0.0255	0.428	0.187	1.22	1.02
V10, T5	186	1338	0.00656	0.0390	0.381	0.195	1.18	1
V10, T5	283	1363	0.00755	0.0516	0.334	0.189	1.15	0.96
V10, T5	462	1391	0.00838	0.0759	0.298	0.189	1.14	0.92

**Table 6.2.** *Quality analysis of linear boundary cases for transients with  $q_i \neq 0$ , section V06.*

Position	$q_i$ (W m <sup>-2</sup> )	$q_f$ (W m <sup>-2</sup> )	$\dot{m}_i$ (kg s <sup>-1</sup> )	$x_i$	$x_{max}$	$\langle x \rangle$	$t_c$ (s)	$t_{Max}$ (s)
V06, T3	0	1080	0.00000	0.0000	0.427	0.171	0.81	0.74
V06, T3	81	1079	0.00230	0.0164	0.317	0.145	0.81	0.63
V06, T3	81	1163	0.00244	0.0154	0.360	0.163	0.73	0.64
V06, T3	81	1165	0.00236	0.0160	0.355	0.160	0.74	0.63
V06, T3	101	1162	0.00261	0.0180	0.350	0.166	0.73	0.65
V06, T3	180	1250	0.00321	0.0261	0.336	0.174	0.69	0.63
V06, T3	204	1249	0.00309	0.0307	0.387	0.200	0.69	0.69
V06, T3	164	1336	0.00288	0.0264	0.410	0.200	0.65	0.64
V06, T3	328	1336	0.00339	0.0450	0.401	0.217	0.65	0.68
V06, T3	452	1421	0.00407	0.0515	0.244	0.155	0.6	0.52
V06, T3	494	1420	0.00408	0.0562	0.242	0.157	0.6	0.52
V06, T3	577	1420	0.00417	0.0642	0.229	0.154	0.6	0.51
V06, T3	662	1421	0.00425	0.0723	0.213	0.150	0.6	0.49
V06, T4	0	911	0.00000	0.0000	0.448	0.177	0.94	0.9
V06, T4	32	911	0.00174	0.0129	0.416	0.178	0.94	0.87
V06, T4	130	994	0.00280	0.0322	0.321	0.159	0.85	0.71
V06, T4	163	993	0.00300	0.0377	0.309	0.160	0.85	0.71
V06, T4	180	1079	0.00311	0.0401	0.334	0.174	0.78	0.69
V06, T4	204	1079	0.00325	0.0436	0.310	0.166	0.78	0.66
V06, T4	245	1078	0.00330	0.0513	0.368	0.200	0.75	0.76
V06, T4	254	1077	0.00330	0.0533	0.363	0.198	0.75	0.75
V06, T4	369	1162	0.00358	0.0714	0.321	0.193	0.73	0.67
V06, T4	410	1162	0.00364	0.0780	0.304	0.188	0.73	0.65
V06, T4	411	1164	0.00388	0.0732	0.274	0.173	0.7	0.61
V06, T4	494	1164	0.00390	0.0877	0.266	0.177	0.7	0.61
V06, T4	662	1249	0.00389	0.1178	0.288	0.204	0.66	0.62
V06, T4	744	1250	0.00388	0.1328	0.284	0.210	0.66	0.63
V06, T5	0	742	0.00000	0.0000	0.439	0.174	1.09	1.09
V06, T5	8	742	0.00084	0.0087	0.439	0.180	1.09	1.09
V06, T5	40	827	0.00181	0.0205	0.437	0.189	0.99	0.98
V06, T5	49	827	0.00195	0.0229	0.414	0.182	0.99	0.95
V06, T5	278	993	0.00337	0.0759	0.339	0.193	0.85	0.76
V06, T5	295	994	0.00344	0.0788	0.326	0.190	0.85	0.75
V06, T5	493	1078	0.00374	0.1211	0.331	0.221	0.77	0.72
V06, T5	493	1079	0.00390	0.1163	0.303	0.206	0.8	0.68

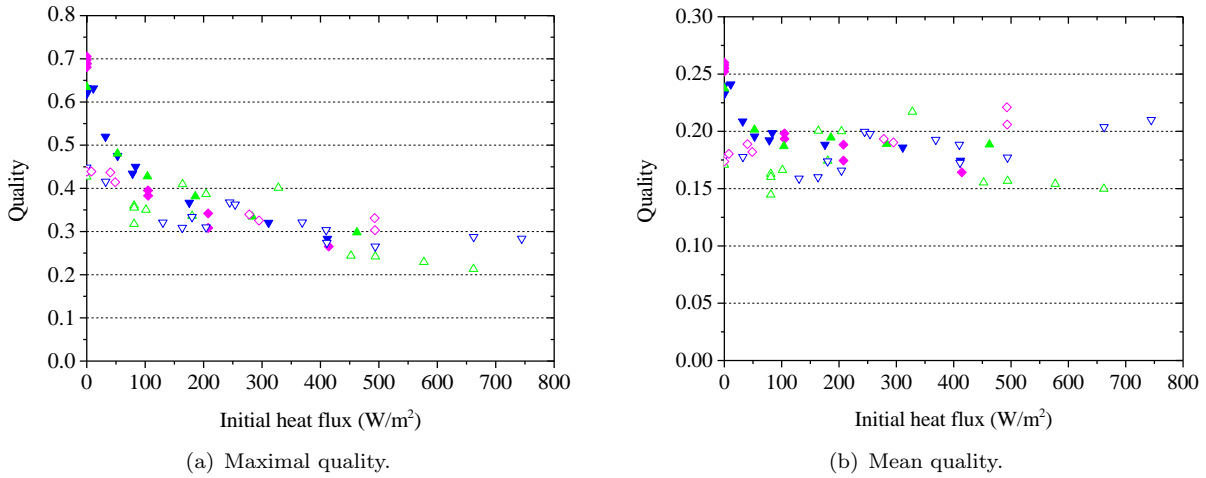


**Figure 6.17.** Simulated transient quality values for incipient cases, as a function of  $q_i$ .  $\blacktriangle$   $T3$ ,  $V10$ ;  $\blacktriangledown$   $T4$ ,  $V10$ ;  $\blacklozenge$   $T5$ ,  $V10$ ;  $\triangle$   $T3$ ,  $V06$ ;  $\triangledown$   $T4$ ,  $V06$ ;  $\diamond$   $T5$ ,  $V06$ .

the bulk is ruled by the bulk quality or void fraction, we calculated the time average of the local bulk quality at the position of interest during the transient,

$$\langle x \rangle (t) = \frac{1}{t} \int_0^t x(t') dt', \quad (6.3)$$

in the monotonously increasing phase, i.e. until the maximum quality takes place:  $\langle x \rangle (t_{Max})$ . This would be representative of how good the vapor removal from the wall could have been in average during the transient; the higher the quality, the worse the removal. A plot of average quality as a function of  $q_i$  is shown in Fig. 6.17(b). Surprisingly, the values obtained do not depend neither on diameter, nor on initial heat flux, and are still independent of position. Except for the cases of  $V10$  at zero power (which will be commented next), in all cases the average values of quality are in the range of 0.16 to 0.22. In fact, the critical mean value with its standard deviation is:  $\langle x \rangle_c = 0.192 \pm 0.028$ .

For the cases with  $q_i = 0$  on  $V10$ , the too high values of maximum quality attained during the transient may be explained by the high difficulty of determining well the very initial evolution of mass flow rates from the Venturi flow-meter. The fact that negative velocities are expected and that the values of pressure drop in those cases are too low make it difficult to correctly interpret the data. Given the exponentially increasing nature of the evolution of quality, small error in the prediction of transit time becomes more influential as time increases.

The relative dispersion of  $\langle x \rangle_c$  is around 15%, specially because of the fact that sometimes for measurements with  $V06$  the best points available are not as close as one would want from the boundary curve. However, it is remarkable that a common denominator of all the incipient cases for both test section and positions is that the average value of quality up to the arrival of the cold front is around this value. If the accumulated average surpasses this value before the arrival of the cold front, boiling crisis by linear regime takes place.

## Summary

With the objective of studying the effect of the initial condition of the loop on its transient behavior in the case of a sudden power injection, experiments were conducted on our loop with the two test sections. In these experiments there were two parameters controlled:  $q_i$  and  $q_f$ . Our attention was particularly directed to the incipience of boiling crisis power range.

The analysis of experimental data allowed identifying qualitative effects of initial heat flux on transient behavior at a given final heat flux. Premature (when  $q_f < q_{c,s}$ ) temporary boiling crisis reduces its intensity and duration as  $q_i$  increases. There is a value of  $q_i$  that inhibits it totally. This has a secondary effect in the particular case of V06, which is the inhibition of premature stable boiling crisis. We remind the reader that both premature boiling crisis events are linked to the bulk-dominated linear regime. The increase of initial power increases the instantaneous values of mass flow rate during the initial stage of the transient, reducing the transit time of the cold front. This reduces the values of void fraction attained during the transient, inhibiting this type of transition to boiling crisis. The effect of this could also be observed for  $q_f > q_{c,s}$ ; in several cases, the increase of  $q_i$  inhibited the occurrence of the bulk-dominated boiling crisis, producing a later onset of boiling crisis in the high- $t_c$  regime.

From all these observations we constructed behavior maps on the plane  $(q_i, q_f)$  on which we identified the four observed types of transient: SBC initiated by bulk-dominated regime, SBC initiated in high- $t_c$  regime, TBC (necessarily initiated by bulk-dominated regime), and SNB.

In order to find a unified and simple criterion to predict the incipience of boiling crisis, we simulated the evolution of the quality spatial profile for all the cases near the experimental boundary of the bulk-dominated regime. We used as input for the simulation the experimental data of mass flow rate evolution. These simulations revealed that the maximum quality of the incipient transients depends on the initial conditions, but the accumulated time average of local quality is a constant that does not depend on diameter, nor position, nor initial conditions. The value of the critical accumulated mean quality is  $0.192 \pm 0.028$ .

Thus, we have found an extremely simple empirical criterion that could be used for predicting the transient behavior during rapidly increasing power inputs regarding boiling crisis by bulk-dominated regime. This criterion summarizes a great amount of experimental evidence. Nevertheless, it relies on the fact that one knows *a priori* the mass flow rate evolution of the system. If the criterion is to be applied for design purpose, it is necessary to count with a reliable tool to estimate it. In chapter 7 we are going to present options for the modeling of the thermohydraulics of a two-phase helium natural circulation loop.



## Chapter 7

# Modeling of the boiling helium loop in transient regime

With the experiments presented in previous chapters it has become evident that the transient evolution of the mass flow rate and the velocity profile plays a major role in transient boiling heat transfer and, in particular, in the transition to boiling crisis. When designing new systems it is desirable to count with model and calculation tools that can predict quite reasonably the thermohydraulics of the cooling system. In answer to this need, in this chapter we present our exploration among some options for modeling the response of a two-phase boiling helium natural circulation loop to sudden power step pulses.

In section 2.4.2, we have seen that the helium properties are such that in most cases the two-phase mixture can be treated as homogeneous. Thus we are going to take as a starting point for our models the 1D homogeneous equilibrium flow model (HEM). In this chapter, we will devote our attention to the solution of this set of equations both analytically and numerically. We will start by defining a 1D domain that represents the elements present in the loop, in section 7.1. Then, in section 7.2, we will study analytically the system of equations, with some additional assumptions particular to our problem, and reach a simplified model. In section 7.3 the implementation of the simplified model in COMSOL is presented. With the aim of improving the predictions of experimental data, in section 7.4 we will also present a numerical method to solve the partial differential equations without any simplification. At each stage, we contrast the solutions provided by our models with the experiments and discuss the limitations of these modeling options. Finally, the quality criterion for the incipience of boiling crisis is evaluated using the mass flow rate evolutions provided by these models in section 7.5.

### 7.1 Representation of the loop in 1D

Given that a natural circulation loop is basically composed by tubes with a diameter much smaller than their length, it is reasonable to take the one-dimensional assumption. In this section we present 1D version of the loop.

The system of interest, depicted in the center of Fig. 7.1, can be divided into the following components:

- phase separator;
- descending branch or down-comer;
- horizontal adiabatic section;

- a vertical adiabatic entrance section;
- heated or test section;
- non-heated riser.

The phase separator will not be included in our model as it is not a duct-type element; it can be considered that it has a big enough volume so that its internal pressure and liquid level are constant in time for the short time scale of the transients. Each of the other elements are represented as tubes of constant or variable cross section area.

The 1-D domain is divided into consecutive segments each representing a tube. The way in which the loop is transformed into a 1D domain is schematized in Fig. 7.1. Let  $s$  be the name of the coordinate for the position on this 1D domain. The local value of gravity acceleration can be  $g$ ,  $0$  or  $-g$ , according to the vertical orientation of each element:

$$\mathbf{g} \cdot \hat{e}_s = \begin{cases} g & \text{if } -L_d - L_u - L_e < s < -L_u - L_e \text{ vertical down-comer section} \\ 0 & \text{if } -L_u - L_e < s < -L_e \text{ horizontal down-comer section} \\ -g & \text{if } -L_e < s < L_h + L_r \text{ vertical heater and riser sections} \end{cases} \quad (7.1)$$

Analogously, the heat generation is defined as:

$$q = \begin{cases} q_0(t) & \text{if } s \in (0, L_h) \text{ vertical heater} \\ 0 & \text{if } s \notin (0, L_h) \end{cases} \quad (7.2)$$

These equations let the reader guess that we placed the  $s = 0$  at the entrance of the vertical heated section. On the negative side we place the down-comer, with a total length of  $L_d$ , the horizontal section of length  $L_u$ , and the non-heated entrance of length  $L_e$  right before  $s = 0$ . The vertical heated section, with length  $L_h$ , and the riser, immediately afterward, with a length  $L_r$ , are on the positive side.

The components may have different cross section areas, which is taken into account in the model, as it can have important consequences on both transient behavior (mainly inertial effects) and steady behavior (introduction of pressure drops).

## 7.2 Development of a simplified model

The analytical treatment of Eqs. (2.28) or (2.29), in conjunction with (2.31) is difficult, if not impossible. Some additional simplifying assumptions shall be made that will allow us getting a deeper insight of the unsteady behavior of the dynamic system at a low algebraic cost.

Unless explicitly stated, given the characteristics of the elements of the loops that we want to represent, in the following paragraphs the cross section of the tubes is considered uniform inside each tube element, i.e. the equations considered are the system in Eq. (2.29).

### 7.2.1 Simplification of the equations

#### Mass and energy conservation

The mass conservation equation can be manipulated in order to find the Lagrangian time derivative of the density:

$$\frac{D\rho}{Dt} = \frac{\partial\rho}{\partial t} + u \frac{\partial\rho}{\partial s} = -\rho \frac{\partial u}{\partial s}. \quad (7.3)$$

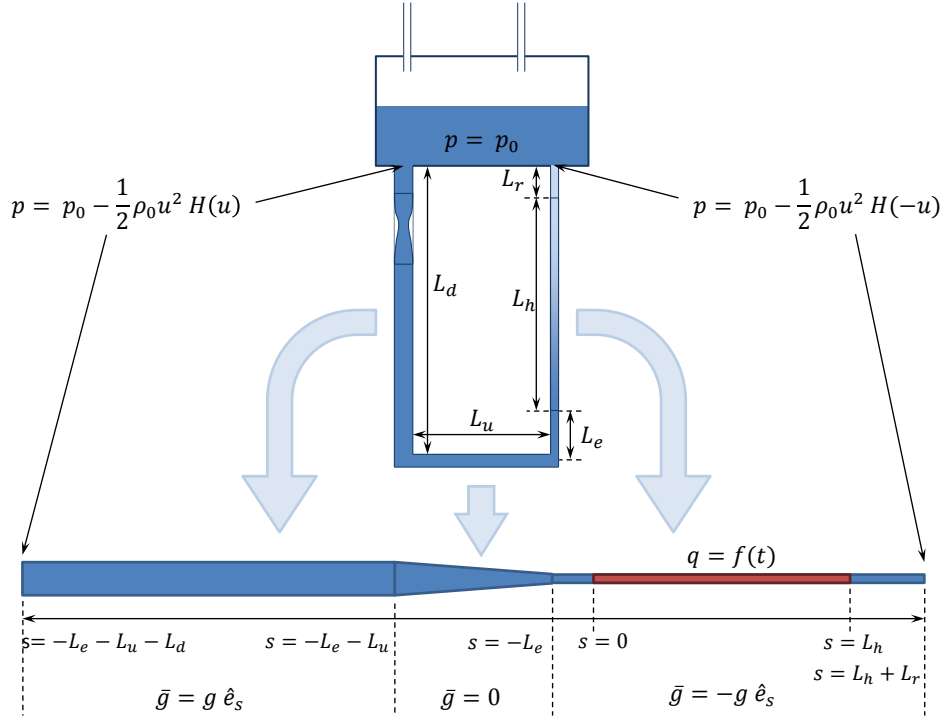


**Figure 7.1.** Transformation of the loop into a 1D domain.

We will consider the case in which *the fluid is incompressible, with varying density*, i.e.:

$$\rho = f_\rho^h(h) = \begin{cases} \rho_l & \text{if } h < h_l \\ \left( \frac{h-h_l}{h_{lg}\rho_g} + \frac{h_g-h}{h_{lg}\rho_l} \right)^{-1} & \text{if } h_l < h < h_g \end{cases} \quad (7.4)$$

where the properties are considered *constant* at the values they would have at initial system pressure, taken as that of the phase separator. This choice is justified by the fact that pressure variations are not expected to be more important than a few millibars (except for only the first one or two hundreds of milliseconds) and that the effect of these slight pressure variations through  $\frac{\partial f_\rho^{h,p}}{\partial p}$  is one or two orders of magnitude smaller than that of typical enthalpy variations along the heated section.

In this frame, when the fluid is a two-phase mixture, i.e. beyond the saturation enthalpy, *variations of  $\rho$  and  $h$  are linked*:

$$\delta\rho = -\rho^2 \frac{v_{lg}}{h_{lg}} \delta h. \quad (7.5)$$

We now refer to the energy conservation equation. In this analytical study, we will consider that the fluid is at its liquid saturation point at the inlet of the heated section, i.e. *we will neglect subcooling*. This is justified by the following facts:

- When the system is not actively cooled and the surroundings are hotter, the liquid will reach saturation at the free surface in the phase separator.
- In steady state, for heat flux higher than 100 W/m<sup>2</sup> for the 10 mm section, the subcooled entrance length is less than 10 cm, rapidly decreasing approximately as the inverse of power.
- The height of the experimental loop is around 1.4 m. The hydrostatic pressure of liquid in this situation is around 1700 Pa. The resulting subcooling is around 20 mK, at most,

and the necessary amount of energy to reach saturation is only 0.08 J/g. With heat flux as low as 100 W/m<sup>2</sup> for the 10 mm section, reaching the saturation point would take less than 250 milliseconds at the bottom of the section, and this time decreases as the inverse of power.

The no-subcooling assumption will be more accurate as the power applied to produce the transient is higher. For very low power values, subcooling will become influential in time evolution, as the time to reach saturation point sets a period over which no appreciable density variations are observed. We should mention that, for simplification, we are assuming *no subcooled boiling* takes place.

If heat income is sufficiently high, *the kinetic energy terms can be neglected* in Eq. (2.29c). This will be generally true given they don't have an extremely fast evolution and from experiments we have found that this term is at least 100 times less significant than heating power, above 100 W/m<sup>2</sup>. Additionally, as the upper reservoir has a great volume in comparison with the heated section, *local pressure is not expected to show great time derivatives*, except maybe for the very initial instants of time right after a power step, i.e. the time it takes the sound to propagate in the section, to propagate pressurization information, and the relaxation of pressurization by expansion. This allows us to rewrite the energy equation as:

$$\begin{aligned} \frac{\partial \left[ \rho \left( h - \frac{p}{\rho} \right) \right]}{\partial t} + \frac{\partial (\rho u h)}{\partial s} &= q_v + \rho (\mathbf{g} \cdot \mathbf{u}) \\ \frac{\partial (\rho h)}{\partial t} + \frac{\partial (\rho u h)}{\partial s} &= q_v + \rho (\mathbf{g} \cdot \mathbf{u}). \end{aligned} \quad (7.6)$$

We recall that  $q_v$  is the volume-specific power defined as  $\frac{4q}{D}$ . Finally, the application of the mass conservation equation to the left term of Eq. (7.6) gives:

$$\rho \left( \frac{\partial h}{\partial t} + u \frac{\partial h}{\partial s} \right) = q_v + \rho (\mathbf{g} \cdot \mathbf{u}). \quad (7.7)$$

Once more, an estimation from the dimensions in our experiments let us assume that *the gravity term can be neglected in the energy equation*, as being smaller than 5% of the heating power for almost any practical case (more than 50 W/m<sup>2</sup> for the 10 mm diameter tube).

Under all the enumerated assumptions, we reach the simplified version of the energy conservation equation

$$\frac{Dh}{Dt} = \frac{\partial h}{\partial t} + u \frac{\partial h}{\partial s} = \frac{q_v}{\rho}. \quad (7.8)$$

The association of Eq. (7.8) with Eqs. (7.3) and (7.5) gives

$$\frac{D\rho}{Dt} = -\rho^2 \frac{v_{lg}}{h_{lg}} \frac{Dh}{Dt} = -\rho \frac{v_{lg}}{h_{lg}} q_v = -\rho \frac{\partial u}{\partial s}, \quad (7.9)$$

which implies two things:

$$\frac{\partial u}{\partial s} = \frac{v_{lg}}{h_{lg}} q_v = \Omega \quad (7.10)$$

and

$$\frac{D\rho}{Dt} = -\Omega\rho. \quad (7.11)$$

In words, under the exposed assumptions, no matter if during transient or at steady state, the velocity profile in the heated section is linear with the position and its slope is directly

proportional to local power; furthermore, velocity is uniform in non heated sections (down-comer and riser). This is what is to be expected in an incompressible fluid. As a result, the velocity profile in the heated section can be expressed as:

$$u(s, t) = u_0(t) + \Omega s, \quad (7.12)$$

where  $u_0$  is the velocity at the inlet of the heated section. At non heated points of the circuit, where the cross section is uniform, the velocity field will be spatially uniform, i.e.

$$u(s, t) = u_S(t), \quad (7.13)$$

where the index  $S$  denotes any particular non-heated section. For the particular case of this loop, the whole down-comer is non-heated, and with a uniform velocity field  $u_d(t)$ . The same is true for the entrance section or riser section, with uniform velocities  $u_e(t)$  and  $u_r(t)$ , respectively.

If no heating is present at a cross section change point,  $\frac{D\rho}{Dt} = 0$ . Taking into account Eq. (2.28a) at a cross section change point:

$$\frac{\partial \rho}{\partial t} + \frac{1}{A} \frac{\partial (\rho u A)}{\partial s} = \underbrace{\frac{\partial \rho}{\partial t} + \frac{u A}{A} \frac{\partial \rho}{\partial s}}_{\frac{D\rho}{Dt}=0} + \frac{\rho}{A} \frac{\partial (u A)}{\partial s} = 0 \implies \frac{\partial (u A)}{\partial s} = 0. \quad (7.14)$$

Thus the relation of velocities and areas on the two sides of a diameter change point is:

$$u_1 A_1 = u_2 A_2. \quad (7.15)$$

This allows reducing the number of unknowns of the system, by reducing the number of parameters of the velocity profile. It is convenient to refer all the velocities present in the system to the inlet velocity of the heated section,  $u_0$ , taken as the reference velocity. Thus for the different elements it gives the following:

- Down-comer

$$u_d(t) = \frac{A_h}{A_d} u_0(t) \quad (7.16)$$

- Horizontal section

$$u_u(t) = \frac{A_h}{A_u} u_0(t) \quad (7.17)$$

- Entrance

$$u_e(t) = \frac{A_h}{A_e} u_0(t) \quad (7.18)$$

- Riser

$$u_r(t) = \frac{A_h}{A_r} (u_0(t) + \Omega L_h). \quad (7.19)$$

We should note that, at sudden power changes,  $\Omega$  will change suddenly, with which the velocity profile will necessarily show time discontinuities. We will address this point later, in section 7.2.2.

### The momentum equation

The time evolution of the velocity field is ruled by the momentum equation. Our aim is to find an evolution law for the integral loop momentum, as has been done in other works intending to simulate two-phase natural circulation loops [78]. Let us define the loop *momentum integral* as:

$$H = \int_{loop} \rho u \, ds. \quad (7.20)$$

The momentum equation can be integrated in the domain to obtain the  $H$  evolution law. However, before doing this, it is necessary to consider that not all the sections of the loop have the same internal diameter and cross section. This plays a very important role in the pressure balance, given that cross section changes imply quasi-instantaneous (from the point of view of the particle) fluid acceleration (kinetic energy changes) at expense of some pressure gradient. The manipulation of Eq. (2.28b) shows that the differential equation of local momentum balance for a tube with varying cross section differs from Eq. (2.29b) in only one additional term:

$$\frac{\partial(\rho u)}{\partial t} + \frac{\partial(\rho u^2)}{\partial s} = -\frac{\partial p}{\partial s} - \frac{\partial p_{fr}(u, \rho)}{\partial s} + \rho \mathbf{g} \cdot \mathbf{e}_s - \frac{\partial A}{\partial s} \frac{\rho u^2}{A}, \quad (7.21)$$

where, in the last term,  $A$  is the local cross section. The geometry of the studied systems allows us to consider  $\frac{\partial A}{\partial s} = 0$  at most of the points of the domain, as the cross section variations are sudden and practically concentrated at the interfaces between tubes. At those points  $\frac{\partial A}{\partial s} \neq 0$  and the effect of this term can be significant. Thus, as has been stated, Eq. (2.29b) is locally valid, but not integrally.

In app. C.3 it is demonstrated that the integral of the last term of Eq. (7.21) between two points on each side of the cross section change is

$$\int_{s_a}^{s_b} \frac{\partial A}{\partial s} \frac{\rho u^2}{A} \, ds = \frac{\rho u_a^2}{2} - \frac{\rho u_b^2}{2}. \quad (7.22)$$

The cross section change has the effect of introducing a momentum contribution equal to the volume-specific kinetic energy change. This result is valid within the frame of validity of the hypotheses leading to Eq. (7.21). However, when the cross section change is not smooth enough for the velocity field to be approximately unidirectional or to avoid recirculation cells at the bigger diameter section, there is an irreversible *concentrated head loss* that depends on the geometrical shape and the relative cross section area change. These losses are well studied and the coefficients are tabulated [41]. They may be expressed as:

$$\Delta p_{sing} = \text{sg}(u_{small}) K_{sing} \frac{\rho u_{small}^2}{2}, \quad (7.23)$$

where  $u_{small}$  is the fluid velocity in the tube with the smallest diameter and ‘sg’ is the *sign function*. Thus, the contribution of the cross section change points to the integral of Eq. (7.21) is

$$\Delta p_{X\text{Change}} = - \int_{s_a}^{s_b} \frac{\partial A}{\partial s} \frac{\rho u^2}{A} \, ds - \Delta p_{sing} = \frac{\rho u_b^2}{2} - \frac{\rho u_a^2}{2} - \text{sg}(u_{small}) K_{sing} \frac{\rho u_{small}^2}{2}. \quad (7.24)$$

We need to mention that Eq. 7.24 is also valid for direction change elbows in the circuit, for which the term  $\frac{\rho u_b^2}{2} - \frac{\rho u_a^2}{2}$  equals 0 if the inlet and outlet diameter of the elbow are identical.

We are ready now to integrate Eq. (7.21):

$$\int \frac{\partial(\rho u)}{\partial t} \, ds = - \int \frac{\partial(\rho u^2)}{\partial s} \, ds - \int \frac{\partial p}{\partial s} \, ds - \int \frac{\partial p_{fr}}{\partial s} \, ds + \int \rho (\mathbf{g} \cdot \mathbf{e}_s) \, ds - \int \frac{\partial A}{\partial s} \frac{\rho u^2}{A} \, ds$$

$$\begin{aligned} \frac{dH}{dt} = & -(\rho u^2)_{out} + (\rho u^2)_{in} + p_{in} - p_{out} - \Delta p_{fr} + \int \rho (\mathbf{g} \cdot \mathbf{e}_s) ds \\ & + \sum_k \left[ \Delta_k \left( \frac{\rho u^2}{2} \right) - \text{sg}(u_{small}) K_{sing,k} \frac{\rho u_{small,k}^2}{2} \right]. \end{aligned} \quad (7.25)$$

All the integrals appearing in these equations are considered over the whole domain, i.e. from  $-(L_d + L_u + L_e)$  to  $L_h + L_r$ . In Eq. (7.25), the quantities with sub-index *in* are to be considered at the entrance of the down-comer and those with sub-index *out* at the exit of the riser. The last term in Eq. (7.25) is a summation over all points of the circuit, nominated with index  $k$ , where the cross section area changes or where there is some concentrated head loss (elbows, for example). Thus  $\Delta_k \left( \frac{\rho u^2}{2} \right)$  denotes the kinetic energy change at singularity  $k$  (in the sense of increasing  $s$ ). Appendix C.2 present an alternative way of obtaining Eq. (7.25).

### The velocity field from the integral momentum

Let us now see how to use Eq. (7.25) to find the velocity field. By definition,  $H$  can be written as:

$$H = \int_{-L_d-L_u-L_e}^{L_h+L_r} \rho u ds = \int_{-L_d-L_u-L_e}^0 \rho u ds + \int_0^{L_{ch}} \rho u ds + \int_{L_h}^{L_r} \rho u ds. \quad (7.26)$$

Using what we know about the velocity profile (Eqs. (7.12), (7.16), (7.17), (7.18) and (7.19)) and defining an index  $j$  that runs through all the elements of the loop upstream the heated section and another one  $k$  through those downstream:

$$\begin{aligned} H(t) &= \sum_j \int_{S_j} \rho u_j(t) ds + \int_0^{L_h} \rho (u_0(t) + \Omega s) ds + \sum_k \int_{S_k} \rho u_k(t) ds \\ H(t) &= u_0(t) \sum_j \frac{A_h}{A_j} \int_{S_j} \rho ds + u_0(t) \int_0^{L_h} \rho ds + \Omega \int_0^{L_h} \rho s ds + (u_0(t) + \Omega L_h) \sum_k \frac{A_h}{A_k} \int_{S_k} \rho ds \\ H(t) &= u_0(t) \left( \sum_j \frac{A_h}{A_j} \int_{S_j} \rho ds + \int_0^{L_{ch}} \rho ds + \sum_k \frac{A_h}{A_k} \int_{S_k} \rho ds \right) \\ &\quad + \Omega \left( \int_0^{L_h} \rho s ds + L_h \sum_k \frac{A_h}{A_k} \int_{S_k} \rho ds \right). \end{aligned} \quad (7.27)$$

In order to simplify the notation in Eq. (7.27), we define two integral moments of  $\rho$ :

$$M_S = \int_S \rho ds, \quad (7.28a)$$

$$I_S = \int_S \rho s ds. \quad (7.28b)$$

with  $S$  being a specific section of the loop. Then, Eq. (7.27) becomes

$$H(t) = u_0(t) \left( \sum_j \frac{A_h}{A_j} M_j + M_h + \sum_k \frac{A_h}{A_k} M_k \right) + \Omega \left( I_h + L_h \sum_k \frac{A_h}{A_k} M_k \right), \quad (7.29)$$

or alternatively

$$u_0(t) = \frac{H(t) - \Omega \left( I_h + L_h \sum_k \frac{A_h}{A_k} M_k \right)}{\sum_i \frac{A_h}{A_i} M_i}. \quad (7.30)$$

Index  $i$  goes through absolutely all loop elements (even the heated section).

### 7.2.2 The resulting simplified model

To summarize, the analysis of equations so far allows us to solve approximately the problem by considering the following system of equations:

$$\frac{\partial h}{\partial t} + u \frac{\partial h}{\partial s} = \frac{q_v}{\rho} + \mathbf{u} \mathbf{g} \cdot \mathbf{e}_s \quad (7.31a)$$

$$\frac{dH}{dt} = -(\rho u^2)_{out} + (\rho u^2)_{in} + p_{in} - p_{out} - \Delta p_{fr} - \Delta p_{sing} + \int \rho \mathbf{g} \cdot \mathbf{e}_s ds + \sum_i \Delta_i \left( \frac{\rho u^2}{2} \right) \quad (7.31b)$$

$$\rho(h) = \begin{cases} \rho_l & \text{in the one-phase region } (h < h_l) \\ \left( \frac{h-h_l}{h_l \rho_g} + \frac{h_g-h}{h_l \rho_l} \right)^{-1} & \text{in the two-phase region } (h > h_l) \end{cases} \quad (7.31c)$$

$$u(s, t) = \begin{cases} \frac{A_h}{A(s)} u_0(t) & \text{if } s < 0 \\ u_0(t) + \Omega(t) s & \text{if } 0 < s < L_h \\ \frac{A_h}{A(s)} [u_0(t) + \Omega(t) L_h] & \text{if } s > L_h \end{cases} \quad (7.31d)$$

$$u_0(t) = \frac{H(t) - \Omega \left( I_h + L_h \sum_k \frac{A_h}{A_k} M_k \right)}{\sum_i \frac{A_h}{A_i} M_i}. \quad (7.31e)$$

The system is formed by a PDE, an ODE and algebraic equations.

The hypotheses or assumptions that have led to this formulation are:

- the flow is one dimensional;
- the two phases are in thermodynamic equilibrium and have a sole velocity;
- fluid density does not depend on pressure (incompressibility), but only on enthalpy;
- pressure time derivatives are neglected in the energy conservation equation;
- gravity work can be neglected in the energy conservation equation;
- subcooling is neglected and the fluid is considered to be at the all-liquid saturation point on the whole segment upstream the heated section;
- cross section area is constant in each element and it changes abruptly only at transition points between them.

### The immediate effect of power discontinuities

There is a feature this simplified model presents, that we mentioned previously and that we shall address in more detail, which is the *velocity field time discontinuity* face to sudden power steps. The time-dependent mass conservation equation, combined with a simplified version of the energy, or rather enthalpy, equation and the non-pressure-dependent closure equation lead

to Eq. (7.10). The reader should note that  $\Omega$  can be a discontinuous function of time in the same measure as  $q_v$  can be so. Let us consider a case where at  $t = t_0$  power changes from a value  $q_{v1}$  to  $q_{v2}$ . The velocity profile along the heated section will then be given by:

$$u(s, t) = \begin{cases} u_0(t) + \Omega_1 s & \text{if } t < t_0 \\ u_0(t) + \Omega_2 s & \text{if } t > t_0 \end{cases} \quad (7.32)$$

Evaluating the function a time  $\epsilon$  right before and after the power change we could get:

$$u(s, t_0 - \epsilon) = u_0(t_0 - \epsilon) + \Omega_1 s \quad (7.33a)$$

$$u(s, t_0 + \epsilon) = u_0(t_0 + \epsilon) + \Omega_2 s \quad (7.33b)$$

with which,

$$u(s, t_0 + \epsilon) - u(s, t_0 - \epsilon) = u_0(t_0 + \epsilon) - u_0(t_0 - \epsilon) + (\Omega_2 - \Omega_1) s. \quad (7.34)$$

In order to test the time-continuity of  $u(s, t)$ , we will calculate the limit when  $\epsilon \rightarrow 0^+$ :

$$\lim_{\epsilon \rightarrow 0^+} [u(s, t_0 + \epsilon) - u(s, t_0 - \epsilon)] = \lim_{\epsilon \rightarrow 0^+} [u_0(t_0 + \epsilon) - u_0(t_0 - \epsilon)] + (\Omega_2 - \Omega_1) s. \quad (7.35)$$

Let us define the instantaneous variation of velocity field and inlet velocity, respectively, as

$$\Delta u(s, t_0) = \lim_{\epsilon \rightarrow 0^+} [u(s, t_0 + \epsilon) - u(s, t_0 - \epsilon)], \quad (7.36a)$$

$$\Delta u_0(t_0) = \lim_{\epsilon \rightarrow 0^+} [u_0(t_0 + \epsilon) - u_0(t_0 - \epsilon)]. \quad (7.36b)$$

The reader should note that in general the velocity profile will be discontinuous at (almost) all  $s$  because the limit in Eq. (7.35) will be different from zero at (almost) all  $s$ . In fact, there is only one point where the LHS of Eq. (7.35) is zero, namely:

$$s = \frac{\Delta u_0(t_0)}{\Omega_1 - \Omega_2}. \quad (7.37)$$

How can we determine the value of  $\Delta u_0$ ? We can make use of Eq. (7.30). By physical considerations, we know that the momentum integral of the system  $H$  cannot be time discontinuous because the overall external forces applied on the system (gravity, friction, pressure at the boundary), which set the derivative of  $H$ , do not exhibit an impulse component (a Dirac delta function behavior) at the power change instant. Furthermore, the mass (or density) present at each point of the circuit is the same right before and after the power change, i.e. does not show time discontinuities. After these considerations, we can calculate  $\Delta u_0(t_0)$ :

$$\Delta u_0(t_0) = \frac{-(\Omega_2 - \Omega_1) \left( I_h + L_h \sum_k \frac{A_h}{A_k} M_k \right)}{\sum_i \frac{A_h}{A_i} M_i}, \quad (7.38)$$

with which, for  $s$  in the heated section region,

$$\Delta u(s, t_0) = (\Omega_2 - \Omega_1) \left( s - \frac{\left( I_h + L_h \sum_k \frac{A_h}{A_k} M_k \right)}{\sum_i \frac{A_h}{A_i} M_i} \right). \quad (7.39)$$

By noting that

$$\frac{I_h}{L_h} = \int_0^{L_h} \rho \underbrace{\frac{s}{L_h}}_{<1} ds < \int_0^{L_h} \rho ds = M_h \quad (7.40)$$

it turns out that

$$0 < \frac{\left(I_h + L_h \sum_k \frac{A_h}{A_k} M_k\right)}{\sum_i \frac{A_h}{A_i} M_i} < L_h, \quad (7.41)$$

with which, the only point where velocity is time-continuous at the instant of power change

$$s_{cont.} = \frac{\left(I_h + L_h \sum_k \frac{A_h}{A_k} M_k\right)}{\sum_i \frac{A_h}{A_i} M_i} \quad (7.42)$$

is contained in the heated section. This is an important implication, because it means that when the power, let us say, increases (decreases), the velocity increases (decreases) instantaneously downstream of this point and decreases (increases) upstream. With this, the simplified model is capable of representing the mass expulsion stage that was mentioned so many times in the previous chapters.

Let us assume for a moment that the pressure is present in the closure equation. Let us consider the homogenous model as given by Eq. (2.29). Let us qualitatively analyze the evolution of the system at a sudden power increase. Let us not accept time discontinuities of the velocity profile. In this case Eq. (2.29a) predicts that immediately after the power increase jump, if the velocity profile stays very close to the previous values, the density profile cannot change instantaneously. But Eq. (2.29c) predicts a time-linear increase of the local value of internal energy, because all terms stay close to the initially-in-dynamic-equilibrium values, except for the generated power  $q_v$ . Thus, the closure equation, for almost constant density but increasing internal energy, predicts a pressure rise inside the heated section. Let us demonstrate this more rigorously. In the initial steady state before the power step, in the heated section:

$$\frac{\partial \rho_0}{\partial t} = 0 = -\frac{\partial(\rho_0 u_0)}{\partial s} \quad (7.43a)$$

$$\rho \frac{\partial e_0}{\partial t} = 0 = q_1 - \rho_0 u_0 \frac{\partial e_0}{\partial s} - \rho_0 g u_0 - \frac{\partial(p_0 u_0)}{\partial s} \quad (7.43b)$$

$$(7.43c)$$

The sub-index 0 denotes that the profiles were the dynamic equilibrium state profiles. An infinitesimal time after the power increase jump,

$$\frac{\partial \rho}{\partial t} = -\frac{\partial(\rho_0 u_0)}{\partial s} = 0 \quad (7.44a)$$

$$\rho \frac{\partial e}{\partial t} = 0 = q_2 - \rho_0 u_0 \frac{\partial e_0}{\partial s} - \rho_0 g u_0 - \frac{\partial(p_0 u_0)}{\partial s} = q_2 - q_1 \quad (7.44b)$$

because the pressure, density, energy and velocity are assumed to be time-continuous fields now. The immediate behavior of the system is that density stays constant while internal energy starts to grow linearly. As in the more realistic representation we have  $p = f_p(\rho, e)$ , the variations of pressure respond to the equation

$$\frac{\partial p}{\partial t} = \frac{\partial f_p}{\partial \rho} \Big|_e \frac{\partial \rho}{\partial t} + \frac{\partial f_p}{\partial e} \Big|_\rho \frac{\partial e}{\partial t}. \quad (7.45)$$

In particular, for the infinitesimal instant after the power step:

$$\frac{\partial p}{\partial t} = \frac{\partial f_p}{\partial \rho} \Big|_{e, @(\rho_0, e_0)} \cdot 0 + \frac{\partial f_p}{\partial e} \Big|_{\rho, @(\rho_0, e_0)} \frac{(q_2 - q_1)}{\rho_0} = \frac{\partial f_p}{\partial e} \Big|_{\rho, @(\rho_0, e_0)} \frac{(q_2 - q_1)}{\rho_0}. \quad (7.46)$$

As generally  $\frac{\partial f_p}{\partial e} > 0$ , immediately after the power step pressure starts to grow at a rate directly proportional to the power increase. In this situation, the momentum equation, Eq. (2.29b),

predicts an acceleration from the interior of the heated section towards the exterior. Thus, velocity will increase near the exit and decrease near the entrance of the heated section (and stay unchanged at some point in the middle). This increase in the velocity gradient will allow the density to decrease, and pressure to diminish, with an increased phase change rate. Thus, the resulting velocity profile, some instants after the power step pulse, has a higher divergence. The details of this relaxation transient exceed the analytical scope treated here, reason why we only speak about it qualitatively. It is only after the density decreasing that gravity will act increasing the amount of total momentum of the circuit, but this happens in a time scale at least one order of magnitude slower than the internal pressure rise.

In a few words, the introduction of compressibility lets the velocity be time-continuous face to a power increase (decrease), but it introduces a pressurization transient that redistributes the linear momentum in the circuit, transferring it from the upstream (downstream) positions to the downstream (upstream) positions. The time scale of this momentum redistribution is shorter than the buoyant force acceleration effect on the whole loop. The incompressible model, as we have shown above, by conserving the whole momentum  $H$  but affecting *instantaneously* the velocity profile, effectuates the momentum redistribution *instantaneously*, producing a time-discontinuity that plays the role of the fast pressure effects.

A consequence of this behavior is that if the power increase is high enough in comparison with the initial power, flow inversion, i.e. negative velocity at the inlet of the heated channel, can take place. Explicitly, according to the simplified incompressible model, this happens when

$$\Delta u_0(t_0) < -u_0(t_0^-) \quad (7.47)$$

or alternatively,

$$\begin{aligned} -\Delta\Omega \left[ \frac{\left( I_h + L_h \sum_k \frac{A_h}{A_k} M_k \right)}{\sum_i \frac{A_h}{A_i} M_i} \right]_{(t_0)} &< -u_0(t_0^-) \\ \Delta\Omega > u_0(t_0^-) \left[ \frac{\sum_i \frac{A_h}{A_i} M_i}{\left( I_h + L_h \sum_k \frac{A_h}{A_k} M_k \right)} \right]_{(t_0)}. \end{aligned} \quad (7.48)$$

Experiments have shown that flow inversion is possible. When initial power is zero, high final power values can produce measurable pressure variations on the Venturi pressure difference that let assume a negative mass flow rate at the beginning of the transient. Furthermore, when turning off power after an experiment, a sudden increase of measured mass flow rate has been observed before this quantity settles down to zero. Thus, the discontinuity in inlet velocity seems to be, at least qualitatively, a good representation of the real behavior of the system. In response to power increase (decrease) inlet velocity shows a quasi-instantaneous decrease (increase).

### 7.3 Implementation of the simplified model in COMSOL

COMSOL<sup>TM</sup> is a commercial software that allows solving problems involving multi-physical coupled phenomena by using built-in advanced numerical tools. The advantage of using such a software is the fact that the user does not need to enter into extreme detail of the solver (although they can do it) and can concentrate only on the physical modeling, i.e. the description of the geometry, the boundary conditions, the equations, source terms, etc.. This section describes how we used COMSOL to obtain the numerical solution of Eqs. (7.31).

### 7.3.1 Description of the environment

The COMSOL interface is very user-friendly, counting with a graphic window on the right where the spatial domain can be appreciated and a model window in which the user can configure the physics of the problem, set up the simulation and visualize the results.

A COMSOL model is composed by the following elements:

- A list of constant parameters defined by the user. It is possible to define one them as function of some of the others.
- A list of user-defined variables. These variables need to be defined through a mathematical expression of the parameters and other variables.
- The geometry, defined by lines, surfaces or volumes, and its meshing.
- Materials, defined by a set of property values, can be assigned to each region of the domain.
- The physical model or models. A set of differential equations to be solved in the domain. These equations have an intrinsic variable that can be used for the definition of the user-defined variables. Furthermore, the source terms or variable coefficient terms can be constructed using the user-defined variables.
- The boundary conditions of the physical model. Depending on the model chosen, a set of boundary conditions is possible.
- The solver configurations: numerical methods, time steps, instants of time for solutions, etc.. It is also possible to configure a parametric sweep, i.e. run automatically several identical simulations changing at each time a given parameter or group of parameters (*a priori* declared in the list).
- The results visualization: The user defines plots, tables, data file export, animations, etc., that are produced from the results of the last run.

The results is a user-friendly platform, where it is easy to change parameters or modeling options, or the numerical method, or export the results in different formats.

### 7.3.2 Solving strategy

In the following paragraphs we present the way in which the natural circulation loop was represented using the elements available in COMSOL.

#### The domain

Let us consider as a departing point the domain as described in section 7.1. The model considers that velocity is uniform in the down-comer and the horizontal link tube (both of which have the largest internal diameter of the loop) and that the fluid is only liquid in these regions. For this reason, it is not interesting to model what happens in this part of the domain as it can be very easily determined from what happens in the ascending branch. Thus, the COMSOL model will have a domain composed only of the components in the ascending branch.

The domain is one-dimensional, and it is divided in three elements: the pre-entrance segment, the heated section and the riser. The boundaries of the domain are at the beginning of the pre-entrance segment and at the end of the riser.

### The equation tools

The system of equations (7.31) is formed by a time dependent partial differential equation (PDE) for the enthalpy  $h$ , an ordinary differential equation (ODE) for the integral momentum  $H$ , and three algebraic equations for the determination of density  $\rho$ , velocity profile  $u(s)$  and inlet velocity  $u_0$ .

In the variables module of the environment, we defined three of the five variables (those that are not the main variable of the differential equations):

- $u_0$ , depending on  $H$  and  $q$ , considered uniform on the domain;
- $u$ , depending on  $u_0$ ,  $q$  and  $s$ ;
- $\rho$ , depending exclusively on  $h$ .

The values of the three variables can be calculated if  $h$  and  $H$  are known; thus, it is necessary to solve the two corresponding differential equations.

For the solution of the PDE for  $h$ , we used the built-in model of *Heated Flow*. The choice of a built-in model is justified by the fact that the numerical algorithm is implemented for each term according to the physics that it intends to represent. In this model the variable is generally interpreted as temperature in K and the equation is:

$$\rho c_p \left( \frac{\partial T}{\partial t} + u \frac{\partial T}{\partial s} \right) = q_v + k \frac{\partial^2 T}{\partial s^2} \quad (7.49)$$

To implement Eq. (7.31a),  $k$  was taken the smallest possible accepted by the solver ( $10^{-10}$  W m<sup>-1</sup> K<sup>-1</sup>),  $c_p = 1$  J kg<sup>-1</sup> K<sup>-1</sup> and the source term  $q_v$  was constructed using the heat flux and the velocity local values of velocity and density:

$$q_v = \frac{4q}{D} - \rho u g. \quad (7.50)$$

The minus sign comes from the fact that we are only considering the ascending branch in the domain. Thus, the variable  $T$  (which is not at all the real temperature of the fluid) has numerically the desired value of  $h$  but the wrong units.  $h$  is defined as  $c_p T$  and the problem is solved.

The ODE for  $H$  was solved using the *Global Equation* tool. This tool allows coupling an ODE with variables constructed from the instantaneous profiles of other variables present in the model. The environment counts with integral or mean operators that can be defined on a given region of the domain, with an arbitrary integrand constructed from the declared variables. This was used for the calculation of the friction and gravity terms.

It is also possible to declare variables that are obtained as the punctual value of a space-dependent variable at a specific value of  $s$ ; these are called *Probes*. This was used for the calculation of the  $\rho u^2$ -terms, the singular head losses terms and the kinetic energy change terms. The pressure difference  $p_{in} - p_{out}$  depends only on the inlet velocity (obtained by *probe* too); this will be further explained in the the next section about boundary conditions.

### Boundary conditions

The boundary conditions for the differential equations of the problem are:

- The incoming enthalpy (and thus density) of the fluid is that at the liquid saturation point, commonly called *Dirichlet* condition.

- The outgoing properties are those of the outgoing particle, commonly called *free flow* condition. Mathematically it is implemented as

$$\frac{\partial T}{\partial s} = 0. \quad (7.51)$$

- Pressure at the boundaries is equal to that of the reservoir for outgoing flow.
- Pressure at the boundary is that of the reservoir affected by the increase of kinetic energy and the eventual concentrated head loss at the entrance:

$$p_{boundary} = p_{reservoir} - (1 + K_{entry}) \frac{1}{2} \rho l u_{boundary}^2. \quad (7.52)$$

The boundary condition for pressure in the case of outgoing flow reflects the fact that a sudden expansion to infinite radius entails a head loss equal to the kinetic energy of the flow. In the case of incoming flow, given that only the ascending branch is simulated,  $u_{boundary}$  for the calculation of  $p_{in}$  is taken at the inlet velocity of the down-comer, equal to  $u_0 \frac{A_h}{A_d}$ . The result is that  $p_{in} - p_{out}$  in the equation for  $H$  becomes

$$p_{in} - p_{out} = - (1 + K_{entry}) \frac{1}{2} \left( u_0 \frac{A_h}{A_d} \right)^2 - \rho l g (z_{in} - z_{out}), \quad (7.53)$$

where  $z_{in}$  and  $z_{out}$  are the vertical positions of the inlet of the down-comer and the exit of the riser, respectively.

### Initial conditions

The initial condition of the system is trivial:

- velocity is zero everywhere, thus  $H(t = 0) = 0$ ;
- enthalpy and density are those at the liquid saturation point everywhere;
- pressure is given by the hydrostatic profile.

If a transient with non-zero initial heat flux needs to be simulated, then a double power step is considered:

$$q(t) = \begin{cases} 0 & \text{if } t < -t_0 \\ q_i & \text{if } -t_0 < t < 0 \\ q_f & \text{if } t > 0 \end{cases} \quad (7.54)$$

where  $t_0$  is the amount of time required for the system to settle at the non-zero heat flux initial condition. The trivial initial condition is applied for the transient that starts at  $t = -t_0$ .

### 7.3.3 Comparison of the simplified model simulations to the experimental data

In order to assess the capability of the simplified formulation of representing correctly the transient dynamics of helium natural circulation loops, a few representative cases, for which experimental data is available, were solved and the solution was compared to the experimental results on section V10.

In Fig. 7.2 we present plots of the mass flow rate of several of these cases in a wide range of power. The simplified model is able to capture all the essential features of the mass flow rate

evolution. At the initiation of the transient, the flow inversion is observed, discontinuously, as predicted in section 7.2.2. The overall shape of the simulated mass flow rate signal is practically identical to the measured one. The slope  $\frac{dm}{dt}$  of the modeled and measured response at the quickly rising stage are sensibly the same, as well as the overshooting value and the time extension of the overshooting interval. Nevertheless there is a phase shift between the simulated evolution and the experimental data. The modeled mass flow rate reaches its maximum around 300 ms earlier than the measured signal. This discrepancy could be a result either of a time delay of the instrumentation associated to the mass flow rate measurement or of the assumption that the pressure evolution has no appreciable effects on the conservation laws. It is possible that immediately after the step pulse the pressure increase inside the heated section be considerable and of a non negligible duration, thus being responsible of part of the phase shift.

Concerning the evolution of the thermohydraulic variables inside the heated section, in Fig. 7.3 we can appreciate, for three selected cases, the evolution of the enthalpy and density profiles with time. On each plot, the represented profiles are successive and obtained at regular time intervals. The model is able to predict the qualitative behavior that has been discussed all along this work. Initially, there is a stage during which the evolution of these variables is uniform in space, because the flow is outgoing on the two ends. As soon as velocity becomes positive at the inlet, the particles that are upstream the inlet start to enter. Initially these particles had been heated for a part of the elapsed time, before being expelled; thus, their quality when entering back the section is positive. Later, after the pre-heated particles have passed, it is the turn for those that had never been inside the heated section; from that moment on, the inlet quality is set to zero. At this stage, a part of the section is still in the uniform evolution phase, and the other has already been reached by the cold particle front. The cold front travels at the local particle velocity, i.e. it accelerates as it approaches the exit. This can be appreciated on the plots, given that, taking into account that profiles are taken at regular intervals, the distance between the discontinuity fronts of successive profiles is greater near the exit.

Predicting the mass flow rate evolution with the good wave function but with an advancing phase shift can be dangerous from the boiling crisis point of view, as it means that the model predicts the arrival of the cold front earlier, and thus, the maximum of quality is under estimated. As concluded in previous chapters, it would mean that we would predict incipient boiling crisis heat flux much higher than it really is. For this reason, it may be necessary to improve the modeling of mass flow rate evolution by revising the assumptions.

## 7.4 Solution of the non-simplified model

In order to determine if the difference in the time response characteristic of the model with respect to the experiments is due to the assumptions of the model, especially the neglect of pressure evolution and its effects on density and saturation properties, it was decided to solve numerically the non simplified equations. To do this, a C-language code that solves the equations in a spatial finite difference scheme was developed.

### 7.4.1 Structure of the program

The program can be separated sequentially as follows:

- **Input reading:** Input files are read in order to inform the solver about:
  - the geometry of the loop;
  - the concentrated head losses of the loop;

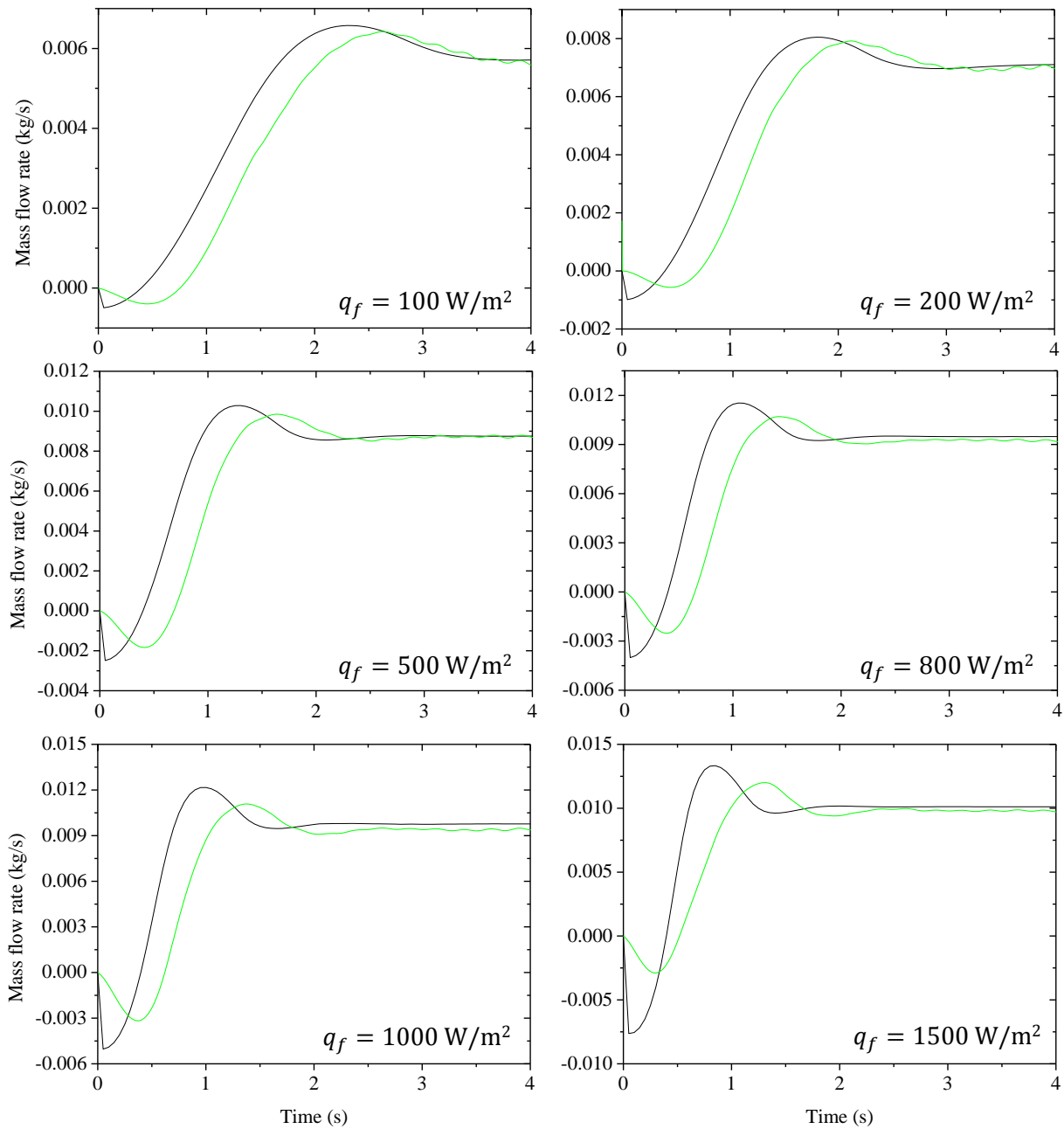


**Figure 7.2.** Comparison of simulated (simplified model) and measured mass flow rate evolutions, for several cases on V10. Initial heat flux is zero for all the cases. — Simulation; — Experiment.

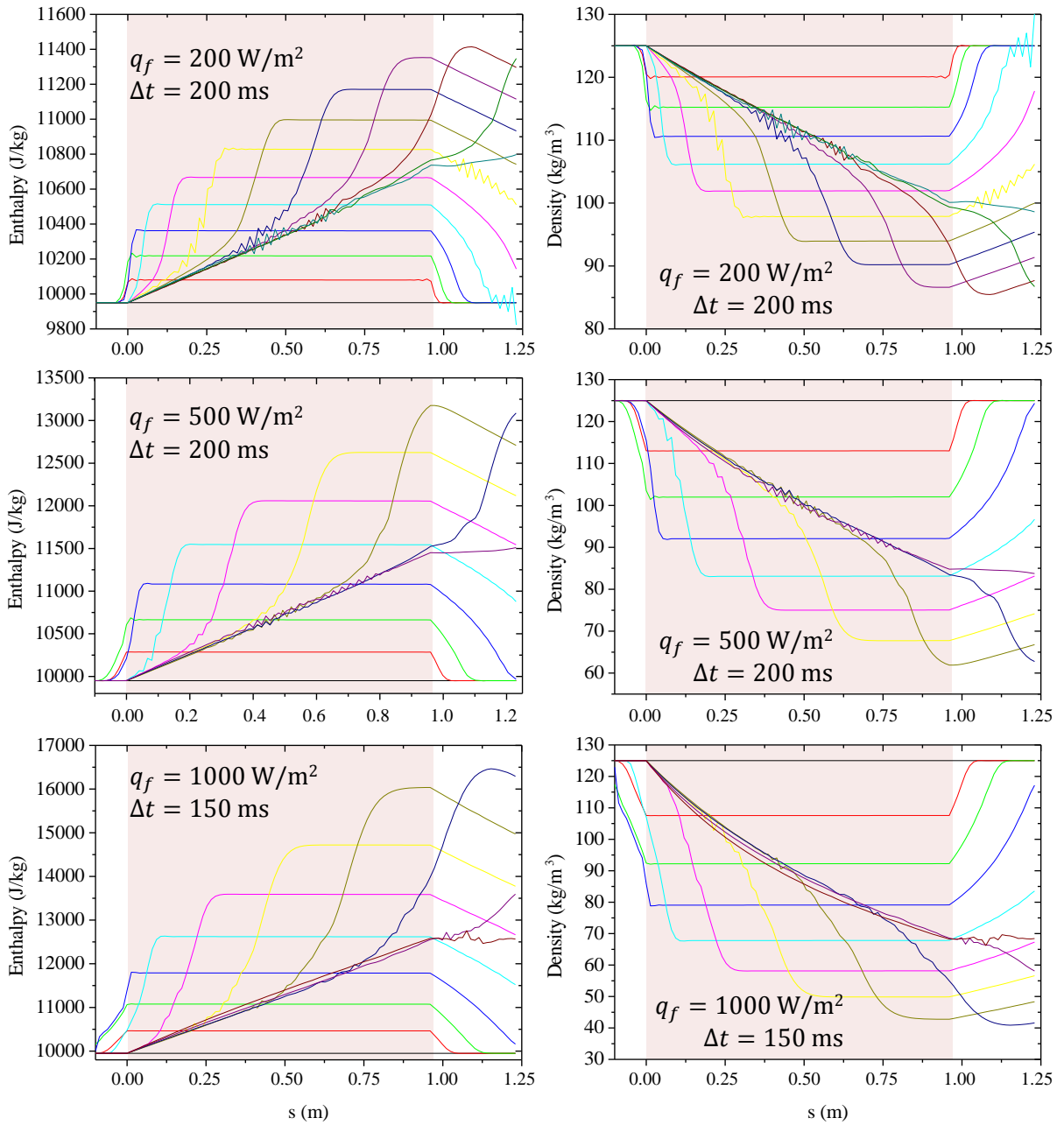


**Figure 7.3.** Simulated time evolution of enthalpy and density profiles with the simplified model, on V10. In each case, the presented profiles are consecutive in time, with a regular time step, indicated on each figure. The initial instant of time is  $t = 0$ . The pink-shaded area represents the heated section.

- the time characteristics of heat load on the loop;
  - the time evolution solver parameters;
  - the punctual probe results to provide at the end of the simulation.
- **Initialization:** Memory is allocated for all the variables according to the requirements in the input. Some of the result files are created at this point.
  - **Simulation:** The time advancement of the equations is solved. Some of the result files are produced during this stage.
  - **Closure:** The result files that can be delivered only at the end of the simulation are closed at this point. Memory is liberated.

### 7.4.2 Input parameters

The geometry of the loop is given in the form of successive tube elements. The information necessary for the program is *the number of tube elements* and for each of them:

- number of nodes for the discretization;
- inlet diameter;
- outlet diameter;
- length;
- inlet vertical position with respect to the free surface in the reservoir (only for the first tube);
- orientation of the tube ( $\frac{\bar{g} \cdot \hat{e}_x}{g}$ ).

The concentrated singularity head losses are treated as a continuously distributed head loss over a short length around a central point. Furthermore, in the case of diameter changes, the coefficients value depends on the direction of the flow<sup>1</sup>. It has been assumed that transient coefficients are the same as in steady state. The information that needs to be provided is the number of concentrated head losses and for each of them in particular:

- the index of the tube on which it is applied;
- the index of the node inside that tube on which the head loss is centered;
- the number of nodes on which it is (artificially) distributed up and downstream;
- the corresponding length over which it is distributed;
- the value of the coefficient for positive velocity;
- the value of the coefficient for negative velocity;
- the index of the tube on which is the reference velocity point;
- the index of the node inside that tube in which is the reference velocity point.

---

<sup>1</sup>Depending on the velocity sign, the change of diameter is seen by the flow like an expansion or a contraction.

For the heating history of the loop, it is necessary to specify for each tube the instants of time at which there is a power change, and the new value of power. Thus for each tube, the input is given by:

- the number of power steps;
- for each power step:
  - the time at which it happens;
  - the new value of power.

The solver input parameters are:

- the final time of the simulation;
- the minimum time step (applied immediately after a power step);
- the maximum time step acceptable;
- the time step increasing factor;
- the number of time steps after which to produce a variables profile file;
- the number of time steps after which to print a record in the punctual probes file;
- the number of iterations per time step.

The punctual probes input has the purpose of printing the time history of a given variable at a given point of the domain. The input required is the *total number of probes* and for each of them:

- the index of the tube on which is the point of interest;
- the index of the node inside that tube for the point of interest;
- an integer value that specifies what variable to consider.

By default, the initial condition of the system is programmed to be the case with zero power and velocity. However, the program contemplates the possibility of providing an arbitrary initial condition with an input file that needs to be in the same format as the output of the program. This way, it is possible to calculate a set of initial (steady state) conditions and store them. This allows to simulate transients with initial power in a more practical manner, as long as the initial power required is in the created data base.

### 7.4.3 Numerical method

As the system of equations presents both time and space derivatives, it is necessary to make a choice for the discretization of the time-space domain and the representation of those derivatives.

The equations of the system can be formulated so as to obtain the material derivative of the variables:

$$\frac{D\rho}{Dt} = \frac{\partial\rho}{\partial t} + u \frac{\partial\rho}{\partial s} = -\frac{\rho}{A} \frac{\partial(uA)}{\partial s} \quad (7.55a)$$

$$\frac{Du}{Dt} = \frac{\partial u}{\partial t} + u \frac{\partial u}{\partial s} = -\frac{1}{\rho} \frac{\partial p}{\partial s} - \frac{1}{\rho} \frac{\partial p_{fr}}{\partial s}(u, \rho) + \mathbf{g} \cdot \mathbf{e}_s \quad (7.55b)$$

$$\frac{D\tilde{e}}{Dt} = \frac{\partial\tilde{e}}{\partial t} + u \frac{\partial\tilde{e}}{\partial s} = \frac{q_v}{\rho} + \mathbf{g} \cdot \mathbf{u} - \frac{1}{\rho A} \frac{\partial(puA)}{\partial s} \quad (7.55c)$$

with

$$p = f_p^{\rho, e}(\rho, e), \quad (7.56a)$$

$$\tilde{e} = e + \frac{u^2}{2}. \quad (7.56b)$$

For its simplicity, it was chosen to discretize the space variable by using finite differences with a regular spacing mesh.

The spatial derivatives in the RHS of Eqs. (7.55) were treated by a centered difference scheme, while a time semi-implicit scheme was used for the variables  $\rho$ ,  $u$ ,  $e$  and  $p$  in all the terms in the RHS. In other words, whenever the variables need to be used to evaluate the RHS, the intermediate value between the present ( $n$ ) and next time step ( $n+1$ ) are used:

$$\alpha_i^{n+1/2} = \frac{\alpha_i^n + \alpha_i^{n+1}}{2}. \quad (7.57)$$

For the convective term, an explicit up-wind scheme was chosen, given this method is known to introduce little artificial diffusion. Thus, the discretized version of the equations is:

$$\rho_i^{n+1} = \rho_i^n + \Delta t \left[ -u_i^n \frac{\rho_{i+}^n - \rho_{i-}^n}{s_{i+} - s_{i-}} - \frac{\rho_i^{n+1/2}}{A_i} \frac{u_{i+1}^{n+1/2} A_{i+1} - u_{i-1}^{n+1/2} A_{i-1}}{s_{i+1} - s_{i-1}} \right] \quad (7.58a)$$

$$u_i^{n+1} = u_i^n + \Delta t \left[ -u_i^n \frac{u_{i+}^n - u_{i-}^n}{s_{i+} - s_{i-}} - \frac{1}{\rho_i^{n+1/2}} \frac{p_{i+1}^{n+1/2} - p_{i-1}^{n+1/2}}{s_{i+1} - s_{i-1}} - \frac{1}{\rho_i^{n+1/2}} \frac{\partial p_{fr}}{\partial s}(u_i^{n+1/2}, \rho_i^{n+1/2}) + g_i \right] \quad (7.58b)$$

$$\tilde{e}_i^{n+1} = \tilde{e}_i^n + \Delta t \left[ -u_i^n \frac{\tilde{e}_{i+}^n - \tilde{e}_{i-}^n}{s_{i+} - s_{i-}} + \frac{q_i^{n+1/2}}{\rho_i^{n+1/2}} + g_i u_i^{n+1/2} - \frac{1}{\rho_i^{n+1/2} A_i} \frac{p_{i+1}^{n+1/2} A_{i+1} u_{i+1}^{n+1/2} - p_{i-1}^{n+1/2} A_{i-1} u_{i-1}^{n+1/2}}{s_{i+1} - s_{i-1}} \right] \quad (7.58c)$$

The indexes  $i^+$  and  $i^-$  are calculated according to the sign of  $u_i$ :

$$u_i > 0 \implies i^+ = i \text{ and } i^- = i - 1 \quad (7.59a)$$

$$u_i < 0 \implies i^- = i \text{ and } i^+ = i + 1 \quad (7.59b)$$

The calculation of the RHS of these equations implies knowing the value of variables at time step  $n+1$ . Thus the collection of all these equations for all the  $i$ 's constitute a non linear system of equations in  $\rho_i^{n+1}$ ,  $u_i^{n+1}$ ,  $\tilde{e}_i^{n+1}$  and  $p_i^{n+1}$ . For simplicity, the solution of Eqs. (7.58) is obtained iteratively by the fixed point method. The initial guess for the variables at time

step  $n + 1$  is taken as their values at time step  $n$ . That is injected in the RHS of Eqs. (7.58), and the LHS are calculated. To be strict, the initial guess of the iteration step is used only on the first equation, which in fact updates the value of density. When entering data on the RHS of the second equation, density is already updated, and as a result velocity will be updated. When calculating the RHS of the third equation, the guesses for velocity and density are already updated and the new guess for the energy is obtained. Finally, the iteration ends with the update of pressure, calculated at the internal points of the domain from  $\rho$  and  $e$ :

$$p_i^{n+1} = f_p^{\rho,e} \left( \rho_i^{n+1}, \tilde{e}_i^{n+1} - \frac{u_i^{n+1}{}^2}{2} \right), \quad (7.60)$$

and applying the boundary conditions at the boundary nodes (see section 7.4.6).

The obtained set of four variables  $\rho_i^{n+1}$ ,  $u_i^{n+1}$ ,  $\tilde{e}_i^{n+1}$  and  $p_i^{n+1}$  is used to calculate the variables at time step  $n + 1/2$  for the RHS, and a new iteration can start.

#### 7.4.4 Fluid properties

The functions of the form  $f_\alpha^{\beta_1, \beta_2}$ , where it is understood that the function calculates property  $\alpha$  from the input properties  $\beta_1, \beta_2$ , were obtained from data provided by HEPAK<sup>TM</sup> [22]. Properties predicted by HEPAK<sup>TM</sup> were approximated by polynomial expressions, as a function of two parameters. The obtained functions have a very high level of accuracy in the range of pressures up to 120000 Pa, which is enough for the kind of transients that we need to model.

#### 7.4.5 Initial conditions

Two kinds of initial conditions have been considered:

- initial power equal to zero;
- non-zero initial power.

In the first case, the velocity in the whole domain is set to zero. The internal energy was considered constant in the whole domain. The pressure at the inlet of the first tube was calculated as:

$$p_{inlet} = P_0 - z_{inlet} g f_\rho^{p,e} \left( P_0 - \frac{1}{2} z_{inlet} g f_\rho^{p,e} (P_0, E_0), E_0 \right) \quad (7.61)$$

$P_0$  is the pressure at the free surface of the reservoir and  $z_{inlet}$  is the relative vertical position of the inlet of the loop with respect to the free surface. The pressure at all other points is obtained by the numerical integration of the hydrostatic force:

$$p_i = p_{i-1} - g (z_i - z_{i-1}) \rho_{i-1}, \quad (7.62)$$

considering the variations of density:

$$\rho_{i-1} = f_\rho^{p,e} (p_{i-1}, E_0). \quad (7.63)$$

We could have opted for considering temperature instead of internal energy as the uniform variable in the initial condition, but that would have involved the calculation of another variable. The equilibrium property profiles for the two initial conditions conditions, uniform temperature or uniform internal energy, were compared. The choice we made represents at most a difference of 2 mK in temperature,  $0.05 \text{ kg m}^{-3}$  in density and  $10 \text{ J kg}^{-1}$  for internal energy. The 2 mK

represents only 10% of subcooling, and the variations in density and energy are extremely small compared to the expected variations in the loop during the simulated transients. No appreciable differences are observed on the pressure profile.

For non-zero initial power, a set of steady state property profiles can be calculated using the code for a list of heat flux values; then, those profiles can be used as a database of initial condition of a transient in which the initial power is one within such set of simulations.

### 7.4.6 Boundary conditions

The numerical recipe presented in Eqs. (7.58) is only valid for those points strictly inside the domain, i.e. those that have at least one point to the left and one point to the right. For the nodes in the boundary, the nodes  $i \pm 1$  may not exist. Furthermore, every PDE need boundary conditions. Thus, for the border nodes, particular update rules were adopted.

#### Density

In the mass conservation equation, pure advection of the density field is considered for outgoing flow ( $\frac{D\rho}{Dt} = 0$ ) and a fixed value of density is given at each boundary for incoming flow. Mathematically:

- At node  $i = 0$  (entrance of the loop), negative velocity  $u_0^n < 0$ :

$$\rho_0^{n+1} = \rho_0^n - \Delta t \left[ u_0^n \frac{\rho_1^n - \rho_0^n}{s_1 - s_0} \right]. \quad (7.64)$$

- At node  $i = 0$  (entrance of the loop), positive velocity  $u_0^n > 0$ :

$$\rho_0^{n+1} = \rho_{inlet}. \quad (7.65)$$

- At node  $i = N$  (exit of the loop), positive velocity  $u_N^n > 0$ :

$$\rho_N^{n+1} = \rho_N^n - \Delta t \left[ u_N^n \frac{\rho_N^n - \rho_{N-1}^n}{s_N - s_{N-1}} \right]. \quad (7.66)$$

- At node  $i = N$  (exit of the loop), negative velocity  $u_N^n < 0$ :

$$\rho_N^{n+1} = \rho_{exit}. \quad (7.67)$$

#### Velocity

For the momentum equation, it is assumed that  $\frac{\partial(uA)}{\partial s} = 0$  at the boundary (in correspondence to the assumption for the mass conservation):

- At node  $i = 0$  (entrance of the loop):

$$u_0^{n+1} = u_1^{n+1} \frac{A_1}{A_0}. \quad (7.68)$$

- At node  $i = N$  (exit of the loop):

$$u_N^{n+1} = u_{N-1}^{n+1} \frac{A_N - 1}{A_N}. \quad (7.69)$$

## Energy

For the energy equation, for outgoing flow the free flow boundary condition is assumed, i.e.  $\frac{\partial \tilde{e}}{\partial s} = 0$ ; for incoming flow, a given value of internal energy is fixed at the boundary:

- At node  $i = 0$  (entrance of the loop), negative velocity  $u_0^n < 0$ :

$$\tilde{e}_0^{n+1} = \tilde{e}_1^{n+1}. \quad (7.70)$$

- At node  $i = 0$  (entrance of the loop), positive velocity  $u_0^n > 0$ :

$$\tilde{e}_0^{n+1} = \tilde{e}_{inlet} + \frac{u_0^{n+12}}{2}. \quad (7.71)$$

- At node  $i = N$  (exit of the loop), positive velocity  $u_N^n > 0$ :

$$\tilde{e}_N^{n+1} = \tilde{e}_{N-1}^{n+1}. \quad (7.72)$$

- At node  $i = N$  (exit of the loop), negative velocity  $u_N^n < 0$ :

$$\tilde{e}_N^{n+1} = \tilde{e}_{exit} + \frac{u_0^{n+12}}{2}. \quad (7.73)$$

## Pressure

The boundary condition for pressure is modeled taking into account the the pressure and head loss at an entry or exit of a tube connected to an infinite medium. For incoming flow, the pressure at the entrance of the tube is considered to be lower than that of the reservoir by the kinetic energy value. For outgoing flow, though, the pressure at the interior of the tube is equal to that of the reservoir, because the sudden expansion produces a head loss equal to the kinetic energy. Thus,

- At node  $i = 0$  (entrance of the loop), negative velocity  $u_0^n < 0$ :

$$\tilde{p}_0^{n+1} = p_{inlet}. \quad (7.74)$$

- At node  $i = 0$  (entrance of the loop), positive velocity  $u_0^n > 0$ :

$$\tilde{p}_0^{n+1} = \tilde{p}_{inlet} - \frac{\rho_{inlet} u_0^{n+12}}{2}. \quad (7.75)$$

- At node  $i = N$  (exit of the loop), positive velocity  $u_N^n > 0$ :

$$\tilde{p}_N^{n+1} = p_{exit} \quad (7.76)$$

- At node  $i = N$  (exit of the loop), negative velocity  $u_N^n < 0$ :

$$p_N^{n+1} = p_{exit} - \frac{\rho_{exit} u_N^{n+12}}{2}. \quad (7.77)$$

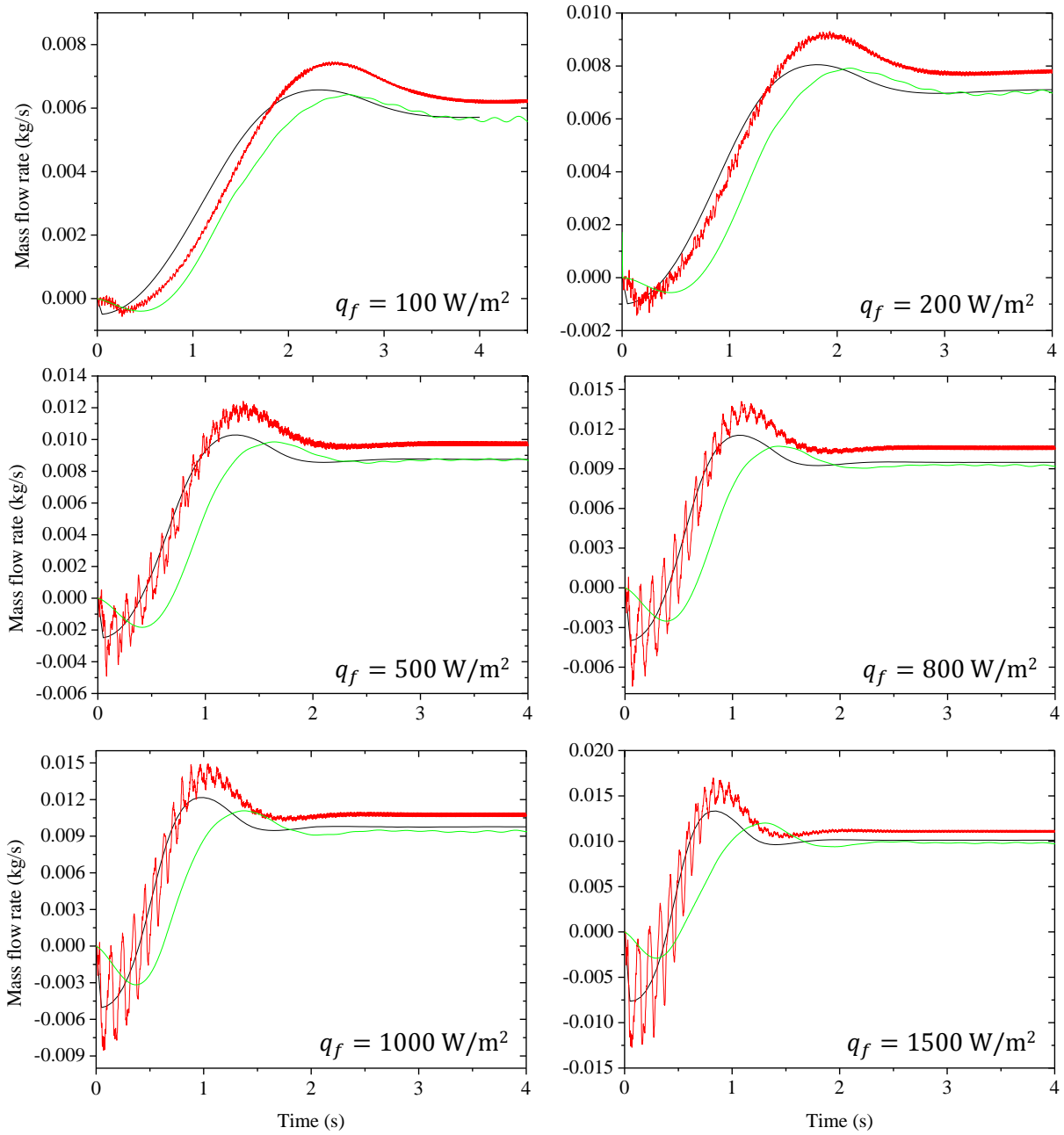


**Figure 7.4.** Comparison of simulated and measured mass flow rate evolutions, for several cases on V10. Initial heat flux is zero for all the cases. — Simplified model; — Non-simplified model; — Experiment.

### 7.4.7 Comparison of simulated and measured evolutions

The same cases whose simplified model solutions were presented in section 7.3.3, were solved by using the non-simplified model. The mass flow rate evolution plots are presented in Fig. 7.4.

The non-simplified model presents a feature that was not present in the simplified model, which consists of high frequency oscillations mounted on the mass flow rate response. At low power these oscillations are not observed, but as power increase their amplitude does too. The fact that the frequency of the oscillations is independent of the power, indicates that these oscillations are controlled by an intrinsic property of the system. A detailed study of all the variables during this transient shows that the pressure in the ascending section (the part of the domain where there is two-phase flow) oscillates with the same frequency. The proposed explanation is that

- when power is suddenly applied, after the shock wave that starts the circulation, the pressure is high inside the heated section and this induces a great expansion acceleration;
- the velocity difference between the exit and the inlet increases considerably, with which the internal pressure drops;
- the internal pressure diminution will tend to decelerate the fluid at the exit and accelerate it at the inlet, stopping the expansion and finally producing contraction;
- finally, the contraction re-pressurizes the interior of the heated section and the cycle restarts.

The two-phase fluid in the heated section acts *as a elastic spring*, as if the velocity inlet-exit difference were the elongation, and the compressibility factor the constant of the spring. This elastic behavior is under-damped, because no transient effects have been considered for the wall friction forces<sup>2</sup> and the transient development of the limit layer. These effects are somehow studied in monotonously accelerating pipe flow [73], but to our knowledge no simple approach for unsteady friction factors in pipe oscillatory flow are available in the literature. It is possible that the actual friction forces, due to transient wall boundary layer dynamics, present in reality, damp these oscillations, reason why we do not observe them experimentally.

Leaving aside the oscillations, the *filtered* mass flow rate signal provided by the non-simplified model follows very closely the one obtained with the simplified model, especially during the initial steps. For this reason we can say that the phase shift of the experimental signal does not seem to be explained by the fast pressure variations at the beginning of the transient.

It is possible that the method used for measuring the mass flow rate introduces a time lag or a low-pass filter time delay in the order of 300 ms. Another possibility is that the homogeneous model has limited validity at the initiation of the transient. The latter could be because during this stage there are points on the heated section where the mixture's velocity is very close to zero, and thus the velocity difference between the two phases may need to be considered; furthermore, high values of void fraction may be rapidly reached. The result is that the HEM overestimates the void fraction, and consequently the buoyant force. As seen in the literature [50], the HEM gives a greater void fraction for a given quality than experiments for low flow velocities. This produces a greater driving force and acceleration in the simulation than in reality. In that case, more sophisticated models should be used, with the complication that they could present in the unsteady case.

---

<sup>2</sup>Admittedly, in the form of a term proportional to acceleration.

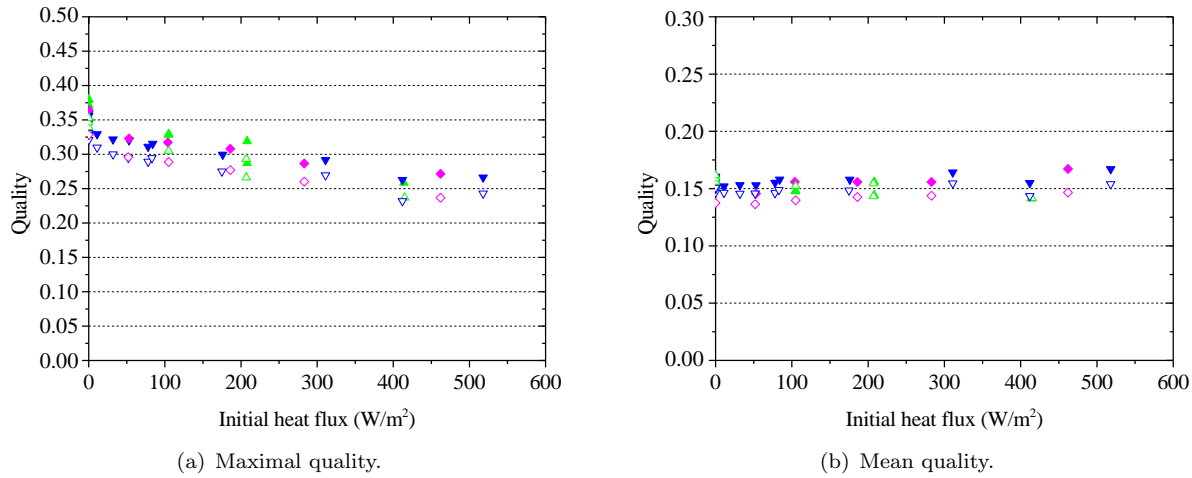


**Figure 7.5.** Quality-based incipient cases analysis using the developed models. ▲ *T3 V10, simplified*; ▼ *T4 V10 simplified*; ◆ *T5 V10 simplified*; △ *T3 V10, non-simplified*; ▽ *T4 V10 non-simplified*; ◇ *T5 V10 non-simplified*.

## 7.5 Evaluation of the transition to boiling crisis criteria with the simulators

In order to evaluate the impact of the discrepancy in the evolution of inlet velocity between the experiments and the simulations on the definition of a criterion for the incipience of boiling crisis, a similar analysis to that presented in section 6.4 was performed on the numerically obtained data.

The transient boiling crisis boundary curve is known experimentally on the parameter space  $q_i, q_f$  (Fig. 6.14). The evolution of local quality at the position transiting to crisis was studied in the same manner as with the experimental data in section 6.4. The same cases as those presented in Table 6.1 were simulated. Figure 7.5 presents the results of maximal and mean quality that would result of these cases if the inlet flow evolved as predicted by the simulations in this chapter.

Given that for a given case the simulators predict a faster evolution of the inlet velocity, the transit time from the inlet to any point of the section are shorter and thus the maximum and mean quality attained are lower than those that could be determined from the experimental data. In this case, the accumulated mean quality for the incipient cases is also independent of initial heat flux and position and has an average value of  $0.154 \pm 0.006$ . This value is 20% lower than the one found from experiments ( $0.193 \pm 0.028$ ). The effect on the maximal values is more notorious than that, especially at low initial power. To visualize this, in Fig. 7.6 the maximal and mean quality obtained from the experimental and simulated evolutions are represented. The effect of the discrepancy in the inlet velocity evolution is more important when the initial velocity is lower, because it is in those cases that the relative velocity difference will be higher and the transit time the more affected.

## Summary

With the objective of producing calculation tools that can simulate the evolution of a boiling helium natural circulation loop, two models of the loop based on the homogeneous equilibrium model (HEM) were conceived, and implemented. The first one consists on a simplified version of the equations in which pressure effects on the fluid properties are neglected, and where the

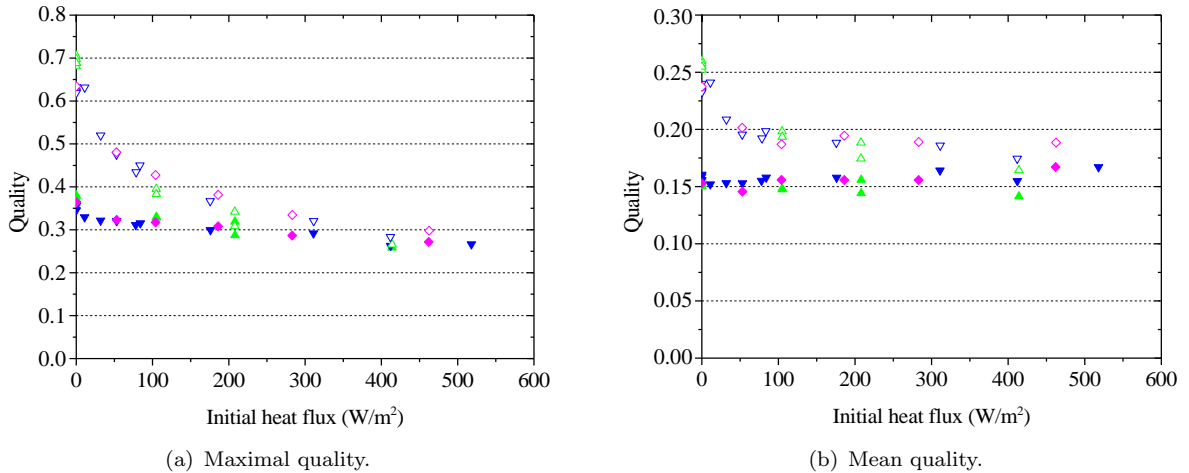


**Figure 7.6.** *Quality-based incipient cases analysis: comparison with experiments.* ▲ *T3 V10, simplified;* ▼ *T4 V10, simplified;* ◆ *T5 V10, simplified;* ▲ *T3 V10, experimental data;* ▼ *T4 V10, experimental data;* ◆ *T5 V10, experimental data.*

velocity profile is known except for an additive constant. The latter is found from an ordinary differential equation. The energy conservation is treated by a transport equation with source and time-space-dependent velocity. This model was implemented in the commercial software COMSOL. The second model consists of the full version of the three time-dependent conservation equations of the HEM with pressure effects present. This model was programmed in C.

The simplified model proved to represent well the waveform of the inlet velocity evolution, although a phase shift with respect to the experimental data was observed. The simulated evolution was faster than the measured one. In order to check on the hypothesis that this was a result of neglecting the pressure effects at the initiation of the transient, simulations were repeated using the non-simplified model.

Considering the pressure effects introduced an oscillation of the inlet velocity of higher frequency than the overall evolution. Nevertheless, with respect to the phase shift, the non-simplified model predicts the same evolution as the simplified one. Thus, the phase shift could not be attributed to the pressure-related simplifications of the model. It is possible that the phase shift is the result of a time delay on the measurement of the Venturi tube pressure drop. More likely, it could be due to the basic assumption of flow homogeneity at all times. At the initiation of the transient, when mixture velocity can be very close to zero in a great part of the heated section, the assumption of no slip between the phases can be erroneous, and a more sophisticated (transient) two-phase model may need to be considered; for example, a two-fluid formulation.

The impact of the discrepancy between simulated and measured inlet velocity was evaluated in the frame of the definition of an incipience criterion for boiling crisis. It was found that the required time-averaged quality for the onset of boiling crisis is 20% lower with the simulated inlet velocity evolution.



# Synthesis and comments

The aim of this work was the study of thermal and hydraulic features of a two-phase boiling helium natural circulation loop, at 4.2 K and 1 atm, in transient regime. To fulfill this goal, experiments were conducted on a 2-m high cryogenic loop with heated sections of around 1 m length and 6 or 10 mm i.d.. Three types of experiments were conducted:

- quasi-steady state progressions (increasing and decreasing power);
- stepwise heat flux injection from a static initial condition (zero initial heat flux);
- stepwise heat flux injection from a dynamic initial condition (non-zero initial heat flux).

Besides the experiments, the dynamics of a boiling helium natural circulation loop was modeled by two approaches:

- a simplified version of the time-dependent homogeneous model equations (neglecting pressure effects);
- the full version of the time-dependent homogeneous model equations.

The quasi-steady state experiments allowed a detailed study of various aspects of the transition to boiling crisis, namely the critical heat flux (CHF), the post-CHF heat transfer at different positions and the hydraulic characteristics of film boiling.

It was possible to validate the method proposed by Katto [44, 46, 48] for the prediction of critical heat flux in tubes between 6 and 10 mm of i.d. for positions along the heated section sufficiently far from the entrance. On the other hand, the near entrance region exhibited CHF anomalies that result in a *sudden extension of the post-CHF region towards the entrance* at a given heat flux. Thus, in this region boiling crisis happens at heat flux appreciably lower than predicted. The occurrence of this phenomenon seems to have an impact on the hysteresis of boiling crisis. *When the sudden extension has taken place, the rewetting of the heated section is simultaneous for the whole length downstream from a given point in the section. When not, almost no boiling crisis hysteresis was observed (CHF is only slightly higher than RHF).*

The study of hydraulic variables of the loop during the boiling crisis spatial development and in the post-CHF regime allowed to observe *the friction pressure drop lessening during film-boiling*. The effect on mass flow rate is more notorious as the diameter of the test section is smaller, given that friction forces become more dominant on the equilibrium equation. This phenomenon had been observed before to different extents in experiments with other fluids [31, 55], but never, to our knowledge, in helium. The available correlation for friction factors in this case [11] overestimated its value; to improve the prediction, *a new film boiling friction model was proposed*, which gives more satisfying results.

The step-pulsed heat load, static initial condition experiments allowed studying the response of the loop to the most drastic solicitation possible.

*The thermohydraulic transient can be separated in two stages. During the first stage, all the variables evolve uniformly inside the heated section, because the expansion of the two phase mixture expels mass out of the heated region through two ends. During this stage, specific enthalpy values higher than final are easily reached. The second stage starts when the diminution of average density in the heated section has produced a driving force for a sufficiently long time so as to have a positive velocity at the entrance of the heated region. During this stage, a front of cold particles travels along the heated section, wiping away the high specific enthalpy profile. After the complete passage of the cold front along the whole ascending section the system is very close to the steady condition.*

This behavior has as a result the existence of an overshoot on the mass flow rate in response to a sudden heat load increase. It could be observed analytically and experimentally that this overshoot's amplitude and occurrence time are related to heat flux by laws of type  $G_{Max} \propto q^{1/3}$  and  $t_{Max} \propto q^{-1/3}$ .

Regarding the thermal aspects, *three main types of responses have been observed*, depending on the level of power:

- transients showing *only nucleate boiling* phenomena;
- transients conducing to *boiling crisis only temporarily*;
- transient conducing to *boiling crisis in a permanent manner*.

Regarding the nucleate boiling initiation, it was observed that if power is sufficiently high, values of temperature quite close to the homogeneous nucleation limit of helium (around 0.3 K) can be attained. As soon as this happens, the activation of nucleate boiling produces a drastic decrease of wall temperature increase rate. However, if the heating rate is too low, the activation of nucleation sites takes place at lower temperature than 0.3 K, since the kinetics of nucleation in this case produces the apparition of vapor before reaching that limit.

It was observed that *transient boiling crisis, especially temporary, but permanent too, can happen at up to 35% lower heat flux than in steady state*. The characteristics of boiling crisis during slowly varying heat flux (sudden spatial extension and its link with hysteresis) were found to have an influence in the case of fast-increasing heat flux. In particular, for the heated section of 6 mm i.d., the values of heat flux that are able to initiate transient boiling crisis at the spatial point that triggers the boiling crisis hysteresis are higher than steady state RHF but lower than steady state CHF in the downstream section. This produced power-premature permanent boiling crisis. Those conditions were not reached in the case of the 10 mm i.d. heated section.

The fact that transient boiling crisis can happen below steady state CHF highlights that the mechanisms initiating it in one case or the other are not the same, at least not in all cases. *Whenever boiling crisis was observed it was initiated after a meta-stable phase of nucleate boiling*. The dependence of the duration of this stage, the critical time, on heat flux presents irregularities that reveal *the existence of different mechanisms*. The mechanism that seem to be associated to onset of boiling crisis in steady state has been observed during transients too, above steady state CHF, and it allows for relatively very high critical times. However, *the mechanism associated to premature boiling crisis, the bulk-dominated regime, has a critical time dependence of type  $t_c \propto q^{-1}$  and the values of  $t_c$  are appreciably shorter (generally below 1 s)*.

It could be determined that this regime is intrinsic to the natural circulation feature of the loop. The fact that the boiling crisis incipience point is below steady state CHF is the result of the competition of the two stages abovementioned, uniform and cold front stages. The numerical

simulation of vapor quality evolution based on the experimental data for mass flow rate evolution allowed determining that the incipience of boiling crisis happens when the transit time of the cold front to the point of interest is greater than the time required to reach a given value of quality (which depends on the diameter, *a priori*). For these heated sections, the heat flux at which this condition is verified was lower than the local steady state CHF values for a great part of the section, going upstream from the exit, reason why premature boiling crisis was observed.

At power values significantly higher than the boiling crisis incipience, it was observed that, always referring to the bulk-dominated regime

- the critical time becomes more strongly dependent of the position along the heated section;
- the trend  $t_c \propto q^{-1}$  can turn into a trend of the type  $t_c \propto q^{-2}$ ;
- the trend  $t_c \propto q^{-2}$  appears at lower heat flux the closer the position is to the exit of the heated section.

The first of these two points can be the result of differences in the flow patterns between different points of the section during the uniform-quality stage. This could result from the fact that flow velocity in this stage is non-uniform along the section (it can even be negative at the entrance and positive at the exit). Furthermore, if the slip ratio of vapor respect to liquid becomes to high, there could be a second order non-uniformity of vapor mass or volume fraction along the section.

The second point could be due to a diffusive behavior of void fraction being produced at the wall of the section. When the production rate is to high, the diffusion is not fast enough to consider the vapor distribution uniform on the cross section at all times. Still it remains unexplained why the transition to this regime is at a lower heat flux for the positions closer to the exit, which is equivalent to having a lower diffusion coefficient for vapor in these positions.

The experiments with initial heat flux different from zero allowed studying the more realistic case in which the system is initially in dynamic equilibrium.

Different aspects of the *effect of the presence of initial circulation* could be appreciated:

- the inhibition (partial or total) of premature temporary boiling crisis;
- the inhibition of premature stable boiling crisis;
- the inhibition of the bulk-dominated boiling crisis onset, in favor of the high- $t_c$  mechanism.

*These three effects, can be attributed to the same cause: not reaching of the incipience condition of the bulk dominated regime at some point of the heated section.* The presence of initial circulation accelerates the arrival of the cold front to any point of the heated section, impeding the growth of quality.

The qualitative observation of the temperature evolution in different cases defined by the pairs  $(q_i, q_f)$  allowed the *construction of charts* on which we placed boundaries for the different behaviors observed, concerning the type of boiling crisis transition.

The extension of the quality analysis performed for the static initial condition experiments revealed that, in the presence of initial heat flux, the maximum quality required for the onset of crisis decreases as initial heat flux increases. This lead us to search for another rule based on the evolution of mass quality that could allow the prediction of boiling crisis, independently of diameter, the position on the section or the initial heat flux. The inspection of quality evolutions showed that *for all the incipient cases, the time-average quality at the moment of the maximum*

was independent of all the aforementioned variables. This critical value of time-average quality is  $0.192 \pm 0.028$ .

The semi-empirical study that allowed determining a quality-based criterion for the onset of boiling crisis highlighted the need of knowing *a priori* the evolution of mass flow rate, in order to evaluate the transit time of the cold front. For this reason the integral modeling of loop thermohydraulics became necessary. This was done taking as a starting point the homogeneous equilibrium flow model (HEM).

A simplified model, whose main assumption is neglecting pressure effects on fluid properties, was able to represent fairly well the overall behavior of the inlet mass velocity of the loop. However, a phase shift of around 300 ms makes the model to predict a faster evolution than measured. Concerned about the fact that this effect could be the result of the simplification, the simulation of the full version of the HEM was realized by a numerical code developed in C. The simulations with this new code ruled out the aforementioned hypothesis. Thus, we think that,

- either the data could present a time delay with respect to the actual values, due to the instrumentation or differential pressure measurement technique;
- or the homogeneous model is not adequate during the initial instants of very fast transients, in which simultaneously vapor fraction is too high and flow velocity is low in a great part of the heated section.

An overestimation of mass flow rate during the initiation of the transient could have a very negative effect in the prediction of boiling crisis. The transit times being underestimated, it could be predicted that the boiling onset conditions are not reached for a given heat flux, when in reality they would. This highlights the need of developing better modeling and simulation tools for future use, if there is a special concern for the boiling crisis power limits during transients in helium natural circulation loops.

During the realization of this work, a significant amount of time was also devoted to the problem of natural circulation loops in which the heated section is horizontal. This was done by performing experiments on the facility described in chapter 3, with a test section consisting of a spirally twisted 4-m long tube. The idea was the natural continuation of the R&D actions that were motivated by the R3B-GLAD project [9, 30]. The study allowed observing an interesting and wide variety of dynamic phenomena, mostly producing transient behavior, even in the case of steady heat load. A part of this research has been presented recently at the Cryogenic Engineering Conference 2015 and accepted for publication [28]. The reader is invited to consult the article's text, included at the end of this document.

# Conclusions and perspectives

The experimental study presented here has allowed to push further the current knowledge of natural circulation loops with boiling helium as coolant.

A thorough characterization of the onset of boiling crisis and its hysteresis in quasi-steady state was achieved. The validation of already existing correlations could be done, however boiling crisis anomalies both during the onset and the hysteresis of boiling crisis have been observed. Furthermore, these anomalies play a non-negligible role in transient boiling crisis, being responsible for the premature permanent boiling crisis.

The friction pressure drop lessening during boiling crisis development was observed, and a model was proposed to improve the prediction of the friction factors in the case of inverted annular film boiling.

The main stages of a thermohydraulic transient originated by a step-pulsed heat flux could be identified, both from the hydraulic and from the heat transfer point of view. Namely, it is very important to notice the existence of two hydraulic phases: an expansion with uniform properties evolution, followed by the onset of natural circulation and the traveling of a cold front through the heated section.

The problem of transient boiling crisis in a helium natural circulation loop was studied, to our knowledge, for the first time. The study shows the transient boiling crisis power limits can be 35% lower than in steady state. For a heated section of 10 mm i.d. no premature *stable* boiling crisis was observed, but for a 6 mm i.d. section, stable boiling crisis has been observed at 23% lower heat flux than in steady state. The dependence of critical time (the time before the crisis onset) on heat flux puts forward the different mechanisms that can originate boiling crisis, which can be divided in two groups: that one identical to the one that triggers boiling crisis in the steady state, and those that are dominated by the transient evolution of bulk quality during the uniform evolution stage. The premature transient boiling crisis regimes correspond in all cases to the second category.

On the other hand, the initial operation of the loop at a given stable heat flux can have an inhibiting effect on the bulk-dominated mechanism that originates the anticipation of boiling crisis. This is caused by the diminution of the transit time of the cold front, resulting from the increase of inlet velocity at all times.

A quality-based criterion was determined, from the experimental data and a thermohydraulic evolution model that takes as an input the heated section inlet velocity evolution, for the prediction of boiling crisis onset and incipience: boiling crisis takes place when the accumulated time-average of local quality reaches a fixed threshold, independent of diameter, position or initial conditions.

The dynamics of the loop were simulated by means of the homogeneous equilibrium flow model (HEM), in two versions: without and with pressure effects. The two models give substantially the same results for inlet velocity evolution, especially concerning the initiation of the transient. Even if the simulators reproduce the overall shape of the time response of inlet

velocity, the signal they provide is in advance with respect to the experimental one. The most probable reason for this discrepancy is the non-validity of the basic assumptions of the HEM during the initial instants of very violent transients.

We emphasize the importance of a good determination of the inlet velocity profile evolution for the correct prediction of transient boiling crisis, since it has been proved that the transport time of particles from one point to another along the loop can be determinant on its occurrence.

The findings of this work show to what an extent wall boiling heat transfer conditions are tightly connected to the thermohydraulic characteristics of the dynamic response of the natural circulation loop.

The experimental study points out some limitations and issues to be addressed in the future. The fact that critical time depends on the position along the section points out that the evolution of vapor fraction along the heated section is not uniform during the expansion stage. Even further, it could be associated to the non-uniform velocity profile or non-uniform flow patterns that are not known during violent boiling transients. Also, the physical mechanisms behind the sudden spatial extension of boiling crisis and the simultaneous rewetting with steady heat load, though phenomenologically identified and described, are not fully explained. Flow visualization experiments through a transparent heated section during all these types of boiling transients could be highly appreciable and useful.

All the research in this work has been focused on the case of a loop with a uniformly heated section and power step-pulses. In real magnet cooling applications, the heat load on the cooling loop is rarely neither uniform in space nor stepwise, as it results from heat conduction in a geometrically complex solid. This arises the question about the validity of our experimental criterion for the determination of boiling crisis incipience in less ideal conditions. To tackle the problem of spatial distribution, experiments could be conducted with a heated section specially designed in order to have a known non-uniform heat load distribution. This could be done, for example, using a spirally glued wire with variable turn pitch. It would be interesting to test heat load distributions monotonously increasing and decreasing along the section as well as peaked or hollow at the center. To analyze the effect of the time waveform, the current experimental apparatus can be used with a proper command of the electrical source.

The numerical study points out the limitation of the homogeneous model as a tool for the simulation of transient behavior, even if it remains quite reliable in steady state flow. In the future, more detailed two-phase flow models will need to be evaluated or even created. Furthermore, the flow visualization could be very useful to decide what are the important phenomena these models need to consider, e.g. taking into account the velocity difference between phases, non-thermal equilibrium and maybe flow patterns too.

The last years' advancements in the field of high temperature superconductors, promises a future in which these materials will find numerous application. Cooling systems based on more conventional cryogenes, as liquid nitrogen are foreseen. A question that arises from our study is the extrapolation of our observations to cooling systems using other fluids. The great difference in properties of helium with respect to more classical fluids could translate into significantly different phenomena in transient boiling in natural circulation loops. Studies should be conducted on this line in order to be prepared for the years to come.

## Appendix A

# Résumé substantiel en français : Étude d'un écoulement en circulation naturelle d'hélium diphase en régime transitoire

### A.1 Introduction

La cryogénie est actuellement indispensable pour permettre de rendre certains matériaux à l'état supraconducteur, utilisés notamment dans le domaine des aimants supraconducteurs. Des basses températures sont requises pour atteindre l'état supraconducteur. Une façon de refroidir ces aimants est d'utiliser une boucle de circulation naturelle à l'hélium en ébullition. Normalement, ces systèmes sont opérés en régime permanent, c'est à dire avec une charge thermique stable dans le temps. Cependant, il peut y avoir des sollicitations thermiques variables dans le temps soit pour des besoins opérationnels, soit dans le cas d'incidents non-contrôlés. Face à de telles excitations, la réponse du système se traduit par un régime transitoire. Or, cette réponse n'est pas toujours connue. Cela pose la question dans quels cas le système de refroidissement est capable de maintenir la température du conducteur en-dessous de celle où le matériau redevient résistif, localement et globalement. Si le matériau devient résistif, la décharge de l'énergie magnétique stockée qui en résulte par effet Joule peut produire des efforts mécaniques destructifs pour la structure.

Les boucles de convection naturelle en hélium diphase ont déjà été étudiées par Baudouy et Benkheira, au CEA Saclay [5, 6, 8, 9]. Ces auteurs ont réalisé des expériences en contrôlant le flux de chaleur appliqué sur un tel système, en régime stationnaire, pour différents types des sections d'essai. Leurs observations ont permis de caractériser complètement l'échange thermique ainsi que les propriétés hydrauliques en régime d'ébullition nucléée. Ils ont aussi montré que, dans leur dispositif, il était possible d'arriver à la crise d'ébullition en paroi. En revanche, ils n'ont pas réalisé d'expériences avec une charge thermique qui évolue dans le temps.

Le littérature présente quelques travaux sur l'échange thermique par ébullition en régime transitoire en hélium et d'autres fluides cryogéniques [43, 63, 67, 71]. La plupart de ces travaux traitent le problème d'un filament ou d'une surface plate immergée dans un bain, et sur lesquelles une puissance électrique est appliquée. Ces expériences ont permis de caractériser les différents régimes de transfert thermique qui suivent une injection soudaine de puissance sur le chauffeur. En particulier, Sinha [68] a démontré que dans le cas d'ébullition sur un filament plongé dans un bain d'azote, les limites de puissance pour l'apparition de la crise d'ébullition peuvent être

plus faibles qu'en régime permanent. Cependant, la phénoménologie observée en ébullition en bain ne peut pas être facilement extrapolée au cas d'écoulements internes et dans tous les cas, ces travaux se focalisent sur des systèmes extrêmement petits (n'excédant pas quelques cm de longueur).

Quelques auteurs ont traité l'échange thermique en régime transitoire en écoulements d'hélium en canaux. Yarmak l'a étudié dans le cas d'un écoulement par convection forcée en canaux très étroits [77] tandis que Schmidt [64], et Babitch et Pavlov [4] dans celui d'un tube ou canal immergé dans un bain (l'écoulement se produisant par circulation naturelle). Ces expériences ont été menées sur des tubes de moins de 25 cm de longueur et moins de 3 mm de diamètre interne. Cela a mis en évidence des phénomènes ayant lieu lors des transitoires d'ébullition en canaux, avec un accent sur la transition à la crise d'ébullition en régime transitoire. Il est observé que celle-ci peut avoir lieu de façon temporaire à des flux de chaleur pariétaux plus faibles qu'en régime permanent. En outre, il est remarqué qu'elle survient après une période d'ébullition nucléée métastable, dont la durée est une fonction de la puissance appliquée, différente de celle obtenue en ébullition en bain. Pavlov et Babitch, en particulier, attribuent ce comportement différent au confinement dans le canal et proposent un modèle pour prédire le temps critique [61]. Néanmoins, non seulement les systèmes étudiés sont trop petits par rapport aux dimensions typiques des systèmes de refroidissement des aimants, mais aussi ces expériences n'ont pas été véritablement conduites dans une boucle de circulation. L'évolution du débit lors de ces transitoires est inconnue, et encore le flux de chaleur d'incidence de la crise d'ébullition (possiblement plus bas qu'en régime permanent) n'est pas discuté et reste imprédictible.

En résumé, des boucles de circulation naturelle en hélium diphasique de grande taille ont été étudiées en grand détail en régime permanent, surtout en régimes sans crise d'ébullition. La littérature montre que, lors d'injections violentes de puissance dans un système de refroidissement par ébullition en paroi, les valeurs de flux de chaleur critique peuvent être appréciablement plus faibles qu'en régime permanent. En revanche, ces études sont restreintes à des systèmes avec ébullition en bain ou des très petits canaux, sans information quantitative sur l'évolution de l'écoulement. Tout ceci a motivé cette étude.

Notre étude consiste à la caractérisation du comportement dynamique des boucles d'hélium en circulation naturelle de grande taille lors de transitoires induits par une augmentation soudaine du flux de chaleur pariétal. Pour ce faire, on a débuté par une étude expérimentale réalisée sur une boucle cryogénique. Dans ce montage, des écoulements transitoires peuvent être créés en contrôlant une puissance électrique, et en même temps températures, débit et perte de charge sont mesurés. L'étude expérimentale a suscité le besoin de réaliser et valider des modèles pour prédire l'évolution thermohydraulique de l'écoulement. Ceci constitue la dernière partie de ce travail.

Les prochaines sections décrivent le montage expérimental utilisé, les expériences menées, les observations qui en résultent et la modélisation de la boucle cryogénique en régime transitoire.

## A.2 Montage expérimental

Les expériences lors de ce travail furent réalisées dans une boucle cryogénique d'une hauteur totale de 2 m, à l'intérieur d'un cryostat. La boucle et le cryostat sont schématisés dans la Fig. 3.1. La boucle consiste principalement en un circuit en forme de U composé des éléments suivants:

- La branche descendante: un tube non chauffée de 4 cm de diamètre et d'environ 1,3 m de longueur. En régime permanent le fluide descend à l'intérieur de ce composant en phase liquide. Elle constitue la branche d'alimentation du système de refroidissement.

- La section d'essai: un tube chauffé électriquement par un fil enroulé et collé sur la paroi externe. Il peut être enlevé du circuit pour le remplacer par un autre. En régime permanent le fluide monte par ce composant en mélange diphasique. Il simule le tube de refroidissement qui est en contact avec l'aimant à refroidir. La chaleur injectée produit de la vapeur sur la paroi interne du tube, ce qui induit la circulation par diminution de densité.
- Le *riser*<sup>1</sup>: un tube non chauffé, en aval de la section d'essai, qui conduit le mélange diphasique au séparateur de phases.
- Le séparateur de phases: un réservoir en haut de la boucle qui reçoit le mélange qui sort de la section ascendante (section d'essai + riser). La vapeur et le liquide se séparent spontanément par gravité. Le liquide est reconduit à la section descendante et le gaz est expulsé pour éviter la sur-pressurisation. Ce réservoir est un cylindre d'un volume d'environ 50 litres et 30 cm de hauteur.

Les sections descendante et ascendante sont connectées par un tube horizontal qui complète le U.

Le cryostat est installé dans un puit dans le sol. La première barrière thermique est un écran d'azote liquide. Ce fluide est contenu dans un récipient disposé concentriquement sur la paroi de ce puit. Ensuite, à l'intérieur de la cavité, un très haut vide est produit par pompage pour limiter les transferts thermiques par convection et conduction. En outre, la boucle est enveloppée par un écran en aluminium qui agit comme un réflecteur de rayonnement thermique. Cet écran est refroidi par la vapeur d'hélium qui échappe du séparateur de phase de la boucle, produite pendant les expériences.

La boucle est attachée à la platine supérieure du cryostat, qui supporte son poids et qui ferme de façon étanche le cryostat. Le circuit d'hélium est maintenu à pression atmosphérique, ainsi la température de saturation est de 4.2 K. Le séparateur de phases peut être rempli de l'extérieur du cryostat. La vapeur qui en échappe, après avoir refroidit l'écran, sort du cryostat et est conduite dans un échangeur de chaleur par ailettes et retournée au système de récupération à température ambiante.

Dans ce travail, deux sections d'essai différentes ont été utilisées. Les deux sont faites à partir de tubes de cuivre de haute pureté désoxygéné (OFHC avec RRR=145), de 1 mm d'épaisseur et environ 1 m de longueur. L'une à 10 mm et l'autre 6 mm de diamètre interne; on les nommera désormais V10 et V06 ('V' voulant dire 'vertical'). Le chauffeur, dans les deux cas, est fait à partir d'un fil de Manganin® collé en spirale à l'extérieur du tube avec une colle époxy cryogénique. Les paramètres géométriques de chaque section d'essai sont présentés dans le tableau 3.1.

En ce qui concerne l'instrumentation, les principales variables mesurées sont:

- la température de paroi le long de la section chauffée;
- la perte de charge sur la section chauffée;
- le débit à l'entrée de la section chauffée.

La température est mesurée à cinq points de la section d'essai avec des capteurs Lakeshore Cernox<sup>TM</sup> placés sur la paroi externe du tube. Ceci donne une mesure non intrusive. Les hautes valeurs de conductivité et diffusivité thermiques du cuivre assurent que la différence de température entre les surfaces interne et externe du tube est plus faible que l'incertitude de la mesure, même en transitoire. La perte de charge hydraulique est mesurée entre les deux extrémités de la section chauffée à l'aide d'un capteur de pression différentielle Validyne<sup>TM</sup>

<sup>1</sup>On utilise le mot en anglais, faute d'une bonne traduction en français.

DP10-22. La section descendante a un tube de venturi pour mesurer le débit d'entrée dans la section chauffée; la mesure de pression différentielle se fait avec un capteur Validyne<sup>TM</sup> DP10-20. L'instrumentation peut être visualisée dans la figure 3.2 et la position exacte des capteurs de température et des prises de pression est présentée dans le tableau 3.1.

Le pilotage de la boucle s'effectue avec une interface LabView. Cette interface permet à l'utilisateur de modifier la puissance de consigne pour la source électrique qui alimente le chauffeur de la section d'essai de façon pratiquement instantanée. Le temps de réponse de l'alimentation est inférieur à 3 ms. En outre, le programme Labview utilise les signaux de tous les instruments, acquis par des cartes National Instruments<sup>TM</sup>, pour produire de graphiques déroulant avec les valeurs physiques des variables mesurées et peut stocker les tensions mesurées dans des fichiers à traiter *a posteriori*.

### A.3 Démarche expérimentale

En utilisant le montage précédemment décrit on a réalisé trois types d'expérience:

- Progressions quasi-statique de puissance;
- Transitoires induits par une marche de puissance à partir d'une condition initiale statique (sans puissance initiale);
- Transitoires induits par une marche de puissance à partir d'une condition initiale en équilibre dynamique (avec puissance initiale non-nulle).

Le premier type d'expérience vise à étudier le système en état quasi-stationnaire. C'est la façon la plus douce d'arriver à une valeur de puissance donnée, sans introduire d'effets transitoires. Le deuxième type consiste à exciter le système de la façon la plus violente concevable en arrivant à une puissance finale donnée. Le dernier type représente une situation intermédiaire et plus réaliste, vu que dans l'opération réelle d'un système de refroidissement, lors d'un incident de haute sollicitation, le système se trouve déjà en opération à une valeur de puissance (souvent) basse. Les résultats de ces trois types d'expérience sont présentés par la suite, ainsi que la discussion qu'ils suscitent.

### A.4 Comportement de la crise d'ébullition en régime permanent

L'étude expérimentale de la boucle en régime permanent fut réalisée en excitant le système avec des progressions lentes de puissance, en montant depuis une puissance nulle et aussi en descendant depuis une puissance élevée. L'acquisition de données a été faite à puissance strictement constante dans le temps. Pour cela, pour passer d'une valeur à autre, des rampes très lentes ont été appliquées au chauffeur (pas de marche brutale); une fois à la valeur désirée de puissance, on a laissé le système s'établir et on a lancé l'acquisition. Les valeurs des différentes variables ont été moyennées dans le temps pour chaque valeur de puissance. C'est ainsi qu'on a obtenu l'évolution des variables en fonction du flux de chaleur, présentée dans les Figs. 4.2 (température), 4.3 (débit) et 4.4 (perte de charge).

#### A.4.1 Le début et développement de la crise d'ébullition

L'évolution de la température de paroi le long de la section chauffée lors d'une progression de puissance ascendante montre qu'à toutes les positions il existe une valeur de flux de chaleur

en paroi ( $q$ ) pour laquelle on passe d'un régime de transfert thermique avec un bon coefficient d'échange ( $h$ ) à un autre où  $h$  peut diminuer même en un facteur 10. Ceci est mis en évidence par une soudaine augmentation de la température de paroi à une valeur de  $q$  donnée. Le régime de basse température correspond à l'ébullition nucléée (NB) en paroi et celui de haute température à l'ébullition en film (FB). Le flux de chaleur auquel a lieu la transition est connu comme *flux de chaleur critique* (CHF) et représente une limite dans l'opération du système de refroidissement, dû aux hautes valeurs de la température de paroi quand il est dépassé. Dans notre boucle, le CHF dépend de la position, vu qu'il est plus bas pour les positions près de la sortie, que pour celles près de l'entrée (voir le tableau 4.1). Ceci est lié au fait que le titre massique (la fraction de vapeur) est plus élevé vers la sortie de la section chauffée.

L'évaluation de la corrélation de Katto pour la détermination du CHF [44, 48, 49], très connue dans la littérature, a montré que les valeurs de CHF à plus de 50 cm de l'entrée peuvent être prédits correctement (voir le tableau 4.2). Cependant, un phénomène anormal a été observé dans le cas des deux sections d'essai. Celui-ci consiste à une extension spatiale soudaine de la région en régime post-CHF vers l'entrée à un certain flux de chaleur. Ceci est induit du fait que, pour V10, T2 et T1 et, pour V06, T3 et T2 on retrouve la même valeur de CHF. Cette anomalie peut être due à un changement de mécanisme de la transition à la crise: en aval la transition est contrôlée par l'apport de vapeur du mélange diphasique au sein de la section, alors qu'en amont le mécanisme est dominé par l'arrachement de la vapeur de la paroi par l'écoulement quasi-liquide.

Des expériences en progression descendante de puissance ont mis en évidence deux comportements possibles pour l'hystérésis de la crise d'ébullition. Quand la puissance initiale a dépassé la valeur pour l'extension soudaine de la région post-CHF, il est nécessaire de baisser  $q$  bien en dessous du CHF pour revenir au régime d'ébullition nucléée. En plus, il a été observé que dans ce cas, la récupération du régime NB est simultanée en terme de  $q$  (ce flux de chaleur est dénommé RHF) et se produit comme une vague qui voyage en aval. Ceci est suggéré par l'évolution temporelle des températures mesurée lors de la récupération du régime NB (voir Fig. 4.7(a)). Quand, initialement, on n'a pas dépassé la valeur de  $q$  pour l'extension soudaine, on n'a pas véritablement observé un hystérésis de la crise d'ébullition. Les valeurs de  $q$  auxquelles le régime NB est récupéré sont à peine plus faibles que le CHF et en conséquence dépendants de la position (voir Fig. 4.7(b)). On peut espérer que ce double comportement de l'hystérésis ait des effets sur le comportement transitoire de la crise d'ébullition.

#### A.4.2 Les effets hydrauliques de la crise d'ébullition

Quant à la réponse hydraulique de la boucle lors de la crise d'ébullition, un effet de réduction des forces de frottement a été mis en évidence. Quand on regarde l'évolution du débit et de la différence de pression entre l'entrée la sortie de la section d'essai en simultanée avec l'extension spatial du régime FB, on voit que le premier augmente et la dernière diminue. Ceci ne peut être dû qu'à la diminution du coefficient de frottement. Ceci est une conséquence du fait que la viscosité de la vapeur est environ 3 fois plus faible que celle du liquide; ainsi, le film de vapeur en paroi agit comme un isolant thermique et comme un lubrifiant. On a aussi observé que lors de l'extension soudaine de la région post-CHF il y a un saut abrupt dans les deux variables hydrauliques mesurées; ceci confirme le lien entre le régime de FB et le phénomène hydraulique en question. De la même manière, dans le cas des progressions de puissance descendante avec hystérésis, les valeurs de perte de charge totale restent bien faibles jusqu'à la récupération du régime NB, moment auquel il y a un saut considérable pour retourner aux valeurs plus élevées correspondants au régime NB.

Le seul modèle d'application simple qu'on peut trouver dans la littérature [11] pour estimer la perte de charge par frottement en FB surestime par un factor 2 ou 3 nos mesures. Pour

cette raison, on a conçu et évalué un nouveau modèle qui tient compte du fait que la vitesse à l'interface du film est significativement plus faible que la vitesse moyenne de l'écoulement. En outre, le profil turbulent peut ne pas être totalement développé à l'intérieur du film de vapeur. Tout ceci peut être plus déterminant dans l'hélium que dans des fluides classiques du fait que les valeurs de densité et viscosité des deux phases sont très proches. Les prédictions de notre modèle sont plus proches des données expérimentales que celles du modèle existant auparavant. Ceci peut être apprécié dans la Fig. 4.10.

## A.5 Transitoires avec condition initiale statique

Avec le but d'étudier la réponse du système dans le cas de la sollicitation la plus violente possible, des expériences ont été réalisées, dans lesquelles le flux de chaleur sur la section chauffée est augmenté soudainement de zéro à une valeur finale donnée. Ainsi, initialement le système se trouve en repos.

Lors de ces transitoires notre attention s'est portée principalement sur l'évolution de la température de paroi le long de la section chauffée et du débit d'entrée. Leur évolution pendant des transitoires avec différentes valeurs de flux de chaleur final  $q_f$  peut être observée dans les Figs. 5.2 à 5.5.

### A.5.1 La réponse hydraulique

L'observation des instants initiaux de l'évolution du débit dans le tube de Venturi montre une période pendant laquelle la vitesse d'entrée dans la section chauffée est négative. Ceci indique que l'injection violente de puissance produit l'échappement de fluide par les deux extrémités de la section chauffée, comme une conséquence de l'expansion induite par le changement de phase liquide vapeur. Quand la densité dans la branche ascendante de la boucle a diminué suffisamment, la force bouillante se met en œuvre et la vitesse à l'entrée de la section d'essai augmente et devient positive. On observe expérimentalement un *overshoot* de cette vitesse par rapport à la valeur finale stable à la fin du transitoire. Ceci témoigne d'une force motrice qui pendant les instants initiaux du transitoire excède les valeurs qui correspondent au régime permanent. Les temps caractéristiques de l'évolution du débit d'entrée ne sont pas constants, mais dépendent de la puissance finale injectée. Ceci est le résultat de la non-linéarité des processus à l'origine de l'évolution thermohydraulique, notamment le transport des cumuls de vapeur dans la section ascendante (des termes advectifs de la forme  $u \frac{\partial}{\partial x}$ ). Expérimentalement, le temps auquel on observe la valeur maximale de vitesse d'entrée est lié au flux de chaleur appliqué par une loi  $t_{Max} \propto q^{-1/3}$ . La valeur du débit maximum suit une loi  $\dot{m}_{Max} \propto q^{1/3}$ .

On souligne à ce point que l'évolution thermohydraulique qui suit l'injection de puissance est composée des deux étapes bien différentes en nature:

- Initialement, il y a une phase où du fluide est expulsé par les deux extrémités de la section chauffée; pendant cette période l'évolution des variables énergétiques (enthalpie, fraction de vapeur) est spatialement uniforme (à premier ordre) dans la section chauffée.
- Plus tard, quand la vitesse d'entrée devient positive, les particules qui rentrent par le bout inférieur ont été moins de temps à l'intérieur de la section chauffée (avant d'être expulsées) ou ne l'ont pas été du tout (dans le cas le plus générale). Ceci induit l'arrivée d'un front froid qui "nettoie" la vapeur de la section ascendante, en se déplaçant depuis l'entrée, jusqu'à la sortie du *riser*.

Un fois que ce front froid est passé par un point donné, la valeur d'enthalpie local (ou fraction de vapeur), est significativement plus faible que celle atteinte pendant la phase d'expansion uniforme. Une modélisation mathématique simplifiée de ce processus permet de trouver analytiquement les lois d'échelle énoncées dans le paragraphe précédent pour  $t_{Max}$  et  $\dot{m}_{Max}$ .

### A.5.2 Les régimes de transfert de chaleur

Du point de vue du transfert thermique, il y a deux aspects qui nous ont occupés: l'initiation de l'ébullition nucléée et le déclenchement de la crise d'ébullition en régime transitoire.

#### L'initiation de l'ébullition

L'étude de l'initiation de l'ébullition nucléée fut réalisée à partir de l'observation des transitoires avec des puissances finales bien faibles ( $q = 15 \text{ W/m}^2$ ) ou modérées (jusqu'à  $900 \text{ W/m}^2$ ). Il est attendu, à partir de la littérature [71], qu'avant la mise en place de l'ébullition il y ait une phase où le seul mécanisme de transfert de chaleur est la conduction solide de la puissance en paroi au sein de la section transversale. Dans ce cas la température évolue en suivant une loi  $\theta \propto \sqrt{t}$ . En identifiant cette étape de l'évolution sur nos mesures de température de paroi (voir Fig. 5.8), on a réussi à déterminer le moment auquel l'ébullition se met en place, défini comme celui auquel la relation  $\theta \propto \sqrt{t}$  n'est plus valable.

A très faible puissance, la mise en place de l'ébullition est lente, ce qui permet d'arriver à des valeurs de surchauffe appréciablement plus élevées que dans le régime permanent obtenu à la fin du transitoire; ainsi l'évolution de température présente un pic. Quand la puissance est plus élevée, l'augmentation de la température est tellement rapide qu'on atteint la limite de nucléation homogène en très peu de temps et de la vapeur se crée très rapidement dans les cavités de la surface; cela active l'ébullition nucléée, en arrêtant l'augmentation rapide de la température. Les valeurs finales de température après le transitoire sont essentiellement les mêmes que celles obtenues en régime quasi-statique; alors, quand ces valeurs sont plus faibles que la limite de nucléation homogène ( $\approx 0,3 \text{ K}$ ), le moment où cela arrive constitue un pic. Pour de très hautes puissances la valeur stable de température est plus élevée que cette limite, alors l'arrivée de la nucléation homogène produit simplement une diminution abrupte du taux de croissance de la température.

#### La crise d'ébullition en régime transitoire

Concernant les transitoires qui conduisent à la crise d'ébullition, ceux-ci ont été identifiés dans les cas de puissance plus élevée par une augmentation plus sévère de la température, c'est-à-dire de plus de  $1 \text{ K}$  (voir les cas présentés dans les Figs. 5.3, 5.4 and 5.5). On a pu identifier (principalement) deux types de comportement qualitativement différents. L'un d'eux consiste en une évolution avec augmentation temporaire de la température pendant une période de temps et une valeur de pic variables (qui augmentent quand  $q_f$  augmente), qui finit avec un rétablissement des valeurs de surchauffe faibles typiques du régime NB; ce type de transitoires a été dénommé TBC (*Temporary Boiling Crisis*). Dans l'autre cas, une excursion à des températures élevées se déclenche et dans l'état final c'est le régime FB qui reste; ce type de transitoires a été dénommé SBC (*Stable Boiling Crisis*). Les observations montrent que:

- Si la valeur de flux de chaleur final est au-dessus du CHF mesuré en régime quasi-statique, le transitoire est de type SBC (les transitoires TBC ont lieu uniquement en-dessous).
- Dans certains cas les transitoires SBC peuvent avoir lieu avec flux de chaleur final en-dessous du CHF quasi-statique.

Alors, en-dessous du CHF quasi-statique les deux comportements sont possibles. Ce qui est alarmant est que *lors de l'injection soudaine de puissance la limite de flux de chaleur pour la crise d'ébullition est plus faible*, spécialement quand on s'éloigne de l'entrée de la section chauffée. Des excursions de température potentiellement dangereuses du point de vue de la protection du supraconducteur ont été observées à des puissances 35% plus faibles qu'en régime permanent. Ceci témoigne d'un mécanisme qui peut produire la crise d'ébullition en transitoire, indépendant de celui en régime permanent. Les valeurs précises d'incipience des deux types de transitoire mesurées pour les deux sections d'essai à toutes les positions sont présentées dans le tableau 5.1. La crise stable en-dessous du CHF quasi-statique (crise stable prématurée) a été observée uniquement pour la section V06. Ceci s'explique du fait que dans cette section d'essai les conditions se donnent pour qu'un flux de chaleur final à peine plus élevé que celui de récupération (RHF) soit capable de produire la crise d'ébullition transitoire dans le point de la section chauffée où se produit en progression quasi-statique l'extension soudaine de la crise d'ébullition; ceci déclenche le mécanisme d'hystérésis de la crise, ce qui la rend stable à ce niveau de puissance. Cela n'arrive pas dans la section V10.

Dans tous les cas qui présentent de la crise d'ébullition de tout type il a été observé qu'il existe une période de temps qui précède la crise pendant laquelle il y a un régime de NB métastable. La durée de cette phase, appelée *temps critique*  $t_c$ , est très fortement dépendante du flux de chaleur appliqué. Cette dépendance fut étudiée de façon systématique, en donnant par résultat le graphique de  $t_c$  vs.  $q_f$  de la Fig. 5.14. Il est possible de distinguer deux régimes différents pour le temps critique:

- un régime de *temps critique élevé*, qui est observé exclusivement dans les positions très proches à l'entrée de la partie chauffée;
- un régime de temps critiques faibles, où  $t_c \propto q_f^{-1}$  approximativement; on dénomme ce régime *linéaire*.

Dans le premier cas, nous estimons que le mécanisme physique qui donne lieu à la crise est le même qui existe en régime quasi-statique, vu que même en transitoire, dans ce régime, la crise est survenue en plusieurs cas une fois que toutes les variables avait déjà atteint leurs valeurs stables. En outre, ce régime n'est observé qu'en-dessous du CHF quasi-statique. Le mécanisme derrière l'autre régime est le seul responsable de la crise prématurée. On a montré que ce mécanisme est fortement lié au fait que pendant la phase thermohydraulique d'expansion uniforme un certain seuil de fraction de vapeur soit atteint avant l'arrivée du front froid. C'est pourquoi on dit que ce régime est *dominé par les propriétés au sein de la section transversale*. A certaines positions, par exemple T2 en V10, on a pu observer une transition entre les deux régimes à une valeur de  $q_f$  en-dessous du CHF quasi-statique. Pour les positions où il y a de la crise prématurée on a pas du tout observé le régime de *temps critique élevé*, dans le cas de transitoires avec condition initiale statique.

L'incipience de la crise d'ébullition par le régime *linéaire* dans le cas de ce type d'excitation s'explique à partir de la concurrence de deux phénomènes. D'un côté il y a l'augmentation de la fraction de vapeur, pour laquelle le temps pour arriver au seuil est  $t_c \propto q_f^{-1}$ . De l'autre, l'arrivée du front froid, pour laquelle la loi est proche de  $t_r \propto q_f^{-1/3}$ . Vu que  $t_r$  diminue plus lentement que  $t_c$  quand  $q_f$  augmente, on peut espérer qu'à partir d'une certaine valeur de  $q_f$  le seuil de fraction de vapeur pour déclencher localement la crise soit atteint. Ce seuil d'incipience fut déterminé pour V06 et V10, à toutes les positions, en utilisant l'évolution mesurée de la vitesse d'entrée pour connaître la position du front froid en fonction du temps. Les valeurs sont présentées dans le tableau 5.3. Elles oscillent entre une fraction massique de vapeur de 0,5 à 0,7.

## A.6 Transitoires avec condition initiale dynamique

Nous avons voulu étudier la situation intermédiaire, plus réaliste, dans laquelle le système de refroidissement se trouve déjà en fonctionnement au moment de l'augmentation soudaine de charge thermique. Pour cela, des expériences furent réalisées en appliquant un flux de chaleur initial  $q_i$  par une montée graduelle de la puissance et en injectant ensuite une valeur plus élevée de flux de chaleur final  $q_f$  de façon instantanée.

Le but fut de faire une étude systématique des effets de la condition initiale sur le déroulement du transitoire. Pour cela, des valeurs de  $q_f$  furent fixés, et la valeur de  $q_i$  fut modifiée à chaque essai.

### A.6.1 Résumé des principaux effets observés

Les Figs. 6.2 à 6.5 montrent des évolutions temporelles en regroupant essais avec les mêmes  $q_f$  et  $q_i$  croissants. Les séries présentées furent choisies pour mettre en évidence un certain effet en particulier.

La Fig. 6.2 montre des cas où à la position du capteur de température et avec  $q_i = 0$  on observait un transitoire du type TBC. L'augmentation de  $q_i$  a un effet inhibitoire sur l'excursion critique de température. D'abord la durée, et puis la valeur maximale diminuent, et finalement l'excursion disparaît complètement. La valeur de  $q_i$  à laquelle la disparition complète de la crise arrive a été dénommé  $q_{inh}$ . La Fig. 6.3 montre des cas où à la position du capteur de température et avec  $q_i = 0$  on observait un transitoire du type SBC prématurée (seulement observé pour V06). En augmentant  $q_i$ , d'abord il y a un changement de type de transitoire: la SBC devient TBC. Finalement, la TBC est inhibée comme dans le cas précédant et disparaît complètement.

Ces deux phénomènes d'inhibition dans le cas de la crise prématurée témoignent des effets que la condition initiale a sur le déroulement de l'évolution thermohydraulique dans la section chauffée. La présence d'un flux de chaleur initial signifie la présence d'un débit initial. Lors de l'injection de  $q_f$ , les valeurs de vitesse d'entrée sont plus élevées que dans le cas sans puissance initiale (voire tout le temps positives). Cela accélère l'arrivée du front froid, en réduisant les valeurs maximales de fraction de vapeur atteintes. Cet effet s'observe d'abord dans les positions près de l'entrée, où l'inhibition totale de la crise prématurée se fait avec un  $q_i$  plus faible que près de la sortie. La SBC prématurée de V06 dévient TBC parce que la crise est inhibée totalement dans le point qui déclenche l'hystérésis, avant que cela se produise pour les positions plus en aval.

La Fig. 6.5 montre ce qui peut arriver avec  $q_f$  au-dessus du CHF quasi-statique. On a choisi des cas où avec  $q_i = 0$  le mécanisme initiant la crise est celui du régime linéaire. Il existe une valeur de  $q_i$  telle que le régime linéaire est inhibé, comme dans les cas précédants, mais au-delà de cette valeur, comme  $q_f$  est plus élevé que le CHF quasi-statique, la crise arrive finalement par le régime de temps critique élevé. Alors la condition initiale dans ce cas induit un changement de mécanisme. La Fig. 6.4 montre le cas où, avec  $q_i = 0$ , on est dans le régime de temps critique élevé. Ici, aucun effet remarquable ne peut être signalé.

En résumé, tous les effets précédents peuvent être expliqués par le fait que la condition initiale a un effet inhibitoire sur le mécanisme associé au régime linéaire de temps critique.

Quant au temps critique  $t_c$ , l'augmentation de  $q_i$  produit une diminution de ce paramètre tant qu'on est dans le régime linéaire de début de la crise, comme le montrent les Figs. 6.10 à 6.13. A faible  $q_i$  l'effet est trop léger, mais il s'accroît à plus hautes valeurs de  $q_i$ , spécialement quand on s'éloigne de l'entrée. Ceci est conséquence de la présence initiale d'une fraction de vapeur dans la section chauffée. Cette fraction est plus élevée dans l'état initial quand  $q_i$  est plus

grand et quand on s'éloigne de l'entrée. Cette quantité initiale de vapeur permet d'atteindre la condition critique plus rapidement.

### A.6.2 Carte de comportements

A partir des observations qualitatives sur le type de transitoire par rapport à la crise d'ébullition, il fut possible de dessiner des cartes de comportement sur le plan défini par les deux paramètres contrôlés, les flux de chaleur initial et final. Dans ces cartes, on peut placer quatre régions selon le type de transitoire: ébullition nucléée stable (SNB), crise d'ébullition temporaire (TBC), crise d'ébullition stable initiée par le régime linéaire (SBC-lin) et crise d'ébullition stable initiée dans le régime de temps critique élevé (SBC-non-lin). Il a deux frontières fondamentales: celle qui limite le mécanisme de transition à la crise en régime linéaire, et celle qui limite l'existence de la crise en régime permanent. Les régions et frontières déterminées expérimentalement sont présentées dans la Fig. 6.14. Les cartes ainsi définies dépendent du diamètre et longueur de la section chauffée et de la position le long d'elle. Bien qu'elles ne sont pas générales, elles permettent de voir comment les frontières se déplacent quand on change de position, par exemple, et de mieux visualiser pourquoi certains régimes ne sont pas observés près de l'entrée de la section, ou pourquoi un type de crise prévaut sur les autres.

### A.6.3 Un critère empirique pour l'arrivée de la crise

L'apparition de la crise d'ébullition en régime permanent est assez bien connue et plusieurs corrélations basées sur des nombres non-dimensionnels existent. Avec le but de généraliser un critère pour le déclenchement de la crise d'ébullition, on a analysé l'évolution locale des variables thermohydrauliques à partir des données expérimentales. Elles furent utilisées comme entrée d'un modèle simple de transport. Ce modèle considère que si on connaît la puissance injectée et la vitesse d'entrée de la section chauffée (qui ont été mesurées), on connaît la vitesse locale et instantanée à tout point, au travers de simplifications sur le modèle homogène d'écoulement diphasique. De cette façon il est possible à partir d'une approche Lagrangienne, de connaître l'évolution de la fraction massique de vapeur.

En utilisant seulement les cas expérimentaux qui sont très proches de la frontière du mécanisme linéaire dans la carte de comportement, on a pu observer que:

- La valeur maximale locale de fraction de vapeur pour les cas de frontière est indépendante de la position le long de la section, légèrement dépendante du diamètre de la section, et décroissante en fonction du flux de chaleur initial (voir Fig. 6.17(a)).
- La valeur moyenne de la fraction de vapeur locale jusqu'au moment de l'arrivée du front froid est une constante indépendante de toutes ces variables (voir Fig. 6.17(b)).

Alors on propose comme critère que la crise d'ébullition par le régime linéaire a lieu si, avant l'arrivée du front froid, la moyenne temporelle accumulée de la fraction de vapeur locale dépasse une valeur de  $0.192 \pm 0.028$ .

Pour l'application générale de ce type de critère, il est nécessaire de connaître l'évolution de la position du front froid, qui résulte de l'évolution de la vitesse d'entrée. Il est nécessaire de disposer d'un outil qui permet de prédire cette évolution.

## A.7 Modélisation de l'écoulement diphasique

Avec le but d'avoir un outil de calcul permettant d'évaluer l'évolution thermohydraulique dans la boucle et éventuellement prédire l'apparition de la crise d'ébullition, des modèles ont été développés à partir du modèle homogène d'écoulement diphasique (Eqs. (2.28)).

### A.7.1 Un modèle simplifié

D'abord les équations du modèle homogène furent traitées analytiquement en faisant quelques simplifications, avec le but d'arriver à une vision intuitive du comportement du système et pour simplifier sa résolution numérique. Les simplifications fondamentales furent de négliger les termes potentiels et cinétiques dans l'équation de conservation de l'énergie, d'ignorer le sous-refroidissement (spécialement dans le cas des puissances trop élevées qui conduisent à la crise) et de négliger les effets de la pression sur les propriétés du mélange diphasique (la densité est uniquement fonction de l'enthalpie). Dans ce cadre, le système à résoudre est composé d'une seule équation en dérivées partielles, pour l'enthalpie, une équation différentielle ordinaire pour l'évolution du moment linéaire intégral, et des équations algébriques qui permettent d'évaluer les autres variables (densité, vitesse, etc.). Ce système est décrit par les Eqs. (7.31). Sa résolution fut implémentée dans le software de simulation commercial COMSOL. La géométrie du système et les propriétés du fluide, ainsi que l'évolution de la charge thermique peuvent très facilement être modifiées de façon paramétrique.

### A.7.2 Le modèle non-simplifié

Pour identifier et quantifier l'impact des simplifications, les équations du modèle homogène sans simplification furent résolues. Pour cela, un code a été développé en C à partir d'une méthode numérique originale. Les équations furent écrites dans la formulation non-conservative (dérivée matérielle = termes de source). La variable spatiale fut traitée par différences finies avec des nuds équidistants. Les termes source furent calculés avec un schéma centré spatialement et leur avancement temporel est semi-implicite. Les termes advectifs de la dérive matérielle ( $u \frac{\partial}{\partial s}$ ) furent traités avec un schéma up-wind spatialement, et d'Euler explicite temporellement (pour éviter de la diffusion numérique artificielle). Vu que les équations résultantes pour trouver les valeurs actualisées des variables à chaque pas de temps sont non-linéaires, on a opté pour une méthode itérative à chaque pas de temps. Les équations pour l'avancement temporelle dans les nuds internes et du bord du domaine sont présentées en détail dans les sections 7.4.3 et 7.4.6.

### A.7.3 Validation et limitations des simulations numériques

L'évolution du débit d'entrée de la section chauffée simulée avec les modèles fut comparée avec les données expérimentales (mesure du tube de Venturi). Dans un premier temps, on a confronté les résultats du modèle simplifié ; ce qui est illustré dans la Fig. 7.2. On a pu constater que le modèle est capable de représenter assez fidèlement la forme globale de l'évolution de cette variable, avec son *overshoot* et les oscillations. En revanche, il y a un déphasage temporel d'environ 300 ms entre les deux signaux (la simulation est en avance par rapport aux mesures). La question fut de savoir si ce déphasage ne résultait de simplifications additionnelles que l'on avait faites aux équations. Quand on compare les mesures avec le modèle non-simplifié (voir Fig. 7.4) on constate que ce déphasage est pratiquement identique.

L'origine la plus probable de cette différence sur le temps d'initiation de la circulation naturelle doit être liée à la non-validité des hypothèses basiques du modèle homogène pendant les

instants initiaux du transitoire. Il doit être nécessaire de considérer que les deux phases n'ont pas la même vitesse et que la fraction de vide ne peut pas être estimée à partir de l'hypothèse d'homogénéité. Il pourrait même être nécessaire de considérer des topologies d'écoulement non homogènes. Il est nécessaire de raffiner la modélisation pour prendre en compte ces aspects.

## A.8 Conclusions

L'étude expérimentale présentée ici a permis d'approfondir la connaissance des boucles de circulation naturelle avec l'hélium comme réfrigérant.

Une caractérisation exhaustive de l'apparition et l'hystérésis de la crise d'ébullition en régime permanent a été accomplie. Des corrélations préexistantes purent être validées dans le cas de ces boucles; néanmoins, des anomalies ont été identifiées durant l'apparition et l'hystérésis de la crise d'ébullition. En outre, ces anomalies jouent un rôle en l'ébullition en régime transitoire, étant responsables d'une transition prématurée (en termes de flux de chaleur) à la crise. L'amointrissement de la perte de charge par frottement lors du développement de la crise d'ébullition fut observé, et un modèle fut proposé pour améliorer la prédiction du facteur effectif de frottement dans le cas d'ébullition en film en écoulement annulaire inversé.

Les étapes principales d'un transitoire thermohydraulique lors d'une marche de flux de chaleur en paroi furent identifiées, des points de vue hydraulique et du transfert thermique. En particulier, il est nécessaire de noter l'existence de deux étapes: une expansion avec une évolution des propriétés spatialement uniforme suivie du déclenchement de la circulation naturelle et un front froid qui voyage le long de la section chauffée.

La crise d'ébullition transitoire dans une boucle de circulation naturelle en hélium fut étudié, à notre connaissance, pour la première fois. On a montré que les limites de puissance pour ce phénomène peuvent être 35% plus basses qu'en régime permanent. En plus, pour la section chauffée plus étroite (6 mm de diamètre interne), la crise d'ébullition permanente fut observée à un flux de chaleur 23% plus bas qu'en régime permanent. La dépendance du temps critique (le temps avant l'excursion de température) comme fonction du flux de chaleur met en évidence les différents mécanismes à l'origine de la crise d'ébullition, qui peuvent être classifiés en deux groupes: ceux qui agissent dans le cas du régime permanent, et ceux qui sont dominés par l'évolution de la fraction de vide pendant la phase d'évolution uniforme. Les régimes de crise prématurée correspondent toujours à la deuxième catégorie.

Le fonctionnement initial de la boucle avec un flux de chaleur initial stable peut inhiber le mécanisme qui produit l'anticipation de la crise d'ébullition. Ceci est dû à la diminution du temps d'arrivée du front froid, résultant de l'augmentation à tout temps de la vitesse d'entrée à la section chauffée.

Un critère fondé sur le titre massique fut déterminé, à partir des données expérimentales et un modèle d'évolution thermohydraulique qui prend comme entrée l'évolution de la vitesse d'entrée, pour prédire l'apparition et l'incipience de la crise d'ébullition. Celle-ci arrive quand la moyenne temporelle accumulée atteint un seuil, indépendante du diamètre, position ou conditions initiales.

La dynamique de la boucle fut simulée en utilisant deux versions du modèle homogène en équilibre: sans et avec des effets de pression sur les propriétés. Les deux modèles donnent substantiellement les mêmes résultats en ce qui concerne l'initiation du transitoire. Cependant, bien que les simulateurs imitent très bien la forme globale de l'évolution de la vitesse d'entrée, le signal simulé est en avance par rapport à celui mesuré. La raison la plus probable de cet écart est l'invalidité des hypothèses basiques du modèle homogène pendant les instants initiaux de transitoires très violents.

Nous soulignons l'importance d'une bonne prédiction de l'évolution de la vitesse d'entrée

pour la bonne prédiction de la crise en transitoire, étant donné son impact directe sur le temps d'arrivée des particules froides à un point donné.

Cette recherche montre à quel point les conditions d'échange thermique en paroi sont intimement liées aux caractéristiques thermohydrauliques de la réponse dynamique de la boucle de convection naturelle.

L'étude expérimentale met en avant quelques limitations et problèmes à être traités dans l'avenir. La dépendance du temps critique par rapport à la position le long de la section met en évidence que la fraction de vapeur n'est pas spatialement uniforme pendant la phase d'expansion ou qu'il y a des effets dus à la non-uniformité du profile de vitesse ou le type d'écoulement (flow pattern). Des expériences de visualisation à travers une section chauffée transparente pourraient être hautement utiles.

L'étude numérique souligne les limitations du modèle homogène comme un outil pour la simulation des transitoires, bien qu'il reste très fiable en regime permanent. Dans l'avenir, des modèles plus détaillés d'écoulement diphasique doivent être évalués ou même créés. La visualisation pourrait signaler les phénomènes nécessaires à inclure dans ces modèles, notamment la différence de vitesse entre les phases, le non-equilibre thermique, les types d'écoulement, etc..

Enfin, envisageant l'utilisation future des supraconducteurs de haute temperature critique (HTS) pour la fabrication de grands aimants supraconducteurs, des études similaires à celle présentée ici devraient être menées en utilisant d'autres fluides cryogeniques de plus haut point d'ébullition, notamment l'azote. La grande différence de propriétés entre ces fluides et l'hélium pourrait induire des différences notables dans le comportement transitoire d'une boucle. En faisant ces études à l'avance, on sera mieux préparé pour l'avenir.



## Appendix B

# The film boiling friction model equations

Equation (4.19) can be expressed non-dimensionally if we take the non-dimensional velocity as

$$\tilde{V} = \frac{V}{V_h}. \quad (\text{B.1})$$

We define the dimensional parameter  $B$  as

$$B = \left( \frac{8}{0.316} \frac{\mu_g}{\delta_{eff}} D^{1/4} \rho_h^{-3/4} \mu_h^{-1/4} \right)^{4/7}. \quad (\text{B.2})$$

Thus, Eq. (4.19) becomes

$$\frac{B}{V_h^{3/7}} \tilde{V}_f^{4/7} + \tilde{V}_f = 1. \quad (\text{B.3})$$

The solution of this equation for  $V_f$  as a function of the non-dimensional parameter

$$\tilde{B} = \frac{B}{V_h^{3/7}} \quad (\text{B.4})$$

is shown in figure B.1. Alternatively, Eq. (B.3) can be solved by the iterative fixed point method:

$$\tilde{V}_{f,n+1} = 1 - \tilde{B} \tilde{V}_{f,n}^{4/7}, \quad (\text{B.5})$$

whose convergence is assured for  $\tilde{B} < \left( \left( \frac{4}{7} \right)^{7/3} + \left( \frac{4}{7} \right)^{4/3} \right)^{-3/7} \approx 1.13$  with an initial guess such that  $\left( \frac{4\tilde{B}}{7} \right)^{3/7} < \tilde{V}_{f,0} < \left( \frac{1}{\tilde{B}} \right)^{7/4}$  or

$$\tilde{V}_{f,n+1} = \left( \frac{1 - \tilde{V}_{f,n}}{\tilde{B}} \right)^{7/4}, \quad (\text{B.6})$$

whose convergence is assured for  $\tilde{B} > \left( \left( \frac{4}{7} \right)^{7/3} + \left( \frac{4}{7} \right)^{4/3} \right)^{-3/7} \approx 1.13$  with an initial guess such that  $\left( \frac{4\tilde{B}}{7} \right)^{3/7} < \tilde{V}_{f,0} < \left( \frac{1}{\tilde{B}} \right)^{7/4}$ . Given that physically, necessarily,  $\tilde{V}_f < 1$ , an initial guess of  $\tilde{V}_{f,0} = 0.4$  is a very good option, because of the slow convergence near  $\tilde{B} = 1.13$ .

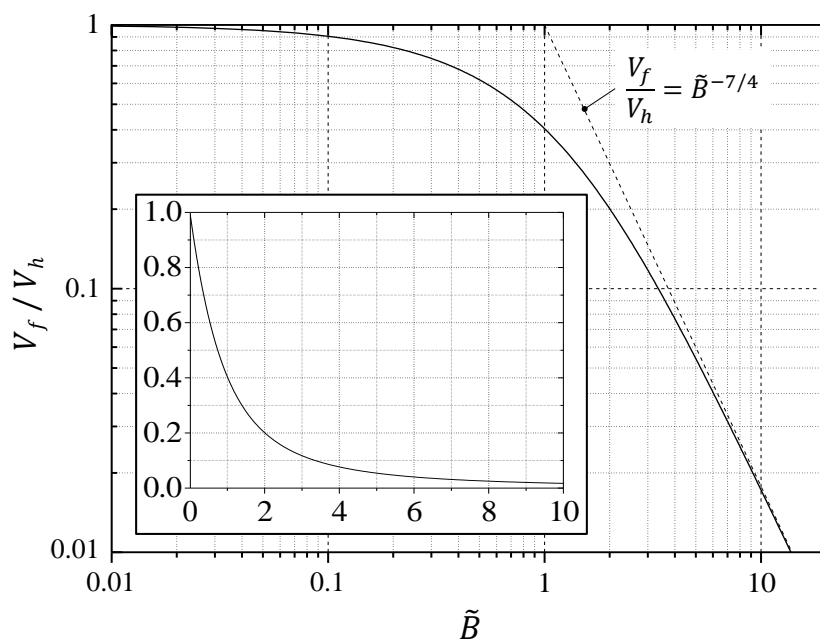


Figure B.1. *FB model chart:  $\tilde{V}_f$  vs.  $\tilde{B}$ .*

# Appendix C

## Demonstrations concerning loop dynamics modeling

### C.1 Simplified velocity profile

The mass conservation equation from 1D homogeneous equilibrium flow model allows expressing Lagrangian time derivative of the density as:

$$\frac{D\rho}{Dt} = \frac{\partial\rho}{\partial t} + u \frac{\partial\rho}{\partial x} = -\rho \frac{\partial u}{\partial x}. \quad (\text{C.1})$$

The density of the two-phase mixture is a function of the energy content of the fluid:

$$\rho = \left( \frac{h - h_l}{h_{lg}\rho_g} + \frac{h_g - h}{h_{lg}\rho_l} \right)^{-1}. \quad (\text{C.2})$$

In this frame, when the fluid is a two-phase mixture, i.e. beyond the saturation enthalpy, variations of  $\rho$  and  $h$  are linked:

$$\delta\rho = -\rho^2 \frac{v_{lg}}{h_{lg}} \delta h. \quad (\text{C.3})$$

The energy conservation equation, neglecting subcooling, pressure transients, potential and kinetic energy (justified for high heat flux values as the ones producing boiling crisis), states:

$$\frac{Dh}{Dt} = \frac{\partial h}{\partial t} + u \frac{\partial h}{\partial x} = \frac{q_v}{\rho}. \quad (\text{C.4})$$

The association of Eq. (C.4) with Eqs. (C.1) and (C.3) gives as a result

$$\frac{D\rho}{Dt} = -\rho^2 \frac{v_{lg}}{h_{lg}} \frac{Dh}{Dt} = -\rho \frac{v_{lg}}{h_{lg}} q = -\rho \frac{\partial u}{\partial x}, \quad (\text{C.5})$$

which implies:

$$\frac{\partial u}{\partial x} = \frac{v_{lg}}{h_{lg}} q_v = \Omega, \quad (\text{C.6})$$

$$\frac{D\rho}{Dt} = -\Omega\rho. \quad (\text{C.7})$$

In words, under the exposed assumptions, no matter if during transient or in steady state, the velocity profile in the heated section is linear with the position and its slope is directly

proportional to local power; furthermore, velocity is uniform in non heated sections (down-comer and riser). This is what is to be expected in the case of an incompressible fluid. Thus, the velocity profile in the heated section can be expressed as:

$$u(x, t) = u_0(t) + \Omega x, \quad (\text{C.8})$$

where  $u_0$  is the velocity at the inlet of the heated section.

## C.2 Alternative approach for the integral momentum equation

Equation (7.25) can also be obtained by considering the momentum equation of individual uniform-cross-section elements. The integral of Eq. (2.29b) for the element  $i$  is:

$$\frac{dH_i}{dt} = -(\rho u^2)_{out,i} + (\rho u^2)_{in,i} + p_{in,i} - p_{out,i} - \Delta p_{frdist,i} + \int_{S_i} \rho (\mathbf{g} \cdot \mathbf{e}_s) ds, \quad (\text{C.9})$$

where  $S_i$  is the segment on  $s$  corresponding to element  $i$ ,  $\Delta p_{frdist,i}$  accounts for the *distributed* friction pressure drop only, and

$$H_i = \int_{S_i} \rho u ds. \quad (\text{C.10})$$

The summation over  $i$  gives:

$$\begin{aligned} \sum_{i=1}^N \frac{dH_i}{dt} &= \frac{dH}{dt} \\ &= (\rho u^2)_{in,1} - (\rho u^2)_{out,N} + \sum_{i=1}^{N-1} [(\rho u^2)_{in,i+1} - (\rho u^2)_{out,i}] + p_{in,1} \\ &\quad - p_{out,N} + \sum_{i=1}^{N-1} (p_{in,i+1} - p_{out,i}) - \sum_{i=1}^N \Delta p_{fr,i} + \sum_{i=1}^N \int_{S_i} \rho (\mathbf{g} \cdot \mathbf{e}_s) ds. \end{aligned} \quad (\text{C.11})$$

The terms  $p_{in,i+1} - p_{out,i}$  correspond to the pressure differences at inter-element interfaces. These can be calculated from regular pipe head loss formulae as

$$p_{in,i+1} - p_{out,i} = \frac{(\rho u^2)_{out,i} - (\rho u^2)_{in,i+1}}{2} - \Delta p_{sing,i}, \quad (\text{C.12})$$

where  $\Delta p_{sing,i}$  is the singular pressure loss at the inter-element point. The association of Eqs. (C.11) and (C.12) gives finally

$$\begin{aligned} \frac{dH}{dt} &= (\rho u^2)_{in,1} - (\rho u^2)_{out,N} + \sum_{i=1}^{N-1} \left[ \frac{(\rho u^2)_{in,i+1} - (\rho u^2)_{out,i}}{2} \right] \\ &\quad + p_{in,1} - p_{out,N} - \sum_{i=1}^N \Delta p_{fr,i} - \sum_{i=1}^{N-1} \Delta p_{sing,i} + \int \rho (\mathbf{g} \cdot \mathbf{e}_s) ds. \end{aligned} \quad (\text{C.13})$$

This equation is identical to Eq. (7.25).

### C.3 Cross section changes

Let us see what gives the integral of the cross section change term of Eq. (7.21) on an interval that contains a single cross section change, between the two points  $x_1$  and  $x_2$ . We will assume that the cross section varies along  $x$  as a derivable function  $A(x)$ . Thus,

$$\int_{s_a}^{s_b} \frac{\partial A}{\partial s} \frac{\rho u^2}{A} ds = \int_{A_a}^{A_b} \frac{\rho u^2}{A} dA = \int_{A_a}^{A_b} \frac{\rho u^2 A^2}{A^3} dA. \quad (\text{C.14})$$

If there is no heating all along the integration interval, mass conservation law gives

$$\frac{\partial}{\partial s} (uA) = 0 \implies uA = u_a A_a = u_b A_b. \quad (\text{C.15})$$

Finally, if  $\rho$  can be considered uniform along the cross section change interval, which is true if this interval is short,

$$\Delta p_{X\text{Change}} = \rho u^2 A^2 \int_{A_a}^{A_b} \frac{1}{A^3} dA = \rho u^2 A^2 \left( \frac{1}{2A_a^2} - \frac{1}{2A_b^2} \right) = \frac{\rho u_a^2}{2} - \frac{\rho u_b^2}{2}. \quad (\text{C.16})$$

As a conclusion, the cross section change has the effect of introducing a pressure contribution equal to the volume-specific kinetic energy change. This result is valid within the frame of validity of the hypotheses leading to Eq. (7.21). However, if the cross section change is not smooth enough for the velocity field to be approximately unidirectional or to avoid recirculation cells at the bigger diameter section, there is a *singular pressure loss* that depends on the geometrical shape and the relative cross section area change. These losses are well studied and the coefficients are tabulated. They may be expressed as:

$$\Delta p_{sing} = K_{sing} \frac{\rho u_{small}^2}{2}, \quad (\text{C.17})$$

where  $u_{small}$  is the fluid velocity in the tube with the smallest diameter.



# List of publications

During the course of the Ph.D. thesis:

## Refereed contributions to journals

- H. Furci, B. Baudouy, A. Four, C. Meuris, “Study of steady state boiling crisis in helium vertically heated natural circulation loops — Part 1: CHF, boiling crisis onset and hysteresis”, *Cryogenics*, *In press*, 2015.
- H. Furci, B. Baudouy, A. Four, C. Meuris, “Study of steady state boiling crisis in helium vertically heated natural circulation loops — Part 2: friction pressure drop lessening”, *Cryogenics*, *In press*, 2015.
- H. Furci, B. Baudouy, “Modelling of dynamics leading to transient boiling crisis in a helium natural circulation loop — Part 1: Static initial condition”, *submitted to the CHATS 2015 Workshop special issue in the Journal Cryogenics*.
- H. Furci, B. Baudouy, A. Four, “Transient DNB induced by heat-load step pulse in a helium vertically heated natural circulation loop — Part 1: Static initial condition”, *to be submitted*.
- H. Furci, B. Baudouy, A. Four, “Transient DNB induced by heat-load step pulse in a helium vertically heated natural circulation loop — Part 2: Dynamic equilibrium initial condition”, *to be submitted*.

## Refereed conferences proceedings

- H. Furci, B. Baudouy, A. Four, C. Meuris, “Transient boiling in two-phase helium natural circulation loops”, *Advances in Cryogenic Engineering*, AIP Conference Proceedings, vol. 1573, pp. 1490–1497, 2014.
- H. Furci, B. Baudouy, A. Four, “Experimental study of stability and transients in a horizontally heated boiling helium thermosyphon”, *Advances in Cryogenic Engineering*, IOP Conference Proceedings, *Presented at the Cryogenic Engineering Conference 2015, Tucson, AZ, USA, and already accepted for publication*.



# References

- [1] M. Andreani and G. Yadigaroglu. Prediction methods for dispersed flow film boiling. *Int. J. Multiphase Flow*, 20:1–51, 1994.
- [2] ATLAS Collaboration. Observation of a new particle in the search for the Standard Model Higgs boson with the ATLAS detector at the LHC. *Phys. Lett. B*, 716(1):1–29, 2012.
- [3] Augyron, Laurence. *Contribution to the study of vertical helium two-phase flows*. PhD thesis, Université Pierre et Marie Curie, 1998.
- [4] V. I. Babitch and Yu. M. Pavlov. *TeploEnergetica*, 9:65, 1985. In Russian, title not available.
- [5] B. Baudouy. Heat and mass transfer in two-phase HeI thermosiphon flow. In *Advances in Cryogenic Engineering*, volume 47 of *AIP Conference Proceedings*, pages 1514–1521, 2002.
- [6] B. Baudouy. Pressure drop in two-phase He I natural circulation loop at low vapor quality. In *Proceedings of the Nineteenth International Cryogenics Engineering Conference*, pages 817–820, 2002.
- [7] B. Baudouy. Heat transfer near critical condition in two-phase He I thermosiphon flow at low vapor quality. In *Advances in Cryogenic Engineering*, volume 49 of *AIP Conference Proceedings*, pages 1107–1114, 2004.
- [8] B. Baudouy. Modeling of a vertical circulation loop in two-phase helium. In *Advances in Cryogenic Engineering*, volume 57 of *AIP Conference Proceedings*, pages 717–723, 2012.
- [9] B. Baudouy, A. Bessette, and A. Four. Modeling of a horizontal circulation open loop in two-phase helium. *Cryogenics*, 53:2–6, 2013.
- [10] B. Baudouy and Cozeret R. Experimental study of film boiling in helium natural convection boiling flow. In *Proceedings of the ICEC 22*, pages 323–327, 2008. International Cryogenic Engineering Conference, Seoul, Korea, 2008.
- [11] D. R. H. Beattie. A note on the calculation of two-phase pressure losses. *Nuclear Engineering and Design*, 25:395–402, 1973.
- [12] L. Benkheira, B. Baudouy, and M. Souhar. Heat transfer characteristics of two-phase HeI (4.2 K) thermosiphon flow. *International Journal of Heat and Mass Transfer*, 50(17-18):3534–3544, 2007.

- [13] L. Benkheira, M. Souhar, and B. Baudouy. Heat and mass transfer in nucleate boiling regime of HeI in a natural circulation loop. In *Advances in Cryogenic Engineering*, volume 51 of *AIP Conference Proceedings*, pages 871–878, 2006. Cryogenic Engineering Conference 2005, Keystone, CO, AUG 29-SEP 02, 2005.
- [14] Benkheira, Lahcène. *Contribution à l'étude des propriétés thermiques et hydrodynamiques d'un écoulement d'hélium normal (He I) diphasique en circulation naturelle pour le refroidissement des aimants supraconducteurs*. PhD thesis, École Doctorale Énergie Mécanique Matériaux de l'Institut National Polytechnique de Lorraine, 2007.
- [15] J. G. Berdnoz and K. A. Müller. Possible high  $T_c$  superconductivity in the Ba-La-Cu-O system. *Z. Phys. B - Condensed Matter*, 64:189–193, 1986.
- [16] L. C. Brodie, D. N. Sinha, C. E. Sanford, and J. S. Semura. Transient heat transfer into liquid helium I. *J Appl Phys*, 48:2882, 1977.
- [17] S. Chatrchyan, others, and CMS Collaboration. The CMS experiment at the CERN LHC. *Journal of Instrumentation*, 3, AUG 2008.
- [18] CMS Collaboration. Observation of a new boson at a mass of 125 GeV with the CMS experiment at the LHC. *Phys. Lett. B*, 716(1):30–61, 2012.
- [19] CMS Collaboration. Observation of a new boson with mass near 125 GeV in pp collisions at  $\sqrt{s}=7$  and 8 TeV. *Journal of High Energy Physics*, 06:081, 2013.
- [20] John G. Collier and John R. Thome. *Convective Boiling and Condensation*. Oxford University Press, 1994.
- [21] Cryodata. *Cryocomp Material Properties version 3.06*, 1999.
- [22] Cryodata. *HEPAK Helium Properties version 3.4*, 1999.
- [23] V. I. Deev, Yu. V. Gordeev, A. I. Pridantsev, V. I. Petrovichev, and V. V. Arkhipov. Hydraulic resistance to forced two-phase flow of helium in narrow channels. *Soviet Atomic Energy*, 42(4):381–383, 1977.
- [24] A. Devred et al. Status of ITER Conductor Development and Production. In *IEEE Transactions on Applied Superconductivity*, volume 22. PACA Reg; CEA; IEEE CSC; Iberdrola Ingenieria & Construcc, SAU; Oxford Superconducting Technol; R KIND; Super Power Inc; Western Superconducting Technol Co Ltd, JUN 2012. 22nd International Conference on Magnet Technology (MT), ITER Org, Marseille, FRANCE, Sep 12-16, 2011.
- [25] G. Disset, C. Berriaud, A. Donati, B. Gastineau, P. Godon, and C. Mayri. R3B-Glad Magnet Cold Mass Manufacture: Coils and Casings Fabrication and Integration. In *IEEE Transactions on Applied Superconductivity*, volume 22, JUN 2012. 22nd International Conference on Magnet Technology (MT), ITER Org, Marseille, FRANCE, Sep 12-16, 2011.
- [26] Y. P. Filippov. Characteristics of horizontal two-phase helium flows - Part I - flow patterns and void fraction. *Cryogenics*, 39(1):59–68, JAN 1999.
- [27] Y. P. Filippov. Characteristics of horizontal two-phase helium flows - Part II: pressure drop and transient heat transfer. *Cryogenics*, 39(1):69–75, JAN 1999.

- 
- [28] H. Furci, Four A., and B. Baudouy. Experimental study of stability and transients in a horizontally heated boiling helium thermosyphon. In *IOP Conference Series: Materials Science and Engineering (MSE)*, In press. Proceedings of the Cryogenic Engineering Conference (CEC), Tucson, AZ, 2015.
- [29] S. Fuzier, B. Baudouy, and S. W. Van Sciver. Steady state pressure drop and heat transfer in HeII forced flow at high Reynolds number. *Cryogenics*, 41:453–458, 2001.
- [30] B. Gastineau, B. Baudouy, C. Berriaud, A. Bessette, D. Bouziat, P. Fazilleau, P. Graf-fin, B. Hervieu, M. Le Bigaut, M. Massinger, C. Mayri, D. Medioni, J. Polinski, and M. Wone. R3B-Glad Magnet R&D Tests Program: Thermosiphon Loop With Horizontal Section, Superconducting Cable Joints at 3600 A, and Reduced Scale “Coil in its Casing” Mock-Up. In *IEEE Transactions on Applied Superconductivity*, volume 22, JUN 2012. 22nd International Conference on Magnet Technology (MT), ITER Org, Marseille, FRANCE, Sep 12-16, 2011.
- [31] R. W. Graham, R. C. Hendricks, Y. Y. Hsu, and R. Friedman. Experimental heat transfer and pressure drop of film boiling liquid hydrogen flowing through a heated tube. *Advances in Cryogenics Engineering*, 6:517–524, 1961.
- [32] D. C. Groeneveld. The occurrence of upstream dryout in uniformly heated channels. In *Proceedings, Fifth International Heat Transfer Conference*, number IV, pages 265–269, Tokyo, 1974.
- [33] D. C. Groeneveld. Post-dryout heat transfer: physical mechanisms and a survey of the prediction methods. *Nuclear Engineering and Design*, 32:283–294, 1975.
- [34] D. C. Groeneveld. The onset of dry sheath condition - a new definition of dryout. *Nuclear Engineering and Design*, 92:135–140, 1986.
- [35] D. C. Groeneveld. Anomalies and other concerns related to critical heat flux. *Nuclear Engineering and Design*, 241:4604–4611, 2011.
- [36] D. C. Groeneveld and G. G. J. Delorme. Prediction of thermal non-equilibrium in the post-dryout regime. *Nuclear Engineering and Design*, 36:17–26, 1976.
- [37] N. Hammouda, D. C. Groeneveld, and S. C. Cheng. An experimental study of sub-cooled film boiling of refrigerants in vertical up-flow. *Int. J. Heat Mass Transfer*, 39(18):3799–3812, 1996.
- [38] N. Hammouda, D. C. Groeneveld, and S. C. Cheng. Two-fluid model of inverted annular film boiling. *Int. J. Heat Mass Transfer*, 40(11):2655–2670, 1997.
- [39] A. P. Hatton and I. S. Hall. Photographic study of boiling on prepared surfaces. In *Proc. 3rd Int. Heat Trans. Conf.*, number IV, pages 24–37, Chicago, 1966.
- [40] Yih-Yun Hsu and Robert W. Graham. *Transport Processes in Boiling and Two-Phase Systems*. American Nuclear Society, 1986.
- [41] I. E. Idel’Cik. *Mémento des pertes de charge (Handbook of hydraulic resistance)*, 3rd Edition. Eyrolles Edition, 1986. [in French].
- [42] Frank P. Incropera, David P. Dewitt, Theodore L. Bergman, and Adrienne S. Lavine. *Fundamentals on Heat and Mass Transfer*, 6<sup>th</sup> edition. John Wiley & sons, 2007.

- [43] Y. Iwasa and B. A. Apgar. Transient heat transfer to liquid helium from bare copper surfaces in a vertical orientation – I: Film boiling regime. *Cryogenics*, 18(5):267–275, 1978.
- [44] Y. Katto. A generalized correlation of critical heat flux for the forced convection boiling in vertical uniformly heated round tubes. *Int. J. Heat Mass Transfer*, 21:1527–1542, 1978.
- [45] Y. Katto. General Features of CHF of forced convection boiling in uniformly heated vertical tubes with zero inlet subcooling. *Int. J. Heat Mass Transfer*, 23:493–504, 1979.
- [46] Y. Katto. Critical heat flux of forced convection boiling in uniformly heated vertical tubes (correlation of CHF in HP-regime and determination of a CHF-regime map). *Int. J. Heat Mass Transfer*, 23:1573–1580, 1980.
- [47] Y. Katto. Critical heat flux. *Int. J. Multiphase Flow*, 20:53–90, 1994.
- [48] Y. Katto and H. Ohno. An improved version of the generalized correlation of critical heat flux for forced convection boiling in uniformly heated vertical tubes. *Int. J. Heat Mass Transfer*, 27:1641–1648, 1984.
- [49] Y. Katto and S. Yokoya. Critical heat flux of liquid helium (I) in forced convective boiling. *Int. J. Multiphase Flow*, 10:401–413, 1984.
- [50] A. Khalil, G. McIntosh, and R. W. Boom. Experimental measurements of void fraction in cryogenic two phase upward flow. *Cryogenics*, 21:411–7, 1981.
- [51] F. Kircher, P. Bredy, et al. Final design of the CMS solenoid cold mass. *IEEE Transactions on Applied Superconductivity*, 10(1):407–410, 2000.
- [52] F. Kircher, P. Bredy, et al. CMS coil design and assembly. In *IEEE Transactions on Applied Superconductivity*, volume 12, pages 395–398, MAR 2002. 17th International Conference on Magnet Technology, Geneva, Switzerland, Sep 24-28, 2001.
- [53] Lakeshore. Cernox temperature sensors. Website <http://www.lakeshore.com/products/cryogenic-temperature-sensors/cernox/models/pages/overview.aspx>. Retrieved Aug 17 2015.
- [54] Y. Lee and K. H. Kim. Inverted annular film boiling. *Int. J. Multiphase Flow*, 13(3):345–355, 1987.
- [55] L. K. H. Leung, D. C. Groeneveld, A. Teyssedou, and F. Aubé. Pressure drops for steam and water flow in heated tubes. *Nuclear Engineering and Design*, 235:53–65, 2005.
- [56] C. P. Marcel, H. F. Furci, D. F. Delmastro, and V. P. Masson. Phenomenology involved in self-pressurized, natural circulation, low thermo-dynamic quality, nuclear reactors: The thermal-hydraulics of the CAREM-25 reactor. *Nuclear Engineering and Design*, 254:218–227, JAN 2013.
- [57] Meamer El Nakla, D. C. Groeneveld, and S. C. Cheng. Experimental study of inverted annular film boiling in a vertical tube cooled by R-134a. *Int. J. Multiphase Flow*, 37:67–75, 2011.

- 
- [58] S. Nukiyama. Maximum and minimum values of heat transmitted from a metal to boiling water under atmospheric pressure. *J. Soc. Mech. Eng.*, 37:206, 1934.
- [59] N. T. Obot and M. Ishii. Two-phase flow transition criteria in post-dryout region based on flow visualization experiments. *Int. J. Heat Mass Transfer*, 31(12):2559–2570, 1988.
- [60] H. Ogata and S. Sato. Critical heat flux for two-phase flow of helium I. *Cryogenics*, 13:610–611, 1973.
- [61] Yu. M. Pavlov and V. I. Babitch. Transient burn-out in liquid helium with rapid rise of heat flux. *Cryogenics*, 27:641–644, 1987.
- [62] Horst Rogalla and Peter H. Kes, editors. *100 Years of Superconductivity*. CRC Press, 2011.
- [63] A. Sakurai, M. Shiotsu, K. Kata, and Y. Takeuchi. Quasi-steady nucleate boiling and its life caused by large stepwise heat input in saturated pool liquid He I. *Cryogenics*, 29:597–601, 1989.
- [64] C. Schmidt and P. Turowski. Heat transfer to liquid helium in vertical cooling channels with constant and pulsed heat flow. Technical report, Institut für Experimentelle Kernphysik, Gesellschaft für Kernforschung M.B.H., May 1974. In German.
- [65] Meinhard T. Schobeiri. *Fluid Mechanics for Engineers*. Springer, 2010.
- [66] M. Shah. Improved general correlation for critical heat flux during upflow in uniformly heated vertical tubes. *Heat and Fluid Flow*, 8(4):326–335, 1987.
- [67] M. Shiotsu, K. Hata, and A. Sakurai. Comparison of transient heat transfer characteristics for large stepwise heat input in He I and He II. *Cryogenics*, 32:455–460, 1992.
- [68] D. N. Sinha, L. C. Brodie, J. S. Semura, and F. M. Young. Premature transition to stable film boiling initiated by power transients in liquid nitrogen. *Cryogenics*, 19(4):225–230, 1979.
- [69] D. N. Sinha, J. S. Semura, and L. C. Brodie. Homogeneous nucleation in  $^4\text{He}$ : A corresponding-states analysis. *Physical Review A*, 26(2):1048–1061, 1982.
- [70] D. N. Sinha, J. S. Semura, and L. C. Brodie. Superheating limits of liquid helium I. *Cryogenics*, 22(8):391–394, 1982.
- [71] G. Steward. Transient helium heat transfer phase I-static coolant. *Int. J. Heat Mass Transf.*, 21:863–874, 1978.
- [72] V. I. Subbotin, V. I. Deev, A. I. Pridantsev, V. K. Andreev, V. V. Arkhipov, V. N. Nokivov, A. N. Savin, and V. V. Solodovnikov. Heat transfer and hydrodynamics in cooling channels of superconducting devices. *Cryogenics*, 25:261–5, 1985.
- [73] A. E. Vardy and J. M. B. Brown. Transient turbulent friction in smooth pipe flows. *Journal of Sound and Vibration*, 259(5):10111036, 2003.
- [74] G. B. Wallis. *One-dimensional two-phase flow*. McGraw-Hill, 1969.
- [75] M. N. Wilson. *Superconducting Magnets*. Clarendon Press, 1986.

- [76] M. K. Wu et al. Superconductivity at 93 K in a new mixed-phase Y-Ba-Cu-O compound system at ambient pressure. *Phy. Rev. Lett.*, 58:908–910, 1987.
- [77] I. L. Yarmak and V. M. Zhukov. Forced liquid helium flow transient heat transfer in a narrow channel under step heat flux. *Cryogenics*, 32(8):729–736, 1992.
- [78] P. Zanocco, M. Gimenez, and D. Delmastro. Modeling aspects in linear stability analysis of a self-pressurized, natural circulation integral reactor. *Nuclear Engineering and Design*, 231(3):283–301, JUL 2004.
- [79] H. K. Zust and W. B. Bald. Experimental observations of flow boiling of liquid helium-I in vertical channels. *Cryogenics*, 21(11):657–666, 1981.

# Experimental study of stability and transients in a horizontally heated boiling helium thermosyphon

H Furci\*, A Four, B Baudouy

CEA Saclay, Irfu/SACM, 91191 Gif-sur-Yvette, France

\*Corresponding author: [hernanfurci@gmail.com](mailto:hernanfurci@gmail.com)

**Abstract.** Experiments were conducted on a liquid helium natural circulation loop with a 4 m long horizontal heated section. Wall temperatures on the heated section, mass flow rate and pressure drop were measured in steady and transient regimes. The stability of the loop has been studied and the power stability limits have been found. Also, different heating configurations were explored and their drawbacks and benefits were observed. The result is that the loop is stable only above a non-zero low power and below a certain upper power limit. The distance from the heating to the vertical riser affects the stability range. It has been found that instabilities at low power or transients following a low power step pulse can produce considerable temperature oscillations, potentially dangerous from the magnet protection point of view.

## 1. Introduction

Natural circulation loops are used as cooling systems in superconducting magnet devices. Examples are the CMS at CERN [1, 2] or R3B-GLAD for GSI [3]. Within the R&D program for the design of the R3B-GLAD spectrometer [4], a study of boiling helium natural circulation loops with horizontal heated sections was started, with the aim of validating this cooling method. In that opportunity the operation of the system was only studied at very low heat input, corresponding to the design requirements. Later, a study was conducted on a wider power range so as to characterize the steady state operation, experimentally and theoretically [5].

In this work we push further the study by investigating the operation regimes that are not steady; either resulting from the fact that the equilibrium of the system is unstable, or from the response to a time varying heat load.

## 2. Experimental setup

The experiments were conducted in the same experimental facility as those presented in references [4, 5] with some modifications. The loop, schematized in figure 1, is composed of an upper liquid helium reservoir and a U-shaped circuit below it. The reservoir, with 50 l capacity, acts as a phase separator. From its bottom descends a 1.4 m long, 4 cm diameter tube, *the descending section*. Then, a horizontal section reduces diameter and connects it to the *ascending section*. The latter is formed by three elements: a *short vertical section* (non-heated, 17 cm long), a horizontal spirally arranged 5 m long tube—which will receive special attention in the next paragraph—and another long vertical section (1.1 m) that we will call *riser* and reenters the bottom of the reservoir. The whole is inside a 2 m deep well cryostat, with a liquid nitrogen shield, reflective aluminum screens and continuous vacuum pumping.

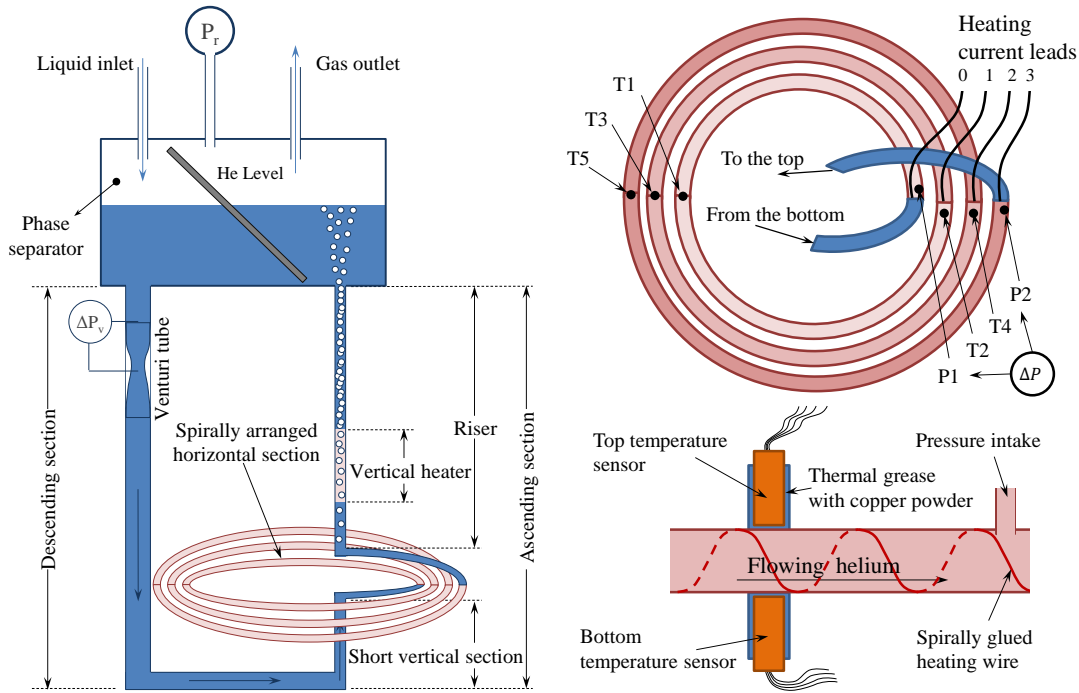


**Figure 1.** Experimental setup diagrams. Left: the elements of the loop; right top: the horizontal section with its instrumentation points; right bottom: the position of the temperature sensors on the tube and the pressure intakes.

**Table 1.** Geometrical parameters of the test section: positions of the temperature and pressure intakes and heating lengths in the 3 configurations. All length in meters.

T1	T2	T3	T4	T5	P1	P2	L(0-1)	L(0-2)	L(0-3)
0.613	1.318	1.968	2.738	3.440	0.018	4.255	1.318	2.738	4.273

The horizontal section of the loop is the *heated section*, shown in figure 1 on the top right; of its 5 m length, 4.27 m can be heated by a spirally glued wire on its external wall (lighter color in the figure). The section is arranged in 3 turns, and the heating can be independently set on one, two or the three of the turns by choosing two of the four current leads (current lead 0 plugs at the entrance of turn 1 and 1, 2 and 3 at the exit of the respective turns). Before the entrance (at the inner turn) and after the exit (outer turn), there are short non-heated horizontal sections (of around 40 cm length). The experiments are conducted by controlling the power applied to the horizontal heated section and on which turns it is applied. The long vertical section has a 17 cm long region that can be heated by a spirally glued wire too. This allows modifying the mass flow rate of the circuit without acting on the main power supply.

Internal wall temperature is measured non-intrusively by placing Lake Shore Cernox AA sensors on the exterior of the heated sections. This can be done because the material of the test section is hyper pure copper, with RRR of 145, and the thermal conductivity and diffusivity are extremely high. There are five couples of temperature sensors placed at the five positions given in table 1 and shown in figure 1. For each couple, one of the sensors is at the bottom of the tube and the other is at the top, to see if phase stratification could induce heat transfer differences. The total mass flow rate is measured with a Venturi tube on the descending section.

**Table 2.** Loop stability power limits. NHHL: non-heated horizontal length after the heated section.

Configuration	NHHL (m)	Lower limit (W)	Upper limit (W)
0-3	0.360(10)	1.2(4)	78(3)
0-2	1.895(10)	2.8(4)	71(2)
0-1	3.315(10)	3.7(2)	60(1)

The Venturi pressure drop and the heated section pressure drop are measured with Validyne differential pressure transducers DP1020 and DP1022, respectively.

The loop was studied for three heating configurations: configuration 0-3: the three turns are heated; configuration 0-2: only the first and second turns are heated; configuration 0-1: only the first turn is heated. The identification numbers refer to the current leads used for the electrical connection of the heater (see figure 1). Thus, the heating configurations differ only in the distance from the end of the heated section to the vertical riser.

### 3. Steady natural circulation and stability limits

The first study consisted in applying a quasi-steadily increasing power to the heated section, i.e. increasing gradually at small steps. At very low power, it was not possible to achieve a stable circulation. The system would exhibit regular mass flow rate bursts, as had already been reported before [4]. The effect was more pronounced with heating configurations 0-1 and 0-2, as the required power for stability was higher. Once the steady condition at steady power was achieved, the mean values of wall temperature, mass flow rate and heated section pressure drop were recorded as a function of power. The values thus obtained are presented in figure 2 as a function of applied heat flux. In order to be able to compare the three configurations, inlet mass flow rate  $\dot{m}$  and pressure drop  $\Delta P$  are also plotted as a function of applied total power. At a certain power value, this time high, the system became unstable again, i.e. a growing oscillating perturbation appears on mass flow rate and the other variables. Thereafter, the time dependent signals were recorded instead. Thus, there are two stability limits, a lower one and an upper one. Stability limits for the three configurations are presented in table 2. The system is stable (constant mass flow rate) in between these values.

Within the stability power range, it is remarkable that the mass flow rate of the loop shows no appreciable difference between heating configurations, as a function of the total heating power. The  $\dot{m}$  dependence on heat flux shows an increase at low power, a maximum and then a decrease. At low power, it is the buoyant force which is the more responsive to the heat flux, producing the  $\dot{m}$  increase. At high power, resistive forces (friction and acceleration gradients) increase strongly with  $q$  (mainly due to the increase in quality) while the gravity term varies only slightly (void fraction varies slowly as a function of quality when quality is high). This results in a decrease of  $\dot{m}$ .  $\Delta P$  is slightly higher for identical total power as the heating is concentrated in a shorter region at the entrance. This results in the increase of local velocity at every point of the horizontal section and riser, which in time increases the friction pressure drop. However, these differences are not high enough to produce a significant effect on mass flow rate.

The wall temperature evolutions show that within the stable region no boiling crisis (dry wall heat transfer regimes) happens. The values are typical of nucleate boiling helium flow in ducts [6, 7]. The differences between configurations are not significant, and are presumably due to the fact that at a given wall heat flux  $\dot{m}$  varies from one configuration to another.

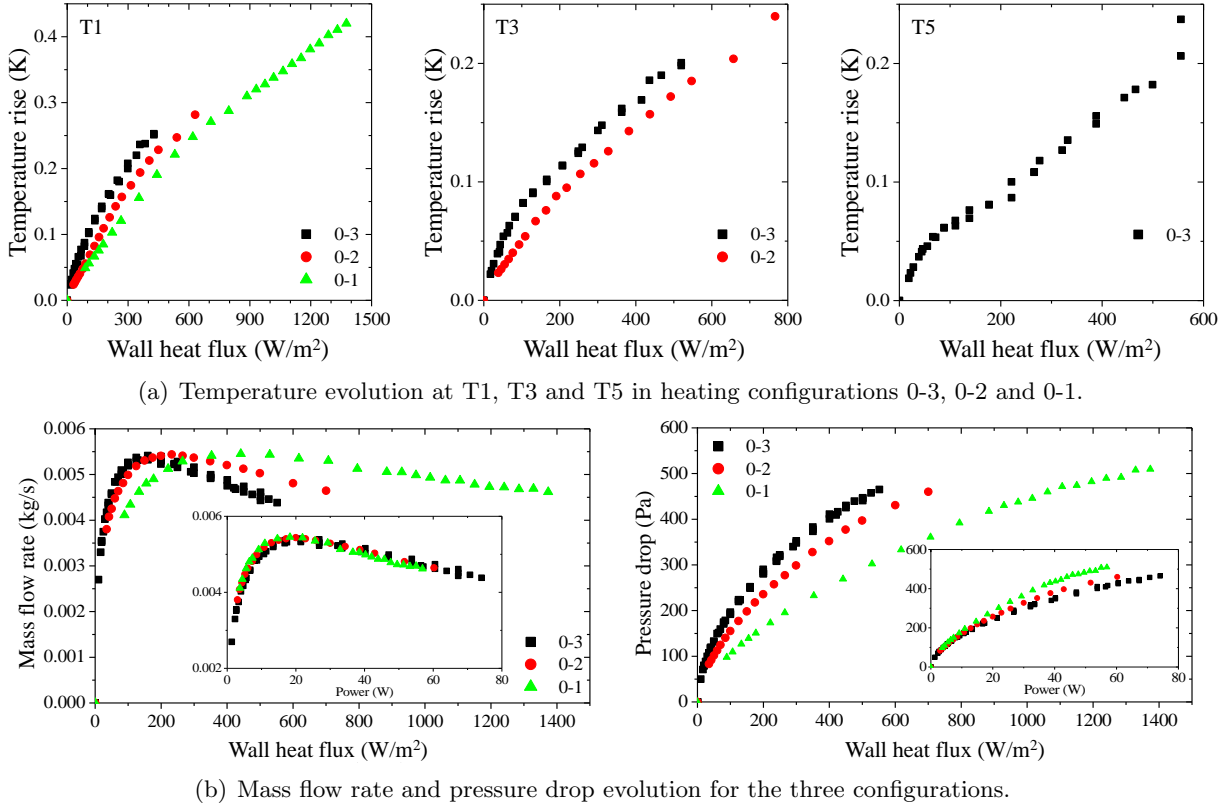


**Figure 2.** System evolution in steady state.

#### 4. The unstable oscillations

Outside the stability limits, it was not possible to observe a steady behavior of the loop. Instead, periodic oscillations were observed. The oscillations are not sinusoidal, but consist of an alternation of periods of apparent hydraulic stability with regular mass flow rate bursts ( $\dot{m}$ -bursts). This puts forward the strong non-linear nature of the phenomenon.

Examples of this behavior for the low power instabilities is presented in figure 3. At low power, the exit quality is strongly influential on density. Furthermore, the equilibrium mass flow rate is low, which results in long transit time. The instabilities are the result of an important transport delay of quality perturbations in response to inlet velocity perturbations from the horizontal heated section, where vapor is produced, to the vertical section of the loop, where it acts on the buoyant force. For example, a positive perturbation in velocity produces a quality decrease front in the heated section that travels at the velocity of the flow. While the front has not reached the riser, no significant effect on the velocity is observed, but as soon as that happens, the buoyant force diminishes, which will induce a quality increase front. When this one reaches the riser, a  $\dot{m}$  peak may happen, which will result in a new low quality front. For long time delays (at low power), the alternation of low and high quality regions may be amplified and at some point, the loop could be completely at rest (no inlet velocity), thus accumulating vapor in the heated section. When the vapor reaches the riser, a  $\dot{m}$ -burst takes place, until the horizontal section is clean of vapor. The high speed of the burst results in an extremely low quality front, so the inlet velocity will quickly decrease to zero again, and the process restarts.

In the high power instability cases, the more influential forces on mass flow rate evolution are the resisting friction and acceleration pressure gradients. The equilibrium mass flow rate diminishes with heat flux, in order to increase quality and produce a greater buoyant force to counterbalance the resisting terms. The friction and acceleration terms can respond immediately

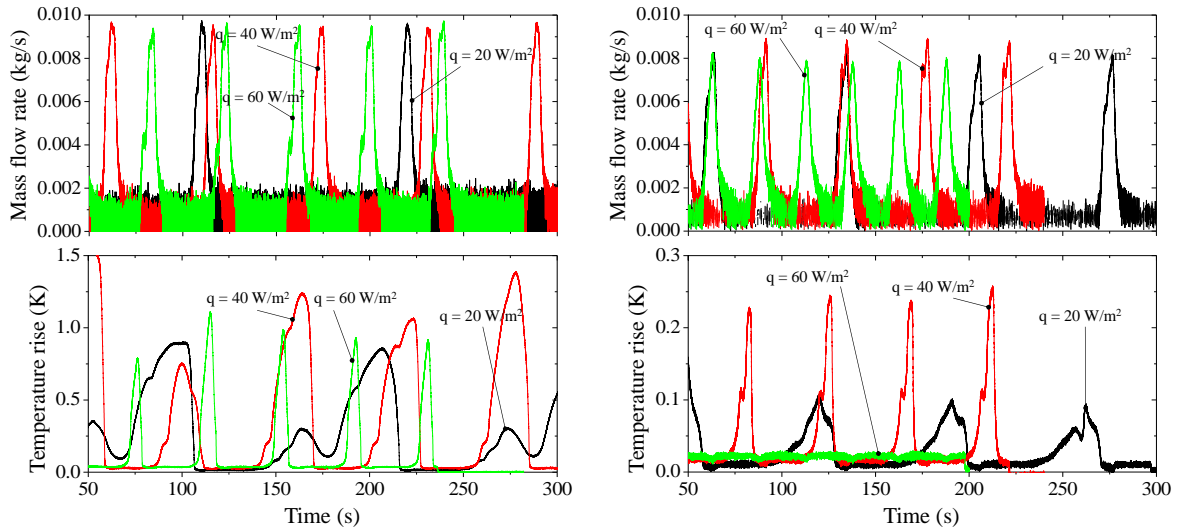


**Figure 3.** Periodic instabilities at low power. Left: configuration 0-2; right: configuration 0-1. The presented temperatures are measured at T1.

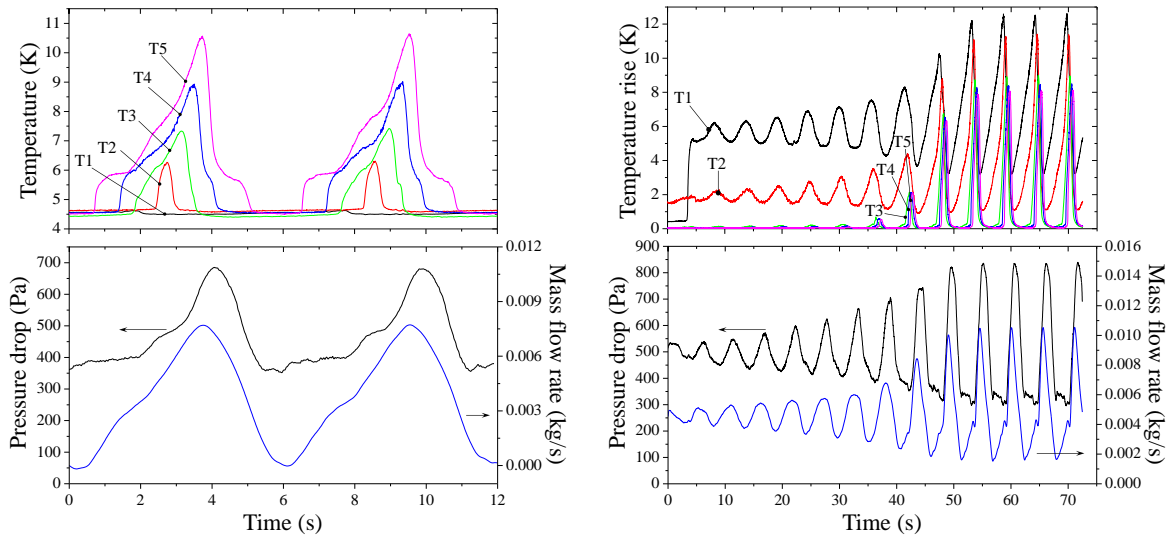


**Figure 4.** Limit cycles of the high power instability. Left: configuration 0-3,  $q = 750 \text{ W/m}^2$ ; right: configuration 0-1,  $q = 1465 \text{ W/m}^2$ .

to inlet velocity perturbations, but the gravity term presents a transport lag. At a certain power at which the resisting forces' influence is dominant, this lag between opposing forces produces instability. The time evolution of the variables in this kind of instability are shown in figure 4. In the case on the right it is possible to observe how the system amplifies the perturbation away from the equilibrium point. Initially, the growth of  $\dot{m}$  is that of a linear second order system (exponentially modulated sinusoidal), but when the size of oscillations is too high the behavior becomes periodic. In dynamic systems jargon, the equilibrium point is linearly unstable and there exists a limit cycle attractor. Some experimental limit cycles in the phase space  $(\dot{m}, \frac{d\dot{m}}{dt})$  are shown in figure 5. In particular, for the case of configuration 0-3 we can appreciate how the limit cycles amplitude increases as power increases.

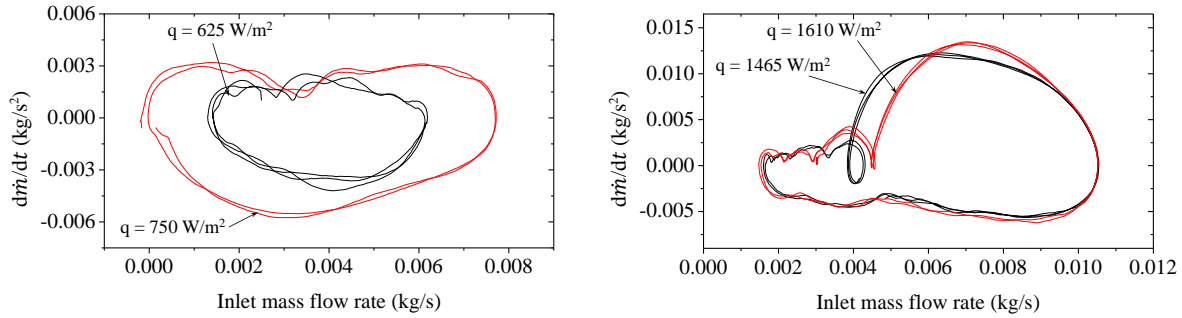


**Figure 5.** Limit cycles in the phase space  $(\dot{m}, \frac{d\dot{m}}{dt})$ . Left: configuration 0-3; right: configuration 0-1.

### 5. Transient response to power steps

The time response of the loop to a varying heat load was studied by applying a power step pulse on the horizontal heated section, with the system initially at rest ( $q = 0$ ). The time evolution of the measured variables was recorded. The general behavior of the loop in response to this kind of solicitation consists of two distinct stages. Initially, there is a stage of *vapor accumulation in the horizontal section*, during which the produced vapor is not capable of creating buoyant force. During this lapse of time there is no appreciable inlet flow. However, it is presumable that phase change expansion will produce a velocity gradient from the entry towards the exit of the heated section and that phase stratification will be more marked where velocity is low, i.e. near the entrance. This movement will originate the second stage of the transient: vapor reaches the vertical riser and creates buoyant force. At this point, natural circulation (positive inlet flow) starts. If the applied power is in the stability range then the flow may oscillate before finally reaching the steady state. Otherwise, the oscillations will conduce to the limit cycles.

The duration of the first stage is directly determined by the transit time of vapor to the riser. The length of the horizontal section, specially the non-heated length downstream the heated section, plays a significant role. Furthermore, heat transfer in the two stages is substantially different. The presence of low velocity at the entrance of the heated section in the initial stage and the consequent stratification can be very critical with respect to the steady state operation. In the following section we will present a particular case that can have harmful consequences from the magnet protection point of view.

### 6. Low power, high temperature excursions

A singular situation was observed at relatively low heat flux. The stepwise application of a heat flux on the system initially in static condition (no heat flux applied) can produce a dangerous temperature evolution. Dangerous in the sense that if in steady state at this heat flux only nucleate boiling regime had been observed, during the transient the wall temperature goes to very higher values during some period of time, up to a few Kelvins. Examples of this situation are presented in figure 6, where a low heat flux of  $100 \text{ W/m}^2$  was applied in stepwise manner in two configurations.

The deterioration of the heat transfer on the heated section, manifested by an appreciable temperature excursion, may be explained by the stratification of the flow during the first stage of the transient. During this stage, there will be a non uniform stratified flow driven by the vapor leaving the heated section, with zero velocity at the entrance of the heated section (the measured inlet mass flow rate is zero). For this reason, the stratification effects are the highest in this region and, at some point, with void fraction increase the most of the perimeter here is dry. The perimeter-averaged heat transfer coefficient drops; furthermore, the vapor may overheat,

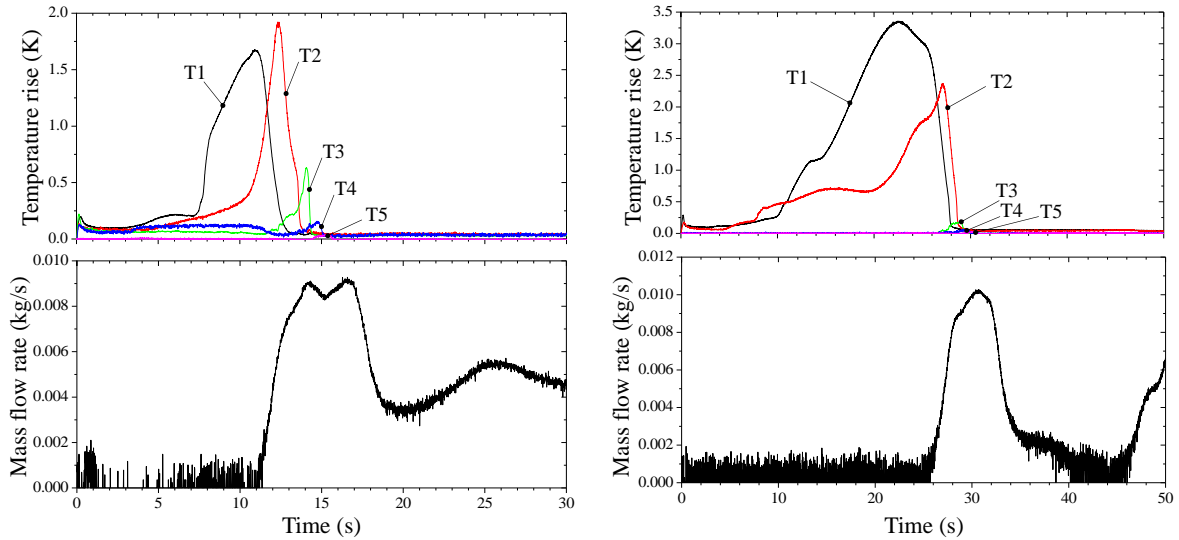


**Figure 6.** Examples of low heat flux, high temperature excursions. Left:  $q_f = 100 \text{ W/m}^2$ , config. 0-2; right:  $q_f=100\text{W/m}^2$ , config. 0-1.

i.e. saturation thermal equilibrium may be lost. This is actually observed by the temperature increases in the non heated region after the  $\dot{m}$ -burst, in figure 6 at the right. This onsets wall overheating. Then, the second stage starts when vapor reaching the riser triggers a  $\dot{m}$ -burst by hydrostatic unbalance. This will promote a cold front from the down-comer into the heated section, and also, the speed increase will promote mixing, breaking phases stratification. That is why, when the mass flow rate appears, the high temperature excursion ends with a transport delay proper to each temperature measurement position.

The effect of the constant presence of a mass flow rate during the first stage of the transient was studied. A flow was created using the auxiliary heating in the riser; the control parameter was the electrical current in the heating wire, which has a  $2 \Omega$  resistance. The results of this experiment are shown in figure 7. A significant mitigating effect on the temperature excursion was observed as the auxiliary heating power (and  $\dot{m}$ ) was increased. The highest power value is  $0.45 \text{ W}$  (for  $I=0.5 \text{ A}$ ) and initial  $\dot{m}$  values are below  $1.5 \text{ g/s}$ . At such low  $\dot{m}$  values the Venturi flow-meter gives a very low pressure drop ( $\approx 1 \text{ Pa}$ ), reason why  $\dot{m}$  is difficult to measure. However, the heated section pressure drop is more sensitive and shows unequivocally increasing values in the first stage as the current is increased, confirming the presence of flow. With the increase of heating current, a diminution of the maximum temperature during the transient is observed up to the point of complete attenuation of the excursion at  $500 \text{ mA}$  of heating current ( $0.45 \text{ W}$ ). This effect is a combination of the permanent presence of flow —that promotes mixing and delays the onset of heat transfer deterioration (see the temperature plots)— and the anticipation of the  $\dot{m}$ -burst due to the diminution of vapor transit time to the riser on the non-heated section (see the  $\dot{m}$  plot)—that puts an end to the excursion—.

## 7. Conclusions

The dynamics of a horizontally heated, boiling helium, natural circulation loop have been studied. It has been demonstrated that this kind of system presents important non-stable behavior at too low or too high heating power. The stability limits are sensitive to the non-heated horizontal length downstream the heated section. Instabilities manifest by the dynamics diverging from the equilibrium point towards a limit cycle, which depends on the applied power. These instabilities can present at some moment of the oscillations very low mass flow rates. This

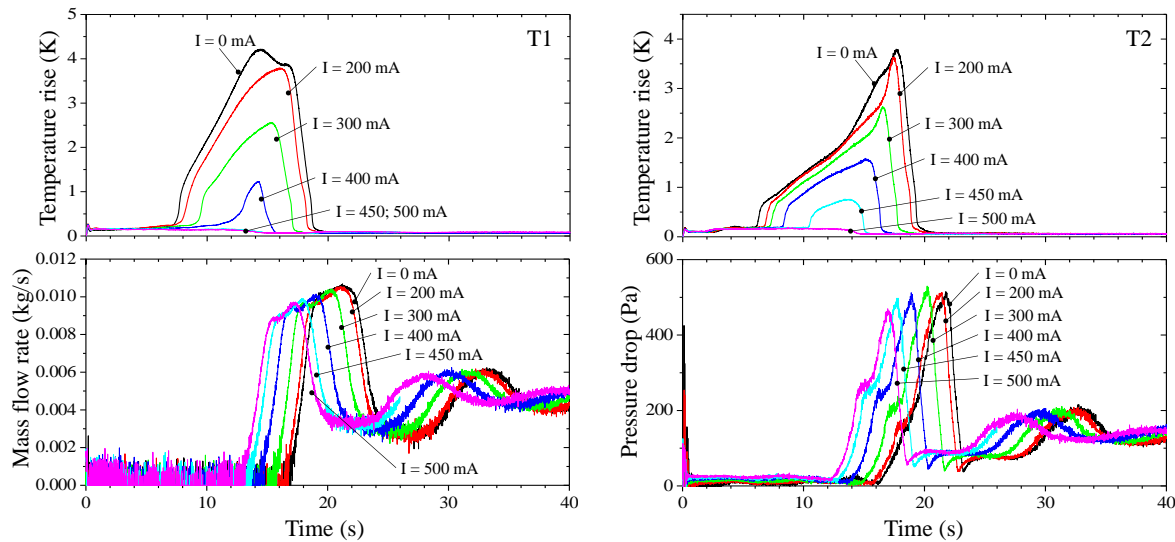


**Figure 7.** Mitigation of low heat flux, high temperature excursions by vertical heater current. Configuration 0-1;  $q_f = 150 \text{ W/m}^2$ ; top left: T1; top right: T2; bottom left:  $\dot{m}$ ; bottom right:  $\Delta P$ .

can have adverse effects on heat transfer, such as the onset of boiling crisis at low power. This can happen too in the case of the stepwise application of a low heat flux. The lag between the step pulse and the start of the circulation allows the fluid to stratify, which conduces finally to a heat transfer deterioration. It has been shown that the resulting temperature excursions can be harmful from the superconducting magnet protection margins viewpoint. However, the constant presence of a low mass flow rate has been shown to be a good solution for avoiding the undesired phenomenon.

## References

- [1] Bredy P, Juster F P, Baudouy B, Benkheira L and Cazanou M 2006 Experimental and theoretical study of a two phase helium high circulation loop *Advances in Cryogenic Engineering, Vols 51A and B (AIP Conference Proceedings vol 823)* pp 496–503 Cryogenic Engineering Conference 2005, Keystone, CO, AUG 29-SEP 02, 2005
- [2] Baudouy B 2002 Heat and mass transfer in two-phase HeI thermosiphon flow *Advances in Cryogenic Engineering (AIP Conference Proceedings vol 47)* pp 1514–1521
- [3] Gastineau B, Mayri C, Baudouy B, Berriaud C, Dissot G, Donati A, Ducret J E, Eppelle D, Fazilleau P, Graffin P, Jannin J L, Loiseau D, Lottin J P, Massinger M, Pes C, Queinec Y, Sun Z, Charon P, Contrepolis P and Neyrial H 2010 *IEEE Transactions on Applied Superconductivity* **20** 328–331 21st International Conference on Magnet Technology (MT-21), Anhui, PEOPLES R CHINA, OCT 18-23, 2009
- [4] Gastineau B, Baudouy B, Berriaud C, Bessette A, Bouziat D, Fazilleau P, Graffin P, Hervieu B, Le Bigaut M, Massinger M, Mayri C, Medioni D, Polinski J and Wone M 2012 R3B-Glad Magnet R&D Tests Program: Thermosiphon Loop With Horizontal Section, Superconducting Cable Joints at 3600 A, and Reduced Scale “Coil in its Casing” Mock-Up *IEEE Transactions on Applied Superconductivity* vol 22 22nd International Conference on Magnet Technology (MT), ITER Org, Marseille, FRANCE, Sep 12-16, 2011
- [5] Baudouy B, Bessette A and Four A 2013 *Cryogenics* **53** 2–6
- [6] Furci H, Baudouy B, Four A and Meuris C 2014 Transient Boiling in Two-Phase Helium Natural Circulation Loops *Advances in Cryogenics Engineering (AIP Conference Proceedings vol 1573)* pp 1490–1497 Joint Conference of the Transactions of the Cryogenic Engineering Conference (CEC) / Transactions of the International Cryogenic Materials Conference, Anchorage, AK, JUN 17-21, 2013
- [7] Benkheira L, Baudouy B and Souhar M 2007 *International Journal of Heat and Mass Transfer* **50** 3534–3544